

1-1-2002

## Heat transfer in microchannel geometries during condensation of R-134a

Todd Matthew Bandhauer  
*Iowa State University*

Follow this and additional works at: <https://lib.dr.iastate.edu/rtd>

### Recommended Citation

Bandhauer, Todd Matthew, "Heat transfer in microchannel geometries during condensation of R-134a" (2002). *Retrospective Theses and Dissertations*. 19790.  
<https://lib.dr.iastate.edu/rtd/19790>

This Thesis is brought to you for free and open access by the Iowa State University Capstones, Theses and Dissertations at Iowa State University Digital Repository. It has been accepted for inclusion in Retrospective Theses and Dissertations by an authorized administrator of Iowa State University Digital Repository. For more information, please contact [digirep@iastate.edu](mailto:digirep@iastate.edu).

Heat transfer in microchannel geometries during condensation of R-134a

by

Todd Matthew Bandhauer

A thesis submitted to the graduate faculty  
in partial fulfillment of the requirements for the degree of  
**MASTER OF SCIENCE**

Major: Mechanical Engineering

Program of Study Committee:  
Srinivas Garimella (Major Professor)  
Michael B. Pate  
Ambar K. Mitra

Iowa State University

Ames, Iowa

2002

Copyright © Todd Matthew Bandhauer, 2002. All rights reserved.

Graduate College  
Iowa State University

This is to certify that the master's thesis of:

Todd Matthew Bandhauer

has met the thesis requirements of Iowa State University

Signatures have been redacted for privacy

---

*To my wife, Karen, who is a ray of light in a world of darkness, my inspiration, and  
my soul mate*

**TABLE OF CONTENTS**

<b>Table of Contents</b>	<b>iv</b>
<b>List of Figures</b>	<b>vii</b>
<b>List of Tables</b>	<b>xiv</b>
<b>Nomenclature</b>	<b>xv</b>
<b>Acknowledgements</b>	<b>xx</b>
<b>Abstract</b>	<b>xxi</b>
<b>Chapter One: Introduction</b>	<b>1</b>
<b>Chapter Two: Literature Review</b>	<b>4</b>
<b>Previous Research on Large Diameter Tubes</b>	<b>4</b>
Gravity-Driven Condensation Heat Transfer	4
Shear-Driven Condensation Heat Transfer	10
<b>Previous Research on Small Diameter Tubes</b>	<b>19</b>
<b>Summary</b>	<b>24</b>
<b>Need for Further Research</b>	<b>25</b>
<b>Chapter Three: Experimental Setup and Procedures</b>	<b>27</b>
<b>Test Sections</b>	<b>27</b>
<b>Experimental Facility</b>	<b>30</b>
Requirements for Accurate Heat Transfer Coefficient Determination	30

Evaporator, Pre- and Post-Condensers	30
Test Section	32
Instrumentation and Data Acquisition	34
<b>Experimental Procedures</b>	<b>35</b>
System Charging	35
System Start-Up	35
Test Condition Establishment	37
<b>Chapter Four: Data Analysis and Results</b>	<b>44</b>
<b>Rectangular Channels</b>	<b>44</b>
Test Section S30 Heat Duty and Uncertainty	44
Test Section S30 Heat Transfer Coefficient and Uncertainty	60
Test Section RK15 Heat Transfer Coefficient and Uncertainty	66
Significance of the Fin Efficiency of the Port Walls	67
<b>Circular Channels</b>	<b>67</b>
Test Section C20 Heat Transfer Coefficient and Uncertainty	67
Test Section C30 Heat Transfer Coefficient and Uncertainty	70
Test Section C60 Heat Transfer Coefficient and Uncertainty	70
<b>Other Microchannel Shapes</b>	<b>71</b>
Test Section B32 Heat Transfer Coefficient and Uncertainty	71
Test Section N21 Heat Transfer Coefficient and Uncertainty	71
Test Section T33 Heat Transfer Coefficient and Uncertainty	72
Test Section W29 Heat Transfer Coefficient and Uncertainty	72
<b>Chapter Five: Discussion of Results</b>	<b>80</b>
<b>Effect of <math>D_h</math> on Condensation Heat Transfer Coefficients</b>	<b>80</b>
<b>Effect of Tube-Shape on Condensation Heat Transfer Coefficients</b>	<b>85</b>

<b>Assignment of Flow Regimes to the Data</b>	<b>90</b>
<b>Comparison with Existing Correlations</b>	<b>97</b>
Intermittent Flow Data	101
Annular Flow Data	110
Flow Regime-Based Correlations	122
Summary	128
<b>Heat Transfer Models</b>	<b>128</b>
Circular Microchannels	129
Non-Circular Microchannels	150
<b>Chapter Six: Conclusions</b>	<b>170</b>
<b>References Cited</b>	<b>173</b>
<b>Appendix A: Test Section Data Point Ranges</b>	<b>179</b>
<b>Appendix B: Flow Transition Equations</b>	<b>184</b>
<b>Appendix C: Non-Circular Tube Flow Regime Maps</b>	<b>186</b>
<b>Appendix D: Circular Tube Comparison with Literature</b>	<b>193</b>

## LIST OF FIGURES

1.	Schematic of a Microchannel-Tube, Multi-Louver Fin Heat Exchanger	2
2.	Representative Microchannel Test Section	27
3.	Schematic of Cross-Sections for the Microchannel Test Sections (All Measurements are in mm)	28
4.	Microchannel Phase-Change Heat Transfer Test Facility	31
5.	Range of Data Points for Test Section S30	41
6.	Test Section Primary and Secondary Coolant Flows	45
7.	Cross-section of Test Section S30	47
8.	Cross-section of Outer Tube Jacket	48
9.	Primary Loop Pressure Drop versus Water Volumetric Flow Rate	49
10.	Micropump Series 5000 H21 Pump Curve	50
11.	Pump Heat Addition versus Flow Rate for the Micropump Series 5000 Model H21 Pump	51
12.	Resistance Network for the Ambient Heat Loss from the Secondary Heat Exchanger	52
13.	Side (a) and Front (b) View Sketches of the Micropump Series 5000 Model H21 Pump Housing (Measurements are in mm; Drawing Not to Scale)	58
14.	Side (a) and Front (b) View Sketch of the Dwyer RMC Series Volumetric Flow Meter (Measurements are in mm; Drawing Not to Scale)	58
15.	Test Section S30 Heat Duty versus Quality for $150 < G < 750 \text{ kg/m}^2\text{-s}$	61
16.	Test Section and Secondary Loop Heat Duties, Ambient Heat Loss, and Pump Heat Addition for Test Section S30 and $G = 450 \text{ kg/m}^2\text{-s}$	60
17.	Heat Transfer Resistance Ratio versus Mass Flux for Test Section S30	64
18.	Test Section S30 R-134a Condensation Heat Transfer Coefficient versus Quality for $150 \text{ kg/m}^2\text{-s} < G < 750 \text{ kg/m}^2\text{-s}$	66
19.	Heat Transfer Resistance Ratio versus Mass Flux for Test Section RK15	67
20.	Test Section RK15 R-134a Condensation Heat Transfer Coefficient versus Quality for $450 \text{ kg/m}^2\text{-s} < G < 750 \text{ kg/m}^2\text{-s}$	68
21.	Test Section S30 Refrigerant-side and Water-side Fin Efficiency	69
22.	Test Section RK15 Refrigerant-side and Water-side Fin Efficiency	69
23.	Refrigerant to Water Resistance Ratio for Test Section C20	73

24.	R-134a Condensation Heat Transfer Coefficient versus Quality for $300 \text{ kg/m}^2\text{-s}$ $< G < 750 \text{ kg/m}^2\text{-s}$ in Test Section C20	73
25.	Refrigerant to Water Resistance Ratio for Test Section C30	74
26.	R-134a Condensation Heat Transfer Coefficient versus Quality for $150 \text{ kg/m}^2\text{-s}$ $< G < 750 \text{ kg/m}^2\text{-s}$ in Test Section C30	74
27.	Refrigerant to Water Resistance Ratio for Test Section C60	75
28.	R-134a Condensation Heat Transfer Coefficient versus Quality for $150 \text{ kg/m}^2\text{-s}$ $< G < 750 \text{ kg/m}^2\text{-s}$ in Test Section C60	75
29.	Refrigerant to Water Resistance Ratio for Test Section B32	76
30.	R-134a Condensation Heat Transfer Coefficient versus Quality for $150 \text{ kg/m}^2\text{-s}$ $< G < 750 \text{ kg/m}^2\text{-s}$ in Test Section B32	76
31.	Refrigerant to Water Resistance Ratio for Test Section N21	77
32.	R-134a Condensation Heat Transfer Coefficient versus Quality for $150 \text{ kg/m}^2\text{-s}$ $< G < 750 \text{ kg/m}^2\text{-s}$ in Test Section N21	77
33.	Refrigerant to Water Resistance Ratio for Test Section T33	78
34.	R-134a Condensation Heat Transfer Coefficient versus Quality for $150 \text{ kg/m}^2\text{-s}$ $< G < 750 \text{ kg/m}^2\text{-s}$ in Test Section T33	78
35.	Refrigerant to Water Resistance Ratio for Test Section W29	79
36.	R-134a Condensation Heat Transfer Coefficient versus Quality for $150 \text{ kg/m}^2\text{-s}$ $< G < 750 \text{ kg/m}^2\text{-s}$ in Test Section W29	79
37.	Comparison of Condensation Heat Transfer Coefficients for Test Sections C30 and C60 with $G = 150 \text{ kg/m}^2\text{-s}$	81
38.	Comparison of Condensation Heat Transfer Coefficients for Test Sections C20, C30, and C60 with $G = 300 \text{ kg/m}^2\text{-s}$	81
39.	Comparison of Condensation Heat Transfer Coefficients for Test Sections C20, C30, and C60 with $G = 450 \text{ kg/m}^2\text{-s}$	82
40.	Comparison of Condensation Heat Transfer Coefficients for Test Sections C20, C30, and C60 with $G = 600 \text{ kg/m}^2\text{-s}$	82
41.	Comparison of Condensation Heat Transfer Coefficients for Test Sections C20, C30, and C60 with $G = 750 \text{ kg/m}^2\text{-s}$	83
42.	Mass Flux Variation for Test Sections C20, C30, and C60	83
43.	Comparison of Condensation Heat Transfer Coefficients for Test Sections B32, C30, S30, T33, and W29 with $G = 150 \text{ kg/m}^2\text{-s}$	86
44.	Comparison of Condensation Heat Transfer Coefficients for Test Sections B32, C30, S30, T33, and W29 with $G = 300 \text{ kg/m}^2\text{-s}$	86

45.	Comparison of Condensation Heat Transfer Coefficients for Test Sections B32, C30, S30, T33, and W29 with $G = 450 \text{ kg/m}^2\text{-s}$	87
46.	Comparison of Condensation Heat Transfer Coefficients for Test Sections B32, C30, S30, T33, and W29 with $G = 600 \text{ kg/m}^2\text{-s}$	87
47.	Comparison of Condensation Heat Transfer Coefficients for Test Sections B32, C30, S30, T33, and W29 with $G = 750 \text{ kg/m}^2\text{-s}$	88
48.	Intermittent Flow Regime Transition (Upper Limit) for the Square Tubes from Coleman (2000)	92
49.	Annular Film Flow Pattern Transitions (Upper and Lower Limits) for the Square Tubes from Coleman (2000)	93
50.	Mist Flow Pattern Transition (Lower Limit) for the Square Tubes from Coleman (2000)	93
51.	Wavy Flow Regime Transitions (Upper and Lower Limits) for the Square Tubes from Coleman (2000)	94
52.	Intermittent Flow Regime Transition (Upper Limit) for Test Sections C20, C30, and C60 Based on Coleman (2000)	95
53.	Annular Film Flow Pattern Transitions (Upper and Lower Limits) for Test Sections C20, C30, and C60 Based on Coleman (2000)	96
54.	Mist Flow Regime Transition (Lower Limit) for Test Sections C20, C30, and C60 Based on Coleman (2000)	96
55.	Experimental Data for Test Section C20 with Superimposed Transition Lines	98
56.	Experimental Data for Test Section C30 with Superimposed Transition Lines	99
57.	Experimental Data for Test Section C60 with Superimposed Transition Lines	100
58.	Comparison of Intermittent Flow Data with Literature (Test Section C30, $G = 300 \text{ kg/m}^2\text{-s}$ )	103
59.	Comparison of Intermittent Flow Data with Literature (Test Section C30, $G = 450 \text{ kg/m}^2\text{-s}$ )	104
60.	Comparison of Intermittent Flow Data with Literature (Test Section C30, $G = 600 \text{ kg/m}^2\text{-s}$ )	104
61.	Comparison of Annular Flow Regime Data with the Literature (Test Section C60, $G = 150 \text{ kg/m}^2\text{-s}$ )	113
62.	Comparison of Annular Flow Regime Data with the Literature (Test Section C60, $G = 300 \text{ kg/m}^2\text{-s}$ )	113
63.	Comparison of Annular Flow Regime Data with the Literature (Test Section C60, $G = 450 \text{ kg/m}^2\text{-s}$ )	114

64.	Comparison of Annular Flow Regime Data with the Literature (Test Section C60, $G = 600 \text{ kg/m}^2\text{-s}$ )	114
65.	Comparison of Annular Flow Regime Data with the Literature (Test Section C60, $G = 750 \text{ kg/m}^2\text{-s}$ )	115
66.	Flow Regime-Based Correlations and Experimental Heat Transfer Coefficients for Test Section C60 at $G = 150 \text{ kg/m}^2\text{-s}$	124
67.	Flow Regime-Based Correlations and Experimental Heat Transfer Coefficients for Test Section C60 at $G = 300 \text{ kg/m}^2\text{-s}$	124
68.	Flow Regime-Based Correlations and Experimental Heat Transfer Coefficients for Test Section C60 at $G = 450 \text{ kg/m}^2\text{-s}$	125
69.	Flow Regime-Based Correlations and Experimental Heat Transfer Coefficients for Test Section C60 at $G = 600 \text{ kg/m}^2\text{-s}$	125
70.	Flow Regime-Based Correlations and Experimental Heat Transfer Coefficients for Test Section C60 at $G = 750 \text{ kg/m}^2\text{-s}$	126
71.	Actual Liquid Reynolds Numbers as a Function of Hydraulic Diameter in Coleman (2000)	133
72.	Churchill (1977b) and Colebrook (1939) Friction Factors for Actual Liquid Reynolds Numbers in Coleman (2000)	134
73.	Condensation Heat Transfer Zones for Test Section C30	137
74.	Predicted versus Experimental Condensation Heat Transfer Coefficients for Test Sections C20, C30, and C60	140
75.	Predicted and Experimental Condensation Heat Transfer Coefficients for Test Section C60 and $G = 150 \text{ kg/m}^2\text{-s}$	140
76.	Predicted and Experimental Condensation Heat Transfer Coefficients for Test Section C60 and $G = 300 \text{ kg/m}^2\text{-s}$	141
77.	Predicted and Experimental Condensation Heat Transfer Coefficients for Test Section C60 and $G = 450 \text{ kg/m}^2\text{-s}$	141
78.	Predicted and Experimental Condensation Heat Transfer Coefficients for Test Section C60 and $G = 600 \text{ kg/m}^2\text{-s}$	142
79.	Predicted and Experimental Condensation Heat Transfer Coefficients for Test Section C60 and $G = 750 \text{ kg/m}^2\text{-s}$	142
80.	Predicted and Experimental Condensation Heat Transfer Coefficients for Test Section C30 and $G = 300 \text{ kg/m}^2\text{-s}$	143
81.	Predicted and Experimental Condensation Heat Transfer Coefficients for Test Section C30 and $G = 450 \text{ kg/m}^2\text{-s}$	143

82.	Predicted and Experimental Condensation Heat Transfer Coefficients for Test Section C30 and $G = 600 \text{ kg/m}^2\text{-s}$	144
83.	Predicted and Experimental Condensation Heat Transfer Coefficients for Test Section C30 and $G = 750 \text{ kg/m}^2\text{-s}$	144
84.	Predicted and Experimental Condensation Heat Transfer Coefficients for Test Section C20 and $G = 450 \text{ kg/m}^2\text{-s}$	145
85.	Predicted and Experimental Condensation Heat Transfer Coefficients for Test Section C20 and $G = 600 \text{ kg/m}^2\text{-s}$	145
86.	Predicted and Experimental Condensation Heat Transfer Coefficients for Test Section C20 and $G = 750 \text{ kg/m}^2\text{-s}$	146
87.	Present Model Condensation Heat Transfer Coefficients as a Function of Quality for Test Section C20, C30, and C60 and $G = 150 \text{ kg/m}^2\text{-s}$	148
88.	Present Model Condensation Heat Transfer Coefficients as a Function of Quality for Test Section C20, C30, and C60 and $G = 300 \text{ kg/m}^2\text{-s}$	148
89.	Present Model Condensation Heat Transfer Coefficients as a Function of Quality for Test Section C20, C30, and C60 and $G = 450 \text{ kg/m}^2\text{-s}$	149
90.	Present Model Condensation Heat Transfer Coefficients as a Function of Quality for Test Section C20, C30, and C60 and $G = 600 \text{ kg/m}^2\text{-s}$	149
91.	Present Model Condensation Heat Transfer Coefficients as a Function of Quality for Test Section C20, C30, and C60 and $G = 750 \text{ kg/m}^2\text{-s}$	150
92.	Cross-Section of One Channel for Test Section T33 with Largest Inscribed Circle 151	
93.	Predicted versus Experimental Condensation Heat Transfer Coefficients for Test Sections N21, S30, RK15, T33, and W29	153
94.	Predicted and Experimental Condensation Heat Transfer Coefficients for Test Section N21 and $G = 300 \text{ kg/m}^2\text{-s}$	155
95.	Predicted and Experimental Condensation Heat Transfer Coefficients for Test Section N21 and $G = 450 \text{ kg/m}^2\text{-s}$	156
96.	Predicted and Experimental Condensation Heat Transfer Coefficients for Test Section N21 and $G = 600 \text{ kg/m}^2\text{-s}$	156
97.	Predicted and Experimental Condensation Heat Transfer Coefficients for Test Section N21 and $G = 750 \text{ kg/m}^2\text{-s}$	157
98.	Predicted and Experimental Condensation Heat Transfer Coefficients for Test Section S30 and $G = 300 \text{ kg/m}^2\text{-s}$	157

99.	Predicted and Experimental Condensation Heat Transfer Coefficients for Test Section S30 and $G = 450 \text{ kg/m}^2\text{-s}$	158
100.	Predicted and Experimental Condensation Heat Transfer Coefficients for Test Section S30 and $G = 600 \text{ kg/m}^2\text{-s}$	158
101.	Predicted and Experimental Condensation Heat Transfer Coefficients for Test Section S30 and $G = 750 \text{ kg/m}^2\text{-s}$	159
102.	Predicted and Experimental Condensation Heat Transfer Coefficients for Test Section RK15 and $G = 600 \text{ kg/m}^2\text{-s}$	159
103.	Predicted and Experimental Condensation Heat Transfer Coefficients for Test Section RK15 and $G = 750 \text{ kg/m}^2\text{-s}$	160
104.	Predicted and Experimental Condensation Heat Transfer Coefficients for Test Section T33 and $G = 150 \text{ kg/m}^2\text{-s}$	160
105.	Predicted and Experimental Condensation Heat Transfer Coefficients for Test Section T33 and $G = 300 \text{ kg/m}^2\text{-s}$	161
106.	Predicted and Experimental Condensation Heat Transfer Coefficients for Test Section T33 and $G = 450 \text{ kg/m}^2\text{-s}$	161
107.	Predicted and Experimental Condensation Heat Transfer Coefficients for Test Section T33 and $G = 600 \text{ kg/m}^2\text{-s}$	162
108.	Predicted and Experimental Condensation Heat Transfer Coefficients for Test Section T33 and $G = 750 \text{ kg/m}^2\text{-s}$	162
109.	Predicted and Experimental Condensation Heat Transfer Coefficients for Test Section W29 and $G = 150 \text{ kg/m}^2\text{-s}$	163
110.	Predicted and Experimental Condensation Heat Transfer Coefficients for Test Section W29 and $G = 300 \text{ kg/m}^2\text{-s}$	163
111.	Predicted and Experimental Condensation Heat Transfer Coefficients for Test Section W29 and $G = 450 \text{ kg/m}^2\text{-s}$	164
112.	Predicted and Experimental Condensation Heat Transfer Coefficients for Test Section W29 and $G = 600 \text{ kg/m}^2\text{-s}$	164
113.	Predicted and Experimental Condensation Heat Transfer Coefficients for Test Section W29 and $G = 750 \text{ kg/m}^2\text{-s}$	165
114.	Comparison of Heat Transfer Coefficients in N-shaped and Circular Tubes for $G = 150, 450, \text{ and } 750 \text{ kg/m}^2\text{-s}$	165
115.	Comparison of Heat Transfer Coefficients in Square and Circular Tubes for $G = 150, 450, \text{ and } 750 \text{ kg/m}^2\text{-s}$	166

116.	Comparison of Heat Transfer Coefficients in Rectangular and Circular Tubes for $G = 450$ and $750 \text{ kg/m}^2\text{-s}$	166
117.	Comparison of Heat Transfer Coefficients in Triangular and Circular Tubes for $G = 150, 450,$ and $750 \text{ kg/m}^2\text{-s}$	167
118.	Comparison of Heat Transfer Coefficients in W-shaped and Circular Tubes for $G = 150, 450,$ and $750 \text{ kg/m}^2\text{-s}$	167
119.	Effect of Tube Shape on Heat Transfer Coefficient, $G = 150 \text{ kg/m}^2\text{-s}$	168
120.	Effect of Tube Shape on Heat Transfer Coefficient, $G = 450 \text{ kg/m}^2\text{-s}$	168
121.	Effect of Tube Shape on Heat Transfer Coefficient, $G = 750 \text{ kg/m}^2\text{-s}$	169

**LIST OF TABLES**

1.	Test Matrix for Heat Transfer Experiments	29
2.	Instrumentation Specifications	34
3.	Measured Data for Test Section S30 Example Calculation	37
4.	Minor Loss Elements in the Primary Loop for the Microchannel Tubes Tests	46
5.	Test Section C30 Data Point Summary for Baseline Comparison of Intermittent Data	101
6.	Test Section C60 Data Point Summary for Baseline Comparison of Annular Data	111
7.	Description of Condensation Heat Transfer Zones in the Present Study	138
8.	Non-Circular Test Section Annular Film Flow Constants for Laminar and Turbulent Liquid Flow	151
9.	Hydraulic and Equivalent Diameters for the Non-circular Tubes	151
10.	Mist Flow Constants and Relative Roughness for the Non-Circular Test Sections	152

## NOMENCLATURE

### Symbols

A	cross-sectional area, laminar friction factor constant
a	calculation parameters in Soliman et al. (1968), function of hydraulic diameter in intermittent flow transition
B	constant in Blasius friction factor calculation
b	function of hydraulic diameter in intermittent flow transition
$C_1, C_2$	constants in Coleman (2000) interfacial friction factor correlation
$C_p$	specific heat (kJ/kg-K)
D	diameter (m)
d	derivative operator
E	constant in Friedel's (1979) correlation for the two-phase multiplier
F	function of liquid Prandtl and Reynolds numbers in Traviss et al. (1973)
f	friction factor
Fr	Froude number
G	mass flux (kg/m <sup>2</sup> -s)
g	gravitational constant (9.81 m/s <sup>2</sup> )
Ga	Galileo number
H	constant in (Friedel 1979) correlation for the two-phase multiplier
h	enthalpy (kJ/kg), condensation heat transfer coefficient (W/m <sup>2</sup> -K), height (m)
ID	inside diameter (m)
j	superficial velocity (m/s)
Ja	Jakob number ( $C_p \cdot \Delta T / h_{iv}$ )
K	Chato's (1962) Constant, slip ratio, minor loss coefficient
k	thermal conductivity (W/m-K)
L	length (m)
LMTD	log-mean temperature difference (K)
$\dot{m}$	mass flow rate (kg/s)
M	parameter for fin efficiency
N	number
n	Reynolds number constant in friction factor calculation
Nu	Nusselt number

$\overline{Nu}$	average Nusselt number
OD	outside diameter (m)
P	pressure (kPa), wetted perimeter (m)
Pr	Prandtl number
Q	heat duty (W)
q"	heat flux (W/m <sup>2</sup> )
R	heat transfer resistance (K/W), radius (m)
r	radial direction
r*	annulus radius ratio
Ra	Rayleigh number
Re	Reynolds number
S	perimeter (m)
T	temperature (°C)
t	thickness (m)
U	absolute uncertainty, axial velocity
u	propagated absolute uncertainty, axial velocity
UA	overall heat transfer conductance (W/K)
V	velocity (m/s)
$\dot{V}$	volumetric flow rate (m <sup>3</sup> /s)
$\dot{W}$	power (W)
w	width (m)
We	Weber number
X	Lockhart-Martinelli parameter
x	quality
y	pseudo-radial direction
z	axial direction in a horizontal tube
$\alpha$	aspect ratio, void fraction
$\beta$	Rosson and Myers (1965) interpolation factor, coefficient of thermal expansion (1/K), bubble to unit cell length ratio
$\Delta$	change, difference
$\delta$	film thickness
$\partial$	partial derivative operator
$\varepsilon$	tube roughness (m), turbulent diffusivity (m <sup>2</sup> /s)
$\eta$	efficiency
$\lambda$	ratio of interface and film velocities

$\mu$	dynamic viscosity (kg/m-s)
$\pi$	3.14159....
$\sigma$	surface tension (N/m), Stefan-Boltzman constant ( $5.67 \times 10^{-8} \text{ W/m}^2\text{-T}^4$ )
$\rho$	density (kg/m <sup>3</sup> )
$\theta$	angle subtended from the top of the tube to the liquid pool level in stratified flow (rad)
$\tau$	torque (N-m), shear stress (kPa)
$\phi$	two-phase multiplier
$\omega$	angular speed (rad/s)

### **Sub-scripts and Super-scripts**

/	modified
~	dimensionless
$\infty$	infinity
act	actual
air	ambient property
ambient	ambient
ann	annular flow
annulus	annulus-side
avg	average
b	stratified region or vapor in the stratified region in the unit cell
bot	liquid pool in stratified flow
bubble	vapor bubble in the unit cell
c	center-tube or refrigerant-side in the test section
crit	critical
d	direct
DB	Dittus-Boelter
E	equivalent
f	friction
film	film, liquid film in unit cell
fin	between microchannels
h	hydraulic, heat
i	interfacial
id	indirect
ideal	ideal
in	inlet

inner	inner
ins	insulation
int	intermittent flow
j	tube-jacket or water-side in the test section
L	average over entire length, slug portion of the unit cell, liquid-phase
l	liquid phase
lam	laminar
lo	liquid only phase
loop	primary loop
low	lower limit
lt	laminar transition
lv	vaporization
m	mixture, momentum
mik	from Mikheev (1956) as manipulated by Boyko and Kruzhilin (1967)
mist	mist flow
nc	natural convection
out	outlet
outer	outer
pool	liquid pool in stratified flow
port	microchannel port
post	post-condenser
pre	pre-condenser
pump	pump
rad	radiation
refg	refrigerant
sat	saturation
sec	secondary loop
shaft	pump shaft input
slug	liquid slug in intermittent flow
surface	at the surface
t	turbulent, total
test	test section
top	laminar film condensation region in stratified flow
total	total, combination multiple flow regimes
tt	turbulent transition

tube	tube
turb	turbulent
up	upper limit
v	vapor phase
vo	vapor only phase
vt	viscous liquid and turbulent vapor
w	water
wall	at the wall, wall
water	water-side
+	dimensional turbulent parameter
*	friction

## ACKNOWLEDGEMENTS

There are many people to thank for completing this work. First, I would like to thank my advisor, Dr. Srinivas Garimella. His insight and multiple exhaustive reviews were essential to the completion of my thesis, and I greatly appreciate his efforts. I also thank Modine Manufacturing Company, Racine WI, and Dr. Stephen B. Memory for providing the test sections and funding to make this project possible. Patience from Dr. Ambar Mitra and Dr. Michael Pate while I finished writing are worth many thanks. Hours spent by Bill Dowling and Dr. John Coleman constructing the test facility and easing my transition to graduate school and the lab do not go unnoticed. Insightful conversations with Jesse Killion always provided food for thought, and Leo Mincks always lent a helping hand. Thanks are also in order for Yirong Jiang, Thomas Swinning, Matt Determan, Karen Bandhauer, Kirk Menges, and Mark Meacham for watching my test loop during class. Finally, thanks to Jesse and Mark for lending their couch.

## ABSTRACT

An experimental study on heat transfer during condensation of refrigerant R-134a in microchannel tubes was conducted. Investigations were carried out on 3 circular and 6 non-circular channels. The non-circular channels included barrel, N-shaped, rectangular, square, and triangular extruded tubes, and a channel with a corrugated insert that yielded triangular microchannels. The hydraulic diameters ranged from 0.424 mm to 1.524 mm. A technique that addresses the conflicting requirements imposed by the need for accurate measurement of low heat transfer rates and high heat transfer coefficients in microchannel tubes was developed. The inlet and outlet qualities to a microchannel test section were measured through energy balances on a pre- and post-condenser. The test section was cooled using water at a high flow rate to ensure that the condensation side presents the governing thermal resistance. Heat exchange with a secondary cooling water stream at a much lower flow rate was used to obtain a large temperature difference, which was in turn used to measure the condensation duty. The use of these primary and secondary coolant loops resulted in very high thermal amplification that enabled the measurement of the low heat duties for local condensation in microchannels, while maintaining refrigerant-to-coolant thermal resistance ratios as high as 30. Local heat transfer coefficients over the range of mass fluxes  $150 < G < 750 \text{ kg/m}^2\text{-s}$  were measured in small increments for the entire saturated vapor-liquid region, spanning several different two-phase flow regimes.

In the three circular tubes ( $D_h = 0.506 \text{ mm}$ ,  $0.761 \text{ mm}$ , and  $1.524 \text{ mm}$ ), the hydraulic diameter did not have a significant influence on heat transfer coefficients for low qualities ( $x < 0.45$ ), whereas the heat transfer coefficient increased as the diameter decreased for higher qualities. Data for the barrel ( $D_h = 0.799 \text{ mm}$ ), square ( $D_h = 0.762 \text{ mm}$ ), and triangular ( $D_h = 0.839 \text{ mm}$ ) extruded tubes and the triangular corrugated insert tube ( $D_h = 0.732 \text{ mm}$ ) were compared with the data for the circular tube with a similar hydraulic diameter ( $D_h = 0.761 \text{ mm}$ ) to document the effect of channel shape. The triangular extruded and corrugated insert tubes have the highest heat transfer coefficients, with the effect of tube shape not being very significant for the other tube shapes.

Flow regime transition criteria proposed by Coleman (2000) were extrapolated to the hydraulic diameter range under consideration to determine the prevailing flow regime for a given combination of mass flux, quality, and diameter. The data collected in the present study were in two flow regimes: intermittent flow and annular flow, with annular flow being further subdivided into the annular film and mist flow patterns. Large flow regime overlaps

occurred throughout the condensation path, especially as the diameter decreases, indicating the existence of multiple flow regimes at a given condition. Only a small portion of the data were exclusively in a single flow patterns for all three circular tubes (3.65% of the total circular data sets in intermittent, 19.5% in annular, and 12.2% in mist). A small portion of the data was in transition regions adjacent to the intermittent flow regime (11% in intermittent/annular and 3.65% in intermittent/annular/mist). However, 50% the circular data are in annular/mist transition flow.

Most of the heat transfer correlations available in the literature were found to over-predict the data from the present study. In other instances, the trends (i.e., the slope of heat transfer versus quality plots) were either much steeper or more gradual than what was observed in the present study. Hence, condensation heat transfer models for annular, mist, and intermittent flow were developed using the data for both the circular and non-circular tubes. Quality-based averaging was used to account for the presence of multiple regimes for a given condition. The annular film flow model was an adaptation to the boundary layer approach of Traviss et al. (1973), where the present study uses the pressure drop correlation of Coleman (2000) to estimate the friction velocity. The mist flow heat transfer coefficient is predicted using a constant multiplier (different depending on geometry) to the single-phase Nusselt number (Churchill 1977a) based on the vapor-liquid mixture properties. The intermittent flow heat transfer coefficient was calculated using a linear interpolation between the liquid only and the annular flow heat transfer coefficient at the regime boundary.

The models predicted 90% of the circular data to within  $\pm 25\%$  and 84% of the non-circular data to within  $\pm 30\%$ . These models are expected to be valid for the following range of conditions:  $0.424 \text{ mm} < D_h < 1.524 \text{ mm}$ ,  $150 \text{ kg/m}^2\text{-s} < G < 750 \text{ kg/m}^2\text{-s}$ , and  $1,240 \text{ kPa} < P < 1,725 \text{ kPa}$ .

## CHAPTER ONE: INTRODUCTION

Conventional air conditioning equipment utilizes round-tube, plate-fin heat exchangers for the condenser and evaporator. The air is blown over the fins to condense or evaporate the refrigerant on the tube side. Since the refrigerant is undergoing phase-change, the air-side heat transfer coefficient is substantially lower than the refrigerant-side heat transfer coefficient. The placement of fins on the air-side counteracts this by increasing the effective heat transfer area. Although the heat transfer may still be dominated by the air-side resistance, the refrigerant resistance becomes more important as the air-side heat transfer area increases. The cost of manufacturing condensers and evaporators constitutes a significant portion of the total cost of air-conditioning equipment, and improving the efficiency of these devices can significantly reduce cost. Optimization techniques such as varying the number of tubes and passes and the fin pitch, height, thickness, and shape have provided some improvement in the effectiveness of heat exchange. However, these advances will achieve only gradual improvements, and more attention should be focused on the refrigerant-side heat transfer geometry.

Automobile heat exchanger manufacturers have designed compact flat-tube, multi-louver fin heat exchangers to replace the traditional round-tube, plate-fin condensers and evaporators. An example of this type of heat exchanger can be seen in Figure 1. The flat tubes offer a lower resistance to air flow, which reduces air-side pumping power requirements. The small hydraulic diameter on the refrigerant-side tends to increase the heat transfer coefficient, and the multi-louver fins reduce the boundary-layer resistance on the air-side to increase its heat transfer coefficient. Hence, the overall heat transfer conductance is increased. The compactness of this type of heat exchanger allows for higher heat transfer areas in a smaller space; thus a larger heat duty can be transferred in a small volume. In addition, the refrigerant charge could be reduced by increasing the amount of surface area relative to the cross-sectional area.

Although this type of heat exchanger is being implemented in industry and the advantages are known, the two-phase pressure drop and heat transfer mechanisms are not very well understood for the small refrigerant tube hydraulic diameters. Pressure drop and heat transfer are strong functions of local vapor quality. To accurately design these types of heat exchangers for condensation, the variation of the two-phase flow patterns and its effect on pressure drop and heat transfer as the refrigerant changes from vapor to liquid needs to be understood. Simply using the average characteristics at a vapor quality of 50% could

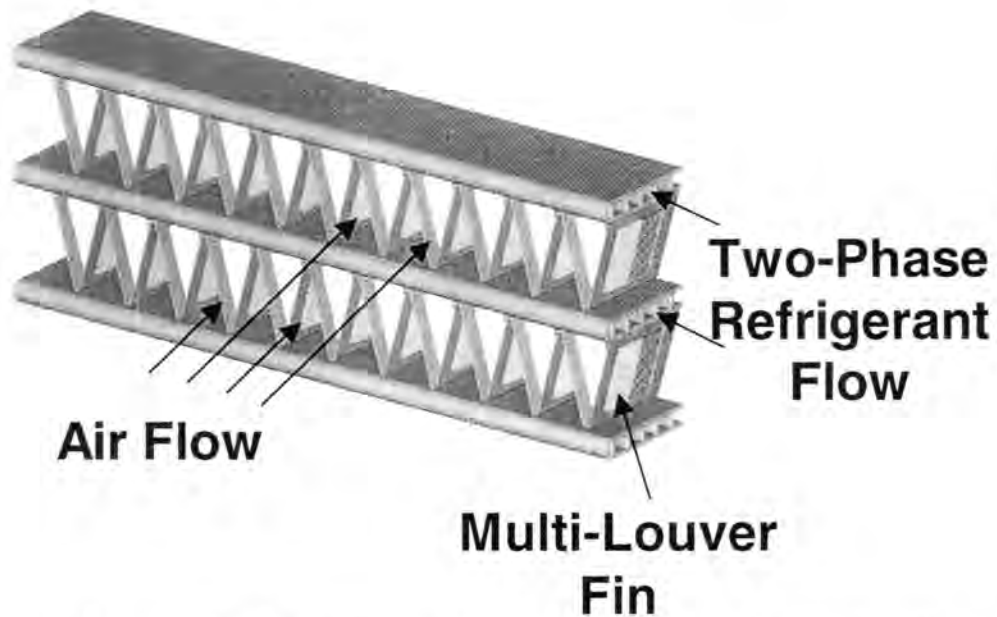


**Figure 1.** Schematic of a Microchannel-Tube, Multi-Louver Fin Heat Exchanger

result in serious over- or under-predictions of the pressure drop and heat transfer, thus leading to inadequate designs. Hence, accurately representing the local heat transfer and pressure drop characteristics using flow regime based correlations is essential for design.

The type of flow regime established at a given mass flux and quality depends upon the relative magnitudes of shear, gravity, and surface tension forces. Recently, Coleman (2000) conducted a comprehensive investigation of the effect of hydraulic diameter, tube shape, and aspect ratio on two-phase flow regimes. Adiabatic air/water and condensing R-134a flow visualization tests were conducted on circular tubes ranging in hydraulic diameter from 5.5 mm to 1.3 mm and rectangular tubes with hydraulic diameters ranging from 5.36 mm to 1 mm and aspect ratios between 0.5 to 2. Subsequently, pressure drop tests were conducted on 5 sets of circular tubes ( $0.506 \text{ mm} < D_h < 4.91 \text{ mm}$ ) and 7 sets of non-circular tube geometries ( $0.424 \text{ mm} < D_h < 0.986 \text{ mm}$ ) to investigate the effect of flow regime on pressure drop for small hydraulic diameter tubes. The hydraulic diameter was found to have a significant effect on the type of flow regime observed. Flow regime-based correlations for pressure drop were developed using the data from flow visualization and pressure drop tests.

Condensation heat transfer coefficients are expected to be dependent on the type of flow regime. In addition, the current literature on condensation heat transfer in large diameter tubes may not be applicable to small diameter tubes. Therefore, in this study, the

effects of two-phase flow regimes on heat transfer in small diameter circular and non-circular tubes were investigated experimentally using the same test facility as in Coleman (2000), with some modifications. The focus of this investigation is to measure and model heat transfer coefficients during the condensation of refrigerant R-134a in small hydraulic diameter ( $0.424 \text{ mm} < D_h < 1.524 \text{ mm}$ ) tubes of circular and non-circular cross-sections. The specific objectives of this study are as follows:

- Determine the local condensation heat transfer coefficients for each set of tubes as a function of mass flux ( $150 \text{ kg/m}^2\text{-s} < G < 750 \text{ kg/m}^2\text{-s}$ ) and quality ( $0\% < x < 100\%$ )
- Investigate the effect of hydraulic diameter on the condensation heat transfer coefficient for the range  $0.424 \text{ mm} < D_h < 1.524 \text{ mm}$
- Investigate the effect of tube shape on the condensation heat transfer coefficient
- Use the results from Coleman (2000) to relate the condensation heat transfer coefficient to the corresponding flow regime
- Compare experimental data with the limited local condensation heat transfer coefficient data and correlations in the literature
- Develop flow regime-based condensation heat transfer coefficient correlations to be used in the design of condensers

The thesis organization is as follows. In Chapter Two, a review of the literature on condensation heat transfer is conducted and the deficiencies in the available literature are identified. The experimental set-up and procedures for determining the condensation heat transfer coefficients are described in Chapter Three. The data analysis techniques are discussed and the results of the experiments are presented in Chapter Four. Chapter Five consists of comparisons between the literature and the experimental data, and the presentation of the flow regime-based heat transfer correlations. Conclusions from this study and recommendations for further research are presented in Chapter Six.

## CHAPTER TWO: LITERATURE REVIEW

Numerous studies have been conducted by previous investigators on condensation of a variety of fluids in different orientations. The literature review presented here will focus primarily on studies of condensation inside horizontal tubes that report models and correlations for the prediction of heat transfer coefficients. Several researchers have also developed theoretical analyses on condensation heat transfer that result in complex numerical schemes, while other researches conduct simple non-dimensional analyses and provide empirical correlations for predicting their data and those of other investigators. There has been success in predicting condensation heat transfer coefficients in larger tubes, but there has been very little research on condensation heat transfer in small tubes, especially with diameters less than about 7 mm.

The discussion of the relevant literature is sub-divided into two main sections: research on large diameter tubes and research on small diameter tubes. The literature on large diameter tubes is further divided into studies on gravity-dominated and shear-dominated condensation, due to the relatively large body of literature for the larger tubes. The purpose of this review is to provide a basis for understanding experimental techniques, theoretical analyses, and important observations and conclusions of previous investigators. This review therefore provides guidance for the present work, and also helps identify deficiencies in the current literature, some of which are addressed in this investigation.

### **Previous Research on Large Diameter Tubes**

#### **Gravity-Driven Condensation Heat Transfer**

Much of the early work on condensation heat transfer is based upon the falling film condensation analysis by Nusselt (1916). In his pioneering work, Nusselt assumed that a thin laminar condensate film formed on an isothermal flat plate with a surface temperature less than the saturation temperature, surrounded by a stationary vapor at the saturation temperature. The condensate flows under the influence of gravity and the film thickens as it moves down the plate. Nusselt further assumed that heat transfer is due to conduction across the film only. In addition, he assumed constant film properties, negligible film subcooling, and a smooth liquid-vapor interface. After conducting an energy balance around a film element and integrating with appropriate relationships for the mass flow rate, the relationship for film thickness is found, which is used to derive the following relationship for the average Nusselt number along a plate with length  $L$ :

$$\overline{\text{Nu}}_L = \frac{\bar{h}_L L}{k_1} = 0.943 \left[ \frac{\rho_l (\rho_l - \rho_v) g \cdot h_{lv} \cdot L^3}{k_1 \cdot \mu_l (T_{\text{sat}} - T_{\text{wall}})} \right]^{1/4} \quad (1)$$

This result provides the foundation for much of the literature on gravity-driven condensation heat transfer.

Rohsenow (1956) presented the solution for the laminar temperature distribution for the condensate film in falling-film condensation, which was employed in Rohsenow et al. (1956) to account for the non-linearity in film temperature. The analysis was similar to Nusselt's falling film condensation model, except that the net enthalpy change in the fluid was accounted for in the energy balance. Therefore, a modified enthalpy of vaporization, as shown below, was introduced to account for film subcooling:

$$h'_{lv} = h_{lv} (1 + 0.68 \cdot \text{Ja}_l) \quad (2)$$

Chato (1962) presented a numerical model for stratified-flow condensation inside horizontal and inclined tubes. The results of the model were compared with experimental data obtained for air/water flowing inside a 27.94 mm diameter horizontal tube and for R-113 condensing inside a 14.53 mm inside diameter tube at various inclinations. The air/water experiments had an open discharge at the test section exit, while the refrigerant test section was in a closed loop. A similarity solution was developed to determine the condensation heat transfer coefficient. The solution depends on the liquid condensate pool thickness, of which the subtended angle was modeled based on open-channel hydraulics. Therefore, the outlet geometry condition defined the slow-moving liquid pool depth. The model was able to predict the outlet pool thickness for turbulent liquid flow, but not as well for laminar flow. Using the numerical solution, the measured condensate subtended angle was predicted within 5 degrees, while the measured heat transfer coefficients were predicted within 15%. In most of their tests, the horizontal tube data predicted the mean vapor angle to be within 8 degrees of 120 degrees. Thus, the following simplified correlation for the local Nusselt number, intended for design purposes, was proposed for the mean vapor angle of 120 degrees:

$$\text{Nu} = \frac{hD}{k_1} = 0.468 \cdot K \left[ \frac{\rho_l (\rho_l - \rho_v) g \cdot h'_{lv} \cdot D^3}{k_1 \cdot \mu_l (T_{\text{sat}} - T_{\text{wall}})} \right]^{1/4} \quad (3)$$

The constant K (a correction for the liquid Prandtl number) was presented graphically. Carey (1992) suggested that K be approximately 1.18, which results in replacing 0.468·K with 0.553. This result for the Nusselt number for condensation inside tubes is very similar to Nusselt's (1916) result for falling-film condensation with Rohsenow's (1956) correction for

film subcooling. However, the constant multiplier was lower in Chato's analysis, primarily due to the increased thermal resistance resulting from the thicker liquid pool condensate at the bottom of the tube.

Rosson and Myers (1965) calculated point values for condensation heat transfer coefficients for methanol and acetone condensing inside a 3/8" (9.53 mm) nominal stainless steel pipe. The experiments were conducted so that the heat flux and wall temperature difference were directly measured via an electrical circuit. For nearly all of the data, stratified flow was observed. The local data were integrated around the tube and compared with data separately obtained from heat balances. The agreement between these methods was reasonable. The authors noted that the condensation heat transfer coefficient decreased linearly from the top portion to a point where an approximately constant value was achieved. Based on this result, a Nusselt-type correlation was derived. For the top portion of the tube, Nusselt's falling film analysis was used, with the constant replaced by a function of the vapor Reynolds number to account for vapor shear as follows:

$$\text{Nu} = 0.31 \cdot \text{Re}_v^{0.12} \left[ \frac{\rho_l (\rho_l - \rho_v) g \cdot h'_{lv} \cdot D^3}{k_l \cdot \mu_l (T_{\text{sat}} - T_{\text{wall}})} \right]^{1/4} \quad (4)$$

For the bottom portion of the tube, the liquid pool heat transfer was not neglected and the von Karman analogy between heat transfer and momentum was used. By assuming the wall shear was approximately equal to the buffer layer shear and that the ratio of heat and momentum eddy diffusivities was 1, a relationship between the Nusselt number and wall shear stress was obtained. After assuming that the average shear was equal to the local shear and employing the Lockhart and Martinelli (1949) method for shear stress, the following Nusselt number correlation for the bottom portion of the tube was obtained:

$$\text{Nu} = \frac{\phi_{lvt} \sqrt{8 \text{Re}_l}}{5 + 5 \text{Pr}_l^{-1} \ln(1 + 5 \text{Pr}_l)} \quad (5)$$

They also defined a parameter  $\beta$  to linearly interpolate between the upper and lower Nusselt number correlations. The results from this correlation were compared with the experimental results. For a 90% confidence interval, the overall, top, and bottom correlations predicted the data within  $\pm 36\%$ ,  $\pm 27\%$ ,  $\pm 41\%$ , respectively.

Rufer and Kezios (1966) developed an analytical model using an approach similar to that of Chato (1962) for condensing stratified flow inside horizontal and tilted tubes. They proposed that film condensation, which was gravity-driven, occurs at the top portion of the tube and continued until the liquid pool condensate was reached at the bottom of the tube.

The model developed a relationship between the simplified one-dimensional conservation equations to track the angle subtended from the top of the tube to the height of the liquid pool. The condensation heat transfer coefficient was determined by the relationship proposed by Hassan and Jakob (1958) for Nusselt-type film condensation inside an infinitely long tube at an arbitrary tube inclination. The one-dimensional energy balance also included the effect of film subcooling, as proposed by Rohsenow (1956). The model employed by Dukler et al. (1962) was used for calculating the pressure drop for the two-phase mixture. Finally, a relationship for the slope of the flow-level angle was derived, which was used to calculate the flow level throughout the condensation process. The film condensate appeared to have a very steep rise in depth near the entrance. Downstream of this, the liquid pool thickness was relatively constant until the end of the condensation process. The results of this analysis agreed well with models of other investigators, and also with some experimental data (Rufer 1965) obtained on the liquid pool depth. This model, however, differed from that presented by Chato (1962), who used open channel hydraulics to develop a relationship for the liquid pool height. In the Rufer and Kezios model, the outlet condition/geometry does not affect the upstream liquid pool thickness. No heat transfer data were presented in conjunction with the analysis. Hence, the results of this research were primarily intended to modify the liquid pool depth analysis by Chato (1962).

Jaster and Kosky (1976) performed experiments on condensing steam inside a 12.5 mm horizontal tube. Coupled with the experimental results from Kosky and Staub (1971), the mass flux ranged from 12.6 to 145 kg/m<sup>2</sup>-s, and the authors viewed three different flow regimes: annular, transition, and stratified. By defining a shear-to-gravity stress ratio and comparing it with their experimental data, they were able to determine the progressions from annular to transition flow and from transition to stratified flow. The authors also presented annular and stratified flow correlations. Jaster and Kosky (1976) developed the annular flow correlation from the Martinelli analogy modified by Kosky and Staub (1971). The stratified correlation was a simplified model of Rufer and Kezios (1966), which accounted for only the film condensation and neglected the liquid pool heat transfer. The result was similar to that of the traditional Nusselt analysis, but multiplied by a different constant (0.725) and Zivi's (1964) correlation for void fraction raised to the  $\frac{3}{4}$  power. The transition region was a linear interpolation between the annular and stratified regimes based upon the stress ratio. From the comparison between experimental and predicted Nusselt numbers, the authors concluded that the transition flow correlation resulted in errors on the same order of magnitude as the correlations for other flow regimes.

Chen and Kocamustafaogullari (1987) presented a numerical model for stratified

condensation inside a smooth horizontal tube. In the model, the authors assumed that the wall temperature was constant. Similar to other authors, a condensate film formed on the top portion of the tube and drained to a condensate pool on the bottom, where it moved axially. The continuity, momentum, and energy equations were applied to the vapor core, laminar falling film, and condensate pool. The accumulation of condensate along the axial direction was accounted for, and the heat transfer coefficients were calculated for the laminar falling film and the condensate pool, with the total heat transfer coefficient being a function of both of these and the subtended liquid pool level angle. The film heat transfer coefficient was an integrated average of the local value, which was calculated from the numerically determined film thickness. The condensate pool heat transfer was found by using the Rosson and Myers (1965) method, which is based upon the von Karman analogy between momentum and heat transfer. This method was compared with an existing condensation heat transfer database, which includes diameters ranging from 10.8 to 16.6 mm. The fluids included R-12, R-113, water, methanol, acetone, and propane. This numerical procedure predicted all of the data within 30%, while the average deviation was 15.5%. Using results from the numerical solution, a simple correlation for the average Nusselt number as a function of the Kutateladze number (i.e. sensible to latent heat ratio), Prandtl number, Galileo number,  $L/D$ , and dimensionless interfacial shear was also developed. The resulting correlation was within 2.8% of the numerical solution, and can be used as an acceptable substitute. This correlation also predicted the data to within an average deviation of 16.2%.

Tien et al. (1988) conducted an experimental investigation of condensation inside a 14.2 mm vertical tube for liquid-vapor co-current flow. The experiments were conducted for a mass flux range of 122.7 to 660.8 kg/m<sup>2</sup>-s. Local condensation heat transfer coefficients and flow patterns were determined as a function of local vapor quality and mass flux. Two flow patterns were identified: annular and non-annular (slug, plug, and churn flow). Annular film condensation occurred at high mass fluxes and qualities, while non-annular flow existed at low mass fluxes and qualities. A general annular flow condensation model that asymptotically approached falling-film and shear-driven condensation limits was developed. This is the same analysis presented in Chen et al. (1987), which is explained subsequently. A vertical non-annular flow model was also developed. Tien et al. (1988) stated that the slug unit consisted of the liquid slug and the vapor bubble, which was surrounded by a slow-moving circumferentially uniform liquid film. They assumed that the void fraction of the liquid slug was zero, that the mixing zone at the front of the slug did not enhance heat transfer significantly, and that the liquid film around the vapor bubble was thin compared to the tube radius. Therefore, the heat transfer coefficient in the slug unit was a time-average of

the liquid slug convective heat transfer coefficient and the vapor bubble condensation heat transfer coefficient. The liquid slug heat transfer coefficient was determined from the Dittus-Boelter correlation. In the vapor bubble region, they derived the heat transfer coefficients for laminar and turbulent liquid films using a Nusselt falling film analysis and an analogous heat transfer factor, respectively. In turbulent film flow, they employed a Fanning friction factor for determining the wall shear stress. The condensation heat transfer coefficient for the bubble/film region was found using the definitions of the analogous heat transfer factor and slip ratio (vapor to liquid velocity ratio) and mass balances on the liquid and vapor phases. Tien et al. (1988) also determined a general condensation heat transfer coefficient correlation that included the non-annular effects. This heat transfer coefficient was an average of the annular bubble/film region (with the asymptotic limits) and the liquid slug heat transfer coefficients. The resulting correlation predicted their data well, except at high qualities, where mist flow is most likely to exist.

In addition to the vertical condensation model, Tien et al. (1988) also presented a horizontal flow model for annular and non-annular flows. For annular flow, the model developed by Chen et al. (1987) for horizontal flow was used. This is the same as the vertical model, but the gravity effects were neglected. In the non-annular flow model, Tien et al. (1988) expected the bubble/film region to be stratified, unlike the annular flow assumed for vertical flow. Using the continuity relationships and the momentum balances on each phase, the angle subtended to the liquid level and the vapor bubble length fraction of the slug unit were found. For the stratified condensation heat transfer coefficient, thin film condensation on the upper tube was modeled using a modified Nusselt approach, while a von Karman heat transfer and momentum analogy was used to find the liquid pool convective heat transfer, similar to the method of Rosson and Myers (1965). The results compared well with the data of Myers and Rosson (1961), who determined local condensation heat transfer data for methanol at low mass fluxes inside horizontal tubes.

Singh et al. (1996) presented data and an empirical model for local condensation heat transfer coefficients inside smooth horizontal tubes for stratified-wavy flow. The data were collected for R-134a condensing inside a 10.92 mm tube for a mass flux range of 50 to 300 kg/m<sup>2</sup>-s. They found that the Traviss et al. (1973), Shah (1979), Dobson et al. (1994), Chato (1962), and Akers et al. (1959) correlations underpredicted the data. Therefore, they proposed a correlation that uses the Chato (1962) correlation for the top portion of the tube (i.e. film condensation). For the forced-convective heat transfer through the condensate at the bottom portion of the tube, they used a two-phase multiplier correction to the Gnielinski (1979) single-phase correlation for  $Re > 2300$  and a modification of the Dittus-Boelter

correlation for  $Re < 2300$ . In their model, data were assigned to the stratified-wavy regime based on the modified Froude number criterion in Dobson et al. (1994), which states that stratified-wavy flow occurs for  $Fr < 7$ . Their correlation predicted the data to within  $\pm 7.5\%$ . (However, it should be noted that the experimental uncertainty was  $\pm 9.3\%$ .)

More recently, Guo and Anand (2000) presented an analytical model for predicting the heat transfer coefficient for R-410a (50/50 mixture of R-32 and R-125) condensing in a 12.7 mm x 25.4 mm horizontal rectangular channel, with the long side vertical. The experimental data encompassed mass fluxes ranging from 30 to 2200 kg/m<sup>2</sup>-s. The model was specifically designed for the stratified-wavy flow regime. The heat transfer coefficient was the area-weighted average of the top, bottom, and vertical wall heat transfer coefficients. For the top wall, the von Karman analogy between heat transfer and momentum was used. The authors noted that the Lockhart and Martinelli (1949) method for determining the interfacial shear stress allowed for good agreement with the data. Hence, a Nusselt number correlation was developed for the top wall that incorporated the two-phase multiplier and superficial friction factor for the liquid phase. The vertical wall heat transfer was modeled numerically. The Nusselt falling film method was adopted, but the analysis included the effect of vapor shear. A mass balance was conducted across a two-dimensional element (vertical and horizontal axes), which was implemented into an integral for the heat flux. The resulting quasi-linear, first-order partial differential equation was solved numerically to get the film thickness as a function of the horizontal and vertical directions. This result was integrated over both walls to get the average heat transfer coefficient for the vertical walls. The heat transfer through the bottom wall was assumed to be due to conduction. The liquid pool at the bottom of the tube accumulated due to the gravitational movement of the vertical falling films. The results from this model were compared with the experimental data of Guo (1998). The mean deviation between the experimental and predicted values was 6.75%, which they stated was better agreement than the correlations of Rosson and Myers (1965) and Dobson and Chato (1998).

### **Shear-Driven Condensation Heat Transfer**

Carpenter and Colburn (1951) obtained experimental data for local and average heat transfer coefficients for the condensation of steam, methanol, ethanol, toluene, and trichloroethylene inside a vertical 11.66 mm ID tube. The data were compared with the Nusselt (1916) equation, which underpredicted the values due to the effect of vapor friction. Carpenter and Colburn stated that the thin condensate layer for annular flow might become turbulent at very low liquid Reynolds numbers (the authors suggest 240). The forces acting

upon this condensate layer were vapor friction, gravity, and the momentum change due to condensation. Using the von Karman universal velocity profile for the liquid film, a relationship for the local condensation heat transfer coefficient was derived, which was a function of the film thickness (i.e. the laminar sublayer thickness), fluid properties, and the sum of the forces acting on the condensate. The gravity force was deemed to be unimportant, which is the case for annular flow. The vapor friction force was determined from an equivalent vapor friction factor, which was higher than for single-phase flow due to the presence of the liquid film. The resulting correlation predicted their data well. The authors also developed a separate correlation for a laminar condensate film with a linear velocity profile. Hence, the condensation process was divided into three different regions: laminar condensate entrance region, turbulent condensate, and laminar vapor exit region (where a Nusselt analysis was more appropriate).

Akers and Rosson (1960) developed three different experimentally validated heat transfer correlations for condensation inside horizontal tubes for “semistratified” flow (annular condensation and run down superimposed on stratified flow), laminar annular flow, and turbulent annular flow. Local values of the condensation heat transfer coefficient were determined experimentally for methanol and R-12 flowing inside a 15.88 mm horizontal tube. For liquid Reynolds numbers below 5,000, the heat transfer coefficient was a function of the Prandtl number, vapor Reynolds number, and thermal potential (i.e. wall temperature difference). For this region, the constant multiplier for the Nusselt number was determined from the experimental data. This constant and the exponent for vapor Reynolds number were different for vapor Reynolds numbers above and below 20,000. For turbulent liquid films, the correlation developed by Akers et al. (1959), which neglected the wall temperature difference, was employed. Akers et al. (1959) defined an all-liquid flow rate that provided the same heat transfer coefficient for condensing annular flow. This all-liquid flow rate was expressed by an “equivalent” mass flux, which was used to define an equivalent Reynolds number. This equivalent Reynolds number was substituted in a single-phase heat transfer equation, which was a function of the liquid Prandtl and Reynolds numbers, to predict the two-phase condensation Nusselt number. The authors reported an average deviation between this correlation and the experimental data of less than 5% with a maximum deviation of 20%.

Boyko and Kruzhilin (1967) presented a modification to the work of Ananiev et al. (1961), which stated that the condensation heat transfer coefficient was equal to Mikheev's (1956) formula for single phase heat transfer multiplied by the square root of the ratio of condensate density to homogenous density. Experimental data from Miropolsky (1962) for the condensation of steam inside 18 mm diameter stainless steel and copper tubes were used

to evaluate the correlation. Based on this comparison, they proposed a modification for the constant multiplier used in Miropolsky's formula, but a different one for each type of tube. This correlation predicted the data within  $\pm 20\%$ . As noted by Carey (1992), the fact that different constants were required for different tube-fluid combinations may reduce the usefulness of the correlation.

Soliman et al. (1968) developed a model for predicting the condensation heat transfer coefficient for annular flow. This paper was a correction of the previous work by Carpenter and Colburn (1951), who apparently incorrectly accounted for the momentum contribution to the wall shear stress. Soliman et al. (1968) and Carpenter and Colburn (1951) both concluded that the wall shear stress was the sum of the contributions due to friction, momentum, and gravity. Soliman et al. (1968) performed momentum balances around the vapor core and the liquid film. By neglecting the vapor and liquid cross-section changes in the axial direction and assuming no slip at the interface, they obtained the relationships between wall shear stress and the friction, momentum, and gravity contributions. They determined the friction contribution by using the Lockhart and Martinelli (1949) pressure gradient correlation. The momentum contribution accounted for the momentum changes in the vapor core and liquid film. They also included the change in momentum due to the vapor condensing into the film, i.e. due to the decrease from the vapor velocity to the liquid film velocity. They used the Zivi (1964) correlation for void fraction, and assumed that the quality changed linearly with axial position. After calculations were made on a tube with some inclination (the value was not specified), they noticed that the friction contribution was important at high-to-intermediate qualities. The momentum contribution became increasingly important for high density ratios, and could dominate at low qualities. This is especially the case for horizontal flows, where no gravity contribution exists. In addition, the gravity term was negligible at high qualities, but it increased in significance as the film thickness increased (i.e. at low qualities). Soliman et al. (1968) used the form proposed by Carpenter and Colburn (1951) for the condensation heat transfer coefficient and the relation developed for wall shear stress, and their own experimental data, to find the Prandtl number exponent and multiplication constants. The fluids used were steam, R-113, ethanol, methanol, toluene, trichloroethylene, and R-22, while the diameters ranged from 7.44 to 11.66 mm for tubes in vertical and horizontal orientations. The resulting correlation agreed well with the data, although no numbers were given.

Traviss et al. (1973) presented a force-convective Nusselt number model for annular flow condensation using a boundary layer approach. The results were compared with experiments conducted on R-12 and R-22 condensing in an 8 mm tube. The analogy

between heat transfer and momentum was applied using the von Karman universal velocity distribution in the liquid film. The interfacial and vapor temperatures were assumed to be at the saturation temperature. Assuming that the liquid film was thin compared to the tube length, flat plate flow was assumed to be valid. The eddy diffusivity ratio (i.e. the turbulent Prandtl number) was assumed to be unity, and the heat flux at the interface was assumed to approximately equal the wall heat flux. Using the assumed liquid velocity profile, a relationship for the condensation heat transfer coefficient was determined as a function of the turbulent film thickness. They then derived a relationship for the liquid Reynolds number as a function of this film thickness. By arguing that the interfacial shear to wall shear ratio was approximately unity, the final relationship for the condensation heat transfer coefficient was found. The data collected included the mass flux range of 161 to 1533 kg/m<sup>2</sup>-s. Agreement with the experimental data was good for qualities as low as 0.1, and the quality range from 0 to 0.1 was predicted well by conducting a linear interpolation between this model and a single phase heat transfer correlation. When the turbulent Martinelli parameter was below 0.155, the correlation had good results. However, for Martinelli parameters above 0.155, most likely a mist flow (high quality and mass flux) condition, the experimental data were underpredicted by the correlation. A correction factor was proposed to improve predictions in this area.

Cavallini and Zecchin (1974) presented an analytical model as well as a simple dimensionless correlation for forced-convective condensation inside smooth horizontal tubes. The results of the analyses were compared with data gathered for the condensation of R-11, R-22, and R-114 inside horizontal tubes. The range of tube diameters was not specified. The idealized annular flow model was assumed with a uniform film thickness around the vapor core. The von Karman universal velocity profile was employed on the liquid film and the analogy between heat transfer and momentum was used. The dimensionless film thickness was found as a function of the liquid Reynolds number. The wall shear stress was assumed to be equivalent to the sum of the adiabatic two-phase shear calculated from the Lockhart and Martinelli (1949) method, and the product of the vapor velocity and condensing mass flux (i.e. the change in momentum due to condensation). The interfacial shear stress was determined from the momentum equation applied to the annular film. In addition, a dimensionless correlation was developed from the data as a function of the density ratio, viscosity ratio, sensible to latent heat ratio, Reynolds number, Prandtl number, Froude number, and the "quality group," which includes the density ratio. The dimensionless correlation was further simplified by including only the Reynolds number, quality group, and Prandtl number terms. The more comprehensive dimensionless correlation predicted the

results from the theoretical analysis to within a standard deviation of 9.9%, while the simplified version had a standard deviation of 13.7%. Most of the experimental data were predicted by all three methods to within a standard deviation of 24%.

Shah (1979) developed a dimensionless correlation for calculating local heat transfer coefficients during film condensation. Based on his previous work on evaporative heat transfer (Shah, 1976), he assumed that film condensation heat transfer was similar to evaporation without nucleate boiling, as long as the tube was completely wetted during condensation. Since the evaporation correlation was based on a two-phase multiplier approach, the author simply used a large set of condensation data (474 data points from 21 different investigators) to develop a new two-phase multiplier for condensation. The range of fluids included water, R-11, R-12, R-22, R-113, methanol, ethanol, benzene, toluene, and trichloroethylene condensing inside horizontal and vertical tubes, as well as an annulus. The mass fluxes ranged from 11 to 211 kg/m<sup>2</sup>-s for tube diameters between 7 and 40 mm and for condensation of vapor qualities between 0% and 100%. The author noted that the correlation should only be valid for the operating ranges of the data considered and for the reduced pressure range 0.002 to 0.44. This correlation predicted all of the data to within an average deviation of  $\pm 17\%$ . Some noticeable discrepancies included the underprediction of the data at high qualities (85% to 100%), which could be due to entrance or entrainment effects. The author also restricted the use of this correlation for liquid Reynolds numbers above 350, due to the limited low Reynolds number data. He also cautioned that the experimental data from these various sources could have high uncertainties for various reasons, including low coolant temperature difference and the uncertainty of quality estimation.

Soliman (1986) developed a heat transfer correlation for condensation in annular-mist flow. The mist flow pattern usually existed at high mass fluxes and occurred over a large range of qualities. The high vapor flow, which causes high interfacial shear, disables the formation of a thin liquid film and causes high liquid entrainment. By using the modified Weber number, which accounts for the vapor inertia, liquid viscosity, and surface tension forces, Soliman (1983) showed that the flow was always in the mist region when  $We > 30$  and always annular for  $We < 20$ . Since the film was thinned by the vapor, the heat transfer coefficient was proposed to be higher for mist flow than for annular flow. Soliman (1986) compared the correlation of Akers et al. (1959) with data from a variety of horizontal and vertical tube data sets, which included steam, R-113, and R-12 condensing inside tubes ranging in diameter from 7.4 to 12.7 mm. He found that although the Akers correlation was successful in predicting the data for  $We > 20$ , the data were seriously underpredicted by this correlation for  $We > 30$ . This was consistent with his annular-to-mist transition criterion

(Soliman, 1983). He also compared the data from Akers et al. (1959) to the correlation developed by Traviss et al. (1973), which he found overpredicted nearly all of the data, and attributed it to property effects. Based on these observations, Soliman (1986) presented an empirical correlation using the homogenous flow assumption for the mist flow regime. The analogy between heat transfer and momentum transfer for single-phase turbulent flow was used as a starting point. Thereafter, the effect of wall temperature difference was accounted for, which resulted in a correlation (valid for  $We > 30$ ) that had a  $\pm 20\%$  deviation from the mist flow heat transfer data.

Chen et al. (1987) developed a film condensation heat transfer correlation based on analytical and empirical approaches. The authors used cocurrent liquid-vapor condensation data for vertical downward flow inside a 30 mm tube. Using the results from the study by Chun and Seban (1971) on laminar film condensation with a wavy interface, the study by Blangetti and Schlunder (1978) on vertical tube condensation, and the study by Soliman et al. (1968) for film condensation with high interfacial shear stress as asymptotic relationships, the general film condensation heat transfer coefficient correlation was developed as a function of the dimensionless interfacial shear stress. The vertical tube correlation was developed using Dukler's (1960) relation for dimensionless shear stress in adiabatic two-phase annular flow. Since condensation inside horizontal tubes for annular flow is dominated only by vapor shear, the gravity terms in the vertical tube correlation were neglected to provide the horizontal tube correlation. The authors stated that this local Nusselt number correlation should only be used for annular flow, which does not include mist flow (high entrainment, thin film). However, a comparison of the horizontal tube correlation with horizontal flow data was not presented.

Nitheanandan et al. (1990) presented a comparison of several heat transfer coefficient correlations with existing condensation data for flow inside horizontal tubes with the intention of developing a more accurate approach to the design of condensers using flow regime criteria. The existing heat transfer database included R-12, R-113, and steam condensing inside tubes with diameters ranging from 7.4 to 15.9 mm. The type of flow was divided into three regimes: wavy, annular, and mist flow. The transition from wavy to annular and mist flows was determined using a constant Froude number criterion similar to that of Soliman (1982), which Nitheanandan et al. (1990) established to be at  $Fr = 7$  from an analysis of their data. The transition from annular to mist flow was determined from the Weber number defined by Soliman (1986), but they chose a Weber number of 40 instead of 30 (which was used by Soliman (1986)) for this transition. For the mist flow regime, the Soliman (1986) correlation predicted 83% of the mist flow database to within  $\pm 30\%$ , which

was better than any other correlation. For the annular flow regime, the Shah (1979) correlation predicted 63% of the annular flow database to within  $\pm 30\%$ , which was slightly better than the Akers and Rosson (1960) correlation. The Akers and Rosson (1960) correlation predicted 77% of the wavy flow data to within  $\pm 30\%$ , which was the best predictor. These three correlations coupled with the transition criteria were recommended for design, and were compared with the heat transfer database. The majority of the data, as expected, were predicted by this method to within  $\pm 30\%$ , with a maximum deviation of 50%.

Ibrahim (1994) developed a numerical model for predicting the local condensation heat transfer coefficient. The model assumes the following: annular flow with no entrainment, vapor and liquid flows are turbulent, constant properties, negligible heat dissipation, negligible angular and axial heat conduction, and also that the interface and saturation temperatures are equal. He solves a non-dimensional form of the energy equation, coupled with a Lockhart and Martinelli (1949) method for calculating the pressure drop. The condensation heat transfer coefficient is calculated from conduction across the liquid film. The finite-difference method compares the results for three liquid film models: turbulent mixing length model, turbulent mixing length model with Van Driest damping, and a laminar liquid film. The model was compared with the experimental data presented by Abis (1969), which was for R-12 condensing inside a 12.7 mm horizontal tube. The Van Driest damping function included in the mixing length turbulent model for the laminar liquid sublayer predicted the data better than a laminar liquid film or the original mixing length model.

Chitti and Anand (1995) presented an analytical model for condensation heat transfer coefficients inside smooth horizontal round tubes. The results were compared with experimental data gathered for R-22 condensing inside an 8 mm horizontal tube. The numerical model included the following simplifying assumptions: annular flow, film condensation through a thin, circumferentially uniform liquid film, negligible liquid entrainment in the vapor core, steady turbulent flow in the liquid film, constant properties in the liquid film with negligible film subcooling, and saturated vapor temperature. Since the film was assumed to be turbulent, the universal law of the wall velocity profile was used. A numerical procedure was developed to obtain the non-dimensional film thickness and the condensation heat transfer coefficient. They noted that the non-dimensional film thickness decreased linearly with quality, but the actual film thickness decreased non-linearly. This showed that the increased resistance to heat transfer was greater at lower qualities, which was borne out by the data, except for the lowest mass flux, where the heat transfer coefficient decrease was more gradual and the flow regime was probably stratified-wavy as opposed to annular. In addition, the local heat transfer coefficient decreased rapidly for qualities less

than 50%, except for the lowest mass flux. The authors also compared this method for calculating the local condensation heat transfer coefficient, along with the correlations of Akers et al. (1959), Boyko and Kruzhilin (1967), Shah (1981), and Traviss et al. (1973), to their experimental data. The data were underpredicted by Akers et al. (1959) at high mass fluxes, with an overall mean deviation of 21.5%. The experimental data were also underpredicted by the Boyko and Kruzhilin (1967) correlation for all mass fluxes, with a mean deviation of 26.2%. The Shah (1981) and Traviss et al. (1973) correlations predicted the data well and with mean deviations of 13.3% and 14.6%, respectively. The model developed by Chitti and Anand (1995) predicted the data within a mean deviation of 15.3%, with most data within  $\pm 25\%$ .

Chitti and Anand (1996a) presented condensation heat transfer coefficient data for an R-32/R-125 mixture (50/50 by weight) with oil concentrations of 0%, 2.6%, and 5.35%, and pure R-22 condensing inside an 8 mm horizontal tube. The results were plotted on a Taitel and Dukler map, which showed that most of the data were in the annular regime. They studied the effects of condensing temperature as well as mass flux on the heat transfer coefficient. The heat transfer coefficient increased with quality, and the results agreed well with the Shah (1981) and Traviss et al. (1973) correlations, but not with the correlations developed by Akers et al. (1959) and Boyko and Kruzhilin (1967). However, at a mass flux of  $208 \text{ kg/m}^2\text{-s}$ , the Shah (1981) and Traviss et al. (1973) correlations deviated from the experimental data by as much as 50% at the lowest quality. As the mass flux was increased to  $392 \text{ kg/m}^2\text{-s}$ , the predictions were much closer. The authors attributed these observations to the closeness to the stratified-wavy to annular transition. As the vapor shear increased, which is the case at the high mass flux, it is more likely that the flow is annular. In addition, from their analysis, Chitti and Anand (1996a) believe that the effect of condensing temperature on the heat transfer coefficient will be minimal ( $\sim 10\%$ ) for refrigerants much below the critical temperature. Moreover, the authors state that the mass flux is the dominant factor affecting the condensation heat transfer coefficient. Chitti and Anand (1996a) also conducted a non-dimensional Nusselt number analysis for the 4 data sets (R-22, and R-32/R-125 with oil concentrations of 0%, 2.6%, and 5.37%). The parameters they included were as follows: flow rate, latent heat of condensation, geometry, liquid and vapor viscosity, density, specific heat and conductivity, liquid film subcooling, and film thickness. The last two parameters were related to the heat conduction across the film. The remaining parameters were absorbed in the liquid Reynolds and Prandtl numbers. Using these parameters, they developed a correlation that showed an average deviation of 8.8% from the data.

In a subsequent paper, Chitti and Anand (1996b) developed a population balance

model with the homogeneous flow assumption for predicting the forced-convective condensation heat transfer coefficient. The results from the model were compared with data gathered for the 4 data sets (R-22, and R-32/R-125 with oil concentrations of 0%, 2.6%, and 5.37%) mentioned previously in Chitti and Anand (1996a). The model was based upon the approach demonstrated by Lin (1979). The following simplifying assumptions were used: homogeneous flow (liquid-vapor “packets”), a packet is initially at  $T_{\text{bulk}}$  when it contacts the cold wall, the packet has “mean” fluid properties, the packet exchanges heat with the wall during contact time and is then replaced by another packet, and expressions for the distribution function and mean residence time were given by Lin (1979). The authors also assumed that heat was transferred from the wall to some thickness from the wall, where the mean flow was at the bulk temperature. By assuming the heat was transferred during the contact time by conduction only, the one-dimensional heat conduction equation (with a “mean” thermal diffusivity) was solved for the temperature profile in the y-direction (a pseudo-radial direction). Using this solution, multiplying it by the distribution function, and integrating with respect to time from the initial condition to infinity resulted in an expression for the mean heat flux, which in turn means the heat transfer coefficient, as a function of the mean residence time. Now, the mean residence time was directly proportional to the condensation length and inversely proportional to the mean velocity. The mean flow velocity was assumed to be a function of the flow rate, flow diameter, mean density, and the average size of the packet. In turn, the mean velocity varies because the packet size (or, equivalently, the liquid condensate area) varies with local quality. Lin (1979), however, assumed that the velocities of the two phases were approximately the same due to vigorous mixing by static mixers, and this velocity could be determined from the volumetric flow rate and density of the condensate film. An energy balance at the surface was used to find an expression for the average packet size, and was then substituted into the mean velocity and residence time equations. Hence, an expression for the Nusselt number was defined as a function of the mean Prandtl and Reynolds number, geometry, sensible and latent heat exchange, and the wall-bulk temperature difference. The Nusselt number relationship with the data was found by fitting a straight line:  $Nu = C\beta + b$ .  $\beta$  was the combination of the parameters in the derived Nusselt number equation, while  $b$  and  $C$  were the intercept and slope, respectively. The results are only valid for  $150 < G < 500 \text{ kg/m}^2\text{-s}$ . This model predicts most of the R-22 data to within  $\pm 20\%$  with an average deviation of  $\pm 16.4\%$ . The pure R-32/R-125 data were predicted with an average error of 12.1%, while the data for 2.6% and 5.37% oil concentrations were predicted, on average, within 13.1% and 10.3%, respectively. For the R-22 data, the model seems to overpredict the heat transfer coefficient for high  $G$ , but it was

still within experimental uncertainty. For all of the R-32/R-125 data sets, the heat transfer coefficient was underpredicted below  $G = 200 \text{ kg/m}^2\text{-s}$  and overpredicted above  $G = 350 \text{ kg/m}^2\text{-s}$ . Good agreement with the data was achieved between these flow rates. Hence, the model was assumed to be valid for mass fluxes between 250 and 350  $\text{kg/m}^2\text{-s}$  and qualities between 0.3 and 0.7.

## Previous Research on Small Diameter Tubes

The papers reviewed thus far have included both gravity-driven and shear-driven heat transfer investigations. Those investigations studied condensation heat transfer inside tubes with larger diameters (i.e. 7 to 50 mm) than those investigated in the present study ( $0.424 \text{ mm} < D_h < 1.524 \text{ mm}$ ). In this section, the somewhat limited literature on tubes with diameters less than 7 mm is discussed.

Breber et al. (1980) compiled flow pattern data from a variety of sources and developed a simple methodology to predict flow regimes during condensation based on the flow regime map of Taitel and Dukler. The fluids include R-12, R-113, steam (adiabatic test), R-11, and n-Pentane, while the tube diameters ranged from 4.8 to 50.8 mm. The four basic flow “zones” identified were: annular and mist-annular, bubble, wavy and stratified, and intermittent (slug and plug). Good agreement was found between the data and the Taitel-Dukler map for tube diameters ranging from 8 to 22 mm, but there was poor agreement for the 4.8 mm tube data. Their simplified flow regime map was developed with dimensionless gas velocity on the ordinate and the Martinelli parameter on the abscissa. The transitions in this map are vertical and horizontal bands instead of the distinct lines found in many other flow-regime maps. They recommend a Nusselt type heat transfer correlation for the wavy and stratified zone, while the Traviss et al. (1973) correlation was recommended for all other zones, including the intermittent zone.

Dobson et al. (1994) presented condensation heat transfer data for R-12 and R-134a flowing inside a 4.57 mm horizontal tube. The condensing mass flux ranged from 75 to 600  $\text{kg/m}^2\text{-s}$ . The flow regimes observed in this study are as follows: wavy, annular, and annular-mist flow. Dobson et al. (1994) based the transition from wavy to annular flow upon the Froude number transition proposed by Soliman (1982), which examined the relative magnitudes of the vapor and gravity forces on the liquid film. They stated that a Froude number of 18 corresponded to this transition. The modified Weber number criterion ( $We = 30$ ) proposed by Soliman (1986) was used as the transition from annular to mist-annular flow. This transition was found by comparing the vapor shear with the liquid viscosity and surface tension forces. The condensation heat transfer coefficient was found to be

proportional to the wall-to-refrigerant temperature difference raised to the 0.25 power. This was consistent with the findings of Chato (1962). Dobson et al. (1994) also provided semi-empirical correlations for the wavy and annular flow regimes. The wavy regime correlation was based on the correlation developed by Chato (1962) with the constant 0.55 replaced by a function of Martinelli parameter to account for the variation of void fraction with quality. This correlation predicted the wavy flow data to within a mean absolute deviation of 8.9%. The annular flow correlation was the Dittus-Boelter single-phase correlation multiplied by a function of the Martinelli parameter, which stems from the analogy between momentum and heat transfer. This correlation predicted the annular flow data to within a mean absolute deviation of 7%. The correlations of Chen et al. (1987), Cavallini and Zecchin (1974), Shah (1979), and Traviss et al. (1973) predicted the annular flow data to within mean absolute deviations of 13%, 18%, 20%, and 31%, respectively. Dobson et al. (1994) also pointed out that the condensation heat transfer coefficient was a function of saturation temperature. For example, the heat transfer coefficients predicted for R-134a were 15% higher for a saturation temperature of 35°C than for 60°C. This was attributed to the decrease in thermal conductivity and slip velocity at the higher temperatures.

Yang and Webb (1996) compared condensation heat transfer data for R-12 flowing inside plain and micro-fin microchannel tubes with hydraulic diameters of 2.637 and 1.564 mm, respectively, for mass fluxes between 400 and 1400 kg/m<sup>2</sup>-s. For both the plain and micro-fin tubes, the total heat transfer area was assumed to be equal to the entire wetted area. Apparently, no fin effects were included, but this may be acceptable if the fin efficiency was high. For both tubes, the authors noted that the condensation heat transfer coefficient increased with increasing heat flux. In fact, the condensation heat transfer coefficient was proportional to the heat flux raised to the power of 0.2. Also, the micro-fin tubes had higher heat transfer coefficients than the plain tube, but the micro-fin heat transfer enhancement decreased with increasing mass flux. This was assumed to happen because the surface tension drainage force increased the heat transfer coefficient in the micro-fin tubes when the film was sufficiently thin, but only until the point when vapor shear completely dominated the heat transfer. They compared their experimental data with the condensation heat transfer correlations proposed by Shah (1979) and Akers et al. (1959). The Shah (1979) correlation overpredicted the data, while the Akers et al. (1959) was close to the experimental data, except at high mass fluxes, where it also overpredicted the data. In addition, the micro-fin tubes had a steeper heat transfer coefficient versus quality slope, but, again, Akers et al. (1959) did a better job of predicting the data.

Dobson and Chato (1998) conducted flow visualization and heat transfer experiments

on smooth tubes, with diameters ranging from 3.14 mm to 7.04 mm, for R-12, R-22, R-134a, and 50/50 and 60/40 blends of R-32/R-125. The purpose of this research was to measure and predict heat transfer coefficient as a function of flow regime. According to their results, the dominant factors affecting the observed flow regimes were mass flux and quality. The authors acknowledged the potential role of surface tension on flow regime transition (especially at smaller diameters), but said that this needs further attention. For the heat transfer experiments, only the 261 points gathered for the 3.14 mm tube and the 387 data points collected for the 7.04 mm tube were used for correlation development. At the lowest mass flux ( $75 \text{ kg/m}^2\text{-s}$ ), the Nusselt number was relatively insensitive to quality. When the mass flux increased to  $300 \text{ kg/m}^2\text{-s}$ , the Nusselt number was relatively constant for data points up to a quality of about 30%, which the authors state was characteristic of wavy flow. Thereafter, the slope changed and the Nusselt number increased with quality, which they said was characteristic of the annular regime. For the wavy regime, the dominant heat transfer mechanism was laminar film condensation, which is gravity-driven. In addition, the heat transfer coefficient depends primarily on film thickness, which does not change much with vapor quality. The authors lumped stratified, wavy, and intermittent flow together because they state that these three regimes are governed primarily by gravity, although it is not clear why the intermittent flow regime was considered to be governed by gravity. For the annular flow regime, the dominant heat transfer mechanism was interfacial shear stress. According to Dobson and Chato, the correlations of Soliman et al. (1968) and Traviss et al. (1973) demonstrated the interdependence of pressure drop and heat transfer coefficient. Since pressure drop increased significantly with quality for shear-driven flow, so should the heat transfer coefficient.

Based on the above considerations, Dobson and Chato (1998) developed two correlations: (1) gravity-driven and (2) shear-driven. For the gravity-driven correlation, they stated that the heat transfer coefficient was dependent on the wall temperature difference and, therefore, the liquid pool heat transfer at the bottom of the tube cannot be neglected. Hence, heat was transferred by film condensation at the top of the tube and liquid pool forced-convective condensation. At low vapor velocities, the film condensate was not affected by vapor shear and the film thickness was not a function of position. Nusselt's solution over a horizontal cylinder would be sufficient and the pool thickness heat transfer can be neglected (no or little movement in the axial direction). As the vapor velocity was increased, the interfacial shear becomes significant and eventually dominates, as in the annular flow regime. The authors solved the conservation equations to find the film thickness in the entry and fully developed regions. Vapor shear determined the length of the entry region, which

was short for low vapor shear and long for high vapor shear. Since high vapor shear corresponds to annular flow, the film condensation solution for low shear was deemed to be appropriate. The resulting correlation, which accounted for both film condensation and liquid pool forced-convective heat transfer, had a 6.6% deviation from the wavy (i.e. intermittent, wavy, and stratified) flow heat transfer data. The authors said that the largest deviations occurred in the 3.14 mm tube data, but no quantitative information was given. They hypothesized that this was from the large uncertainty in the data (heat duty was on the order of 50 W). For the annular flow regime, the primary resistance to heat transfer existed in the laminar sublayer and buffer regions. Therefore, the resistance to heat transfer increases very rapidly until the film thickness becomes large. The correlation by Travis et al. (1973) was used as a guide for the annular flow heat transfer correlation. A simple force balance showed that the Nusselt number is proportional to the square root of the pressure drop. Film Reynolds numbers above 1125 correspond to turbulent flow, and most data in annular flow have  $Re_{film} > 1125$ . A two-phase multiplier approach was used to develop the correlation. The Dittus-Boelter single-phase heat transfer coefficient was multiplied by a function of the Martinelli parameter, which approaches 1 as the quality approaches 0 and results in the single-phase heat transfer coefficient. But this was not the case as the quality approaches 1. The authors recommended that the wavy flow correlation be used for  $G < 500$   $kg/m^2\cdot s$  and  $Fr < 20$  and that the annular flow correlation be used for all  $x$  when  $G \geq 500$   $kg/m^2\cdot s$  and for  $Fr \geq 20$  when  $G < 500$   $kg/m^2\cdot s$ . This method was compared with their experimental data for the 3.14 mm and 7.04 mm tubes. The R-134a data were predicted within a mean deviation of 4.4%; the R-22 data were predicted within a mean deviation of 4.9%; and the 50/50 and 60/40 blends of R-32/R-125 data were predicted within mean deviations of 5.9% and 6.1%, respectively.

Moser et al. (1998) presented a new equivalent Reynolds number model for condensation heat transfer coefficient prediction. The model was a modified version of the model developed by Akers et al. (1959). In both models, the assumption was that the condensing heat transfer coefficient could be calculated using a modified single-phase heat transfer coefficient for an equivalent liquid flow. In Akers et al. (1959), the equivalent mass flux was the sum of the actual and fictitious (determined from the vapor flow and shear) liquid mass fluxes. Moser et al. (1998) point out that Akers et al. (1959) incorrectly assumed that the vapor and liquid friction factors were equal and that the driving temperature difference was not the bulk-wall temperature difference, but the interface-to-wall temperature difference. The new equivalent Reynolds number proposed by Moser et al. (1998) was found from a shear stress relationship and the friction pressure gradient definition. They also

defined a new correction factor for the interface-wall temperature difference, which was found from the following assumptions: von Karman universal velocity profile, thin film annular flow, uniform film thickness, no liquid entrainment in the vapor core, and a turbulent Prandtl number of unity. Using the Petukhov (1970) equation for single-phase flow and the newly developed multiplier with the new equivalent Reynolds number, they compared the results with local and average condensation data from various authors for tube diameters ranging from 3.14 to 20 mm. The fluids in these studies were R-11, R-12, R-22, R-125, R-134a, and R-410a. The total data set was predicted within an absolute mean deviation of 13.64%. This new method proved to be better at predicting the heat transfer coefficient than both the Shah (1979) and Traviss et al. (1973) methods, which predicted the average and local data to within 14.27% and 20.01%, respectively.

Hurlburt and Newell (1999) presented condensation heat coefficient and pressure drop models for annular flow inside smooth horizontal tubes. The results were compared with experimental data reported by Sacks (1975) for R-11, R-12, and R-22 and Dobson (1994) for R-22 and R-134a. The tube diameters ranged from 3 mm to 10 mm. The following assumptions were employed in the model: vapor heat transfer resistance was small compared to the liquid resistance, liquid interface was circumferentially uniform, tube wall temperature was circumferentially uniform, and the bulk temperature was a mass flow average temperature, which was equal to the interface temperature. For the liquid film, von Karman's universal velocity profile was used. Their analysis utilizes an empirical interfacial shear correlation by Asali et al. (1985), rather than a specified void fraction correlation. The pressure drop was related to the interfacial shear stress, which was solved simultaneously with the wall shear stress, film thickness, and interface velocity. The heat transfer coefficient was found using the Law of the Wall temperature profile. It should be noted that the heat transfer coefficient was dependent on the film thickness, which could be in three different layers: viscous, buffer, and turbulent. Hence, the heat transfer coefficient model was presented as a piecewise function of the film thickness. The model tended to underpredict R-11 pressure drop and overpredict R-12 and R-22 pressure drop, which suggested that the interfacial shear model needs to be improved, especially as the liquid-vapor density ratio decreases away from air-water (i.e. higher pressure refrigerants). The model predicts the R-11 heat transfer data well. For the R-12 and R-22 data and qualities below 70%, the model overpredicted the data for high mass fluxes, and underpredicted the data at low mass fluxes. At high qualities, the model lost both qualitative and quantitative agreement. At high qualities, the thinning of liquid film causes deviation, while the dominant heat transfer mechanism at low qualities was gravity. For the Dobson (1994) data, the model

underpredicted the small diameter tube data ( $D = 3.14$  mm), while predicting the large diameter tube data well. The authors attributed the deviation in the  $D = 3.14$  mm data to neglecting the energy content of the near-wall fluid, thus causing systematic deviation in the bulk temperature.

## Summary

The above review of the literature shows gravity-driven heat transfer has been studied using a variety of techniques ranging from simple correlations to complex numerical analyses. For simplified correlations, many investigators (i.e. Chato (1962), Rosson and Myers (1965), Jaster and Kosky (1976), and Dobson et al. (1994)) proposed an adaptation of the Nusselt falling film analysis for condensation inside a horizontal tube. Jaster and Kosky (1976) and Dobson et al. (1994) included the effect of changing void fraction in their stratified flow correlation. Although investigators such as Chato (1962) and Dobson et al. (1994) have chosen to neglect the heat transfer through the bottom portion of the tube, others such as Rosson and Myers (1965), Singh et al. (1996), Dobson and Chato (1998), and Guo and Anand (2000) have included this effect. In addition, Chato (1962), Rufer and Kezios (1966), Chen and Kocamustafaogullari (1987), and Guo and Anand (2000) have presented numerical analyses of stratified flow condensation with varying complexity. Due to the complicated nature of their analyses, Chato (1962) and Rufer and Kezios (1966), Chen and Kocamustafaogullari (1987) have also presented simplified correlations that agree relatively well with the numerical results. For intermittent flow, Tien et al. (1988) have presented a model that included single-phase liquid slug heat transfer combined with vapor/liquid gravity-driven condensation.

Annular flow condensation has been studied the most because it is the dominant flow mechanism in a wide variety of two-phase flow applications. A variety of techniques have been used to develop annular flow heat transfer correlations. Carpenter and Colburn (1951) pioneered the concept of a shear-based correlation. They postulated that the condensation heat transfer coefficient could be related directly to the wall shear stress, which was the sum of the friction, momentum, and gravity contributions. Soliman et al. (1968) corrected the momentum contribution determined by Carpenter and Colburn (1951) and provided their own correlation for annular flow condensation. Chen et al. (1987) later postulated that their vertical annular flow shear-dominated correlation could be related to horizontal flow by neglecting the gravity contribution. Their analysis was similar to Soliman et al. (1968) except that the momentum and gravity contributions were neglected and a new pressure drop model was employed.

Another type of method that has been explored for annular flow condensation is the two-phase multiplier approach. In this case, a factor was multiplied to an existing single-phase correlation to yield an expression for two-phase flow. Cavallini and Zecchin (1974), Shah (1979), and Dobson et al. (1994) all use modified versions of the Dittus-Boelter equation for finding the two-phase condensation heat transfer coefficient. After modifying the equivalent Reynolds number analysis by Akers et al. (1959), Moser et al. (1998) used the Petukhov (1970) single-phase correlation as a basis for their two-phase correlation.

More theoretically based correlations have also been developed through boundary layer analyses. Traviss et al. (1973) conducted a thorough investigation of annular flow condensation assuming the von Karman analogy between heat transfer and momentum. Hurlburt and Newell (1999) noticed that the resistance to heat transfer was primarily in the viscous sublayer and buffer regions and developed their correlation accordingly. Dobson and Chato (1998) developed their annular flow correlation based on the analysis by Traviss et al. (1973), and the result was very similar to the two-phase multiplier result published by Dobson et al. (1994). In addition to these boundary layer results, Ibrahim (1994) and Chitti and Anand (1995) conducted numerical analyses for determining the annular flow condensation heat transfer coefficient.

In the annular flow correlations, there are several assumptions that are consistently used. The liquid film is assumed to be circumferentially uniform, and the liquid vapor interface is at the saturation temperature. In addition, it is assumed that no liquid entrainment in the vapor core exists for the annular flow. For cases with liquid entrainment, the homogeneous flow correlations developed by authors such as Boyko and Kruzhilin (1967), Chitti and Anand (1996b) and the mist flow correlation developed by Soliman (1986) are more appropriate.

## **Need for Further Research**

Although there are a variety of approaches to annular flow modeling, no specific type has emerged as the most appropriate style. Unfortunately, the existing database of correlations is fairly dependent on the type of experimental data covered by the researcher. This is also the case for gravity-driven condensation. Attempts have been made by Dobson and Chato (1998) and Nitheanandan et al. (1990) to provide a general condensation correlation that takes flow regime dependence into account with some success. In this investigation, the following deficiencies in the literature will be addressed:

- non-dimensional criteria available in the literature for determining the flow regimes may not be applicable to the tubes investigated in this study, and the heat transfer

coefficient as a function of quality may be discontinuous (although a method similar to the ones in Jaster and Kosky (1976) can remedy this)

- the applicability of all the different correlations for tubes with hydraulic diameters less than about 3 mm needs to be further studied
- the intermittent flow regime has been lumped into different flow regimes (i.e. different heat transfer mechanisms) by different investigators (Dobson and Chato (1998) include it in wavy flow, while Breber et al. (1980) include it in annular), the appropriateness of which needs to be studied
- the applicability of the horizontal intermittent flow model proposed in Tien et al. (1988) needs to be examined

The above issues are addressed in the current work. The following chapter discusses the experimental approach and the test facility developed for this research.

## CHAPTER THREE: EXPERIMENTAL SETUP AND PROCEDURES

This chapter provides detailed descriptions of the experimental setup and procedures, and is divided into three parts: test sections, experimental facility, and testing procedures. The test section geometry and the test matrix are described first. The requirements of the experiments and the test loop configuration are described in the experimental facility section, while the test setup and test condition establishment are described in the section on test procedures.

### Test Sections

The purpose of this study was to investigate the effects of hydraulic diameter and tube geometry on the condensation heat transfer coefficient. Previously, Coleman (2000) documented these effects on two-phase flow patterns for air/water mixtures and R-134a, and pressure drop for R-134a. In this study, heat transfer in the test sections used by Coleman (2000) in the R-134a pressure drop experiments is investigated. Figure 2 shows a representative test section consisting of rectangular tubes brazed together, supplied by Modine Manufacturing Company. The R-134a flows through the middle tube as a two-phase liquid/vapor mixture, and is partially condensed by the coolant flowing in a counter-flow orientation in the two outer tube jackets.

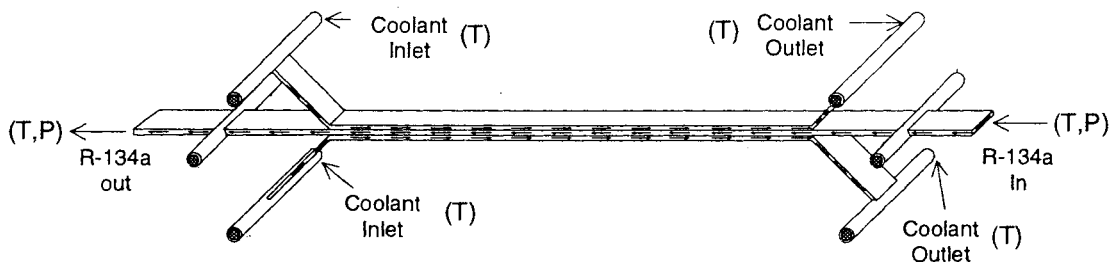


**Figure 2. Representative Microchannel Test Section**

The cross-sections of the 9 different test sections used in these experiments can be seen in Figure 3, with the corresponding geometric details such as the number of ports, total free flow area, total wetted perimeter, and tube outer height and width specified by the manufacturer shown in Table 1. Each tube has multiple flow channels of a circular, square, rectangular, barrel, “N”-shape, or triangular geometry. The multiple channels represent actual tubes in condensers, and also avoid the problems associated with measurements of

exceedingly small flow rates and heat duties in single channels. The hydraulic diameter for these channels is calculated as follows:

$$D_h = \frac{4 \cdot A_t}{P_t} \quad (6)$$

For example, test section S30, with a total free flow area and wetted perimeter of 9.871 mm<sup>2</sup> and 51.816 mm, respectively, has a hydraulic diameter of 0.762 mm.

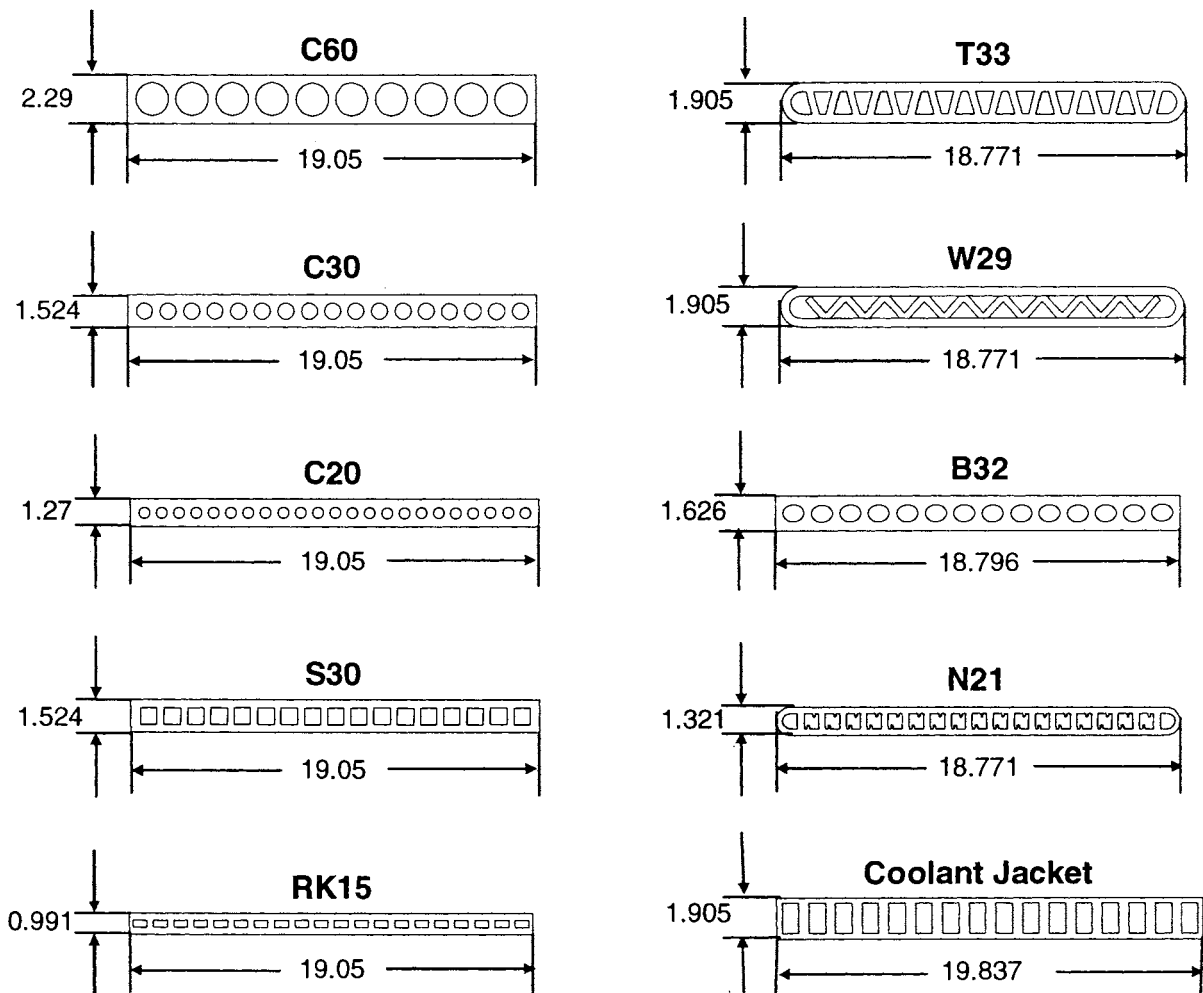


**Figure 3. Schematic of Cross-Sections for the Microchannel Test Sections (All Measurements are in mm)**

Table 1 also provides the port height and width, and the aspect ratio for test sections S30 and RK15, as well as the outer tube jacket. The port height and width was determined from the specified total free flow area, wetted perimeter and number of ports as follows:

$$A_t = N_{\text{port}} \cdot h_{\text{port}} \cdot w_{\text{port}} \quad (7)$$

$$P_t = 2 \cdot N_{\text{port}} (h_{\text{port}} + w_{\text{port}}) \quad (8)$$

**Table 1. Test Matrix for Heat Transfer Experiments**

Tube	Geometry	$N_p$	$A_t$ , mm <sup>2</sup>	$P_t$ , mm	$D_h$ , mm	$t_{ho}$ , mm	$t_{wo}$ , mm	$p_{ho}$ , mm	$p_{wo}$ , mm	$\alpha$
C60	Circle, Extruded	10	18.242	47.878	1.524	2.290	19.050	---	---	---
C30	Circle, Extruded	17	7.742	40.691	0.761	1.524	19.050	---	---	---
C20	Circle, Extruded	23	4.645	36.703	0.506	1.270	19.050	---	---	---
S30	Square, Extruded	17	9.871	51.816	0.762	1.524	19.050	0.762	0.762	1.000
RK15	Rectangle, Extruded	20	4.065	38.379	0.424	0.991	18.771	0.316	0.644	0.491
T33	Triangle, Extruded	19	13.419	64.008	0.839	1.905	18.771	---	---	---
W29	Triangle, Insert	19	12.277	67.135	0.732	1.905	18.771	---	---	---
B32	Barrel, Extruded	14	10.000	50.056	0.799	1.626	18.796	---	---	---
N21	N-shape, Extruded	19	7.871	58.763	0.536	1.321	18.771	---	---	---
Jacket	Rectangle, Extruded	16	17.032	69.088	0.986	1.905	19.837	1.397	0.762	0.545

The 17 ports in test section S30 have a height and width of 0.762 mm, while the 20 ports of test section RK15 have a height and width of 0.316 mm and 0.644 mm, respectively. The 16 ports in the tube jacket have a port height and width of 1.397 mm and 0.762 mm, respectively. The aspect ratio is found by dividing the short side by the long side. Test section S30 has an aspect ratio of 1, while test section RK15 and the tube jackets have aspect ratios of 0.491 and 0.545, respectively.

These tubes were tested at five mass fluxes (corresponding to nominal values of 150

kg/m<sup>2</sup>-s, 300 kg/m<sup>2</sup>-s, 450 kg/m<sup>2</sup>-s, 600 kg/m<sup>2</sup>-s, 750 kg/m<sup>2</sup>-s) for vapor qualities ranging nominally from 0.05 to 0.95 in increments of approximately 0.15 to 0.30. The mass flow rate required for a given mass flux is calculated as follows:

$$\dot{m} = G \cdot A \quad (9)$$

For example, the area of one port in test section S30 is 0.581 mm<sup>2</sup>. For a mass flux of 150 kg/m<sup>2</sup>-s, the mass flow rate through one port in this test section would be 8.710 x 10<sup>-5</sup> kg/s, a very low flow rate resulting in significant uncertainties. But the provision of 17 ports increases the flow rate to 0.00148 kg/s, which results in acceptable uncertainties.

## Experimental Facility

### Requirements for Accurate Heat Transfer Coefficient Determination

Accurate determination of the condensation heat transfer coefficients during phase change imposes several conflicting requirements on the design of the test facility and the test procedures. First, the test conditions must be accurately established and measured, which requires the following:

- Accurate determination of test-section inlet quality
- Accurate determination of test-section outlet quality
- Establishment of a wide range of qualities for the desired range of mass fluxes
- Small quality change in the test section to represent local phenomena

In addition, accurate determination of the condensation heat transfer coefficient imposes two other requirements:

- Accurate determination of the test section heat transfer rate
- Accurate determination of the refrigerant condensation heat transfer coefficient from measured temperatures, pressures, and flow rates

The other complicating aspect is that the requirements for heat transfer rate determination are in direct conflict with those for the determination of the condensation heat transfer coefficient. Several innovative features were incorporated into the design of the test facility to address these requirements, and are described below. The test facility was originally used for the condensation pressure drop experiments in Coleman (2000). Modifications that are described below enable its use for the heat transfer experiments. Figure 4 shows this microchannel phase-change heat transfer test facility.

### Evaporator, Pre- and Post-Condensers

Subcooled refrigerant enters a coiled tube-in-tube evaporator, where steam flowing in counter-flow heats the refrigerant to a superheated state. The superheated state was verified by a combination of a sight glass and temperature and pressure measurements. This

superheated vapor enters one of two pre-condensers. Both pre-condensers were straight tube-in-tube counterflow heat exchangers (6.35 mm and 12.7 mm inner and outer tube diameters, each with a 0.89 mm wall thickness) designed to partially condense the refrigerant using city water. The short pre-condenser is 0.419 m long, while the long pre-condenser is 1.35 m long. The different heat transfer areas provided by the two pre-condensers and varying cooling water flow rates allow for a wide range of vapor qualities at the test section inlet.

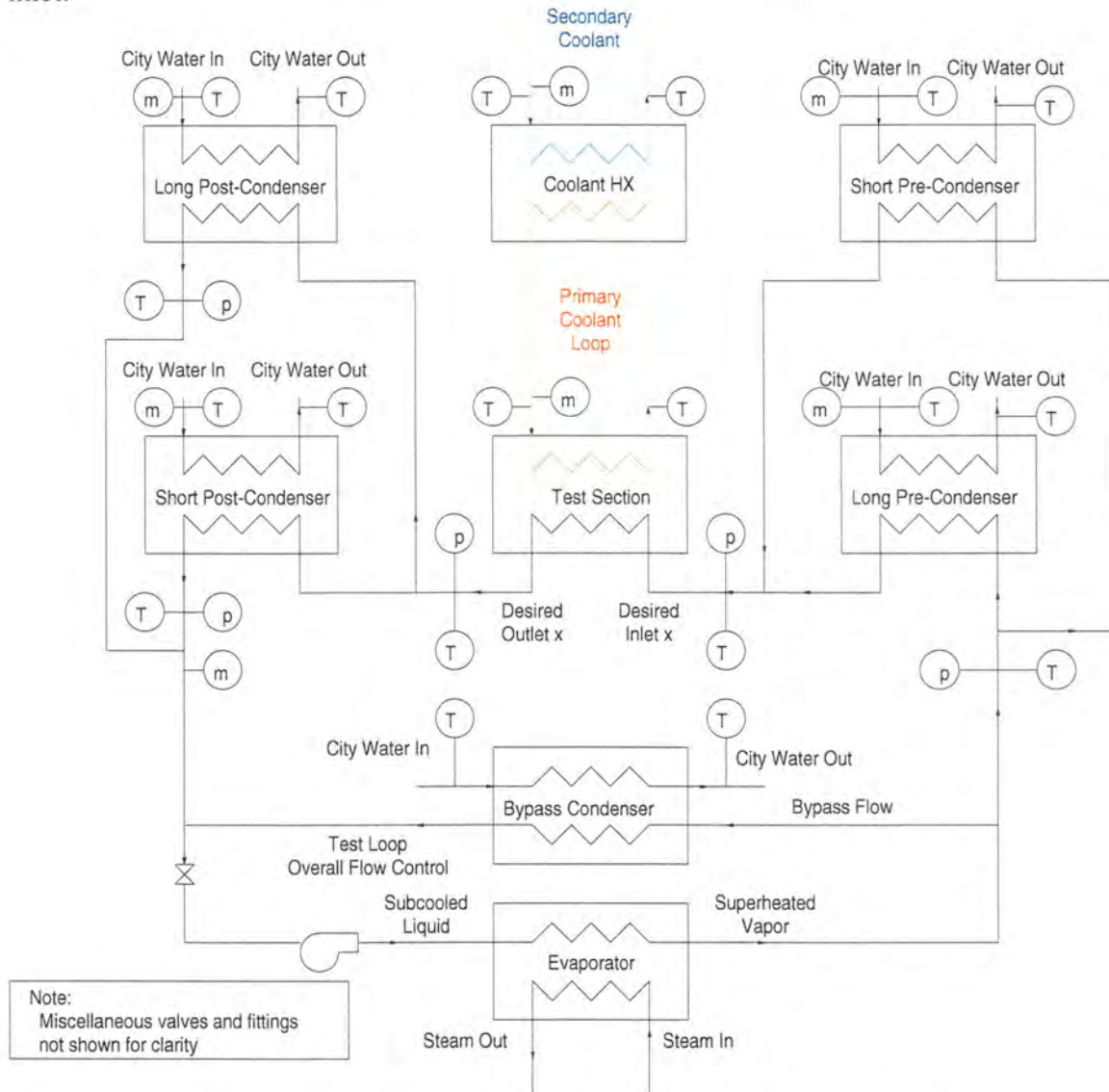


**Figure 4. Microchannel Phase-Change Heat Transfer Test Facility**

The partially condensed R-134a entering the test section is condensed further to a lower vapor quality. Upon exiting the test section, the refrigerant enters one of two post-

condensers (similar in design and function to the pre-condensers) and is completely condensed by city water to a subcooled liquid. The subcooled state at the outlet of the post-condenser is verified by a combination of a sight glass and temperature and pressure measurements. Heat balances on the post-condensers enable prediction of the post-condenser inlet quality (which is also the test section outlet quality.) The subcooled liquid mass flow rate was measured at the outlet of the post-condenser. A pump (Cole Parmer model number 74011-21) located at the mass flow meter outlet sends the refrigerant back to the evaporator. A bladder-type accumulator (Accumulators Inc., model number A1-3100) was located upstream of the evaporator to maintain the system pressure at a constant value. A nitrogen tank connected to the accumulator was used to vary the bladder pressure to obtain the desired system pressure.

### Test Section

The test section inlet and outlet qualities are determined from the pre-condenser and post-condenser energy balances, and the difference between these qualities offers an estimate of the test section heat duty. However, for the determination of the variation in heat transfer coefficient with quality (local phenomena), this quality change must necessarily be small. These small quality changes make the determination of the test section heat duty from the inlet and outlet quality calculations prone to high uncertainties. This is illustrated here using a representative data point. The test section heat duty can be determined from the quality change as follows:

$$Q_{\text{test}} = \dot{m} \cdot h_{\text{fg}} \cdot \Delta x \quad (10)$$

At 1,400 kPa, the enthalpy of vaporization for R-134a is 148.9 kJ/kg. At a mass flow rate of 0.00444 kg/s (450 kg/m<sup>2</sup>-s for test section S30), a test section heat duty of 150 W results in a quality change of 0.23 (which approaches the limits of acceptability for understanding local phenomena). If the inlet and outlet qualities are known to within  $\pm 0.05$  (a reasonable assumption) each, then the *average quality* will be known to within  $\pm 0.035$  (using an uncertainty propagation technique explained in a subsequent section). However, the *quality change* will be known to within  $\pm 0.071$ . Without including the uncertainties in pressure and flow measurements, the uncertainty in the test section heat duty will be  $\pm 31.3\%$  (46.95 W) due to the uncertainty in the quality change, which is unacceptable. Increasing the test section heat transfer can reduce the uncertainty in the quality change, but representing local phenomena will be sacrificed. Hence, the test section heat duty must be obtained independently.

An alternative measurement of the test section heat duty can be made on the coolant

side. To measure the coolant side heat duty accurately, the coolant-side temperature difference must be measurable. To accurately measure the condensation heat transfer coefficient, on the other hand, the refrigerant resistance must dominate over the wall and coolant resistances. The tube wall in the test section is made of highly conductive aluminum ( $k = 192.1 \text{ W/m-K}$ ) so that the wall resistance is negligible compared to the refrigerant resistance. To decrease the coolant-side heat transfer resistance, the heat transfer area and/or coefficient must be increased. Increased heat transfer area (using a longer test section) would decrease the thermal resistance on both sides, thus not changing the resistance ratio. In addition, this would also unduly increase the heat duty. To maintain a high heat transfer coefficient, water was used due to its superior thermophysical properties. However, water has a high specific heat, and the need for a measurable temperature difference implies that low coolant flow rates must be used. This in turn decreases the heat transfer coefficient, thus increasing the resistance. Therefore, keeping the refrigerant heat transfer resistance dominant and accurately measuring the heat duty are conflicting problems.

To address this interconnected set of design requirements, the two issues were decoupled by introducing primary and secondary coolant flow loops (see Figure 4). The primary coolant (which condenses the refrigerant) is circulated in a closed loop at a high flow rate, which results in the desired low coolant-side thermal resistance. The colder secondary coolant flows in an open loop and receives heat from the primary coolant in a 2.13 m long tube-in-tube heat exchanger (12.7 mm, 0.89 mm wall and 25.4 mm diameter, 1.651 mm wall tubes). The secondary coolant flow rate is maintained at much lower values than the primary coolant flow rate, which results in a commensurately larger temperature difference in this coolant, thus enabling an accurate measurement of the heat duty. This technique, however, requires that all extraneous heat transfers in the primary loop be minimized and also estimated with reasonable accuracies. Thus, the heat addition into the primary loop from the circulation pump for this coolant, and the ambient heat losses from the primary loop must be minimized and their contributions estimated. The ambient heat loss was minimized by using low conductivity insulation (Belform® phenolic foam,  $k = 0.019 \text{ W/m-K}$ ), while the pump heat addition was reduced by selecting a high efficiency pump (Micropump 5000 series H21). These measures yielded condensation heat transfer coefficients for the geometries and test conditions under consideration with acceptable uncertainties, as will be demonstrated in Chapter 4.

## Instrumentation and Data Acquisition

A summary of the instrumentation, measurement ranges, and accuracies is presented in Table 2. Omega type Pr-13 platinum resistance temperature devices (RTDs) with a factory-calibrated accuracy of  $\pm 0.5^{\circ}\text{C}$  were used for all temperature measurements. The pressures at various locations were measured using Rosemount model 2088 absolute pressure transducers with an accuracy of 0.25% of span. The maximum span for these transducers is 0 kPa to 5,515.8 kPa, which results in an accuracy of  $\pm 13.79$  kPa. Refrigerant mass flow rates were measured using a Micromotion Elite flow sensor model number CFM025, which measures flow rates in the range of 0 to 0.3 kg/s with an accuracy of  $\pm 0.15\%$  of the reading. The secondary coolant mass flow rate was measured using a Micromotion type D6 sensor, which has a range of 0 to 0.015 kg/s with an accuracy of  $\pm 0.2\%$  of the reading. The pre- and post-condenser volumetric flow rates were each measured using a set of three Gilmont Accucal flow meters, with the flow rate ranges of 0.2 to 4.5 liters per minute, 0.2 to 2.2 liters per minute, and 0.1 to 0.78 liters per minute. These flow meters have an accuracy of  $\pm 2\%$  of the reading. The primary coolant volumetric flow rate was measured using a Dwyer (model #RMC-142-SSV) rotameter, which has a range of 0.76 to 8.3 liters per minute. (As explained in a subsequent section, the accuracy of this flow meter is not very significant for data analysis).

**Table 2. Instrumentation Specifications**

Fluid	Manufacturer	Model	Range	Accuracy
<b>Temperature</b>				
R-134a and Water	Omega	Pr-13	600°C (Max)	$\pm 0.5^{\circ}\text{C}$
<b>Mass Flow Rate</b>				
R-134a	Micromotion	CFM025	0-0.3 kg/s	$\pm 0.15\%$ Reading
Secondary Loop Water	Micromotion	D6	0-0.015 kg/s	$\pm 0.2\%$ Reading
<b>Volumetric Flow Rate</b>				
Pre- and Post-Condenser Water	Gilmont	Accucal	0.1-0.78 lpm	$\pm 2\%$ Reading
	Gilmont	Accucal	0.2-2.2 lpm	$\pm 2\%$ Reading
	Gilmont	Accucal	0.2-4.5 lpm	$\pm 2\%$ Reading
Primary Loop Water	Dwyer	RMC-142-SSV	0.76 to 8.3 lpm	N/A
<b>Pressure</b>				
R-134a	Rosemount	2088	0-5515.8 kPa	$\pm 13.97$ kPa

Temperature, pressure, and mass flow rates were recorded using a TEMPSCAN data acquisition system, which is capable of recording 992 channels at speeds of up to 960 channels per second.

## **Experimental Procedures**

### **System Charging**

The refrigerant-side of the test facility (shown in Figure 4) was initially pressurized to 1,379 kPa with nitrogen gas and a trace amount of R-134a. An electronic leak detector (CPS model L-709a) was used around all of the fittings to verify that the system had no leaks. The test facility was evacuated to a system pressure of 150 microns (20.03 Pa) using a vacuum pump (DV Industries model DV-85N). A Thermal Engineering vacuum gauge (model 14571) with the capability of measuring pressures as low as 10 microns (1.33 Pa) was used to measure the vacuum pressure. Immediately after evacuation, the system was charged with approximately 3.4 kg of R-134a, and the system pressure was monitored over a 24-hour period to verify system integrity. The system was also charged with cooling water in the primary loop and leak-tested. A relief valve in the primary loop was used to purge the air from this loop.

### **System Start-Up**

Testing commenced with the pre- and post-condenser water flow, refrigerant flow, primary and secondary water flow, and steam flow being turned on in this order. The desired refrigerant mass flow rate was achieved through a combination of needle valves and a variable speed motor on the pump. The different specific volumes of the refrigerant for different test conditions were accommodated by controlling the external pressure to the accumulator; thus maintaining the refrigerant pressure at around 1,379 kPa.

The coolant flow rate (and volumetric flow meter) and the heat exchanger (out of the two available long and short pre-condensers) were selected based upon the mass flux under consideration and the desired test section inlet quality. For example, at a low refrigerant flow rate and high test section inlet quality, the low-range water flow meter and short heat exchanger were selected for the pre-condenser. Using the refrigerant superheated inlet enthalpy and mass flow rate, and the measured water-side heat duty, the pre-condenser outlet quality (also the test section inlet quality) was calculated. The test-section primary-coolant flow rate was selected to obtain a low coolant heat transfer resistance and pump heat addition. The secondary flow rate was set to obtain a large temperature difference across the secondary heat exchanger, which allows for the test section heat duty to be measured

accurately. In addition, the secondary water flow rate indirectly controlled the condensation rate in the test section by removing the desired heat duty from the circulating primary coolant. (With the secondary coolant inlet temperature fixed by the city water temperature, the flow rate determined the outlet temperature, and thus the temperature difference available for heat transfer between the primary and secondary coolants.) The post condenser water flow rate and heat exchanger (out of the two available) were selected to ensure a measurable temperature difference and refrigerant subcooling at the outlet. The refrigerant subcooled outlet enthalpy and mass flow rate, and the water-side heat duty were used to calculate the post-condenser inlet (also the test section outlet) vapor quality. Subcooling the refrigerant to a single-phase liquid condition allowed for pumping of the refrigerant around the loop, and also measurement of its flow rate by the coriolis flow meter.

The system pressures, temperatures, and flow rates were constantly monitored during the test. Steady state conditions took between 30 minutes and 3 hours to obtain, depending on the specific test condition under consideration. A preliminary data point was taken and analyzed to estimate the test section inlet and outlet quality. If the calculated values corresponded to the desired qualities, the system was run at this condition until steady state was confirmed by ensuring that the results from successive data points were the same. After steady state was established, the data point was recorded, with each point representing the average of 121 scans taken over a two-minute interval. Water flow rates for the pre- and post-condensers and the primary and secondary coolants (as necessary) were then adjusted to obtain another average test section quality at the same refrigerant flow rate. This process was repeated until approximately seven data points, in the range  $0.05 < x < 0.95$  in increments of about 15%, were taken for each mass flux of 150, 300, 450, 600, and 750 kg/m<sup>2</sup>-s.

It should be noted that some of the mass fluxes were unattainable or could only be represented by one or two data points. For example, the mass flow rates for the mass fluxes of 150 and 300 kg/m<sup>2</sup>-s for test section RK15 (which had the smallest flow area of all the test sections) were  $6.098 \times 10^{-4}$  kg/s and 0.00122 kg/s, respectively, even with the multiple channels, and are not accurately measurable. Also, a test section heat duty of 150 W for the 450 kg/m<sup>2</sup>-s mass flux case for this test section corresponds to a quality change of 0.551 at a pressure of 1,400 kPa. Thus, for this mass flux, only one or two points, with a relatively large quality change, were possible, at the required accuracies. Thus, local phenomena could not be measured with a high degree of resolution for this test section.

## Test Condition Establishment

Each data point for each test section was analyzed using *Engineering Equation Solver* software (Klein and Alvarado, 2000). The calculation of the average test section quality and its associated uncertainty are demonstrated here for a data point with a mass flux of 454.01 kg/m<sup>2</sup>-s and a quality of  $x = 0.465$  for test section S30.

**Table 3. Measured Data for Test Section S30 Example Calculation**

Variable	Measured Value	Description
$P_{pre,in}$	1,553 kPa	Pressure, pre-condenser inlet
$P_{pre,out}$	1,546 kPa	Pressure, pre-condenser outlet
$P_{post,in}$	1,531 kPa	Pressure, post-condenser inlet
$P_{post,out}$	1,532 kPa	Pressure, post-condenser outlet
$\dot{m}_{refg}$	$4.48 \times 10^{-3}$ kg/s	Mass flow rate, refrigerant
$\dot{m}_{sec}$	$1.24 \times 10^{-3}$ kg/s	Mass flow rate, secondary water
$\dot{V}_{pre,w}$	0.22 liter/min	Volumetric flow rate, pre-condenser water
$\dot{V}_{post,w}$	0.95 liter/min	Volumetric flow rate, post-condenser water
$\dot{V}_{test,w}$	6.25 liter/min	Volumetric flow rate, primary loop water
$T_{pre,in}$	103.50°C	Temperature, pre-condenser inlet
$T_{pre,out}$	56.56°C	Temperature, pre-condenser outlet
$T_{pre,w,in}$	18.77°C	Temperature, pre-condenser water inlet
$T_{pre,w,out}$	50.72°C	Temperature, pre-condenser water outlet
$T_{test,in}$	56.94°C	Temperature, test inlet
$T_{test,out}$	55.17°C	Temperature, test outlet
$T_{test,w,in}$	53.00°C	Temperature, primary loop water inlet
$T_{test,w,out}$	53.33°C	Temperature, primary loop water outlet
$T_{sec,w,in}$	17.49°C	Temperature, secondary loop water inlet
$T_{sec,w,out}$	52.33°C	Temperature, secondary loop water outlet
$T_{post,in}$	55.06°C	Temperature, post-condenser inlet
$T_{post,out}$	32.20°C	Temperature, post-condenser outlet
$T_{post,w,in}$	16.47°C	Temperature, post-condenser water inlet
$T_{post,w,out}$	21.92°C	Temperature, post-condenser water outlet

### Average Test Section Quality

Table 3 shows the measured data that were input to the EES program. These quantities are used to determine the inlet, outlet, and average test section qualities. At the inlet of the pre-condenser, the refrigerant is a superheated vapor. Therefore, the refrigerant enthalpy at that state is calculated from the pressure ( $P_{pre,in}$ ) and temperature ( $T_{pre,in}$ ) measurements. For this example,  $P_{pre,in}$  and  $T_{pre,in}$  are 1,553 kPa and 103.5°C, respectively, which yields a pre-condenser inlet enthalpy of 480.32 kJ/kg.

The superheated refrigerant enters the pre-condenser and is partially condensed by flowing cold water. The mass flow rate of the water is calculated as follows:

$$\dot{m}_{pre,w} = \dot{V}_{pre,w} \cdot \rho_{pre,w} \quad (11)$$

With a volumetric flow rate and density of 0.22 liters per minute and 999.87 kg/m<sup>3</sup>, respectively, the mass flow rate is 3.667 x 10<sup>-3</sup> kg/s.

The pre-condenser outlet is a liquid-vapor mixture and, therefore, its enthalpy cannot be directly determined from the temperature and pressure measurements. The water-side heat duty and an energy balance with the refrigerant-side are used to predict the pre-condenser outlet enthalpy. The water-side heat duty is given by:

$$Q_{pre,w} = \dot{m}_{pre,w} \cdot \Delta h_{pre,w} \quad (12)$$

The pre-condenser water inlet and outlet temperatures of 18.77°C and 50.72°C yield enthalpy values of 79.13 kJ/kg and 212.55 kJ/kg, respectively. The pre-condenser water-side heat duty is therefore 489.14 W.

The pre-condenser is covered with three layers of fiberglass pipe-wrap insulation followed by an outer shell of rigid fiberglass insulation. In addition, the cooling water is on the annulus-side of the tube-in-tube pre-condenser. The small temperature difference between the ambient air (~20°C) and the cooling water and the several layers of fiberglass insulation minimized the heat loss or gain in the pre-condenser to negligible values. The refrigerant-side heat duty in the pre-condenser is therefore given by:

$$Q_{pre} = \dot{m}_{refg} \Delta h_{pre} = \dot{m}_{refg} (h_{pre,in} - h_{pre,out}) \quad (13)$$

The pre-condenser heat duty, refrigerant mass flow rate, and refrigerant inlet enthalpy of 489.14 W, 4.48 x 10<sup>-3</sup> kg/s, and 480.32 kJ/kg, respectively, yield a refrigerant outlet enthalpy of 371.13 kJ/kg. The pre-condenser outlet quality is a function of pressure and enthalpy as follows:

$$x_{pre,out} = f(P_{pre,out}, h_{pre,out}) \quad (14)$$

A measured outlet pressure and calculated enthalpy of 1,546 kPa and 371.13 kJ/kg yield a

quality of 0.62. This partially condensed refrigerant from the pre-condenser outlet enters the test section. The short length of tubing connecting the pre-condenser and test section is covered with the fiberglass insulation combination as described above. Therefore, it is assumed that the test section inlet quality is the same as the pre-condenser outlet quality.

After exiting the test section, the refrigerant enters a post-condenser, where it is completely condensed and subcooled by cooling water. The mass flow rate of the cooling water is calculated as follows:

$$\dot{m}_{\text{post},w} = \dot{V}_{\text{post},w} \cdot \rho_{\text{post},w} \quad (15)$$

A water volumetric flow rate and density of 0.95 liters per minute and  $1,000.7 \text{ kg/m}^3$  yield a water mass flow rate of  $1.584 \times 10^{-2} \text{ kg/s}$ .

The post-condenser water-side heat duty is calculated as follows:

$$Q_{\text{post},w} = \dot{m}_{\text{post},w} \Delta h_{\text{post},w} \quad (16)$$

The water inlet and outlet temperatures of  $16.47^\circ\text{C}$  and  $21.92^\circ\text{C}$  correspond to enthalpies of  $69.5 \text{ kJ/kg}$  and  $92.32 \text{ kJ/kg}$ , respectively, and with a mass flow rate of  $0.01584 \text{ kg/s}$ , the post-condenser heat duty is  $361.47 \text{ W}$ .

The refrigerant exits the post-condenser as a subcooled liquid. Hence, the post-condenser outlet enthalpy can be deduced from the pressure ( $P_{\text{post},\text{out}}$ ) and temperature ( $T_{\text{post},\text{out}}$ ) measurements. Given the post-condenser refrigerant outlet temperature and pressure of  $32.2^\circ\text{C}$  and  $1,532 \text{ kPa}$ , respectively, the enthalpy is  $244.93 \text{ kJ/kg}$ .

Similar to the pre-condenser, the post-condenser is a tube-in-tube heat exchanger with the water flowing through the annulus and covered with layers of insulation. Therefore, the post-condenser refrigerant-side heat duty is considered to be equal to the water-side duty and is used to calculate the refrigerant inlet enthalpy as follows:

$$Q_{\text{post}} = \dot{m}_{\text{refg}} \Delta h_{\text{post},w} = \dot{m}_{\text{refg}} (h_{\text{post},\text{in}} - h_{\text{post},\text{out}}) \quad (17)$$

With a refrigerant mass flow rate of  $4.48 \times 10^{-3} \text{ kg/s}$ , heat duty of  $361.47 \text{ W}$ , and outlet enthalpy of  $244.93 \text{ kJ/kg}$ , the post-condenser inlet enthalpy is  $325.61 \text{ kJ/kg}$ . The post-condenser inlet quality is calculated from the measured pressure and calculated inlet enthalpy as follows:

$$x_{\text{post},\text{in}} = f(P_{\text{post},\text{in}}, h_{\text{post},\text{in}}) \quad (18)$$

The post-condenser inlet pressure and enthalpy of  $1,553 \text{ kPa}$  and  $325.61 \text{ kJ/kg}$ , respectively, yield a quality of 0.31. The refrigerant at the post-condenser inlet flows directly from the test section outlet, and the length of tubing connecting the post-condenser and test section is covered with the fiberglass insulation. Hence, the post-condenser inlet quality is assumed to

be the same as the test section outlet quality.

The average test section quality is determined as follows:

$$x_{\text{test}} = \frac{(x_{\text{test,in}} + x_{\text{test,out}})}{2} \quad (19)$$

For this example, the average test section quality is 0.465.

The procedure described above for calculating the average test section quality was repeated for all data points. Figure 5 shows the mass flux versus the test section average quality (including the corresponding error bands described in the following section) for all of the data points taken for test section S30. Data were obtained for an acceptable range of average test section qualities for all mass fluxes except 150 kg/m<sup>2</sup>-s, for which only one data point with an average quality of 0.48 representing total condensation was collected due to the low refrigerant flow rate. Similar graphs for each test section can be seen in Appendix A.

### Uncertainty Analysis for Test Section Quality

The uncertainty in the inlet quality is deduced from the pre-condenser heat duty using an uncertainty propagation technique (Taylor and Kuyatt, 1994) as follows:

$$U_{Q_{\text{pre}}}^2 = \left( \frac{\partial Q_{\text{pre}}}{\partial \dot{V}_{\text{pre,w}}} u_{\dot{V}_{\text{pre,w}}} \right)^2 + \left( \frac{\partial Q_{\text{pre}}}{\partial h_{\text{pre,w,out}}} u_{h_{\text{pre,w,out}}} \right)^2 + \left( \frac{\partial Q_{\text{pre}}}{\partial h_{\text{pre,w,in}}} u_{h_{\text{pre,w,in}}} \right)^2 \quad (20)$$

The influence of density (which is needed to calculate the mass flow rate of water from the measured volumetric flow rate) on uncertainty was neglected in the above calculation. The partial derivatives of heat duty with respect to the volumetric flow rate and inlet and outlet enthalpy are as follows:

$$\frac{\partial Q_{\text{pre}}}{\partial \dot{V}_{\text{pre,w}}} = \rho \Delta h_{\text{pre,w}} = 133,403 \text{ (kJ/m}^3\text{)} \quad (21)$$

$$\frac{\partial Q_{\text{pre}}}{\partial h_{\text{pre,w,in}}} = -\dot{V}_{\text{w,pre}} \rho = -0.003667 \text{ (kg/s)} \quad (22)$$

$$\frac{\partial Q_{\text{pre}}}{\partial h_{\text{pre,w,out}}} = \dot{V}_{\text{w,pre}} \rho = 0.003667 \text{ (kg/s)} \quad (23)$$

The relative uncertainty in the volumetric flow rate is  $\pm 2\%$  of the reading, which is 0.0044 liters per minute in this case. The uncertainty in coolant enthalpy is given by:

$$U_h = \frac{\partial h}{\partial T} u_T = C_p \cdot u_T \quad (24)$$

The specific heat is 4.18 kJ/kg-K, while the uncertainty in temperature is  $\pm 0.5^\circ\text{C}$ . Therefore,

the uncertainty in inlet enthalpy is  $\pm 2.09$  kJ/kg. Similarly, the uncertainty in outlet enthalpy is  $\pm 2.09$  kJ/kg, which yields an uncertainty in heat duty (481.14 W) of  $\pm 14.6$  W. By using a similar method, the post-condenser heat duty of 361.47 W is known to within  $\pm 47.42$  W.

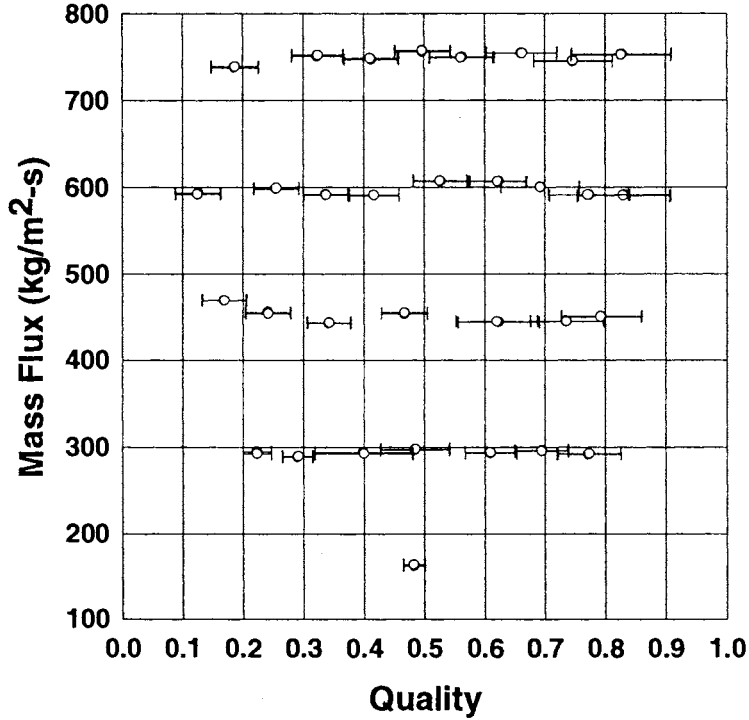


Figure 5. Range of Data Points for Test Section S30

The uncertainty in refrigerant test section inlet (pre-condenser outlet) enthalpy is calculated as follows:

$$U_{h_{pre,out}} = \left( \frac{\partial h_{pre,out}}{\partial h_{pre,in}} u_{h_{pre,in}} \right)^2 + \left( \frac{\partial h_{pre,out}}{\partial Q_{pre}} u_{Q_{pre}} \right)^2 + \left( \frac{\partial h_{pre,out}}{\partial \dot{m}_{refg}} u_{\dot{m}_{refg}} \right)^2 \quad (25)$$

The partial derivatives are evaluated as follows:

$$\frac{\partial h_{pre,out}}{\partial h_{pre,in}} = 1 \quad (26)$$

$$\frac{\partial h_{pre,out}}{\partial Q_{pre}} = \frac{1}{\dot{m}} = -223.2 \text{ (s/kg)} \quad (27)$$

$$\frac{\partial h_{\text{pre,out}}}{\partial \dot{m}_{\text{refg}}} = \frac{Q_{\text{pre}}}{(\dot{m}_{\text{refg}})^2} = 2.397 \cdot 10^7 (\text{J} \cdot \text{s} / \text{kg}^2) \quad (28)$$

The refrigerant mass flow rate is measured with a mass flow meter with a relative uncertainty of  $\pm 0.15\%$ , which in this case is  $\pm 6.72 \times 10^{-6}$  kg/s. The uncertainty in the pre-condenser inlet enthalpy is as follows:

$$U_h^2 = \left( \frac{\partial h}{\partial T} u_T \right)^2 + \left( \frac{\partial h}{\partial P} u_P \right)^2 \quad (29)$$

The uncertainties in temperature and pressure measurements are  $\pm 0.5^\circ\text{C}$  and  $\pm 13.97$  kPa, respectively, while the partial derivative with respect to temperature is evaluated as follows:

$$\frac{\partial h}{\partial T} = \frac{h(T + u_T, P) - h(T - u_T, P)}{2u_T} \quad (30)$$

The elevated and reduced temperature enthalpies of 480.95 kJ/kg and 479.84 kJ/kg yield a partial derivative of 1.11 kJ/kg-K. The partial derivative with respect to pressure is as follows:

$$\frac{\partial h}{\partial P} = \frac{h(T, P + u_P) - h(T, P - u_P)}{2u_P} \quad (31)$$

The elevated and reduced pressure enthalpies of 480.57 kJ/kg and 480.23 kJ/kg yield a partial derivative of -0.0122 kJ/kg-kPa, which yields an uncertainty in the pre-condenser inlet enthalpy of 0.58 kJ/kg. Hence, the test section inlet enthalpy of 371.13 kJ/kg is known to within  $\pm 3.31$  kJ/kg. Similarly, based on an uncertainty analysis on the post-condenser, the test section outlet enthalpy of 325.61 kJ/kg is known to within  $\pm 10.61$  kJ/kg.

The test section inlet quality is a function of enthalpy and pressure, with the corresponding uncertainty given by:

$$U_x^2 = \left( \frac{\partial x}{\partial h} u_h \right)^2 + \left( \frac{\partial x}{\partial P} u_P \right)^2 \quad (32)$$

The partial derivative with respect to enthalpy is as follows:

$$\frac{\partial x}{\partial h} = \frac{x(h + u_h, P) - x(h - u_h, P)}{2u_h} \quad (33)$$

The qualities at the elevated and reduced enthalpies of 480.57 kJ/kg and 480.23 kJ/kg are 0.644 and 0.598, respectively, which yields a partial derivative of  $6.95 \times 10^{-3}$  kg/kJ. The partial derivative with respect to pressure is as follows:

$$\frac{\partial x}{\partial P} = \frac{x(h, P + u_p) - x(h, P - u_p)}{2u_p} \quad (34)$$

The elevated and reduced qualities are 0.619 and 0.623, respectively, which yields partial derivative of  $-1.432 \times 10^{-4}$  1/kPa. Hence, the test section inlet quality of 0.62 is known to within  $\pm 0.023$ . Similarly, the test section outlet quality of 0.31 is known to within  $\pm 0.074$ . The uncertainty in the average test section quality is calculated as follows:

$$U_{x_{avg}}^2 = (0.5 \cdot u_{x_{in}})^2 + (0.5 \cdot u_{x_{out}})^2 \quad (35)$$

This shows that the average test section quality of 0.465 is known to within  $\pm 0.039$ . The uncertainties associated with all the data points for test section S30 can be seen in Figure 5. Similar graphs for the other test sections are presented in Appendix A. Heat transfer related quantities for each data point were computed for each of these qualities and are reported in Chapter 4.

## CHAPTER FOUR: DATA ANALYSIS AND RESULTS

The data collected from the experimental procedures described in the previous chapter are presented here. This section includes a description of the calculation of the test section heat duty and the local condensation heat transfer coefficient for the microchannel tubes. The tubes are divided into 3 sets: rectangular, circular, and other.

### Rectangular Channels

#### Test Section S30 Heat Duty and Uncertainty

The calculation of test section heat duty and its associated uncertainty is illustrated here for test section S30. The specific data point used for this illustration has a mass flux of  $454 \text{ kg/m}^2\text{-s}$  and an average quality of 0.467, and the various temperatures and pressures in the system can be seen in Table 3 in Chapter 3.

Figure 6 shows the configuration for the secondary loop. The test section rejects heat into the primary loop. This coolant in turn rejects heat to the secondary coolant. In addition, the primary loop rejects some heat to the ambient and also gains heat dissipated by the primary coolant circulation pump. These various heat transfers can be summarized in the following energy balance equation:

$$Q_{\text{test}} = Q_{\text{sec}} + Q_{\text{ambient}} - Q_{\text{pump}} \quad (36)$$

The secondary loop heat duty can be calculated from the flow rate and temperature rise in the secondary coolant as follows:

$$Q_{\text{sec, w}} = \dot{m}_{\text{sec, w}} \Delta h_{\text{sec, w}} \quad (37)$$

For this example, the secondary water flowing at  $1.24 \times 10^{-3} \text{ kg/s}$  enters and exits the secondary loop at  $17.49^\circ\text{C}$  and  $52.33^\circ\text{C}$  with enthalpies of  $73.5 \text{ kJ/kg}$  and  $219.0 \text{ kJ/kg}$ , respectively. The corresponding heat duty is  $180.7 \text{ W}$ .

The calculation of the pump heat addition into the primary coolant and the ambient heat loss is described below.

#### Pump Heat Addition

The pressure drop in the primary loop must be calculated first to determine the pumping power required for water circulation. The pressure drop in the primary loop is the sum of the pressure drop in the tubing and fittings, the water flow meter, the test section, and the secondary heat exchanger. The inside tube diameter of the primary loop plumbing is calculated as follows:

$$ID = OD - 2 \cdot t_{\text{wall}} \quad (38)$$

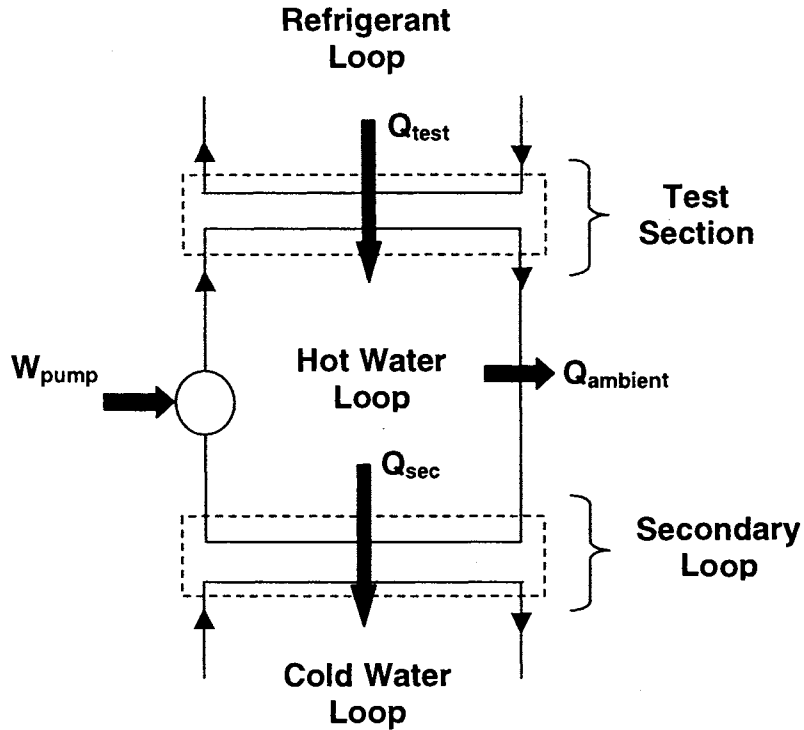


**Figure 6. Test Section Primary and Secondary Coolant Flows**

The stainless steel tubing has an outside diameter of 12.7 mm and a wall thickness of 0.89 mm, which yields an inside tube diameter of 10.92 mm.

The velocity of the circulating fluid is calculated from the volumetric flow rate and the cross-sectional area as follows:

$$V = \frac{\dot{V}}{A} = \frac{4\dot{V}}{\pi ID_{\text{tube}}^2} \quad (39)$$

For a measured volumetric flow rate of 6.25 liters per minute, the fluid velocity is 1.11 m/s. The Reynolds number is calculated from this velocity as follows:

$$Re = \frac{\rho \cdot V \cdot ID_{\text{tube}}}{\mu} \quad (40)$$

With a fluid density = 986.6 kg/m<sup>3</sup> and a viscosity = 5.193 x 10<sup>-4</sup> kg/m-s, the Reynolds number is 23,057.

The Churchill correlation (1977b) is used to calculate the friction factor from the Reynolds number and tube relative roughness as follows:

$$\frac{f}{8} = \left[ \left( \frac{8}{Re} \right)^{12} + \left( \left[ -2.457 \cdot \ln \left( \left[ \frac{7}{Re} \right]^{0.9} + 0.27 \cdot \frac{\epsilon}{ID_{tube}} \right) \right]^{16} + \left[ \frac{37530}{Re} \right]^{16} \right)^{-1.5} \right]^{(1/12)} \quad (41)$$

With a roughness for drawn tubes of 0.0015 mm (Munson et al. 1998), the friction factor is 0.0253.

The pressure drop in the tubing is calculated as follows:

$$\Delta P_{tube} = \frac{1}{2} \cdot f \cdot \rho \cdot V^2 \cdot \frac{L_{tube}}{ID_{tube}} \quad (42)$$

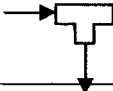
For 8.12 m of tubing in the primary loop, the pressure drop is 11.45 kPa.

Minor losses are also incurred in the fittings in the primary loop. Table 4 shows the type of fitting with its associated inside diameter (Swagelok, 1995), minor loss coefficient (Munson et al. 1998), and the number of each type of fitting in the primary loop. The fluid velocity through all of the fittings for a volumetric flow rate of 6.25 liters per minute is 1.22 m/s. The minor losses through the fittings were calculated as follows:

$$\Delta P_{fitting} = \frac{1}{2} \cdot \rho \cdot V^2 \cdot K \quad (43)$$

The resulting pressure drops in the elbows, ball valves, branch tees, and run tees are 3.76 kPa, 0.04 kPa, 4.42 kPa, and 0.29 kPa, respectively, which yields a total minor loss of 8.51 kPa.

**Table 4. Minor Loss Elements in the Primary Loop for the Microchannel Tubes Tests**

Type	ID (mm)	K	#
90° compression elbow	10.414	0.3	17
Fully-open ball valve	10.414	0.05	1
Branch tee 	10.414	1	6
Run tee 	10.414	0.2	2

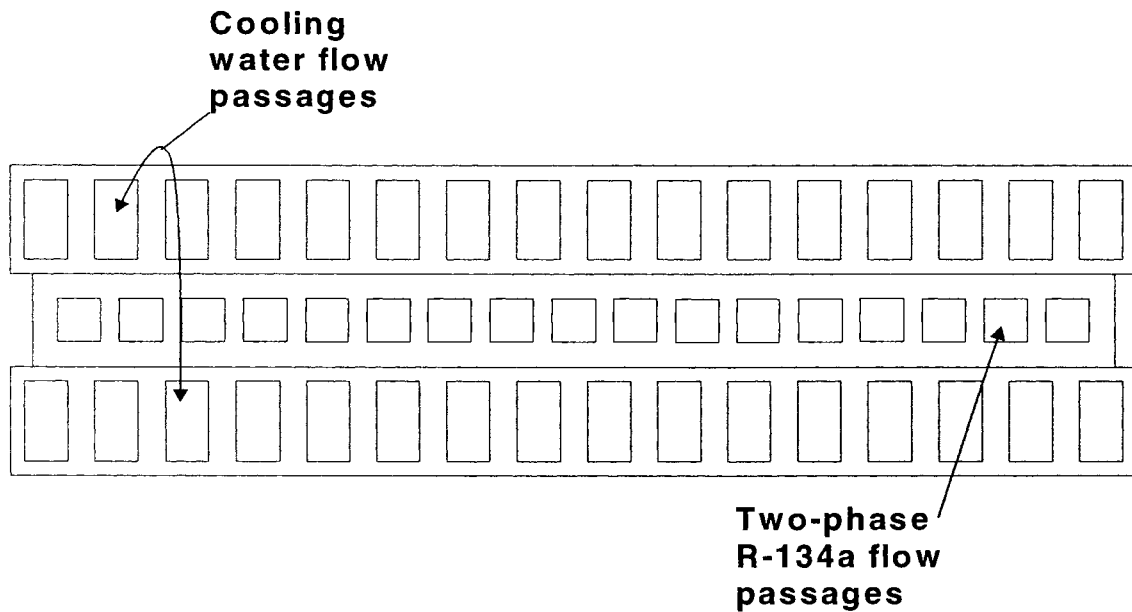


**Figure 7. Cross-section of Test Section S30**

The pressure drops at the minimum (0.76 lpm) and maximum (8.33 lpm) flow rates through the volumetric flow meter are 3.45 kPa and 8.22 kPa, according to manufacturer specifications. For convenience, interpolation between the minimum and maximum flow rates was used to find the pressure drop for the test flow rate. For example, the pressure drop through the volumetric flow meter at 6.25 liters per minute is 6.91 kPa.

The cross-section of test section S30 is shown in Figure 7. The coolant flows through the outer 2 tube jackets, while the refrigerant condenses in the center tube. The velocity of the water flowing through one port in the outer jacket is calculated as follows:

$$V = \frac{\dot{V}}{2 \cdot A_{\text{total}}} \quad (44)$$

The manufacturer-specified cross-sectional area for one of the tube jackets is  $17.03 \text{ mm}^2$ , and the volumetric flow rate of 6.25 liters per minute yields a velocity of 3.056 m/s. Since the wetted perimeter for the entire tube is 69.088 mm, the tube jacket hydraulic diameter is 0.986 mm. For a density and viscosity of  $986.6 \text{ kg/m}^3$  and  $5.193 \times 10^{-4} \text{ kg/m-s}$ , the coolant Reynolds number is 5,726. The procedure described in Kakac et al. (1987) is used for calculating the friction factor, with the relative roughness for the square channel given by Coleman (2000) as 0.0009. Figure 8 shows the cross-section of the outer tube jacket. The manufacturer supplied the total free flow area and wetted perimeter, as well as the number of ports. Hence, the port height and width are found by simultaneously solving the following

two equations:

$$A_{\text{total}} = N_{\text{port}} \cdot h_{\text{port}} \cdot w_{\text{port}} \quad (45)$$

$$P_{\text{total}} = 2 \cdot N_{\text{port}} (h_{\text{port}} + w_{\text{port}}) \quad (46)$$

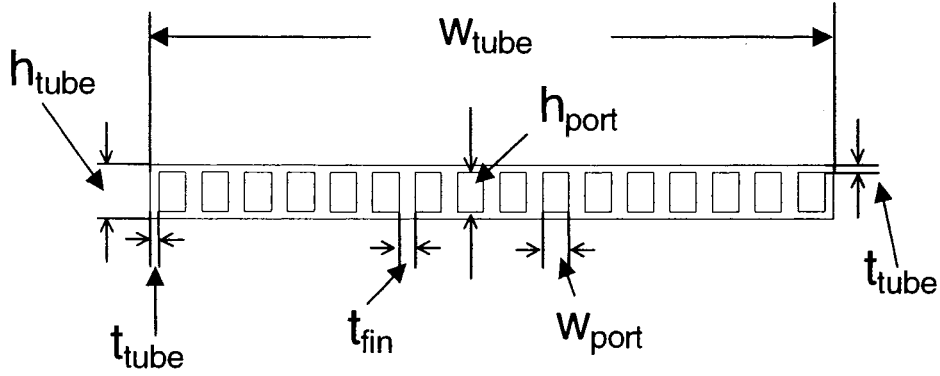


**Figure 8.** Cross-section of Outer Tube Jacket

For the 16 ports in this tube, the port height and width are 1.397 mm and 0.762 mm, respectively, which yields an aspect ratio of 0.545. The aspect ratio is used to find a transition Reynolds number as follows (Kakac et al. 1987):

$$Re_{\text{critical}} = 4650 \frac{m \cdot n}{(m+1) \cdot (n+1)} \quad (47)$$

The parameter  $n$  is 2 for an aspect ratio less than  $1/3$ ; otherwise, it is defined as follows:

$$n = 2 + 0.3 \cdot (\alpha - 1/3) \quad (48)$$

In this case  $n$  is 2.064, while parameter  $m$  is given by:

$$m = 1.7 + 0.5 \cdot \alpha^{-1/4} \quad (49)$$

This parameter is 2.869 in this case, which yields a critical Reynolds number of 2,323. The laminar and turbulent friction factors are defined as follows (Kakac et al. 1987):

$$f_{\text{laminar}} = 96 \cdot \frac{(1 - 1.3553 \cdot \alpha + 1.9469 \cdot \alpha^2 - 1.7012 \cdot \alpha^3 + 0.9564 \cdot \alpha^4 - 0.2537 \cdot \alpha^5)}{Re} \quad (50)$$

$$f_{\text{turbulent}} = (1.0875 - 0.1125 \cdot \alpha) \cdot f_{\text{churchill}} \quad (51)$$

Since the flow is in the turbulent regime in this case, the friction factor is 0.03855. The tube jackets have an entire length (not the brazed heat exchanger length) of 0.4572 m, which yields a test section pressure drop of 82.37 kPa.

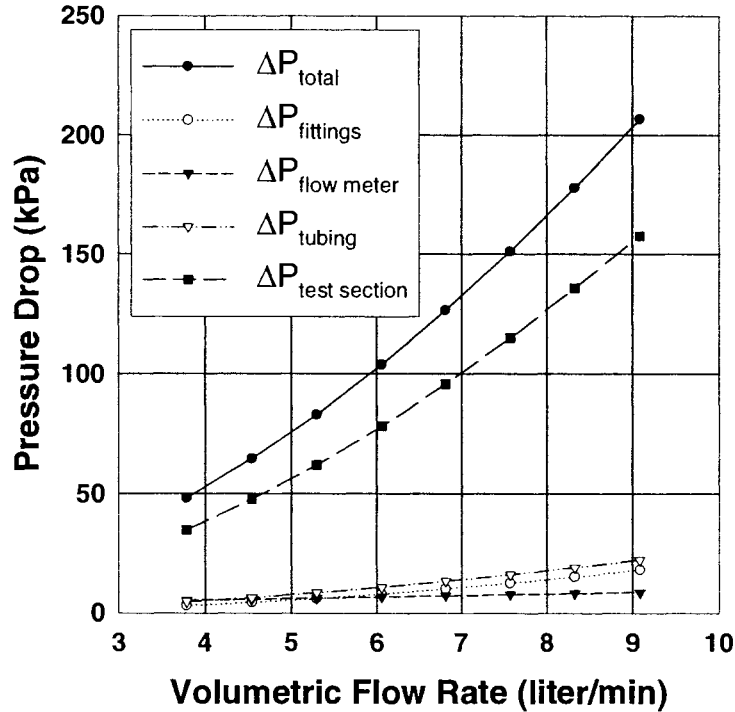


**Figure 9. Primary Loop Pressure Drop versus Water Volumetric Flow Rate**

The total pressure drop in the primary loop is the sum of the pressure losses in the tubing, fittings, water flow meter, test section, and secondary loop. For this case, the total pressure drop in the primary loop is 109.24 kPa.

The pressure drop in each component in the primary loop as a function of volumetric flow rate is shown in Figure 9. The results from this pressure drop calculation were used to determine the pump heat addition, as described below.

The pressure rise supplied by the circulation pump is the pressure drop in the primary loop calculated above. The ideal pump work is given by:

$$W_{\text{ideal}} = \dot{V} \cdot \Delta P_{\text{loop}} \quad (52)$$

For a volumetric flow rate of 6.25 liters per minute and a total loop pressure drop of 109.24 kPa, the ideal pump work is 11.37 W. The operating shaft work is calculated as follows:

$$W_{\text{shaft}} = \tau \cdot \omega \quad (53)$$

The operating applied torque and shaft rotational speed are supplied by the manufacturer (Micropump) and shown in Figure 10 for the Micropump Series 5000 H21 pump head model. The applied torque is a function of the loop pressure drop (or pump pressure rise). In

this case, the loop pressure drop of 109.24 kPa (15.84 psi) yields an applied torque of 0.229 N-m. The intersection between the operating flow rate and pressure drop in Figure 5 yields the operating pump shaft rotational speed. For a loop pressure drop of 109.24 kPa (15.84 psi) and a volumetric flow rate of 6.25 liters per minute (1.65 gpm), the rotational speed is approximately 154.5 radians per second (~1475 RPM). Finally, a torque of 0.229 N-m and a speed of 1475 RPM result in an applied shaft work of 35.45 W.

The pump efficiency as a function of pump ideal and shaft works is defined as follows:

$$\eta = \frac{W_{ideal}}{W_{shaft}} \tag{54}$$

The ideal and shaft works of 11.37 W and 35.45 W result in a pump efficiency of 0.32. The heat added to the primary coolant from the circulation pump is a function of the pump efficiency and the shaft work as follows:

$$Q_{pump} = (1-\eta) \cdot W_{shaft} \tag{55}$$

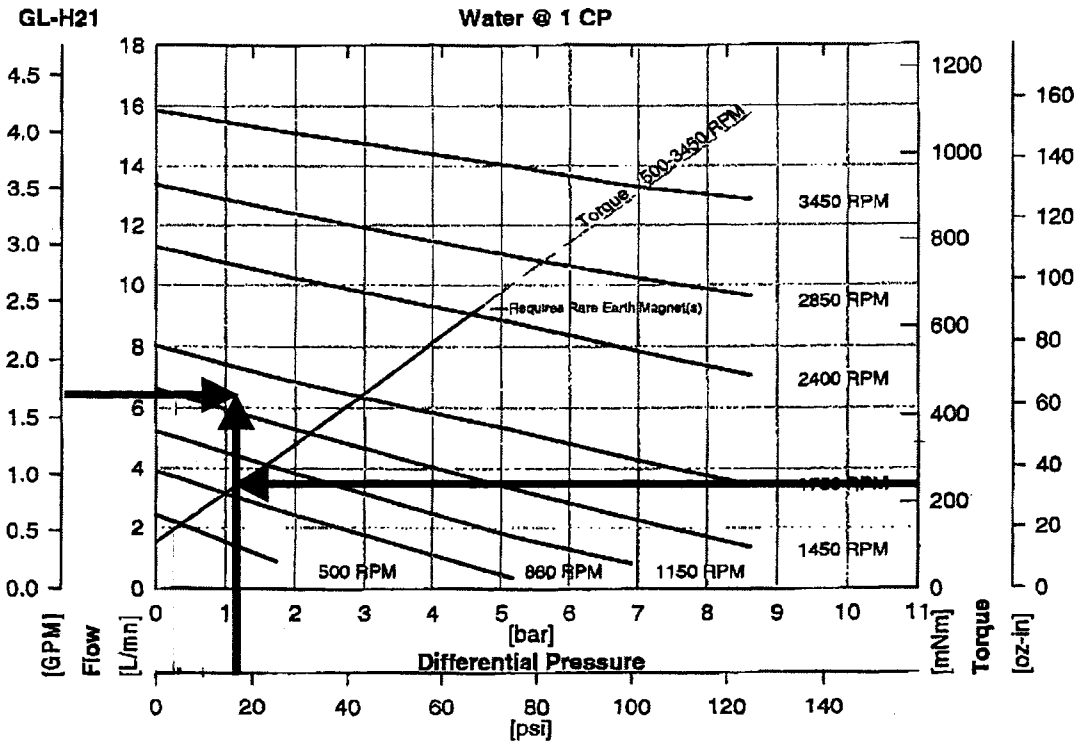
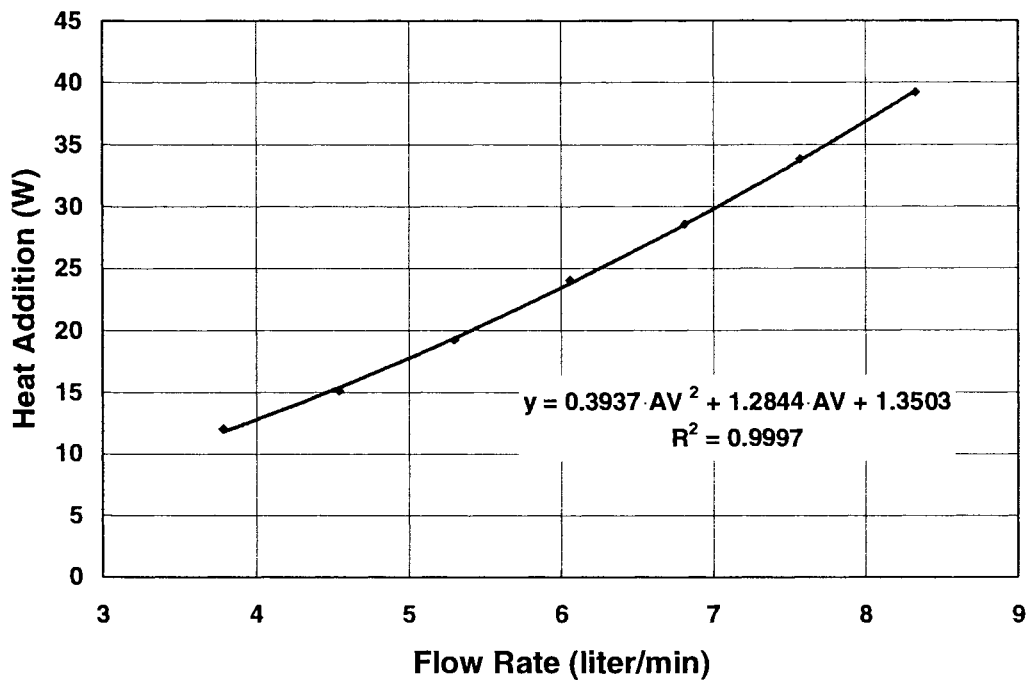


Figure 10. Micropump Series 5000 H21 Pump Curve



**Figure 11. Pump Heat Addition versus Flow Rate for the Micropump Series 5000 Model H21 Pump**

For this case, the pump heat addition is 24.08 W. Figure 11 shows the pump heat addition as a function of volumetric flow rate. A second-order polynomial least squares curve fit was developed from the data in Figure 11. This polynomial was used to estimate the pump heat addition for the experiments in this study, which was 24.73 W in this case.

### **Ambient Heat Loss**

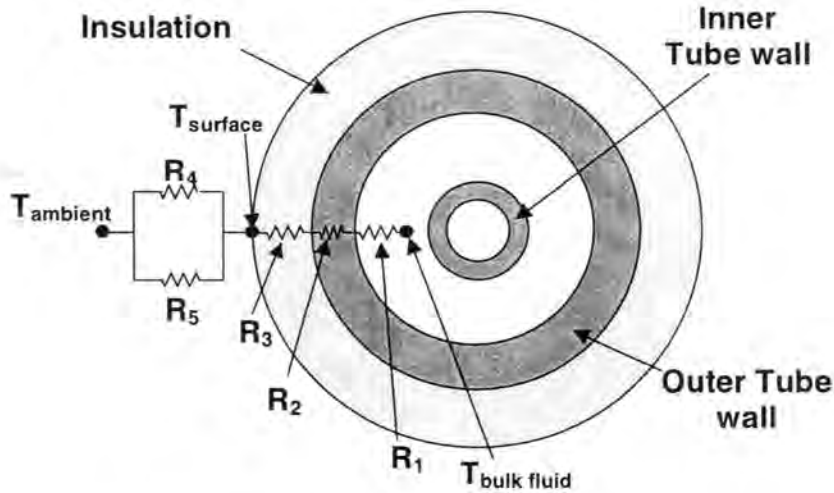
The heat lost from the primary and secondary coolants to the ambient is required for determining the test section heat duty. The calculation of this heat loss is described below.

#### *Secondary Heat Exchanger*

Figure 12 shows the resistance network for the ambient heat loss from the secondary heat exchanger. The heat is assumed to be lost from the average primary coolant temperature to the ambient temperature ( $\sim 20^{\circ}\text{C}$ ). The heat flows through the following resistances: water, outer tube wall, insulation, natural convection, and radiation.

The outside diameter and wall thickness of the outer tube of this annulus are 25.4 mm and 1.651 mm, respectively, which yield an inner diameter of 22.098 mm. With the outside diameter of the inner tube of 12.7 mm, the hydraulic diameter of the annulus is calculated to be 9.398 mm using the following equation:

$$D_h = \frac{4A}{P} = ID_{outer} - OD_{inner} \quad (56)$$



- R<sub>1</sub> = Water resistance**
- R<sub>2</sub> = Tube wall resistance**
- R<sub>3</sub> = Insulation resistance**
- R<sub>4</sub> = Natural convection resistance**
- R<sub>5</sub> = Radiation resistance**

**Figure 12. Resistance Network for the Ambient Heat Loss from the Secondary Heat Exchanger**

The cross-sectional area of the annulus is calculated as follows:

$$A_{annulus} = A_{outer} - A_{inner} = \frac{\pi}{4} (ID_{outer}^2 - OD_{inner}^2) \quad (57)$$

The inner tube outside, and outer tube inside, diameters of 12.7 and 22.098 mm, respectively, yield a cross-sectional area of 256.9 mm<sup>2</sup>. The average secondary water temperature is 34.91°C, yielding an average density and viscosity of 994.3 kg/m<sup>3</sup> and 7.209 x 10<sup>-4</sup> kg/m-s, respectively. For a mass flow rate of 1.24 x 10<sup>-3</sup> kg/s, the fluid velocity through this annulus is 4.86 x 10<sup>-3</sup> m/s, and the Reynolds number is 63.04. The annulus radius ratio is defined as follows:

$$r^* = \frac{OD_{inner}}{ID_{outer}} \quad (58)$$

For this heat exchanger, this ratio is 0.575. The transition Reynolds numbers for annuli are

functions of the radius ratio. These transition functions are simple curvefits to the results of Walker et al. (1957) by Garimella (private communication). Thus the lower transition Reynolds number (laminar to transition) is given by:

$$Re_{lt} = 2089.26 + 686.15 \cdot r^* \quad (59)$$

For this heat exchanger, this lower transition Reynolds number is 2,484. Similarly, the upper transition Reynolds number (transition to turbulent) is given by:

$$Re_{tt} = 2963.02 + 334.16 \cdot r^* \quad (60)$$

For this heat exchanger, this Reynolds number is 3,155. Based on these transition Reynolds number values, the secondary coolant flowing through the annulus is in the laminar regime.

Garimella and Christensen (1995) developed the following curve fits for the laminar and turbulent Nusselt numbers in annuli using the results of Kays and Leung (1963):

$$Nu_{lam} = \frac{1}{0.186 + 0.029 \cdot \ln(r^*) - 0.008 \cdot [\ln(r^*)]^2} \quad (61)$$

$$Nu_{turb} = 0.025 \cdot Re^{0.78} \cdot Pr^{0.48} \cdot r^{*-0.14} \quad (62)$$

For the transition region, the Nusselt number is calculated using a logarithmic interpolation between the Nusselt numbers at the lower and upper critical Reynolds numbers. Since the flow is laminar in this case, Equation 61 yields a Nusselt number of 5.971. The heat transfer coefficient is evaluated from the Nusselt number as follows:

$$h = \frac{Nu_{D_h} \cdot k}{D_h} \quad (63)$$

For a thermal conductivity of 0.6235 W/m-K and hydraulic diameter of 9.398 mm, the heat transfer coefficient is 396.1 W/m<sup>2</sup>-K. The water-side heat transfer area is defined as follows:

$$A = \pi \cdot ID_{outer} \cdot L \quad (64)$$

The secondary loop heat exchanger has a length of 2.134 m and an outer tube ID of 22.098 mm, which results in a heat transfer area of 0.148 m<sup>2</sup>. The heat transfer resistance of the water-side is calculated as follows:

$$R_{water} = \frac{1}{h \cdot A} \quad (65)$$

For this case, the heat transfer resistance is 0.01704 K/W.

The tube-wall resistance is calculated as follows:

$$R_{\text{wall}} = \frac{\ln\left(\frac{\text{OD}}{\text{ID}}\right)}{2 \cdot \pi \cdot L \cdot k} \quad (66)$$

The stainless steel tube, with a thermal conductivity of 15 W/m-K, has outside and inside diameters of 25.4 mm and 22.098 mm, respectively, which yields a resistance of  $6.92 \times 10^{-4}$  K/W.

The insulation resistance is also calculated using equation 66. With an insulation thickness of 25.4 mm (OD = 76.2 mm) and a thermal conductivity of 0.019 W/m-K, the resistance is 4.313 K/W.

Heat transfer from the insulation to the ambient air is due to natural convection and radiation. The natural convection resistance is based on the Rayleigh number, which is defined as follows:

$$Ra = \frac{g \cdot \beta \cdot (T_{\text{surface}} - T_{\infty}) \cdot \text{OD}^3 \cdot \rho^2 \cdot \text{Pr}}{\mu^2} \quad (67)$$

Since air can be approximated as an ideal gas, the volumetric coefficient of thermal expansion is the inverse of the average between the surface and the ambient temperatures. For surface and ambient temperatures of 20.82°C and 20°C, respectively, the average fluid temperature and volumetric coefficient of thermal expansion are 20.41°C and  $3.406 \times 10^{-3} \text{ K}^{-1}$ , respectively. (It should be noted that the surface temperature calculation required here is iterative because this depends on the heat transferred to the ambient.) At this average temperature, the density, viscosity, and Prandtl number are 1.202 kg/m<sup>3</sup>,  $1.827 \times 10^{-5}$  kg/m-s, and 0.7308, respectively, which yields a Rayleigh number of 38,346. The natural convection heat transfer coefficient is determined using a correlation by Churchill and Chu (1975) for flat, horizontal, circular tubes as follows (Incropera and DeWitt, 1996):

$$h_{\text{nc}} = \frac{k_{\text{air}}}{\text{OD}} \left( 0.60 + \frac{0.387 Ra^{1/6}}{\left[ 1 + \left( \frac{0.559}{\text{Pr}} \right)^{9/16} \right]^{8/27}} \right)^2 \quad (68)$$

The resulting natural convection heat transfer coefficient is 2.016 W/m<sup>2</sup>-K. For an insulation diameter of 76.2 mm, the heat transfer area is 0.5108 m<sup>2</sup>, which results in a natural convection resistance of 0.971 K/W.

The radiation heat transfer coefficient is defined as follows:

$$h_{\text{radiation}} = \sigma \cdot (T_{\text{ambient}} + T_{\text{surface}}) \cdot (T_{\text{ambient}}^2 + T_{\text{surface}}^2) \quad (69)$$

With surface and ambient temperatures of 20.82°C and 20°C, respectively, the radiation heat transfer coefficient is 5.737 W/m<sup>2</sup>-K, and the radiation resistance is 0.3412 K/W.

The heat lost to the ambient is determined from the energy balance between the insulation surface and the ambient, and between the bulk water temperature and insulation surface as follows:

$$Q_{\text{ambient}} = \frac{(T_{\text{water}} - T_{\text{surface}})}{R_{\text{water}} + R_{\text{wall}} + R_{\text{insulation}}} = \frac{(T_{\text{surface}} - T_{\text{ambient}})}{R_{\text{natural convection}}} + \frac{(T_{\text{surface}} - T_{\text{ambient}})}{R_{\text{radiation}}} \quad (70)$$

For water, surface, and ambient temperatures of 34.91°C, 20.82°C, and 20°C, respectively, the resulting heat loss is 3.25 W, with 0.845 W being transferred by natural convection and 2.403 W being transferred by radiation.

#### *Test Section Heat Exchanger*

Most of the calculations for ambient heat loss in the test section are similar to those described for secondary heat exchanger. However, the primary water heat transfer resistance calculation in the test section is different because the water is not flowing through an annulus, but rather through the microchannel tube jackets. The laminar Nusselt number is calculated using a correlation for rectangular channels available in (Kakac et al. 1987) as follows:

$$Nu_{\text{laminar}} = 8.235 \cdot (1 - 2.0241 \cdot \alpha + 3.0853 \cdot \alpha^2 - 2.4765 \cdot \alpha^3 + 1.0578 \cdot \alpha^4 - 0.1861 \cdot \alpha^5) \quad (71)$$

For the turbulent regime, the Nusselt number is calculated using the following correlation developed by Churchill (1977a):

$$Nu = \left[ 4.364^{10} + \frac{\exp\left[\frac{2200 - Re}{365}\right]}{4.364^2} + \frac{1}{\left[ 6.3 + 0.079 \cdot \left(\frac{f}{8}\right)^{0.5} \cdot Re \cdot \frac{Pr}{(1 + Pr^{0.8})^{5/6}} \right]^2} \right]^{-5} \Bigg]^{1/10} \quad (72)$$

By using the same transition criteria outlined in the pump heat addition section, the flow is determined to be turbulent and the Nusselt number is 42.1 in this case. In addition, the Nusselt number is multiplied by a property correction for viscosity, which is as follows:

$$\text{Correction} = \left( \frac{\mu(T_{\text{wall}})}{\mu(T_{\text{bulk}})} \right)^{-0.11} \quad (73)$$

With a bulk water temperature of 53.17°C and a wall temperature of 53.5°C (validated iteratively through the apportioning of  $\Delta T$ s across various resistances), the viscosity property correction is 1.001. For a thermal conductivity of 0.6472 W/m-K, the water-side heat transfer coefficient is 27,652 W/m<sup>2</sup>-K.

The heat transfer area for the water-side is defined as follows:

$$A_{\text{water}} = A_{\text{d,water}} + A_{\text{id,water}} \cdot \eta_{\text{fin}} \quad (74)$$

The direct and indirect heat transfer area are calculated as follows:

$$A_{\text{d,water}} = 2 \cdot N_{\text{port}} \cdot w_{\text{port}} \cdot L \quad (75)$$

$$A_{\text{id,water}} = (4 \cdot N_{\text{port}} \cdot h_{\text{port}} + 2 \cdot N_{\text{port}} \cdot w_{\text{port}}) \cdot L \quad (76)$$

It should be noted that the indirect area shown above includes the area of the two faces of both internal webs of both jackets plus the area of the outer walls of the jackets. For this test section, the direct and indirect heat transfer areas are 0.01115 m<sup>2</sup> and 0.05203 m<sup>2</sup>, respectively. The fin efficiency for the internal webs is defined as follows:

$$\eta_{\text{fin}} = \frac{\tanh(M \cdot L_{\text{fin}})}{M \cdot L_{\text{fin}}} \quad (77)$$

For the water-side, the length of the fin is the port height, while the fin parameter  $M$  is calculated as follows:

$$M = \sqrt{\frac{h_{\text{water}} \cdot p_{\text{fin}}}{k_{\text{tube}} \cdot A_{\text{fin}}}} \quad (78)$$

The thermal conductivity of aluminum is 192.1 W/m-K, while the fin perimeter and cross-sectional area are given by:

$$p_{\text{fin}} = 2 \cdot (L + t_{\text{fin}}) \quad (79)$$

$$A_{\text{fin}} = L \cdot t_{\text{fin}} \quad (80)$$

The fin thickness is calculated as follows:

$$t_{\text{fin}} = \frac{w_{\text{tube}} - 2 \cdot t_{\text{tube}} - N_{\text{port}} \cdot w_{\text{port}}}{N_{\text{port}} - 1} \quad (81)$$

The tube thickness is given by:

$$t_{\text{tube}} = \frac{h_{\text{tube}} - h_{\text{port}}}{2} \quad (82)$$

The tube outer height and width are 1.905 mm and 19.837 mm, respectively. For these tubes, the tube and fin thickness are 0.254 mm and 0.476 mm, respectively. The corresponding fin efficiency of 0.732 results in a total water-side heat transfer area of 0.0492 m<sup>2</sup>, and a water-side heat transfer resistance of 7.345 x 10<sup>-4</sup> K/W.

The wall resistance is found by first calculating an effective outer tube diameter by approximating it as a circular tube as follows:

$$OD_{\text{eff}} = \frac{A_{\text{outer,tube}}}{\pi \cdot L} = \frac{2 \cdot w_{\text{tube}} + 4 \cdot h_{\text{tube}} + 2 \cdot h_{\text{inner,tube}}}{\pi} \quad (83)$$

In this case, the effective tube outside diameter is 16.02 mm, and the wall thickness is the previously calculated tube thickness (0.254 mm), which yields an effective tube ID of 15.51 mm. The resulting wall resistance is 5.84 x 10<sup>-5</sup> K/W.

The insulation has a thermal conductivity of 0.019 W/m-K, thickness of 25.4 mm, and an outside diameter of 66.82 mm, yielding an insulation resistance of 26.16 K/W.

As done in the secondary ambient heat loss calculation, an energy balance between the insulation surface and the ambient, and between the bulk water temperature and insulation surface, respectively, is used to determine the ambient heat loss. In this case, the heat lost to the ambient (T~20°C) in the test section is 1.21 W.

#### *Primary Loop*

The heat lost to the ambient in the rest of the primary loop is calculated from an analysis similar to that described for the test section and secondary heat exchangers. However, in this case, the water flow is through a single tube with an outside diameter of 12.7 mm and a wall thickness of 0.889 mm, which yields an inside diameter of 10.922 mm. For a volumetric flow rate of 6.35 liters per minute, the flow velocity is 1.11 m/s, which results in a Reynolds number of 23,057 and a friction factor of 0.0253. These two parameters are used to find the Nusselt number using equation 72. The resulting Nusselt number is 123.5, which yields a heat transfer coefficient of 7320 W/m<sup>2</sup>-K. The procedure described in equations 64 through 70 is now followed to calculate the ambient heat loss in the rest of the primary loop. The total test section length used here includes the 12.7 mm tubing that connects the secondary heat exchanger to the test section heat exchanger, as well as “equivalent” lengths for the pump housing and flow meter. Figure 13 shows the outside of the pump housing, which has a total surface area of 0.0513 m<sup>2</sup>. The equivalent length is calculated as follows:

$$L_{\text{equivalent}} = \frac{A}{\pi \cdot D} \quad (84)$$

The resulting equivalent length of 12.7 mm tubing for the pump housing is 1.495 m. Figure 14 shows the surface of the water flow meter, which has a surface area of  $0.0944 \text{ m}^2$ . The resulting equivalent length is 2.37 m. Hence, the total length of the primary loop (minus the secondary heat exchanger length) is 9.85 m.

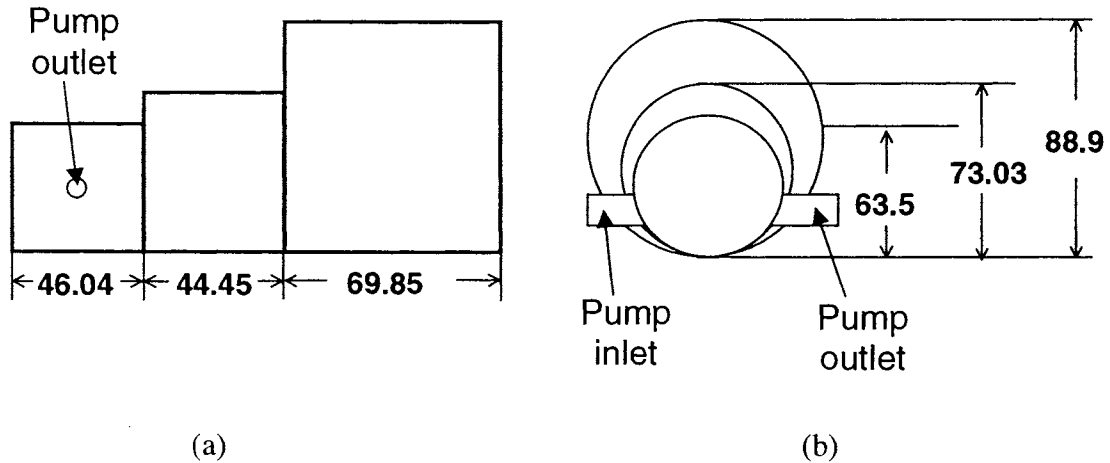


**Figure 13.** Side (a) and Front (b) View Sketches of the Micropump Series 5000 Model H21 Pump Housing (Measurements are in mm; Drawing Not to Scale)

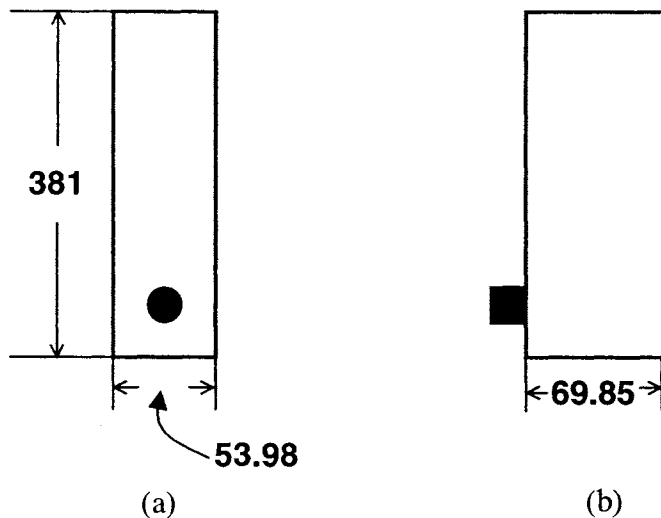


**Figure 14.** Side (a) and Front (b) View Sketch of the Dwyer RMC Series Volumetric Flow Meter (Measurements are in mm; Drawing Not to Scale)

With water, tube, insulation, radiation, natural convection and total resistances of  $4.041 \times 10^{-4}$  K/W,  $1.624 \times 10^{-4}$  K/W, 1.368 K/W, 1.809 K/W, and 4.275 K/W, respectively, the heat lost to the ambient is 23.17 W. Therefore, the heat lost to the ambient from the entire primary loop (including the portion in the secondary and test heat exchangers) is 27.64 W.

### Test Section Heat Duty Calculation

The calculations described above are now combined in the overall primary loop energy balance as follows:

$$Q_{\text{test}} = Q_{\text{sec}} + Q_{\text{ambient}} - Q_{\text{pump}} = 180.7 + 27.64 - 24.73 = 183.6 \text{ W} \quad (85)$$

The corresponding values for each term for this sample case are also shown in the above equation. This equation shows that the net contribution of the extraneous heat transfer term (pump heat addition and ambient heat loss, which almost compensate each other) is extremely small (1.58%), which validates this technique for heat duty measurement.

### Uncertainty Calculation

By applying an uncertainty propagation technique to equation 1, the error in the test section heat duty can be found as follows:

$$U_{Q_{\text{test}}}^2 = \left( \frac{\partial Q_{\text{test}}}{\partial Q_{\text{sec}}} u_{Q_{\text{sec}}} \right)^2 + \left( \frac{\partial Q_{\text{test}}}{\partial Q_{\text{ambient}}} u_{Q_{\text{ambient}}} \right)^2 + \left( \frac{\partial Q_{\text{test}}}{\partial Q_{\text{pump}}} u_{Q_{\text{pump}}} \right)^2 \quad (86)$$

Since the partial derivatives are either 1 or -1, equation 51 reduces to:

$$U_{Q_{\text{test}}}^2 = (u_{Q_{\text{sec}}})^2 + (u_{Q_{\text{amb}}})^2 + (u_{Q_{\text{pump}}})^2 \quad (87)$$

The pump heat addition and ambient heat loss calculations described above could have large uncertainties, and were conservatively estimated to be  $\pm 50\%$ . For this case, the uncertainty in the pump heat addition and ambient heat loss are 12.37 W and 13.82 W, respectively.

The error in the secondary loop heat duty was found by applying an uncertainty propagation technique to equation 2, which results in the following:

$$U_{Q_{\text{sec}}}^2 = \left( \frac{\partial Q_{\text{sec}}}{\partial \dot{m}_{w,\text{sec}}} u_{\dot{m}_{w,\text{sec}}} \right)^2 + \left( \frac{\partial Q_{\text{sec}}}{\partial h_{w,\text{sec},\text{in}}} u_{h_{w,\text{sec},\text{in}}} \right)^2 + \left( \frac{\partial Q_{\text{sec}}}{\partial h_{w,\text{sec},\text{out}}} u_{h_{w,\text{sec},\text{out}}} \right)^2 \quad (88)$$

The partial derivatives are evaluated as follows:

$$\frac{\partial Q_{\text{sec}}}{\partial \dot{m}_{w,\text{sec}}} = \Delta h_{w,\text{sec}} = 145.5 \text{ kJ/kg} \quad (89)$$

$$\frac{\partial Q_{\text{sec}}}{\partial h_{\text{w,sec,in}}} = -\dot{m}_{\text{w,sec}} = -1.24 \times 10^{-3} \text{ kg/s} \quad (90)$$

$$\frac{\partial Q_{\text{sec}}}{\partial h_{\text{w,sec,out}}} = \dot{m}_{\text{w,sec}} = 1.24 \times 10^{-3} \text{ kg/s} \quad (91)$$

The uncertainty in the mass flow rate is  $\pm 0.2\%$  of the measured value (manufacturer specifications), which is, in this case,  $2.48 \times 10^{-6} \text{ kg/s}$ . The uncertainty in enthalpy can be found as follows:

$$u_h = \frac{\partial h}{\partial T} u_T = C_p \cdot u_T \quad (92)$$

Therefore, the uncertainty in refrigerant inlet enthalpy is  $\pm 2.091 \text{ kJ/kg}$ . Similarly, the uncertainty in the outlet enthalpy is  $\pm 2.089 \text{ kJ/kg}$ . Therefore, the uncertainty in the secondary loop heat duty is  $\pm 3.68 \text{ W}$ . This is combined with the uncertainty in the pump heat addition and ambient heat loss to calculate the uncertainty in the test section heat duty, which in this case is  $\pm 18.91 \text{ W}$ . This result shows that the test section heat duty can be determined accurately (within  $\pm 10.3\%$  in this case) using the technique in this study as long as the pump heat addition and ambient heat loss are small fractions of the test section heat duty. Figure 15 shows the test section heat duties, with their associated uncertainties, for test section S30. Figure 16 shows the test section and secondary heat duties, as well as the ambient heat loss and pump heat addition, for test section S30 at a nominal mass flux of  $450 \text{ kg/m}^2\text{-s}$ . These figures show that the method described for calculating the test section heat duty is adequate.

### Test Section S30 Heat Transfer Coefficient and Uncertainty

The procedures for the calculation of the condensation heat transfer coefficient and its associated uncertainty are described here for test section S30. The methods are illustrated with the same data point as in the test section heat duty calculation.

#### Heat Transfer Coefficient Calculation

The log mean temperature difference is defined as follows:

$$\text{LMTD}_{\text{test}} = \frac{(\Delta T_1) - (\Delta T_2)}{\ln[(\Delta T_1)/(\Delta T_2)]} \quad (93)$$

where:

$$\Delta T_1 = T_{\text{test,sat,i}} - T_{\text{test,w,out}} \quad (94)$$

$$\Delta T_2 = T_{\text{test,sat,o}} - T_{\text{test,w,in}} \quad (95)$$

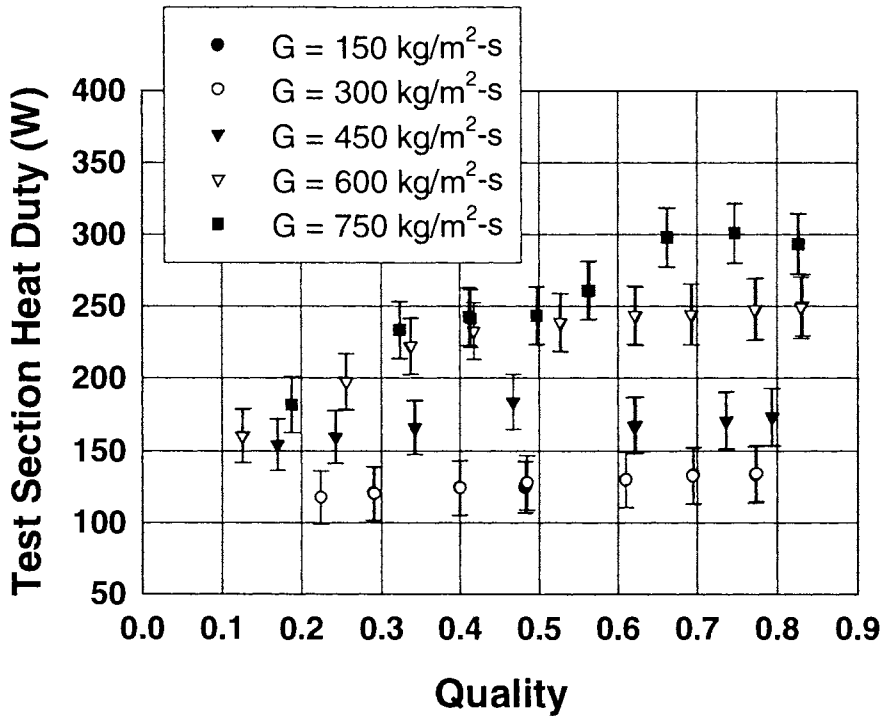


Figure 15. Test Section S30 Heat Duty versus Quality for  $150 < G < 750 \text{ kg/m}^2\text{-s}$

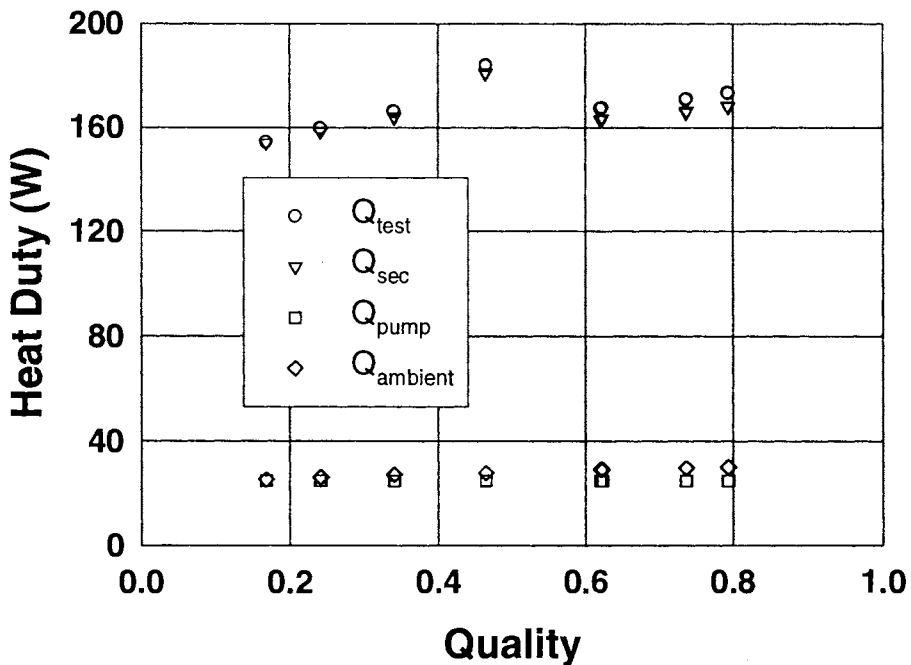


Figure 16. Test Section and Secondary Loop Heat Duties, Ambient Heat Loss, and Pump Heat Addition for Test Section S30 and  $G = 450 \text{ kg/m}^2\text{-s}$

Since the refrigerant enters and exits the test section as a two-phase mixture, the test section inlet and outlet temperatures are found from the measured test section inlet and outlet pressures. For inlet and outlet pressures of 1,546 kPa and 1,531 kPa, respectively, the saturation temperatures are 56.45°C and 56.04°C. Also, the test section primary coolant inlet and outlet temperatures are 53.0°C and 53.33°C, respectively, which results in a log mean temperature difference of 3.08 K.

The condensation heat transfer coefficient for test section S30 is deduced from the overall heat transfer conductance UA, which is determined as follows:

$$UA_{\text{test}} = \frac{Q_{\text{test}}}{\text{LMTD}_{\text{test}}} \quad (96)$$

For this data point, the test section heat duty of 183.6 W and log mean temperature difference of 3.08 K yield an overall UA of 59.6 W/K.

The calculation of the water-side heat transfer coefficient was described with the test section heat duty calculation and estimated to be 27,652 W/m<sup>2</sup>-K. The heat transfer area was also described in the same section, except that the brazed length of 0.3048 m is used here to result in an effective area of 0.03282 m<sup>2</sup> and a resistance of 1.102 x 10<sup>-3</sup> K/W.

The port height and width for test section S30 are found in the same way as for the tube jackets, except that the height and width are the same for test section S30, which has a square cross section. For a total free flow area and wetted perimeter of 9.871 mm<sup>2</sup> and 51.816 mm, respectively, and 17 flow passages, the port height and width are both 0.762 mm. The direct and indirect heat transfer areas are calculated as follows:

$$A_{d,\text{water}} = 2 \cdot N_{\text{port}} \cdot w_{\text{port}} \cdot L \quad (97)$$

$$A_{id,\text{water}} = 2 \cdot N_{\text{port}} \cdot h_{\text{port}} \cdot L \quad (98)$$

Therefore, the direct and indirect heat transfer areas are both 7.897 x 10<sup>-3</sup> m<sup>2</sup>. For the outer tube height of 1.524 mm and outer tube width of 19.05 mm, the tube and fin thickness are 0.381 mm and 0.333 mm, respectively, which yield the fin perimeter and cross-sectional area of 0.6103 m and 101.62 mm<sup>2</sup>, respectively. However, the fin efficiency needs to be solved iteratively because it is a function of the refrigerant heat transfer coefficient.

The wall resistance is determined as follows:

$$R_{\text{wall}} = \frac{t_{\text{total}}}{k_{\text{tube}} \cdot A_{\text{tube}}} \quad (99)$$

The total wall thickness was the sum of the tube jacket and center tube wall thickness, which is 0.635 mm, while the thermal conductivity is 192.1 W/m-K. The tube area used for the

above calculation is based on the average contact area between the refrigerant and cooling water sides. Thus:

$$A_{\text{tube}} = \frac{A_{j,\text{in}} + A_{j,\text{out}} + A_{c,\text{in}} + A_{c,\text{out}}}{4} \quad (100)$$

The tube jacket outside area and inside (sum of the web thickness and the port width for all ports) areas are calculated as follows:

$$A_{j,\text{out}} = 2 \cdot L \cdot w_{\text{tube}} \quad (101)$$

$$A_{j,\text{in}} = 2 \cdot L \cdot \left[ (N_{\text{port}} - 1) \cdot t_{\text{fin}} + w_{\text{port}} \cdot N_{\text{port}} \right] \quad (102)$$

These 2 tube areas are 0.0121 m<sup>2</sup> and 0.0118 m<sup>2</sup>, respectively. Similarly, the center tube outside and total bottom port areas are 0.0116 m<sup>2</sup> and 0.0112 m<sup>2</sup>, respectively. Therefore, the total tube area is 0.0117 m<sup>2</sup>, which yields a tube-wall resistance of 2.825 x 10<sup>-4</sup> K/W.

The overall UA for the test section is defined as follows:

$$UA_{\text{test}} = \frac{1}{R_{\text{wall}} + R_{\text{water}} + R_{\text{refrigerant}}} \quad (103)$$

With  $R_{\text{wall}} = 2.825 \times 10^{-4}$  K/W,  $R_{\text{water}} = 1.102 \times 10^{-3}$  K/W, and  $UA_{\text{test}} = 59.63$  W/K, the refrigerant-side heat transfer resistance is 0.0154 K/W. Based on this value, the ratio of refrigerant resistance to water resistance is 13.96. Clearly, the refrigerant heat transfer resistance dominates, which reduces the uncertainty in the condensation heat transfer coefficient. Figure 17 shows the resistance ratio as a function of mass flux for all the tests conducted in this study on test section S30. Whenever possible, the resistance ratios were kept above 3 to ensure the accuracy of the results. As Figure 18 shows, the resistance ratios were greater than 5 for all of the tests. Using the same procedure that was used for the tube jackets, with ½ the port height equal to the fin height, the refrigerant-side fin efficiency and effective heat transfer area are 0.994 and 0.01574 m<sup>2</sup>, respectively, yielding a condensation heat transfer coefficient of 4,128 W/m<sup>2</sup>-K.

### Uncertainty Calculation

The uncertainty in the overall heat transfer conductance is calculated as follows:

$$u_{UA}^2 = \left( \frac{\partial UA}{\partial Q} u_Q \right)^2 + \left( \frac{\partial UA}{\partial \text{LMTD}} u_{\text{LMTD}} \right)^2 \quad (104)$$

The partial derivatives are evaluated as follows:

$$\frac{\partial UA}{\partial Q} = \frac{1}{\text{LMTD}} = 0.325 \text{ (1/K)} \quad (105)$$

$$\frac{\partial UA}{\partial \text{LMTD}} = -\frac{Q}{(\text{LMTD})^2} = 19.35 (\text{W/K}^2) \quad (106)$$

The uncertainty in the heat duty was previously found to be  $\pm 18.91$  W, and the uncertainty in the log-mean temperature difference is calculated as follows:

$$u_{\text{LMTD}}^2 = \left( \frac{\partial \text{LMTD}}{\partial T_{\text{hi}}} u_T \right)^2 + \left( \frac{\partial \text{LMTD}}{\partial T_{\text{ho}}} u_T \right)^2 + \left( \frac{\partial \text{LMTD}}{\partial T_{\text{ci}}} u_T \right)^2 + \left( \frac{\partial \text{LMTD}}{\partial T_{\text{co}}} u_T \right)^2 \quad (107)$$

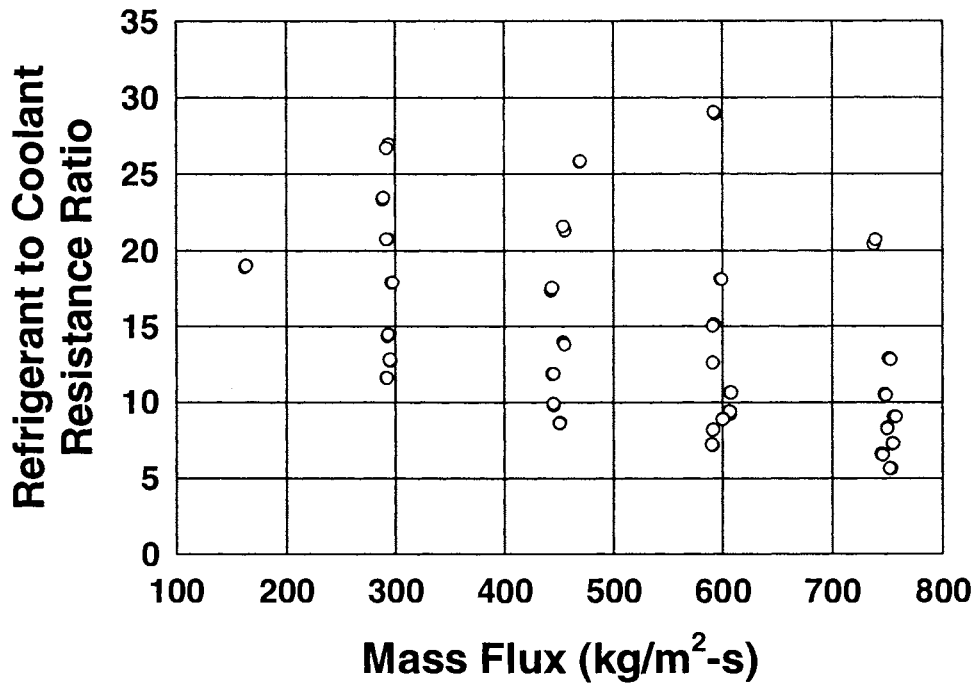


Figure 17. Heat Transfer Resistance Ratio versus Mass Flux for Test Section S30

The partial derivatives are calculated as follows:

$$\frac{\partial \text{LMTD}}{\partial T_{\text{hi}}} = \frac{1}{\ln(\Delta T_1/\Delta T_2)} - \frac{\Delta T_1 - \Delta T_2}{[\ln(\Delta T_1/\Delta T_2)]^2} \frac{1}{\Delta T_1} = 0.4957 \quad (108)$$

$$\frac{\partial \text{LMTD}}{\partial T_{\text{ho}}} = -\frac{1}{\ln(\Delta T_1/\Delta T_2)} + \frac{\Delta T_1 - \Delta T_2}{[\ln(\Delta T_1/\Delta T_2)]^2} \frac{1}{\Delta T_2} = -0.5044 \quad (109)$$

$$\frac{\partial \text{LMTD}}{\partial T_{\text{ci}}} = \frac{1}{\ln(\Delta T_1/\Delta T_2)} - \frac{\Delta T_1 - \Delta T_2}{[\ln(\Delta T_1/\Delta T_2)]^2} \frac{1}{\Delta T_2} = 0.5044 \quad (110)$$

$$\frac{\partial \text{LMTD}}{\partial T_{\text{co}}} = -\frac{1}{\ln(\Delta T_1/\Delta T_2)} + \frac{\Delta T_1 - \Delta T_2}{[\ln(\Delta T_1/\Delta T_2)]^2} \frac{1}{\Delta T_1} = -0.4957 \quad (111)$$

The uncertainty in primary coolant temperature is given as  $\pm 0.5^\circ\text{C}$ . However, the refrigerant temperatures are deduced from the pressure measurement, and this uncertainty is calculated as follows:

$$u_T = \frac{\partial T}{\partial P} u_P \quad (112)$$

The partial derivative of temperature with respect to pressure is given by:

$$\frac{\partial T}{\partial P} = \frac{T(P + u_P) - T(P - u_P)}{2u_P} \quad (113)$$

The uncertainty in pressure measurement is  $\pm 13.79$  kPa. Therefore, the elevated and reduced temperatures in equation 113 are  $56.82^\circ\text{C}$  and  $56.09^\circ\text{C}$ , respectively, which yield uncertainties in inlet and outlet refrigerant temperatures of  $\pm 0.37^\circ\text{C}$ . (This uncertainty is lower than the RTD uncertainty and shows why the saturation pressure measurements were used instead of the directly measured temperatures.) Hence, the log mean temperature difference is known within  $\pm 0.44^\circ\text{C}$ , and the overall UA is known within  $\pm 10.5$  W/K (or  $\pm 17.6\%$ ).

Equation 103 can be re-written as follows:

$$h_{\text{refg}} = \frac{1}{(1/UA - 1/h_{\text{water}}A_{\text{water}} - R_{\text{wall}})A_{\text{refg}}} \quad (114)$$

The propagation of uncertainty for the refrigerant heat transfer coefficient is as follows:

$$u_{h_{\text{refg}}}^2 = \left( \frac{\partial h_{\text{refg}}}{\partial UA} u_{UA} \right)^2 + \left( \frac{\partial h_{\text{refg}}}{\partial h_{\text{water}}} u_{h_{\text{water}}} \right)^2 \quad (115)$$

The uncertainties in the heat transfer area and wall resistance are neglected. As a conservative estimate, the uncertainty in the water-side heat transfer coefficient is assumed to be  $\pm 25\%$ , which is  $6,913$  W/m<sup>2</sup>-k in this case. The partial derivatives of refrigerant heat transfer coefficient with respect to overall UA and water-side heat transfer coefficient are as follows:

$$\frac{\partial h_{\text{refg}}}{\partial UA} = \frac{1}{A_{\text{refg}}} \frac{1}{(UA)^2} \frac{1}{(1/UA - 1/h_{\text{water}}A_{\text{water}} - R_{\text{wall}})^2} = 75.47 \text{ m}^{-2} \quad (116)$$

$$\frac{\partial h_{\text{refg}}}{\partial h_{\text{water}}} = \frac{A_{\text{water}}}{A_{\text{refg}}} \frac{1}{(h_{\text{water}} A_{\text{water}})^2} \frac{1}{(1/UA - 1/h_{\text{water}} A_{\text{water}} - R_{\text{wall}})^2} = 0.01069 \quad (117)$$

As a result, the condensation refrigerant heat transfer coefficient of  $4,128 \text{ W/m}^2\text{-K}$  is known within  $\pm 797.2 \text{ W/m}^2\text{-K}$  (or  $\pm 19.3\%$ ). The uncertainties in the condensation heat transfer coefficients for test section S30 can be seen in Figure 18.

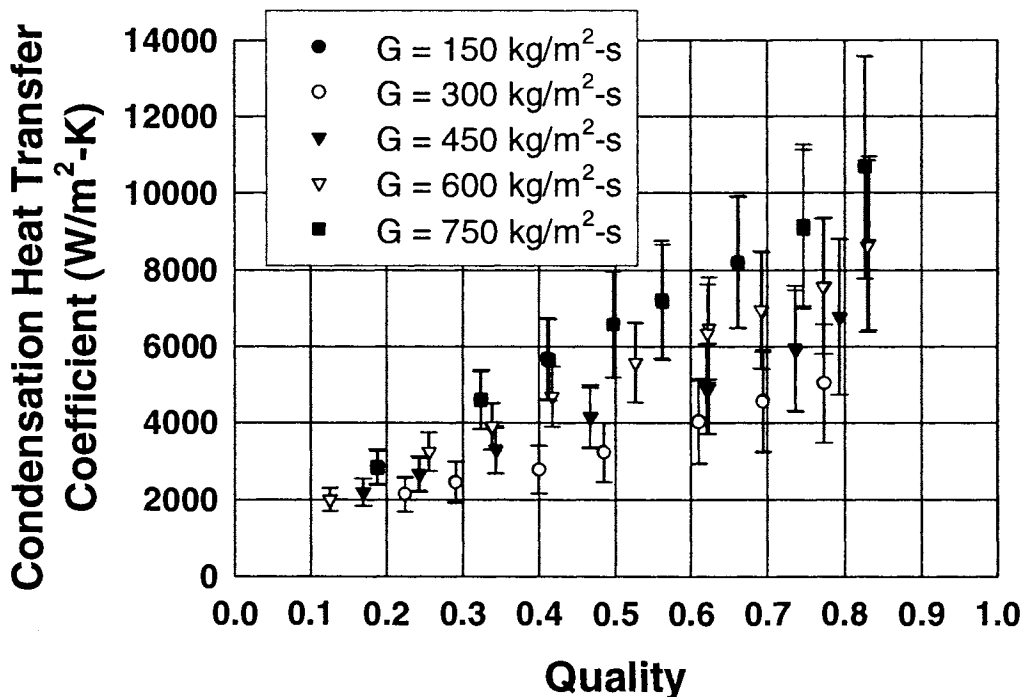


Figure 18. Test Section S30 R-134a Condensation Heat Transfer Coefficient versus Quality for  $150 \text{ kg/m}^2\text{-s} < G < 750 \text{ kg/m}^2\text{-s}$

### Test Section RK15 Heat Transfer Coefficient and Uncertainty

The condensation heat transfer coefficients for test section RK15 are calculated using the same methodology described above for test section S30, only with a rectangular port tube geometry. The cross-section of the refrigerant-side of test section RK15 can be seen in Figure 3 in Chapter 3. The outer tube jackets are exactly the same as for test section S30 (see Figures 7 and 8). For a total free flow area and wetted perimeter of  $4.065 \text{ mm}^2$  and  $38.379 \text{ mm}$ , respectively, and 20 flow passages, the port height and width are  $0.316 \text{ mm}$  and  $0.644 \text{ mm}$ , respectively, and the hydraulic diameter is  $0.424 \text{ mm}$ . The heat transfer coefficients and resistance ratios for test section RK15 are found using the method described for test section

S30. Figure 19 shows the resistance ratio as a function of mass flux for all the tests conducted in this study on test section RK15. All of the resistance ratios are above 5 to ensure low uncertainties in the calculation of the condensation heat transfer coefficient from the measured UA. The heat transfer coefficients (with their associated uncertainties) as a function of quality are shown in Figure 20 for the mass flux range of 450 to 750 kg/m<sup>2</sup>-s. The heat transfer coefficient increases with mass flux, especially at higher qualities, and quality. However, the uncertainty in the heat transfer coefficient is large for the high mass flux and quality points. This is due to the inaccuracy in the log mean temperature difference – at such high heat transfer coefficients and the low heat transfer duties for this test section with the smallest free flow area, the LMTD is extremely low, 1.4 K < LMTD < 2.76 K. The mass fluxes of 150 and 300 kg/m<sup>2</sup>-s were not included for test section RK15 because of the inability to measure the extremely low flow rates required ( $6.097 \times 10^{-4}$  and  $1.219 \times 10^{-5}$  kg/s for the 150 and 300 kg/m<sup>2</sup>-s mass flux cases, respectively). Only one point was included (with an average quality of 0.47, and  $x_{in} = 0.81$  and  $x_{out} = 0.12$ ) for the mass flux of 450 kg/m<sup>2</sup>-s due to the low flow rate and test section heat duty.

### **Significance of the Fin Efficiency of the Port Walls**

In the discussion thus far, the microchannel port walls have been treated as fins with the associated efficiencies reflecting the fact that this surface area is not in direct contact with the cooling water side. However, if the fin efficiency approaches unity for the microchannels, the indirect heat transfer area may be treated as direct area, with a negligible loss of accuracy. Figures 21 and 22 show the refrigerant-side and water-side fin efficiencies for the data points taken for test sections S30 and RK15, respectively. The refrigerant-side fin efficiencies are very near unity for both test sections, while the water-side fin efficiencies are about 25% less. This is due to the high thermal conductivity of Aluminum, the small fin height (1/2 the port height), and the relatively thick webs between the ports. Thus, these figures show that the refrigerant-side fin effects can be neglected, while the water-side fin effects cannot. Consequently, the fin effects on the water-side are included for the test sections with ports of circular and other shapes, while the refrigerant-side fin effects are neglected.

## **Circular Channels**

### **Test Section C20 Heat Transfer Coefficient and Uncertainty**

The condensation heat transfer coefficients for test section C20 are calculated using the same methodology presented above for test section S30, with the only difference being

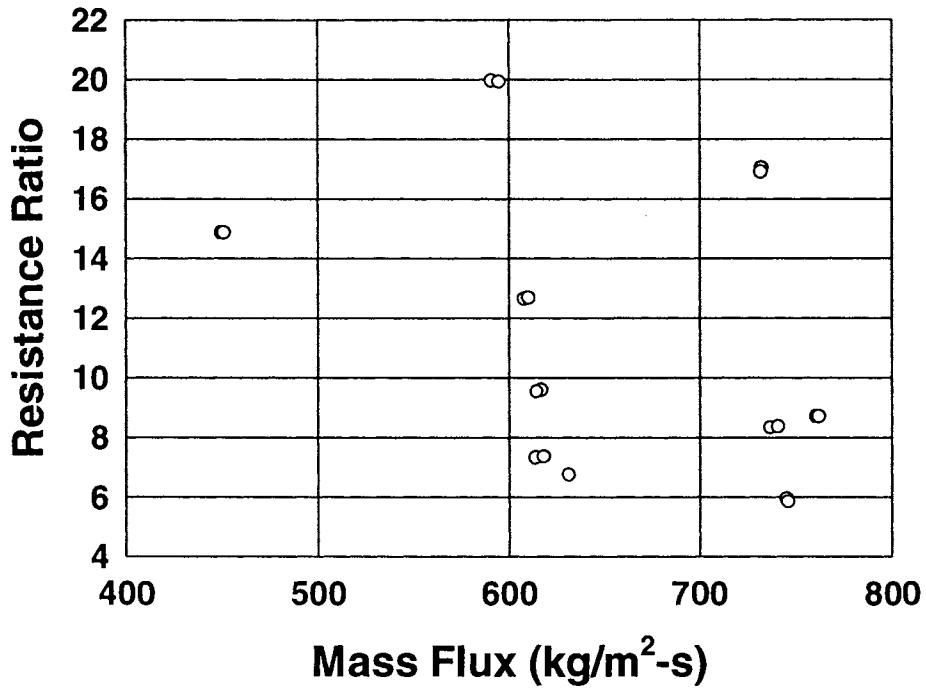


Figure 19. Heat Transfer Resistance Ratio versus Mass Flux for Test Section RK15

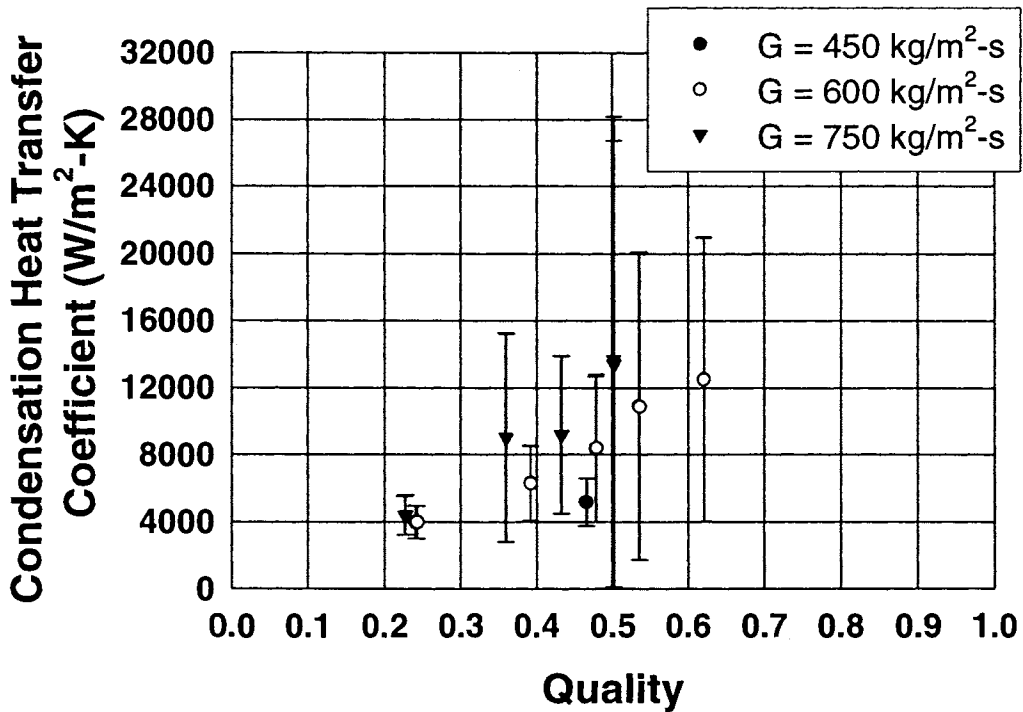


Figure 20. Test Section RK15 R-134a Condensation Heat Transfer Coefficient versus Quality for  $450 \text{ kg/m}^2\text{-s} < G < 750 \text{ kg/m}^2\text{-s}$

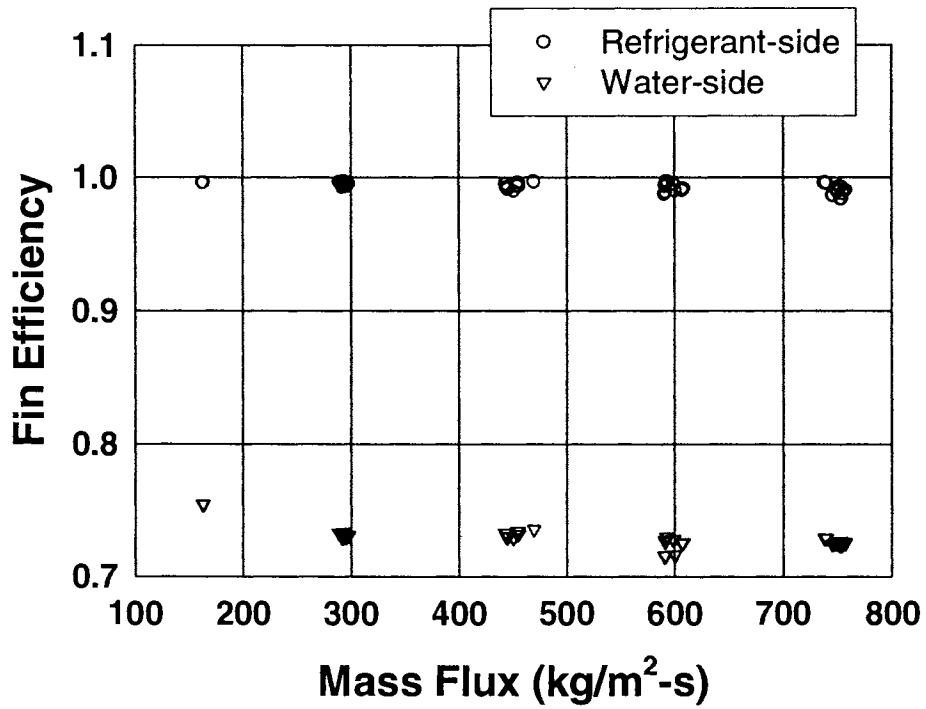


Figure 21. Test Section S30 Refrigerant-side and Water-side Fin Efficiency

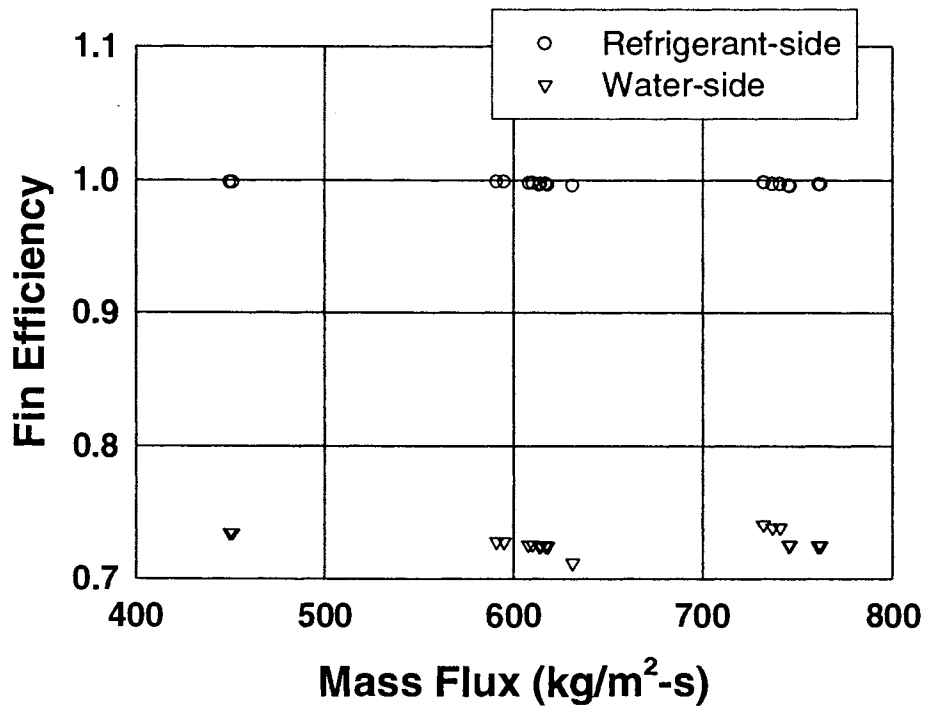


Figure 22. Test Section RK15 Refrigerant-side and Water-side Fin Efficiency

the tube geometry. The cross-section of the refrigerant-side of test section C20 can be seen in Figure 3 in Chapter 3. The outer tube jackets are exactly the same as for test section S30. The total free flow area and wetted perimeter of 4.645 mm<sup>2</sup> and 36.703 mm, respectively, yields a hydraulic diameter of 0.506 mm for 23 flow passages. Neglecting refrigerant-side fin effects, the refrigerant heat transfer area is calculated as follows:

$$A_{\text{refrigerant}} = P_{\text{total}} \cdot L \quad (118)$$

For a test section length of 0.3048 m, the refrigerant heat transfer area is 0.0112 m<sup>2</sup>. Figure 23 shows the resistance ratio as a function of mass flux for all the tests conducted in this study on test section C20. All of the resistance ratios are above 5 to ensure low uncertainties in the calculation of the heat transfer coefficients. The heat transfer coefficients (with their associated uncertainties) as a function of quality are shown in Figure 24 for the mass flux range of 300 to 750 kg/m<sup>2</sup>-s. The heat transfer coefficients tend to increase with mass flux, especially at higher qualities, and quality. For the high quality and mass flux cases, the uncertainty in the heat transfer coefficients increases due to the low LMTDs at such high heat transfer coefficients. Furthermore, the mass flux of 150 kg/m<sup>2</sup>-s was not tested for test section C20 because of the inability to accurately measure the low flow rate (6.967 x 10<sup>-4</sup> kg/s). In addition, even for a mass flux of 300 kg/m<sup>2</sup>-s, the low flow rate (1.39 x 10<sup>-3</sup> kg/s) and correspondingly low heat duty (163.4 W) only allowed one data point representing condensation from x = 0.82 to x = 0.09.

### **Test Section C30 Heat Transfer Coefficient and Uncertainty**

The cross-section of the refrigerant-side of test section C30 can be seen in Figure 3 in Chapter 3. The total free flow area and wetted perimeter of 7.742 mm<sup>2</sup> and 40.691 mm, respectively, yields a hydraulic diameter of 0.761 mm for 17 flow passages. Figure 25 shows that the resistance ratios for all data points for this test section are > 5. The heat transfer coefficients (with their associated uncertainties) as a function of quality are shown in Figure 26 for the mass flux range of 150 to 750 kg/m<sup>2</sup>-s. The heat transfer coefficients tend to increase with mass flux, especially at higher qualities, and quality. Only one data point representing condensation from x = 0.74 to x = 0.12 was taken for the mass flux of 150 kg/m<sup>2</sup>-s due to the low flow rate (1.33 x 10<sup>-3</sup> kg/s) and consequently low test section heat duty (106 W).

### **Test Section C60 Heat Transfer Coefficient and Uncertainty**

The cross-section of the refrigerant-side of test section C60 can be seen in Figure 3 in Chapter 3. The total free flow area and wetted perimeter of 18.242 mm<sup>2</sup> and 47.878 mm, respectively, yields a hydraulic diameter of 1.524 mm for 10 flow passages. Figure 27 shows

that the resistance ratios for all data points for this test section are  $> 5$ . The heat transfer coefficients (with their associated uncertainties) as a function of quality are shown in Figure 28 for the mass flux range of 150 to 750 kg/m<sup>2</sup>-s. The heat transfer coefficients tend to increase with mass flux, especially at higher qualities, and quality, especially at higher mass fluxes.

## Other Microchannel Shapes

### Test Section B32 Heat Transfer Coefficient and Uncertainty

The cross-section of the refrigerant-side of test section B32 with “barrel-shaped” ports can be seen in Figure 3 in Chapter 3. The total free flow area and wetted perimeter of 10.00 mm<sup>2</sup> and 50.056 mm, respectively, yields a hydraulic diameter of 0.762 mm for 14 flow passages. Figure 29 shows that the resistance ratios for all data points for this test section are  $> 5$ . The heat transfer coefficients (with their associated uncertainties) as a function of quality are shown in Figure 30 for the mass flux range of 150 to 750 kg/m<sup>2</sup>-s. Only one point was taken for the mass flux of 150 kg/m<sup>2</sup>-s representing condensation from  $x = 0.79$  to  $x = 0.10$  due to the low flow rate ( $1.5 \times 10^{-3}$  kg/s) and consequently low test section heat duty (115.2 W). The data recorded on test section B32 seemed to be inconsistent with the expected mass flux trend. At lower qualities ( $x < 0.45$ ), the mass fluxes of 600 and 750 kg/m<sup>2</sup>-s had lower or equal heat transfer coefficients than for  $G = 300$  and 450 kg/m<sup>2</sup>-s. At higher qualities, the  $G = 750$  kg/m<sup>2</sup>-s data produced the highest heat transfer coefficients, but the  $G = 600$  kg/m<sup>2</sup>-s data were lower than the  $G = 450$  kg/m<sup>2</sup>-s data. Due to these inexplicable trends, these data are not included in the further analysis of the results.

### Test Section N21 Heat Transfer Coefficient and Uncertainty

The cross-section of the refrigerant-side of test section N21 can be seen in Figure 3 in Chapter 3. The total free flow area and wetted perimeter of 7.871 mm<sup>2</sup> and 58.763 mm, respectively, yields a hydraulic diameter of 0.536 mm for 19 flow passages. Figure 31 shows that the resistance ratios for all data points for this test section are  $> 3$ . The heat transfer coefficients (with their associated uncertainties) as a function of quality are shown in Figure 32 for the mass flux range of 150 to 750 kg/m<sup>2</sup>-s. The heat transfer coefficients tend to increase with mass flux, especially at higher qualities, and quality. Only one point for the mass flux of 150 kg/m<sup>2</sup>-s representing condensation from  $x = 0.71$  to  $x = 0.03$  due to the low flow rate ( $1.35 \times 10^{-3}$  kg/s) and consequently low test section heat duty ( $\sim 120$  W), and two points for the mass flux of 300 kg/m<sup>2</sup>-s representing condensation from  $x = 0.6$  to  $x = 0.1$  and  $x = 0.93$  to  $x = 0.33$  due to small LMTDs ( $\sim 1.9$  K).

### **Test Section T33 Heat Transfer Coefficient and Uncertainty**

The cross-section of the refrigerant-side of test section T33 can be seen in Figure 3 in Chapter 3. The total free flow area and wetted perimeter of 13.419 mm<sup>2</sup> and 64.008 mm, respectively, yields a hydraulic diameter of 0.839 mm for 19 flow passages. Figure 33 shows that the resistance ratios for all data points for this test section are > 3. The heat transfer coefficients (with their associated uncertainties) as a function of quality are shown in Figure 34 for the mass flux range of 150 to 750 kg/m<sup>2</sup>-s. The heat transfer coefficients tend to increase with mass flux, especially at higher qualities, and quality. With lower LMTDs (as low as 1.6 K), the high quality, high mass flux heat transfer coefficients tend to have large uncertainties.

### **Test Section W29 Heat Transfer Coefficient and Uncertainty**

The cross-section of the refrigerant-side of test section W29 can be seen in Figure 3 in Chapter 3. The total free flow area and wetted perimeter of 12.277 mm<sup>2</sup> and 67.135 mm, respectively, yields a hydraulic diameter of 0.732 mm for 19 flow passages. Figure 35 shows that the resistance ratios for nearly all data points for this test section are > 3. The heat transfer coefficients (with their associated uncertainties) as a function of quality are shown in Figure 36 for the mass flux range of 150 to 750 kg/m<sup>2</sup>-s. The heat transfer coefficients tend to increase with mass flux, especially at higher qualities, and quality. The heat transfer coefficients for the highest quality at  $G = 750 \text{ kg/m}^2\text{-s}$  have large uncertainties due to the low log mean temperature difference. Only two points were taken for the mass flux of 150 kg/m<sup>2</sup>-s representing condensation from  $x = 0.54$  to  $x = 0.06$  and  $x = 0.86$  to  $x = 0.27$  due to the low flow rate ( $1.8 \times 10^{-3} \text{ kg/s}$ ) and consequently low test section heat duty (~110 W). The uncertainty in the high quality data points for the 750 kg/m<sup>2</sup>-s mass flux is extremely large ( $\pm 114\%$  of the value) due to the small LMTD (1.8 K).

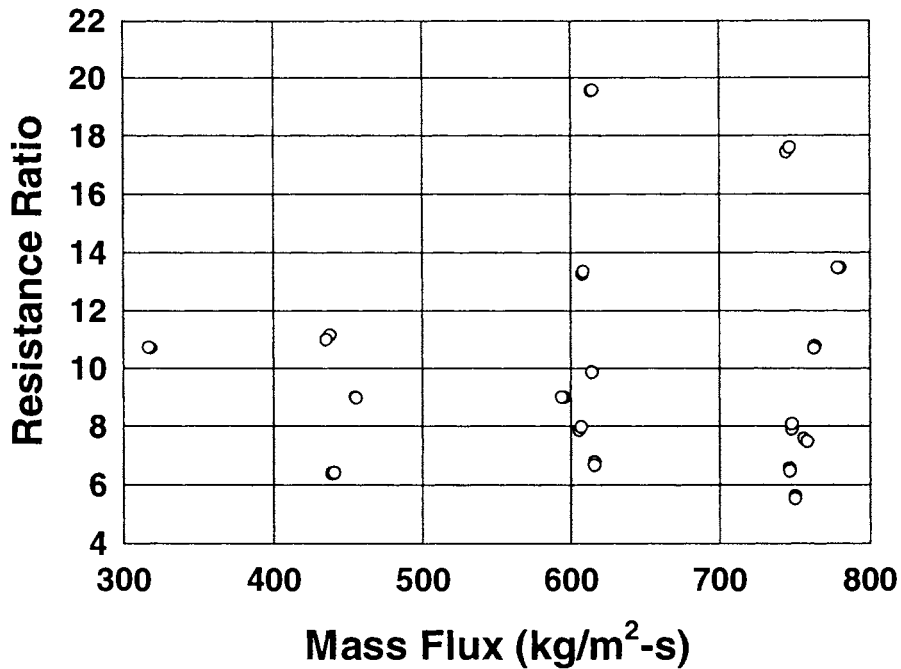


Figure 23. Refrigerant to Water Resistance Ratio for Test Section C20

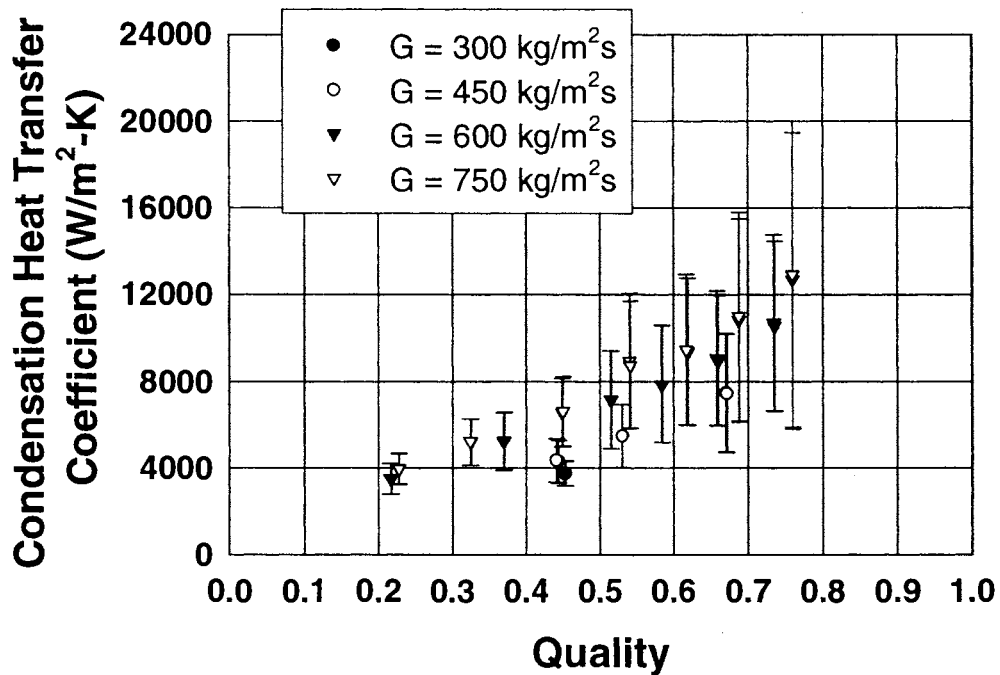


Figure 24. R-134a Condensation Heat Transfer Coefficient versus Quality for  $300 \text{ kg/m}^2\text{-s} < G < 750 \text{ kg/m}^2\text{-s}$  in Test Section C20

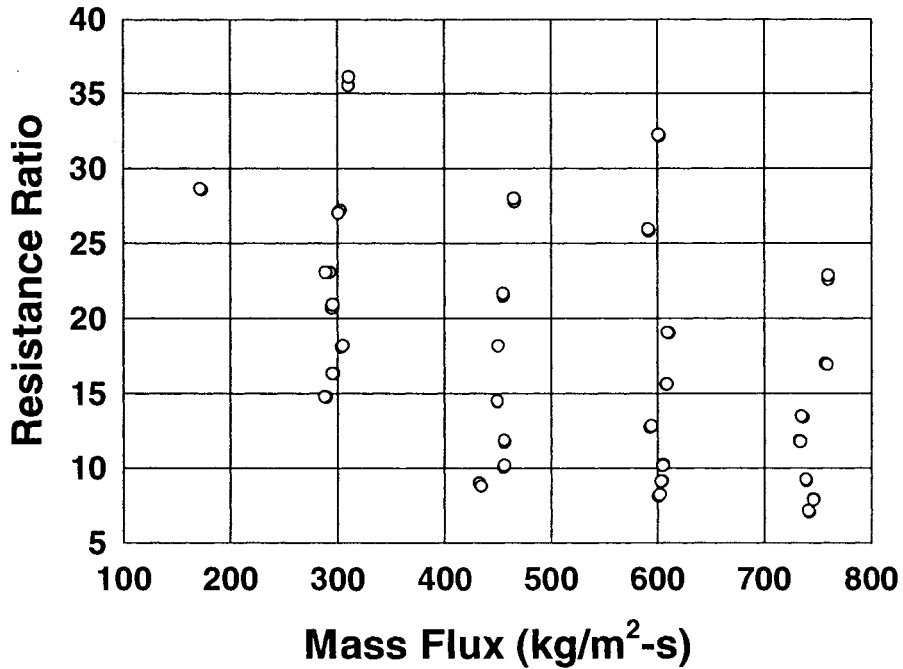


Figure 25. Refrigerant to Water Resistance Ratio for Test Section C30

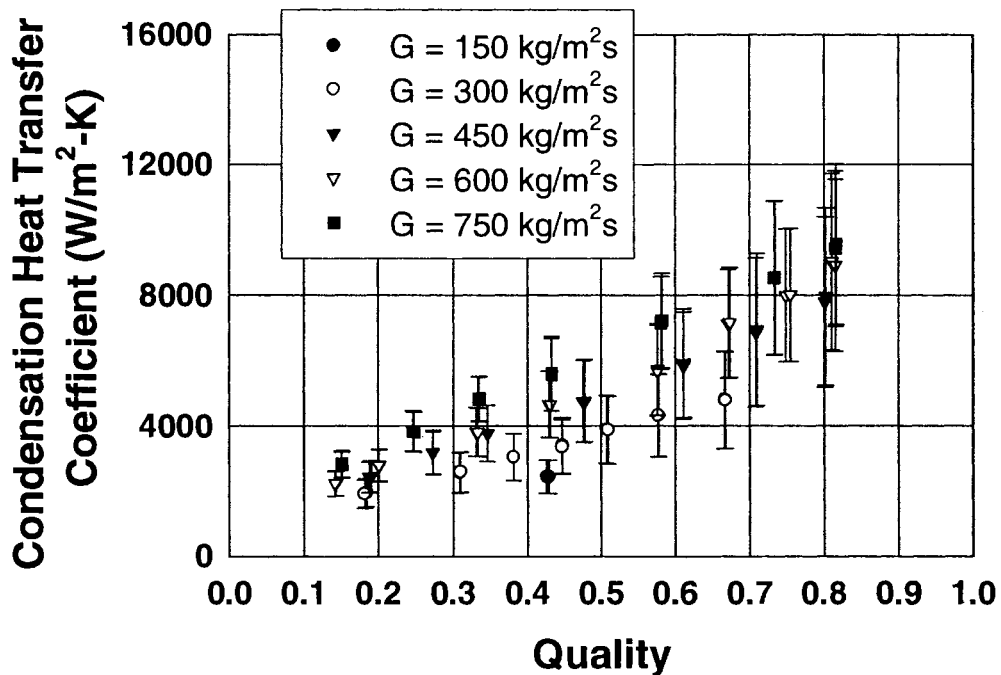


Figure 26. R-134a Condensation Heat Transfer Coefficient versus Quality for  $150 \text{ kg/m}^2\text{-s} < G < 750 \text{ kg/m}^2\text{-s}$  in Test Section C30

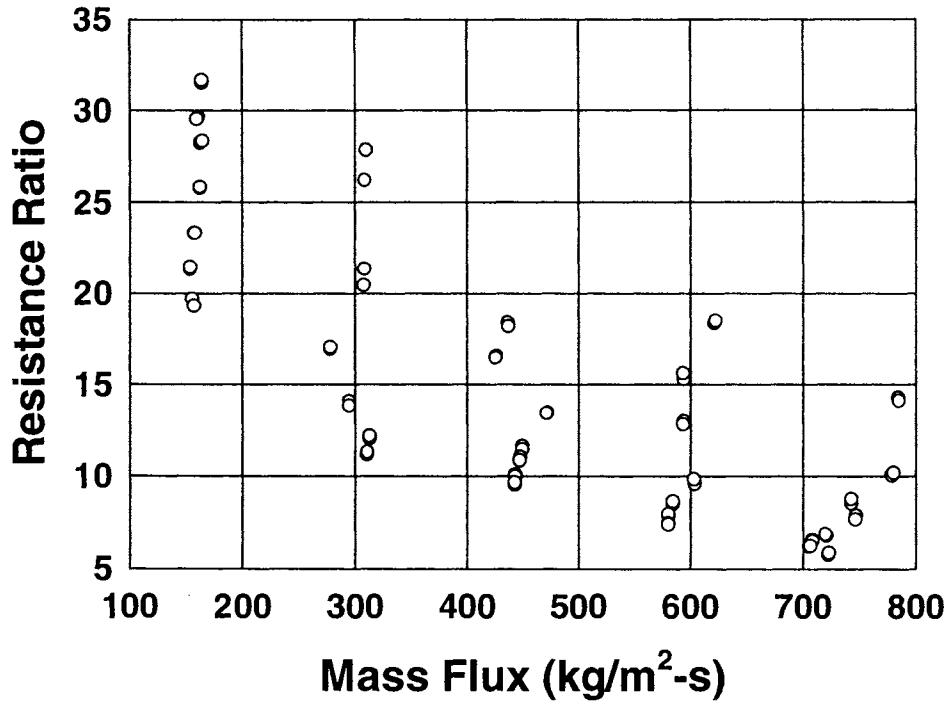


Figure 27. Refrigerant to Water Resistance Ratio for Test Section C60

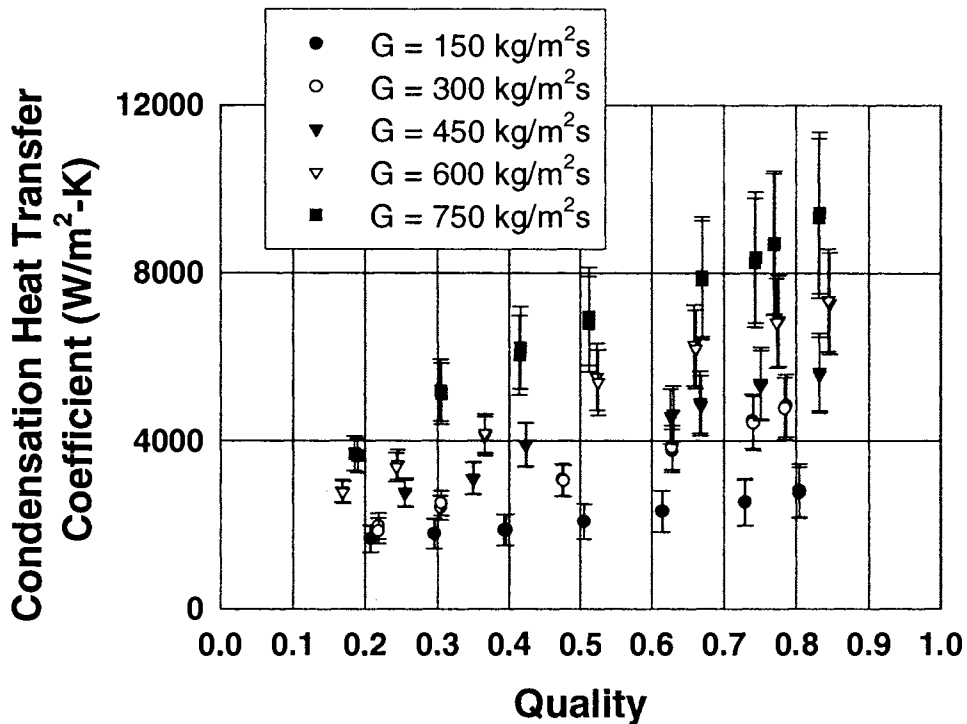


Figure 28. R-134a Condensation Heat Transfer Coefficient versus Quality for  $150 \text{ kg/m}^2\text{-s} < G < 750 \text{ kg/m}^2\text{-s}$  in Test Section C60

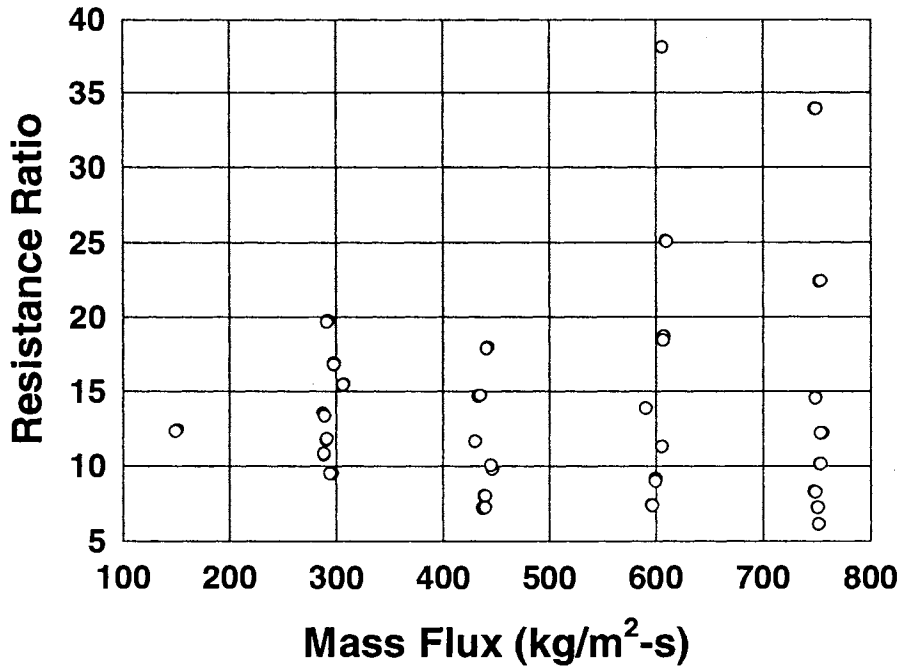


Figure 29. Refrigerant to Water Resistance Ratio for Test Section B32

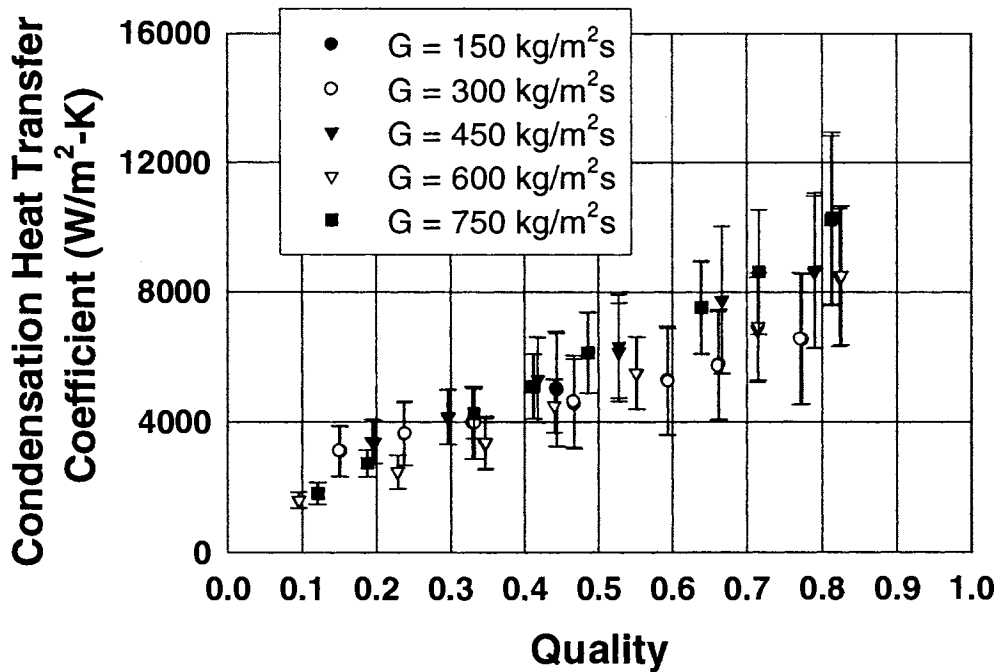


Figure 30. R-134a Condensation Heat Transfer Coefficient versus Quality for  $150 \text{ kg/m}^2\text{-s} < G < 750 \text{ kg/m}^2\text{-s}$  in Test Section B32

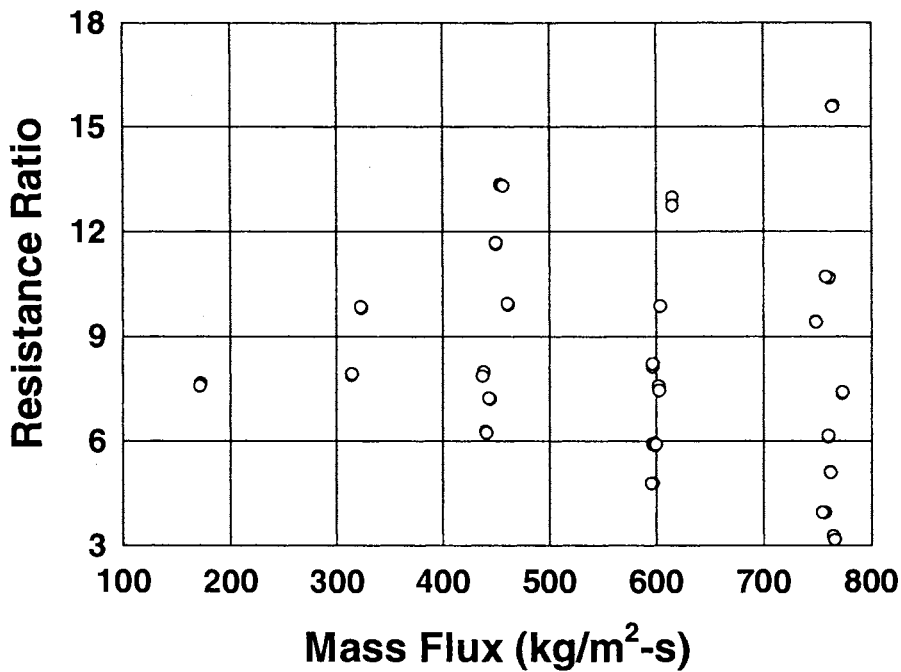


Figure 31. Refrigerant to Water Resistance Ratio for Test Section N21

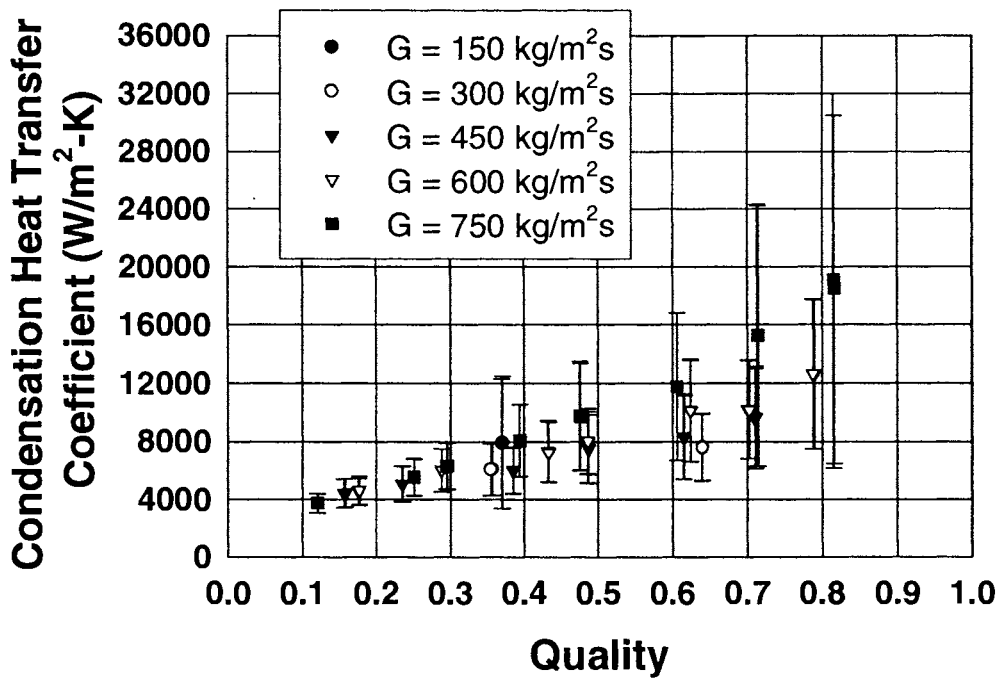


Figure 32. R-134a Condensation Heat Transfer Coefficient versus Quality for 150 kg/m<sup>2</sup>-s < G < 750 kg/m<sup>2</sup>-s in Test Section N21

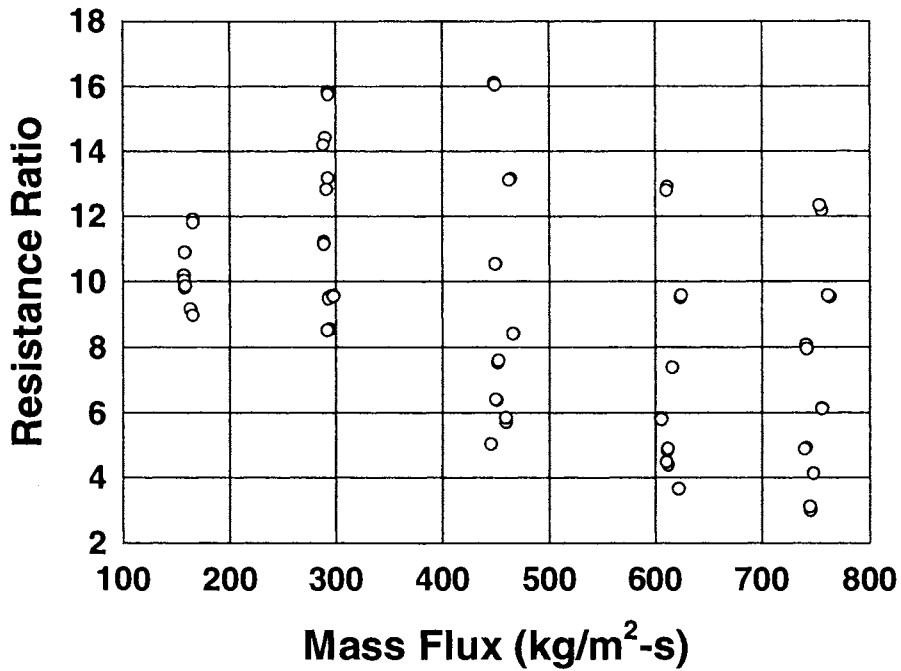


Figure 33. Refrigerant to Water Resistance Ratio for Test Section T33

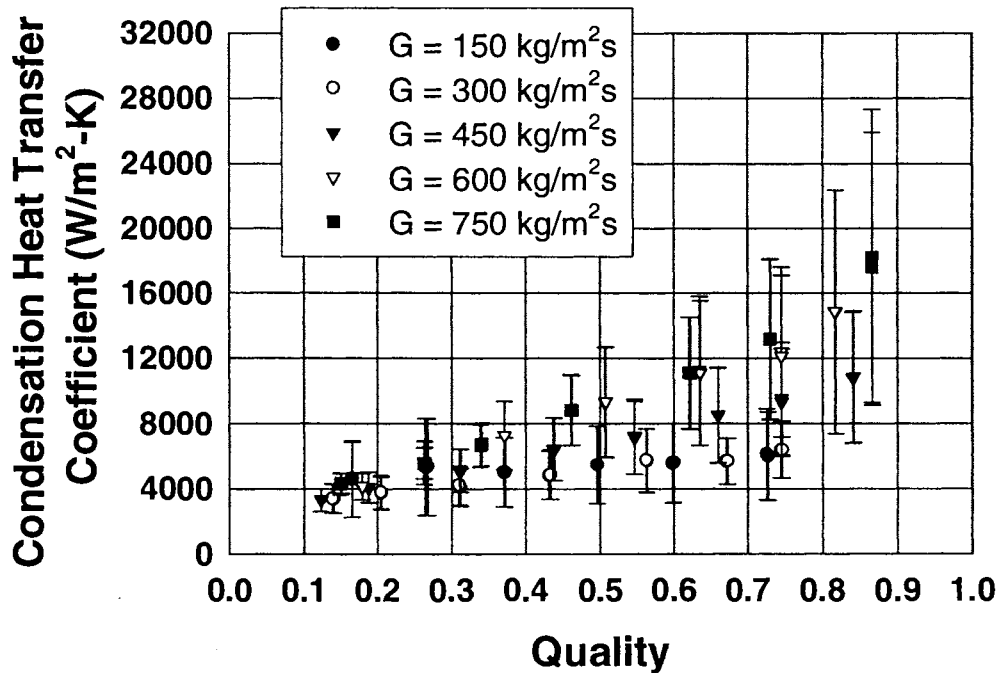


Figure 34. R-134a Condensation Heat Transfer Coefficient versus Quality for  $150 \text{ kg/m}^2\text{-s} < G < 750 \text{ kg/m}^2\text{-s}$  in Test Section T33

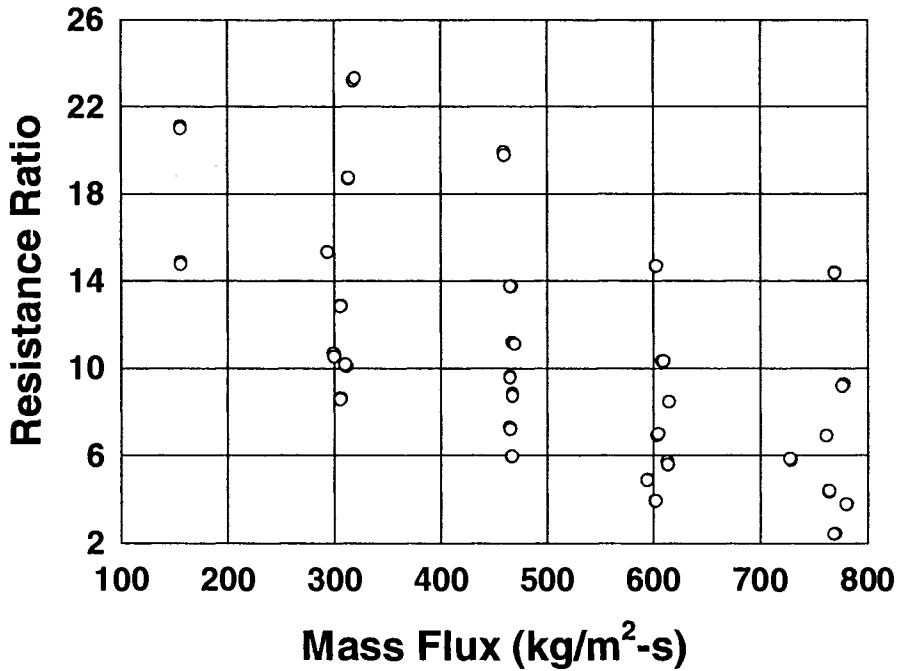


Figure 35. Refrigerant to Water Resistance Ratio for Test Section W29

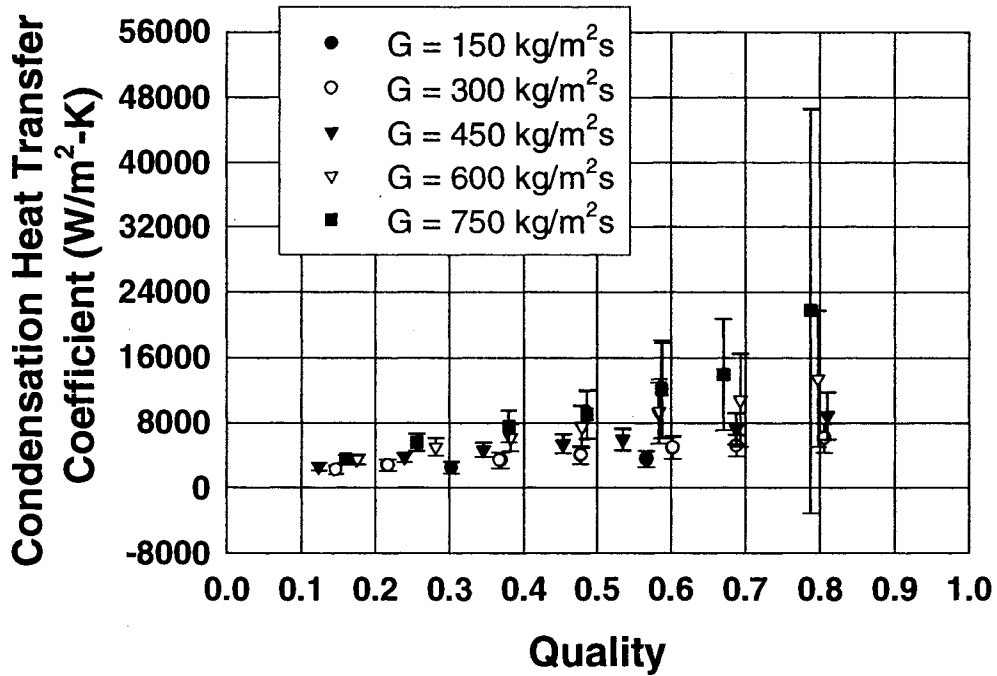


Figure 36. R-134a Condensation Heat Transfer Coefficient versus Quality for 150 kg/m<sup>2</sup>-s < G < 750 kg/m<sup>2</sup>-s in Test Section W29

## CHAPTER FIVE: DISCUSSION OF RESULTS

This chapter contains a discussion of the experimental results. The effects of hydraulic diameter and tube shape on the condensation heat transfer coefficients are presented first. Next, the data points are categorized according to the expected flow regime. Also, these results are compared with some of the literature on condensation heat transfer. Thereafter, flow regime based heat transfer correlations are developed for the microchannel tubes tested in these experiments.

### Effect of $D_h$ on Condensation Heat Transfer Coefficients

Test sections C20, C30, and C60 have circular microchannels with hydraulic diameters of 0.506 mm, 0.761 mm, and 1.524 mm, respectively. Figures 37-42 show the condensation heat transfer coefficients for test sections C20, C30, and C60 as a function of average vapor quality for each tested mass flux. For the nominal mass flux of  $150 \text{ kg/m}^2\text{-s}$  (Figure 37), no data were taken for test section C20, and one data point was taken for test section C30 due to the low required flow rates. Similarly, one and three data points were obtained for test section C20 at nominal mass fluxes of 300 and  $450 \text{ kg/m}^2\text{-s}$  (see Figures 38 and 39), respectively. For all other mass fluxes and test sections, larger data sets were collected. Figure 42 shows the mass flux and quality for all of the data points represented in Figures 37 through 42. This figure shows the variance of the mass flux within each nominal mass flux range. This shows that some of the variations in heat transfer coefficient presented in Figures 37-42 may be attributed to deviations from the nominal mass flux, rather than the hydraulic diameter.

In general, Figures 37-41 show that the heat transfer coefficient increases with decreasing diameter. For the nominal mass flux of  $150 \text{ kg/m}^2\text{-s}$  (Figure 37), the one data point for test section C30, with an average test section quality of 0.43, is about 20% higher than the trend for test section C60. However, it should be noted that the measured mass flux for this data point is about  $10 \text{ kg/m}^2\text{-s}$  higher than fluxes for test section C60, and the data point is not representative of local phenomena (this point has a quality change of 0.62 across the test section).

For the nominal mass flux of  $300 \text{ kg/m}^2\text{-s}$  (Figure 38), the condensation heat transfer coefficient increases with decreasing diameter for average qualities above 0.45. At qualities below 0.45, the heat transfer coefficients are very similar for both test sections C30 and C60. With an average quality of 0.45, the one data point for test section C20 (representing average

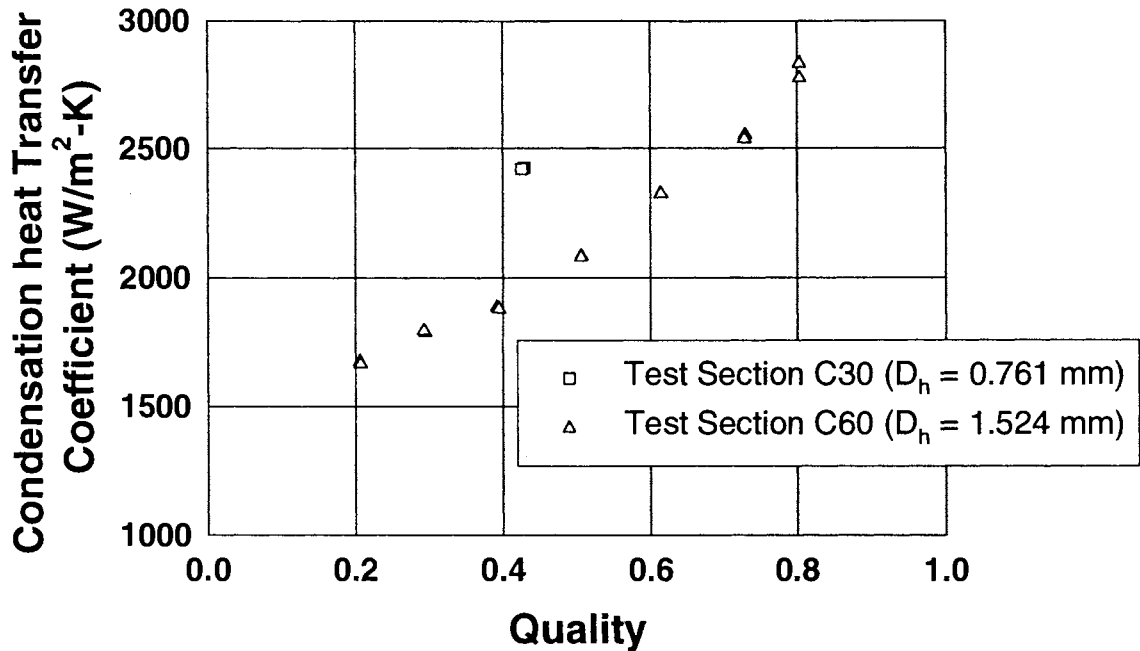


Figure 37. Comparison of Condensation Heat Transfer Coefficients for Test Sections C30 and C60 with  $G = 150 \text{ kg/m}^2\text{-s}$

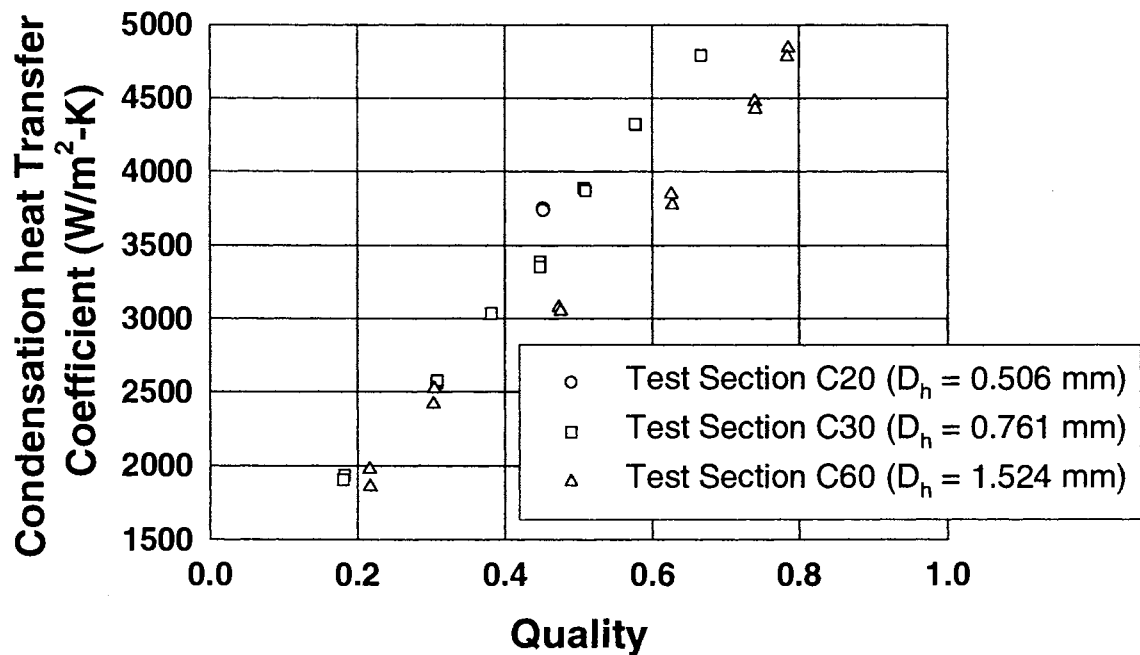


Figure 38. Comparison of Condensation Heat Transfer Coefficients for Test Sections C20, C30, and C60 with  $G = 300 \text{ kg/m}^2\text{-s}$

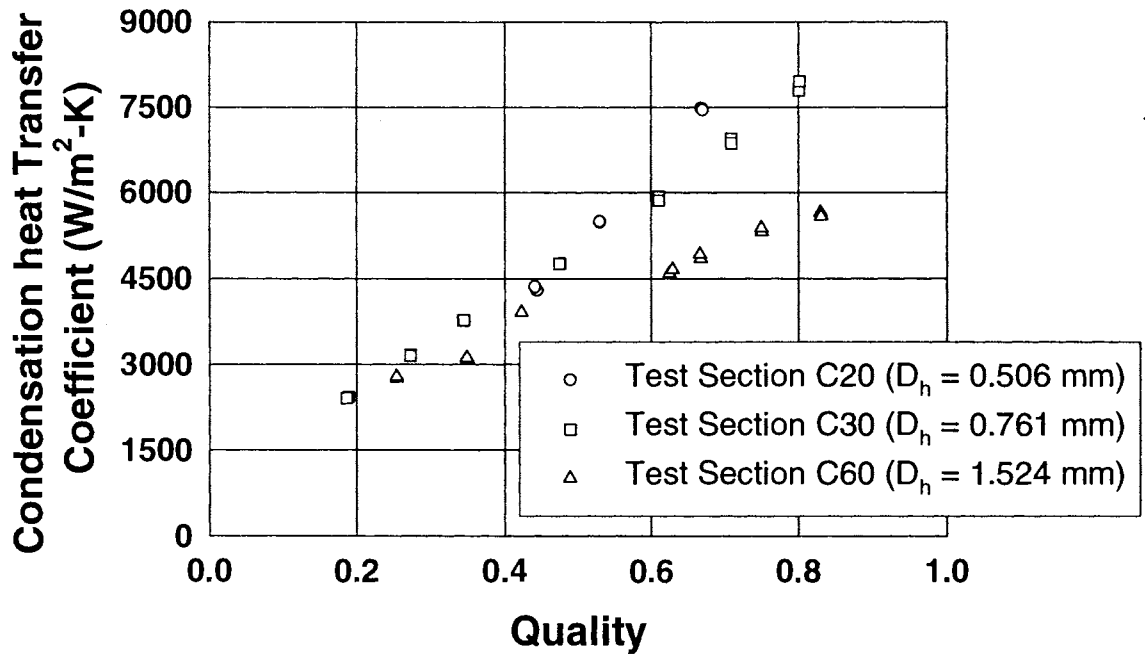


Figure 39. Comparison of Condensation Heat Transfer Coefficients for Test Sections C20, C30, and C60 with  $G = 450 \text{ kg/m}^2\text{-s}$

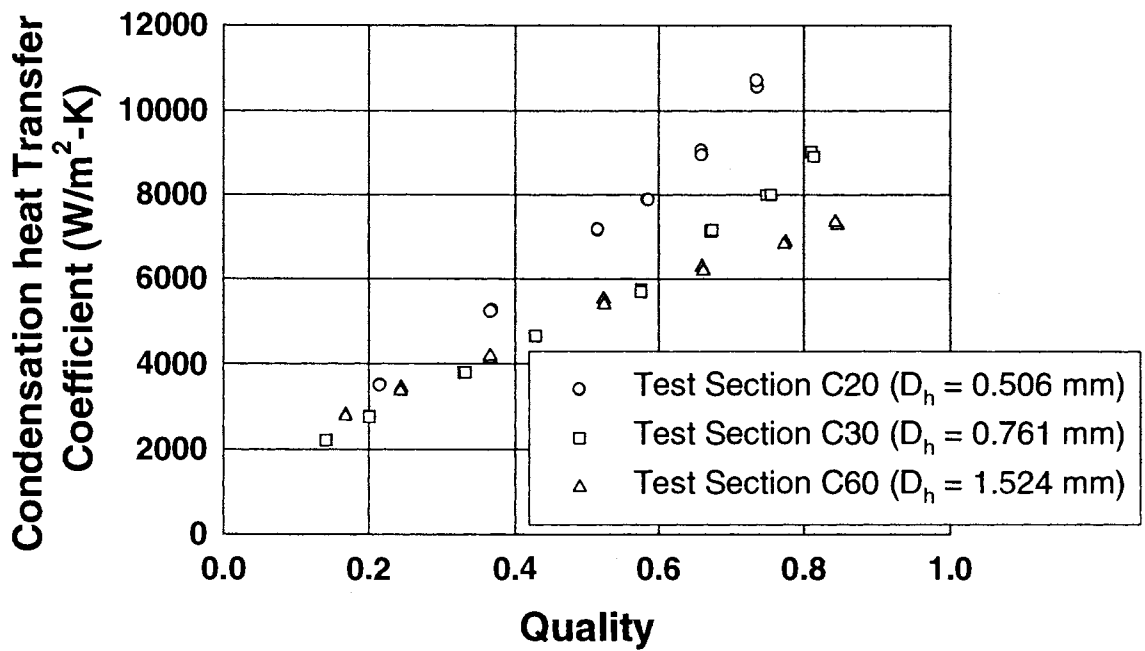


Figure 40. Comparison of Condensation Heat Transfer Coefficients for Test Sections C20, C30, and C60 with  $G = 600 \text{ kg/m}^2\text{-s}$

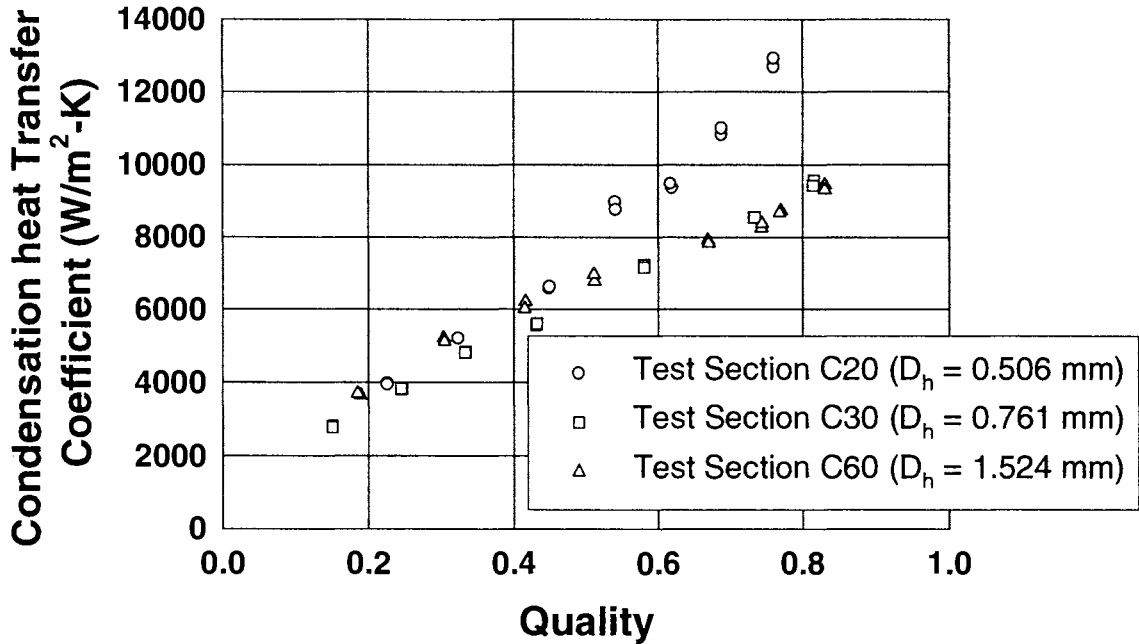


Figure 41. Comparison of Condensation Heat Transfer Coefficients for Test Sections C20, C30, and C60 with  $G = 750$   $kg/m^2-s$

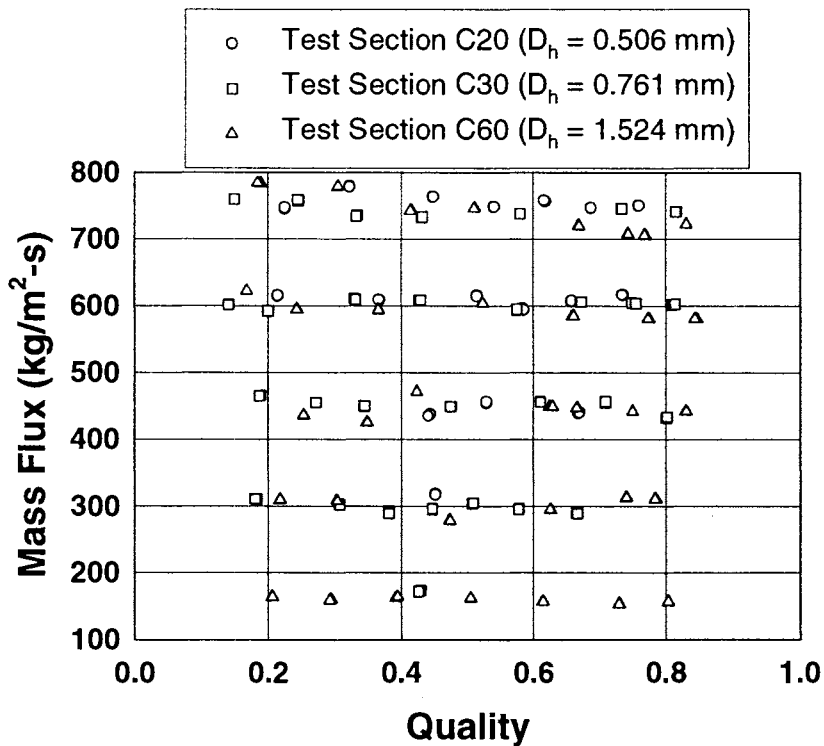


Figure 42. Mass Flux Variation for Test Sections C20, C30, and C60

as opposed to local phenomena due to the low flow rate) is about 10% higher than the data for test section C30. However, the mass flux for this point is about 20 kg/m<sup>2</sup>-s higher than the mass flux for the data taken on test section C30, potentially masking the effect of hydraulic diameter. The data for test section C30 are about 10% higher than the data for test section C60 for qualities above 0.45.

For the nominal mass flux of 450 kg/m<sup>2</sup>-s (Figure 39), the effect of hydraulic diameter becomes significant for qualities above about 0.45, with almost no effect seen below this quality. The heat transfer coefficients for test section C30 for qualities between 0.45 and 0.65 are about 20% higher than those for test section C60, while the heat transfer coefficients for test section C20 are between 10% and 15% higher than those for test section C30 within this same quality range. Above a quality of 0.65, the heat transfer coefficients for test section C30 are about 40% higher than those for test section C60. However, due to the low LMTDs for these points (caused by a very large overall UA), the uncertainties for the test section C30 data are around 35%. Similarly, the heat transfer coefficients for test section C20 are about 10% higher than those for test section C30, but are known only to within  $\pm 35\%$  for qualities above 0.65.

The condensation heat transfer coefficient also increases with decreasing diameter for the nominal mass flux of 600 kg/m<sup>2</sup>-s (Figure 40). The heat transfer coefficients for test section C30 are between 10% and 20% higher than those for test section C60 for qualities above 0.65, while test section C20 is between 25% and 40% higher than for test section C30 for qualities above 0.45. The heat transfer coefficients for test section C30 for qualities above 0.65 are known to within between  $\pm 20\%$  and  $\pm 30\%$ . The test section C30 data for this mass flux are more accurate than for the mass flux of 450 kg/m<sup>2</sup>-s because the test section heat duty can be larger for the same quality change, and this could allow for larger test section LMTDs if the increase in overall UA is lower than the heat duty increase. However, the C20 data for qualities > 0.45 are still known only to within  $\pm 35\%$  due to the low LMTDs for the small flow rate and high overall UAs.

The heat transfer coefficients for the nominal mass flux of 750 kg/m<sup>2</sup>-s (Figure 41) yields somewhat different results than for the other mass fluxes. Very little difference exists between the heat transfer coefficients for test sections C30 and C60 for all qualities. However, the heat transfer coefficients for test section C20 are between 20% and 40% higher than for the other two test sections for qualities > 0.5. The uncertainties in these heat transfer coefficients for test section C20 are 33% and 55% (increasing with quality and, therefore, overall UA), which may indicate that not all of this difference can be attributed to the effect of hydraulic diameter.

In summary, the heat transfer coefficient increases between 10% and 40% for qualities above 0.45 as the diameter is reduced from 1.524 mm to 0.761 mm to 0.506 mm. This effect is more prominent for a decrease in hydraulic diameter from 0.761 mm to 0.506 mm. The effect of hydraulic diameter may be explained on the basis of the flow regimes for the respective data points. For a given flow rate, for example, the quality at which the mist flow regime occurs will decrease with decreasing diameter due to increased interfacial shedding. As liquid entrainment increases, the heat transfer coefficient will increase due to the thinning of the liquid film Soliman (1986). The effect of flow regime will be discussed further in the section that discusses the assignment of flow regimes to the data points.

## **Effect of Tube-Shape on Condensation Heat Transfer**

### **Coefficients**

This section discusses the effects of tube-shape on the condensation heat transfer coefficient. The heat transfer coefficients for test sections B32, C30, S30, T33, and W29 were compared for the nominal mass flux range of 150 to 750 kg/m<sup>2</sup>-s. The circular tube (test section C30,  $D_h = 0.761$  mm) was used as the base tube for comparison with the barrel-shaped tube (test section B32,  $D_h = 0.769$  mm), square tube (test section S30,  $D_h = 0.762$  mm), triangle tube (test section T33,  $D_h = 0.839$  mm), and triangle-shaped insert tube (test section W29,  $D_h = 0.732$  mm). All these tubes have similar hydraulic diameters, with the primary difference being tube shape.

Figures 43 through 47 show the condensation heat transfer coefficients for test sections B32, C30, S30, T33, and W29 as a function of average vapor quality for each tested mass flux. For the nominal mass flux of 150 kg/m<sup>2</sup>-s (Figure 43), one data point each was taken for test sections B32 ( $A_t = 10.0$  mm<sup>2</sup>), C30 ( $A_t = 7.742$  mm<sup>2</sup>), and S30 ( $A_t = 9.871$  mm<sup>2</sup>). Test section W29 has a larger free-flow area (12.277 mm<sup>2</sup>) than these test sections, but still only two data points were taken at this mass flux. Test section T33 has the highest free-flow area (13.419 mm<sup>2</sup>); therefore, six data points were taken for  $G = 150$  kg/m<sup>2</sup>-s. For all other mass fluxes, the flow rates were high enough to maintain reasonable energy balances. Hence, data were taken for a wide range of average test section qualities for the nominal mass fluxes of 300 kg/m<sup>2</sup>-s, 450 kg/m<sup>2</sup>-s, 600 kg/m<sup>2</sup>-s, and 750 kg/m<sup>2</sup>-s.

Test section B32 has higher heat transfer coefficients than test section C30, but this effect diminishes as the mass flux decreases. At a nominal mass flux of 150 kg/m<sup>2</sup>-s, the heat transfer coefficient for the one data point for test section B32 is about twice as high as the one data point for test section C30. However, the uncertainty in this point for test section

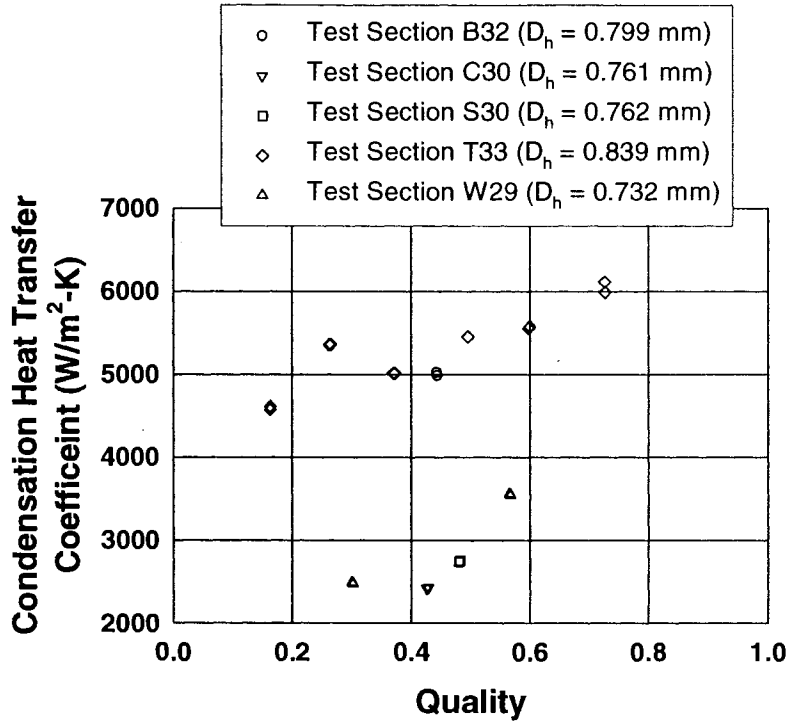


Figure 43. Comparison of Condensation Heat Transfer Coefficients for Test Sections B32, C30, S30, T33, and W29 with  $G = 150 \text{ kg/m}^2\text{-s}$

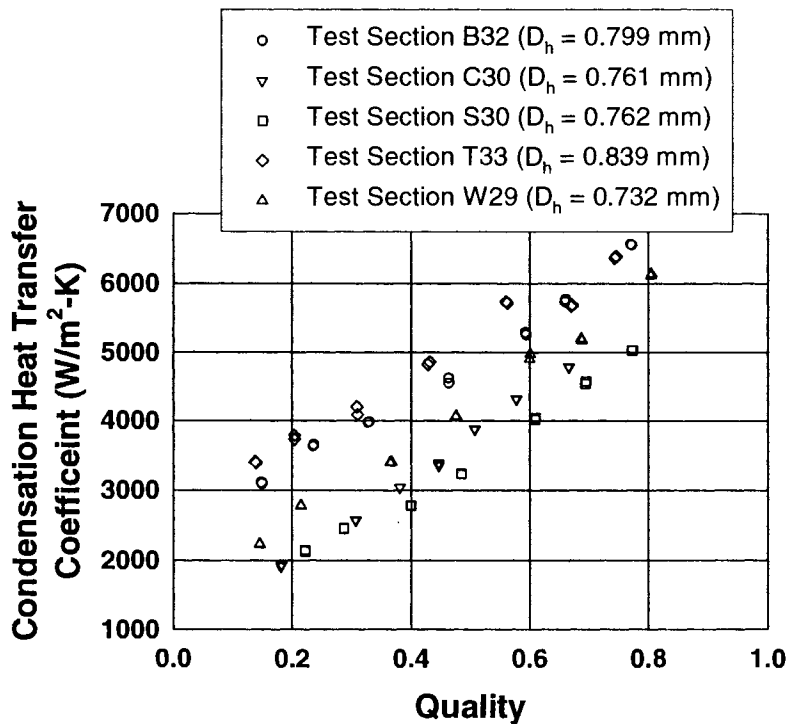


Figure 44. Comparison of Condensation Heat Transfer Coefficients for Test Sections B32, C30, S30, T33, and W29 with  $G = 300 \text{ kg/m}^2\text{-s}$

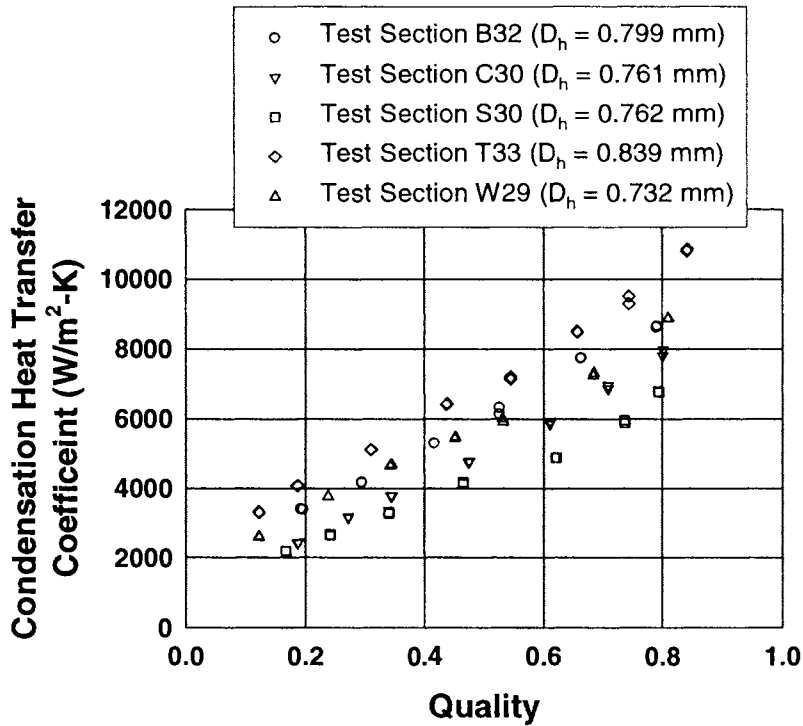


Figure 45. Comparison of Condensation Heat Transfer Coefficients for Test Sections B32, C30, S30, T33, and W29 with  $G = 450 \text{ kg/m}^2\text{-s}$

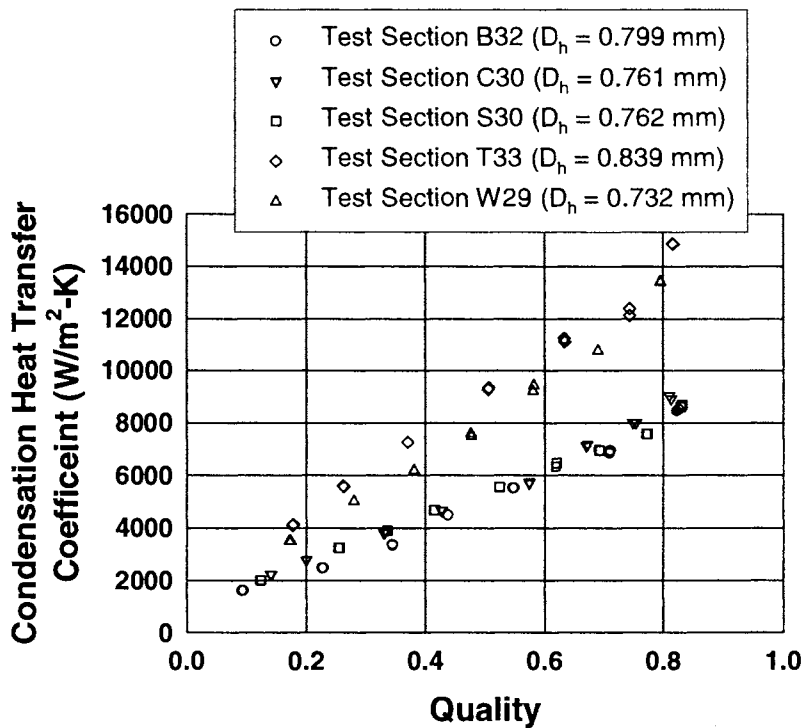
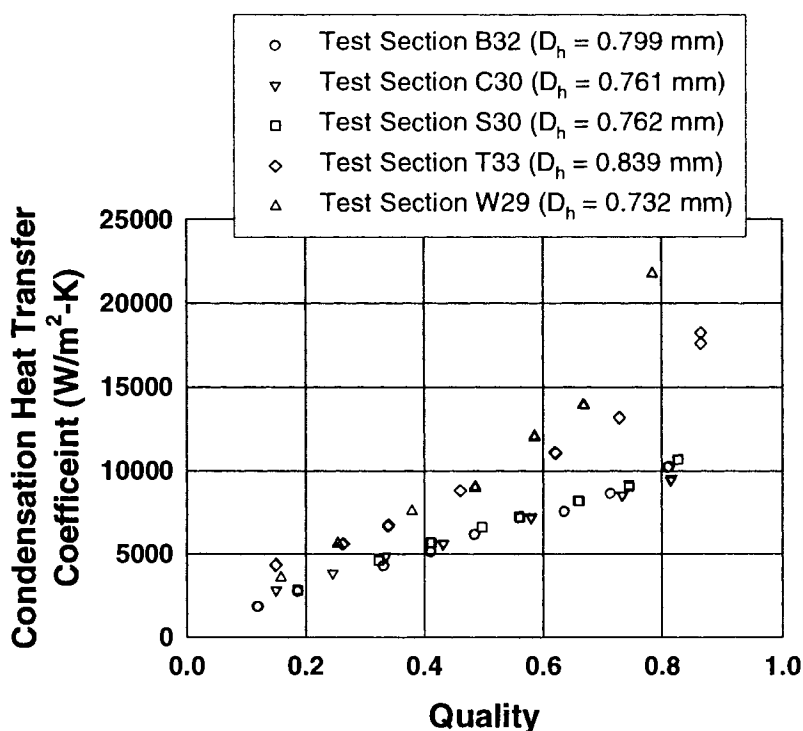


Figure 46. Comparison of Condensation Heat Transfer Coefficients for Test Sections B32, C30, S30, T33, and W29 with  $G = 600 \text{ kg/m}^2\text{-s}$



**Figure 47. Comparison of Condensation Heat Transfer Coefficients for Test Sections B32, C30, S30, T33, and W29 with  $G = 750$  kg/m<sup>2</sup>-s**

B32 is 35%, which may exaggerate this difference. At a nominal mass flux of 300 kg/m<sup>2</sup>-s, the heat transfer coefficients are higher for test section B32 than for test section C30, but the difference is smaller. The data for test section B32 are about 60% higher at a vapor quality of 0.18 and 20% higher at a quality of 0.67, with the percentage increase decreasing as the quality increases for this range. The results are similar for the nominal mass flux of 450 kg/m<sup>2</sup>-s, except that the test section B32 data are 40% higher at a quality of 0.19 and 10% higher at a quality of 0.8. However, the uncertainties for both test sections are between 19% and 34% (increasing with quality), which may affect the difference. As the mass flux is increased to 600 and 750 kg/m<sup>2</sup>-s, the heat transfer coefficients for both test section B32 and C30 are very similar throughout the entire range of vapor qualities. These effects could be explained by looking at the trends in test section B32 data. As explained in Chapter 4, the data obtained for this test section seemed to be inconsistent with expected mass flux trend. The data for  $G = 450$  kg/m<sup>2</sup>-s were higher than the data for  $G = 750$  kg/m<sup>2</sup>-s for qualities below 0.45 and all of the  $G = 600$  kg/m<sup>2</sup>-s data. This should not be the case. Therefore, the data for test section B32 are presumed to be in error; either the low mass flux data are incorrect or the high mass flux data are incorrect.

The heat transfer coefficients for test section S30 and C30 are very similar for all mass fluxes. For the nominal mass flux of 150 kg/m<sup>2</sup>-s, the available data points for test

sections S30 ( $x = 0.48$ ) and C30 ( $x = 0.43$ ) cannot be accurately compared due to the difference in quality, but they do not seem to be quantitatively different at equivalent qualities. At nominal mass fluxes of 300 and 450  $\text{kg/m}^2\text{-s}$ , the heat transfer coefficients for test section S30 are about 10% below the data for test section C30. However, the heat transfer coefficients for both test section are known to within  $\pm 15\%$  to  $\pm 34\%$  (increasing with quality), which implies that this difference is not significant. The nominal mass fluxes of 600 and 750  $\text{kg/m}^2\text{-s}$  show virtually no difference between the heat transfer coefficients of test section S30 and C30. The hydraulic diameters for these two test sections are almost the same, so the difference between condensation heat transfer coefficients in square and circular ports may be minimal.

Test sections T33 and W29 exhibit substantially higher condensation heat transfer coefficients than those for test section C30 (and B32 and S30). For a nominal mass flux of 150  $\text{kg/m}^2\text{-s}$ , the heat transfer coefficients for test section T33 are about twice those for test section C30. However, it should be noted that uncertainties associated with the data for test section T33 are rather high ( $\pm 40\%$ ) due to the low flow rates. At a nominal mass flux of 300  $\text{kg/m}^2\text{-s}$ , the heat transfer coefficients for test section T33 are between 70% higher at a quality of 0.3 and 18% higher at a quality of 0.67 than for test section C30. The percent increase decreases almost linearly within this quality range. At a nominal mass flux of 450  $\text{kg/m}^2\text{-s}$ , the heat transfer coefficients for test sections T33 are between 35% and 70% higher than for test section C30. The percentage increase decreases sharply from 70% to 35% as the quality is increased from 0.18 to 0.35, with the percentage increase being relatively constant at 35% at qualities above 0.35. However, for qualities above 0.35, both test section T33 and C30 have uncertainties ranging from 33% to 37%. For a nominal mass flux of 600  $\text{kg/m}^2\text{-s}$ , the heat transfer coefficients for test section T33 are known to within  $\pm 35\%$  to  $\pm 50\%$ , with the uncertainties increasing with quality, particularly for qualities above 0.5 due to the low LMTDs ( $\sim 1.6$  K). The trends in the heat transfer coefficients for test section T33 for the nominal mass flux range of 750  $\text{kg/m}^2\text{-s}$  are very similar to those described for the mass flux of 600  $\text{kg/m}^2\text{-s}$ .

For a nominal mass flux of 150  $\text{kg/m}^2\text{-s}$ , the data for test section W29 are about 10% to 15% higher than the data for test section C30, but the test section W29 data are known to within  $\pm 30\%$ . For a nominal mass flux of 300  $\text{kg/m}^2\text{-s}$ , the heat transfer coefficients for test section W29 are between 8% and 20% higher than for test section C30. However, the uncertainties for all the data points of test sections W29 and C30 are within  $\pm 22\%$  to  $\pm 31\%$ , which implies that the effect of tube shape may not be significant at this mass flux. For the nominal mass flux of 450  $\text{kg/m}^2\text{-s}$ , the heat transfer coefficients for test section W29 are

between 10% and 20% higher than those for test section C30. Again, these heat transfer coefficients for both test sections are known only to within  $\pm 16\%$  to  $\pm 35\%$ . At the nominal mass flux of  $600 \text{ kg/m}^2\text{-s}$ , the heat transfer coefficients for test section W29 are 25% higher at a quality of 0.2 than for test section C30, while for  $x > 0.2$ , the heat transfer coefficients are 50% to 60% higher. However, the data for test section W29 are known to within  $\pm 33\%$  to  $\pm 62\%$ , with the uncertainties increasing with quality. The reason for the large uncertainties is the small LMTDs ( $\sim 1.8 \text{ K}$ ) at this flow rate, especially as the quality is increased. For the nominal mass flux of  $750 \text{ kg/m}^2\text{-s}$ , the heat transfer coefficients for test section W29 are 25% higher at a quality of 0.15 than those for test section C30, and as much as 130% higher at a quality of 0.82. However, the data for test section W29 for  $x > 0.5$  have extremely high uncertainties, as much as  $\pm 114\%$  for the quality of 0.82, due to the low LMTDs ( $\sim 1.8 \text{ K}$ ).

Overall, test sections T33 and W29 seem to have the highest heat transfer coefficients, with the effect of tube shape not being very significant for the other test sections. However, the large pressure drops in these two test sections (as high as 210 kPa for test section W29) led to steep drops in the refrigerant saturation temperatures across the test section. This invariably lowers the LMTD, and in turn decreases the accuracy of the calculated UA values.

## Assignment of Flow Regimes to the Data

To compare the experimental data for test sections C20, C30, and C60 with existing heat transfer correlations, the data were categorized based on the applicable flow regimes. Coleman (2000) provided transition criteria for assigning flow patterns to the data based on the mass flux, quality, and geometry. He presented flow visualization results for air/water mixtures for four round tubes and one rectangular tube ( $\alpha = 0.725$ ) with hydraulic diameters ranging from 1.3 mm to 5.5 mm. Coleman (2000) also presented adiabatic and condensation flow visualization experiments for R-134a flow inside one circular tube and ten rectangular tubes with hydraulic diameters and aspect ratios ranging from 1 mm to 4.91 mm and 0.5 to 1, respectively. R-134a pressure drop experiments were also conducted on the same test facility as the facility described for the heat transfer tests in this study (including the same test sections) for adiabatic and condensing flows.

For the R-134a tests, Coleman (2000) observed four separate flow regimes: annular, wave, dispersed, and intermittent. Each flow regime was further subdivided into flow patterns. During the refrigerant condensation tests, the stratified flow regime (without a circumferential annular film) was not observed.

According to Coleman (2000), the annular flow regime is characterized by the separation of the liquid and gas phases. In this regime, a liquid film coats the circumference of the wall, and the vapor flows through the core with or without liquid droplet entrainment. The flow patterns within the annular flow regime include mist, annular ring, wave ring, wave packet, and annular film patterns. The mist flow pattern is the only flow pattern without a clearly discernable film and is characterized by a uniform vapor mist with liquid droplets entrained in the vapor. This could be considered a homogenous flow pattern. The annular ring pattern occurs when annular “rings” of liquid appear periodically in the flow, while the wave ring pattern occurs when these rings appear noticeably thicker on the bottom than on the top. The wave packet pattern occurs when a collection of waves, which do not reach the top of the tube, appear periodically in the flow, and the effect of gravity has increased in this flow pattern. The annular film pattern with typically a wavy liquid film exists for intermediate mass fluxes and qualities.

In the wavy flow regime, the liquid flows primarily on the bottom of the tube while the vapor flows above the liquid with liquid waves at the interface. A thin liquid film exists around the vapor at the top of the tube, similar to annular flow. As the gas velocity increases, the interface becomes more Kelvin-Helmholtz unstable and the intensity of the waves increases until the dispersed wave flow pattern, which was characterized by a large number of secondary waves with no dominant wavelength or amplitude, is achieved.

The dispersed flow regime exists when the liquid phase is turbulent and the vapor phase is either laminar or turbulent. When the vapor is laminar, small vapor bubbles form and congregate at the top of the tube; this flow pattern is characterized as bubble flow. As the vapor becomes turbulent, the bubbles disperse across the entire tube, thus becoming the dispersed bubble pattern.

The intermittent flow regime is characterized by discontinuities in the liquid and vapor phases, where a continuous stream of intermittent vapor “plugs” or “slugs” surrounded by a liquid film is interrupted by slugs of liquid. The slug flow pattern occurs when the front of the vapor is rounded, while the rear could be vertical, inclined, or have elongated vapor trails. The liquid slugs also have vapor entrainment, and the vapor slugs could be accompanied by large discrete waves. The plug flow pattern is similar to the slug flow pattern, except that there are no elongated trails and the vapor plugs are fairly uniform. The liquid surrounding the vapor slugs could be either stratified or non-stratified.

Coleman (2000) investigated the effect of hydraulic diameter on the intermittent, annular, and wavy flow regimes by comparing the experimental data for condensing R-134a inside the 4 x 4 mm, 3 x 3 mm, 2 x 2 mm, and 1 x 1 mm tubes. Figure 48 shows the

transition from intermittent flow for the four rectangular tubes. Representing the transition lines on the mass flux versus quality graph facilitates the assignment of flow regimes to the data. The intermittent flow regime expanded as the hydraulic diameter decreased due to the increased influence of surface tension. The annular film and mist flow patterns within the annular flow regime were treated as separate flow patterns in Coleman's (2000) work. The upper and lower annular film flow pattern transitions for three of the four rectangular tubes are shown in Figure 49. Coleman (2000) did not observe this flow pattern for the 4 x 4 mm tube, while the 3 x 3 mm tube exhibited only a very small annular film region. However, the annular film flow pattern range increased dramatically as the diameter decreased. The lower limits of the mist flow pattern for the four square tubes are shown in Figure 50. The mist flow pattern increased in size as the tube diameter decreased. In the case of the 1 x 1 mm tube, the mist flow pattern encompassed nearly 40% of the data collected by Coleman (2000). As seen in Figure 51, the size of the wavy flow pattern decreased as the hydraulic diameter decreased, with the 1 x 1 mm tube exhibiting no wavy flow at all. It should be

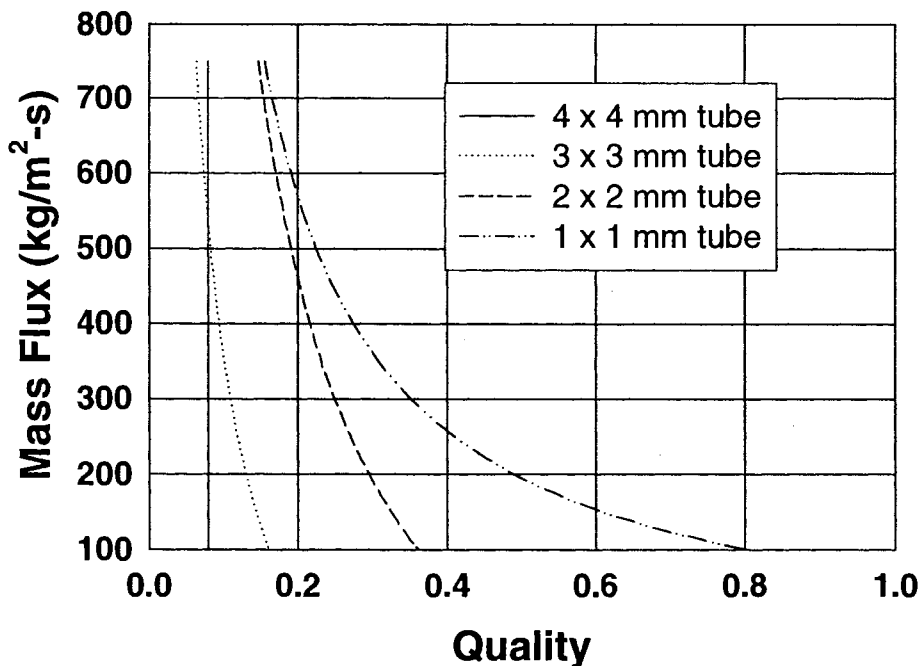


Figure 48. Intermittent Flow Regime Transition (Upper Limit) for the Square Tubes from Coleman (2000)

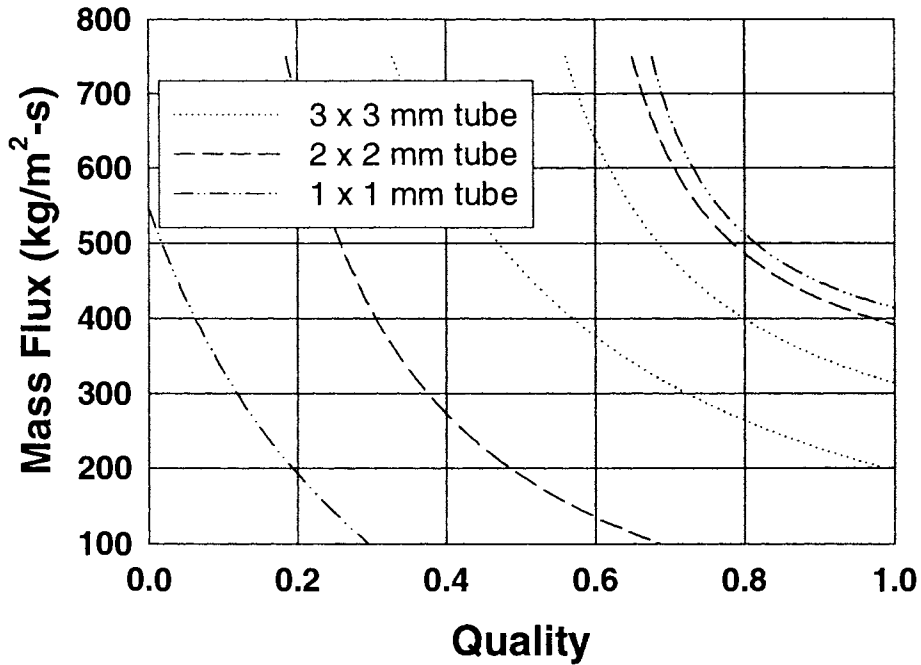


Figure 49. Annular Film Flow Pattern Transitions (Upper and Lower Limits) for the Square Tubes from Coleman (2000)

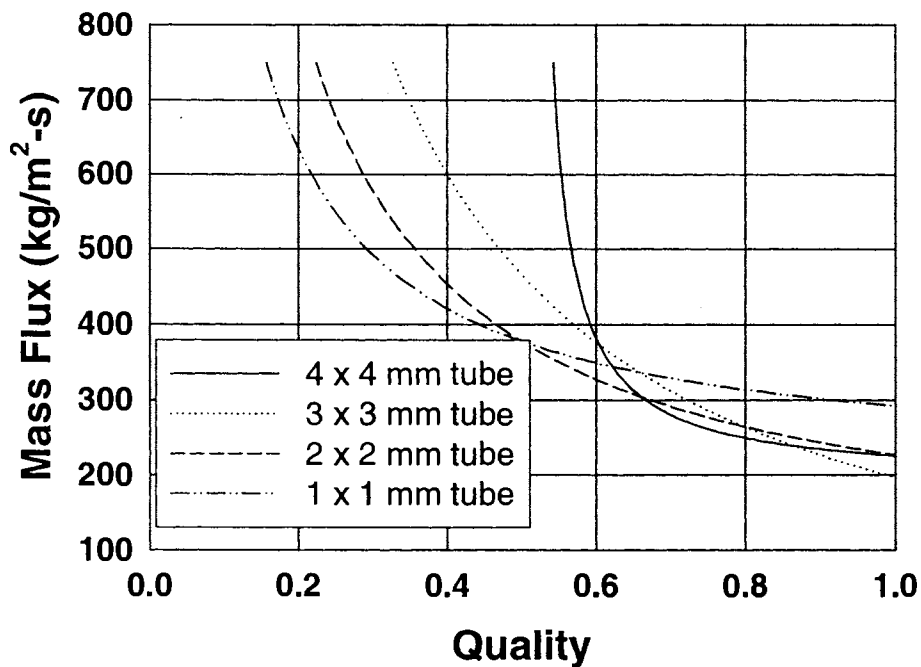
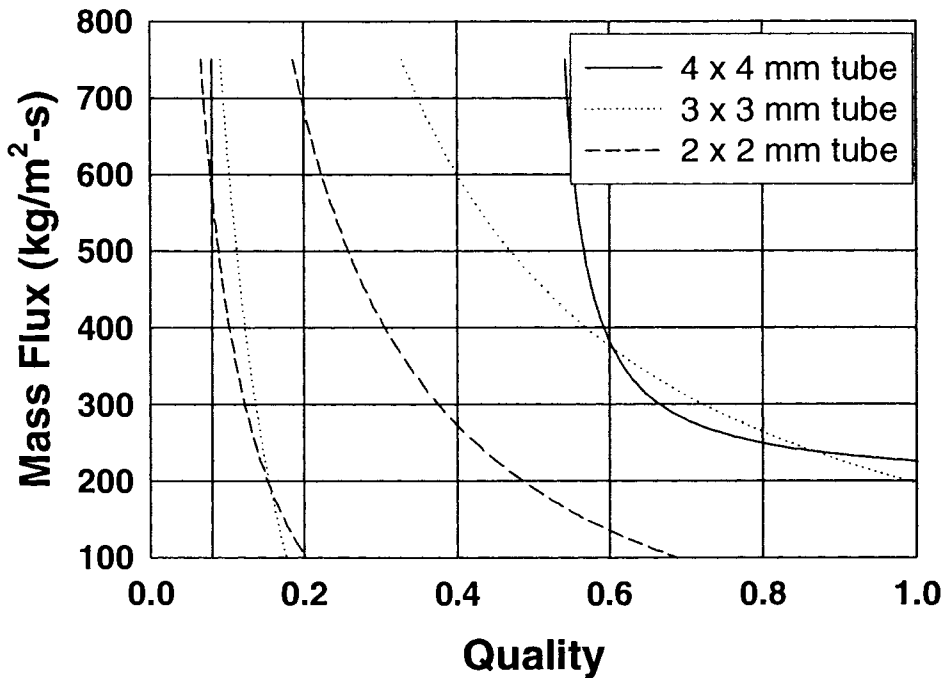


Figure 50. Mist Flow Pattern Transition (Lower Limit) for the Square Tubes from Coleman (2000)



**Figure 51. Wavy Flow Regime Transitions (Upper and Lower Limits) for the Square Tubes from Coleman (2000)**

noted that the intermittent regime and the annular film and mist flow patterns existed simultaneously in some cases, especially for the smaller diameters, which are transition flows.

Figures 48-50 were used as a guide to estimate the corresponding transition lines for test sections C20, C30, and C60. It should be noted that the transition criteria developed by Coleman (2000) were for square tubes, whereas the tubes under consideration here are circular tubes. However, in the absence of relevant information from the literature, it was assumed that Coleman's criteria for tubes with similar hydraulic diameters may be used for these circular tubes. Since wavy flow did not exist for the 1 x 1 mm tube ( $D_h = 1$  mm), it is assumed that wavy flow will not exist for either test section C20 ( $D_h = 0.506$  mm) or C30 ( $D_h = 0.761$  mm). Also, it is assumed that test section C60 ( $D_h = 1.524$  mm) will have an insignificant wavy flow region; therefore, the wavy flow regime is neglected.

Coleman's transition criteria for individual tubes were used to develop curve-fits for the circular tubes under consideration that accounted for the effect of hydraulic diameter. For example, the intermittent flow transition was represented as follows:

$$G \leq a + b/x \quad (119)$$

where:

$$a = 16.67 - 137.5 \cdot D_h \quad (120)$$

$$b = 190 - 35 \cdot D_h \quad (121)$$

The hydraulic diameters for equations 120 and 121 are in mm. For test section C60, constants  $a$  and  $b$  are  $-192.9$  and  $136.7$ , respectively. Similar equations for the other transition lines were also developed and are provided in Appendix B.

Figure 52 shows the upper limit of the intermittent flow regime for test sections C20, C30, and C60, as well as the experimental transitions developed by Coleman (2000) for the  $1 \times 1$  mm and  $2 \times 2$  mm square tubes. This figure shows a dramatic increase in the intermittent flow pattern as the hydraulic diameter decreases. In fact, for test section C20, nearly all of the data points for a mass flux of  $150 \text{ kg/m}^2\text{-s}$  are in the intermittent flow regime. The transitions for annular film and mist flows are found similarly, with the results presented graphically in Figures 53 and 54. Annular film flow encompasses almost the entire range of experimental data point gathered for this study, especially when the diameter is decreased.

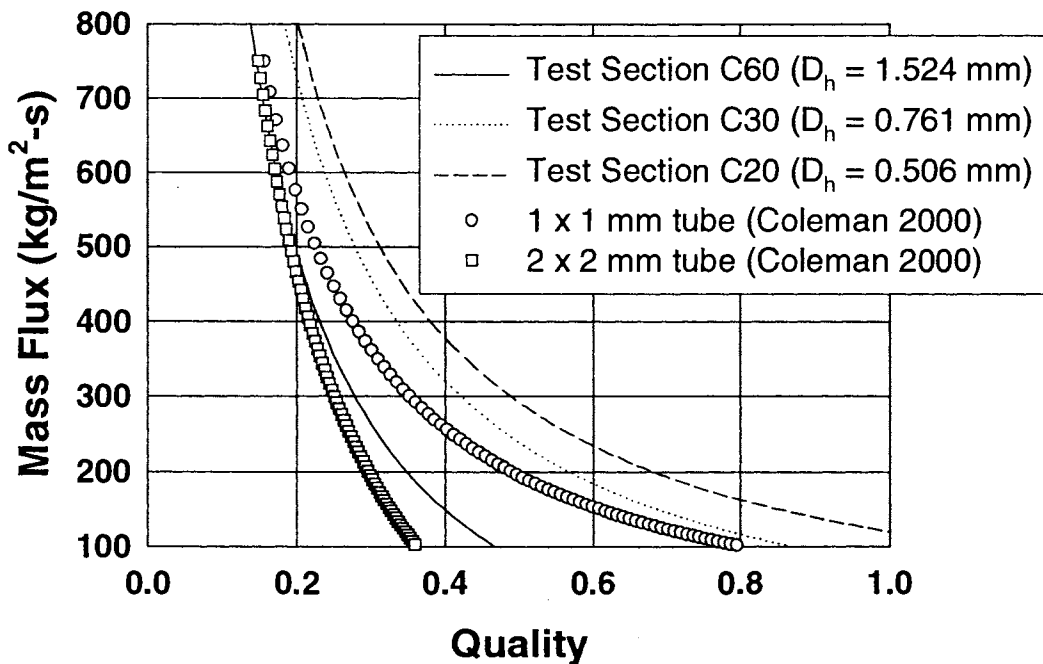


Figure 52. Intermittent Flow Regime Transition (Upper Limit) for Test Sections C20, C30, and C60 Based on Coleman (2000)

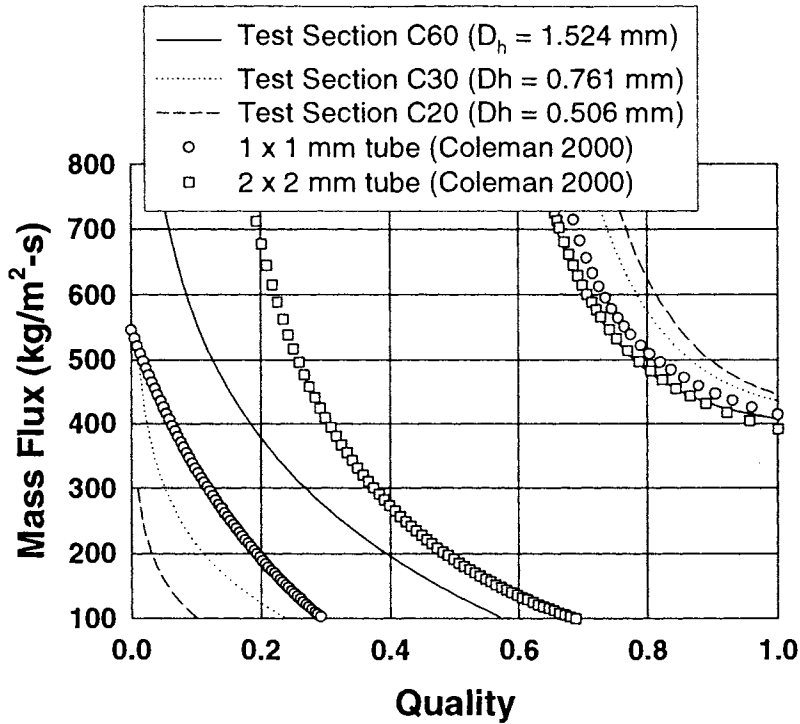


Figure 53. Annular Film Flow Pattern Transitions (Upper and Lower Limits) for Test Sections C20, C30, and C60 Based on Coleman (2000)

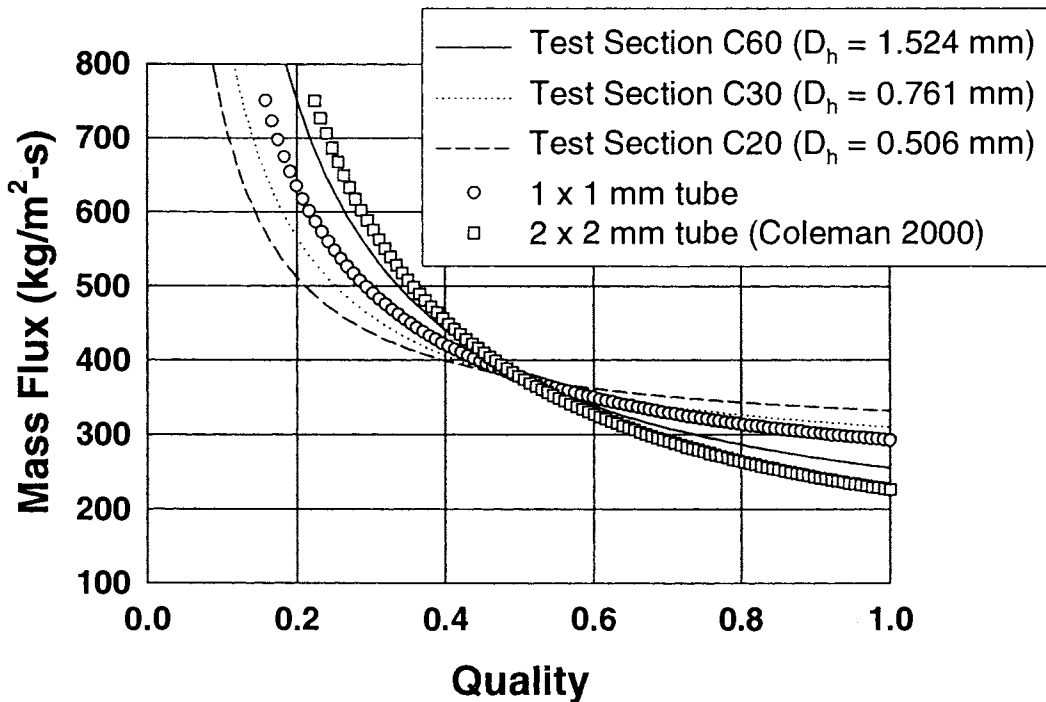


Figure 54. Mist Flow Regime Transition (Lower Limit) for Test Sections C20, C30, and C60 Based on Coleman (2000)

The mist flow pattern covers a large portion of the experimental data, especially for high qualities and mass fluxes. As seen in Figures 52-54, there is a considerable overlap of flow patterns for these microchannel test sections. This could mean that the flow is transitioning between the respective flow regimes in the overlap regions during the condensation process (Coleman, 2000).

Figures 55 through 57 show the experimental data with the transition lines for test sections C20, C30, and C60. Similar flow regime maps for the non-circular microchannel tubes are in Appendix C. During the condensation process, the flow changes from mist flow (where applicable) to annular film flow to intermittent, with large overlaps in the types of flow resulting in transition flow. The three types of transitioning flow seen in the data include: intermittent/annular, intermittent/annular/mist, and annular/mist. For all three circular tubes, only a small portion of the data exhibit only one kind of flow pattern (3.65% of the total data sets in intermittent, 19.5% in annular, and 12.2% in mist). Similarly, a small portion of the data is in transition regions adjacent to intermittent flow (11% in intermittent/annular and 3.65% in intermittent/annular/mist). However, 50% of the data are in annular/mist transition flow.

The flow regime designation presented here for the circular microchannel test sections is used as the basis for comparison of the measured heat transfer coefficients with the information available in the literature. It is also used to develop flow regime based models.

## **Comparison with Existing Correlations**

This section presents a comparison of the data from the present study with the existing literature. As stated above, the experimental data points for the circular microchannel test sections were either intermittent, annular film, or a combination thereof. Within the annular flow regime, the data were in both the mist and annular film flow patterns. To facilitate a comparison of the measured heat transfer coefficients with the literature, data in the intermittent flow regime (including data that had overlapping intermittent and annular regimes) were referred to as intermittent regime data. The remaining points were considered to be annular regime data. The intermittent data includes 18.3% of the circular microchannel tube data, while annular data are the remaining 81.7%. The gravity-driven correlations of Chato (1962), Jaster and Kosky (1976), and Rosson and Myers (1965), as well as the horizontal intermittent model of Tien et al. (1988), were compared with the intermittent data set. The annular flow data were compared with the shear-driven correlations of Soliman et al. (1968), Traviss et al. (1973), Cavallini and

Zecchin (1974), Shah (1979), Chen et al. (1987), and Moser et al. (1998), and the homogenous correlations of Boyko and Kruzhilin (1967) and Soliman (1986). Finally, all of

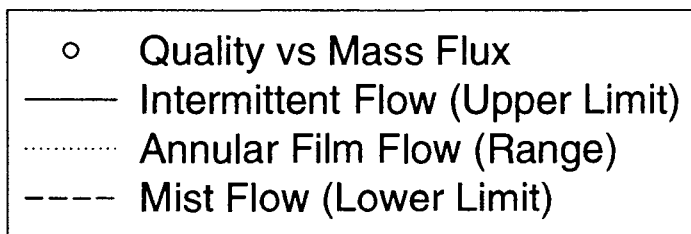
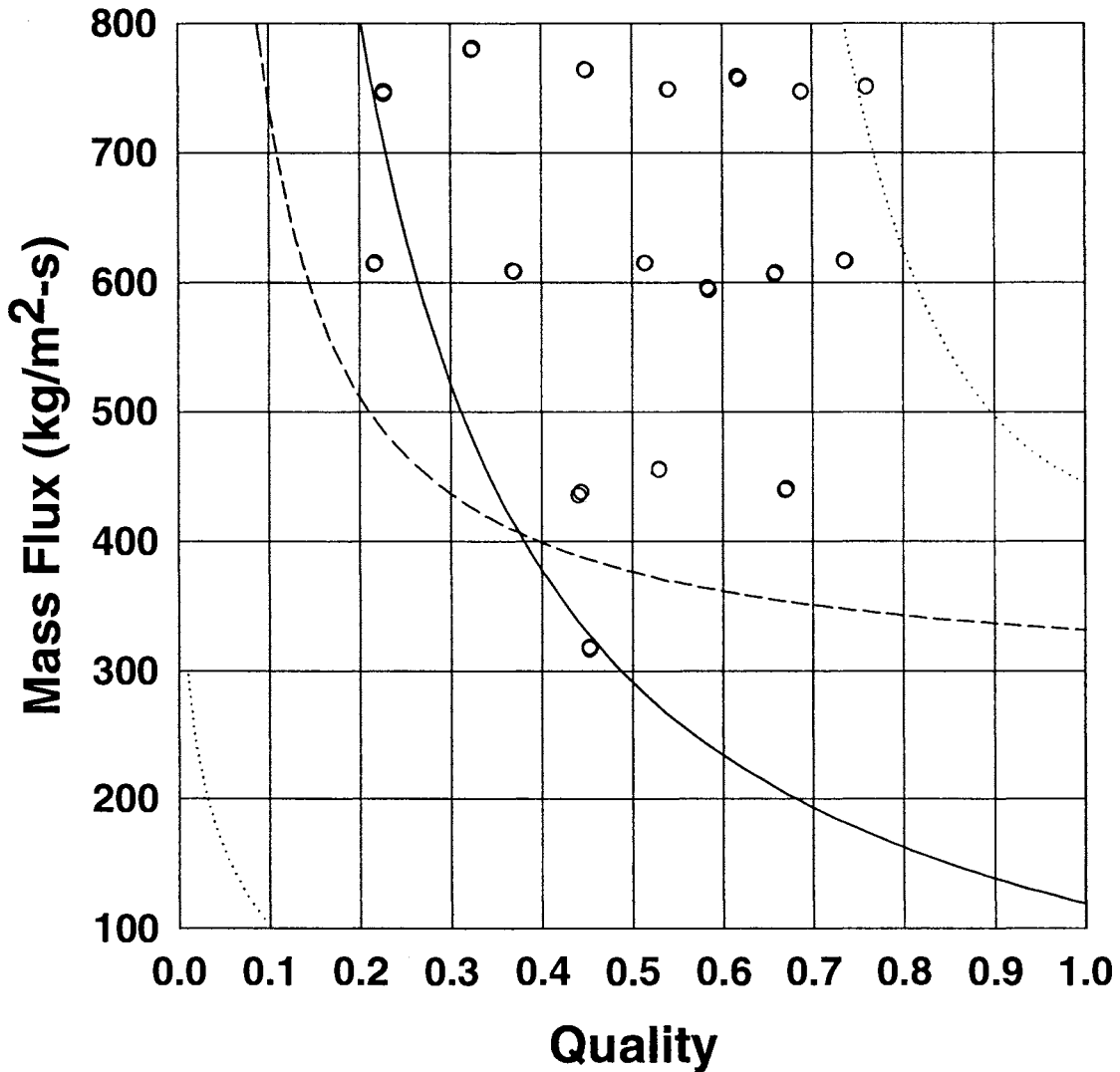


Figure 55. Experimental Data for Test Section C20 with Superimposed Transition Lines

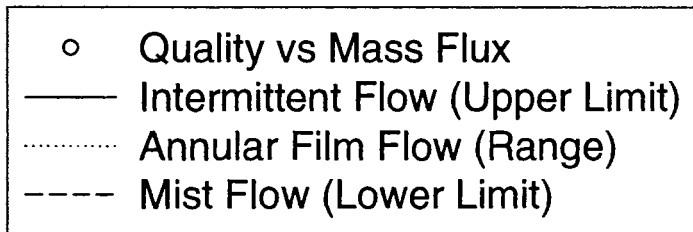
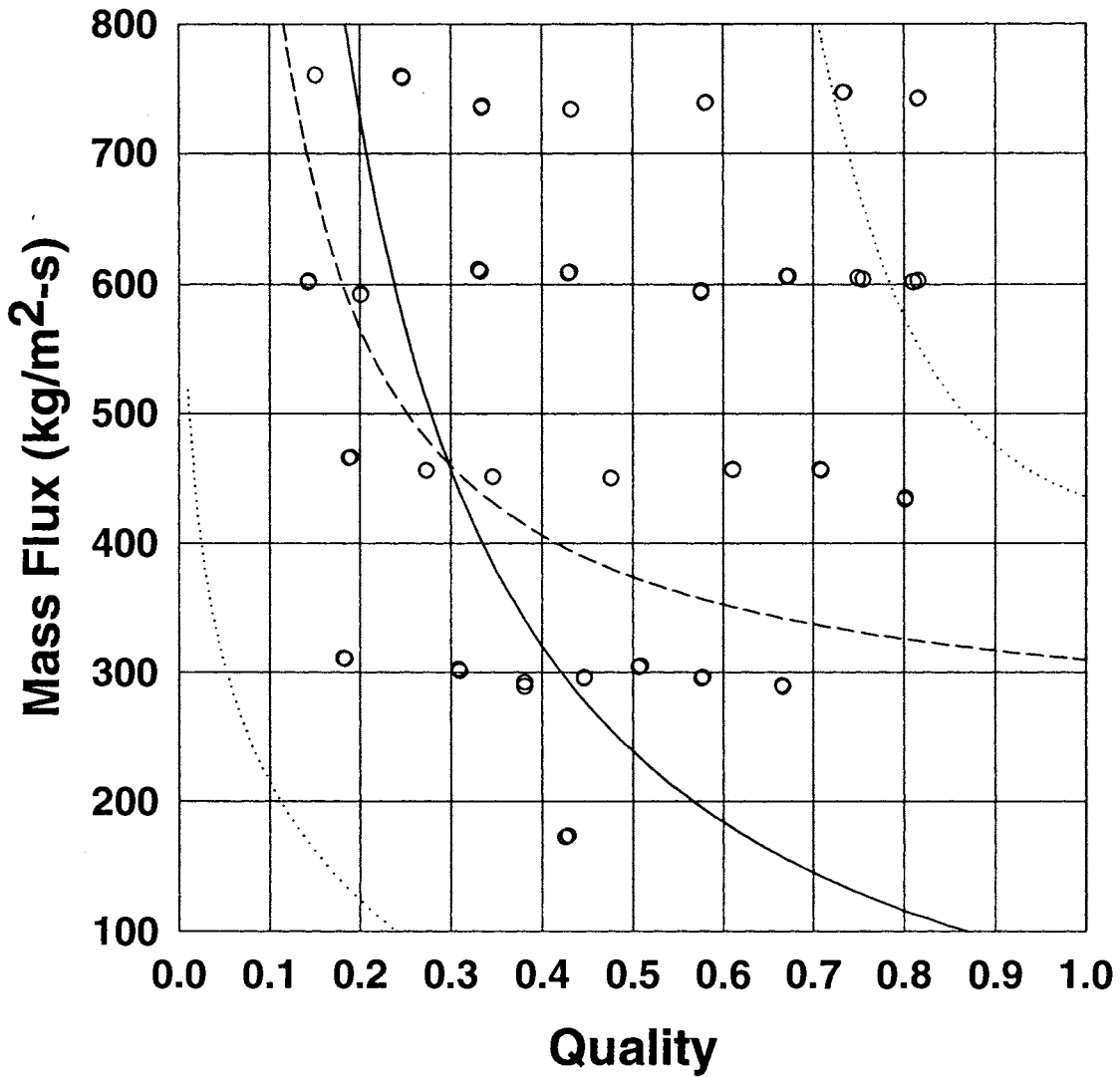


Figure 56. Experimental Data for Test Section C30 with Superimposed Transition Lines

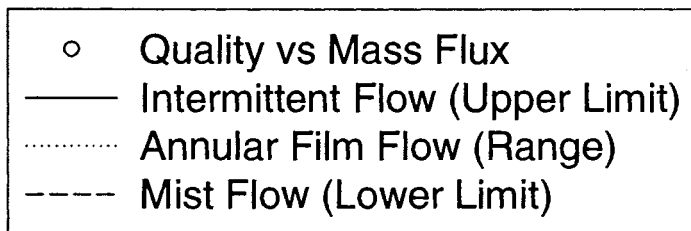
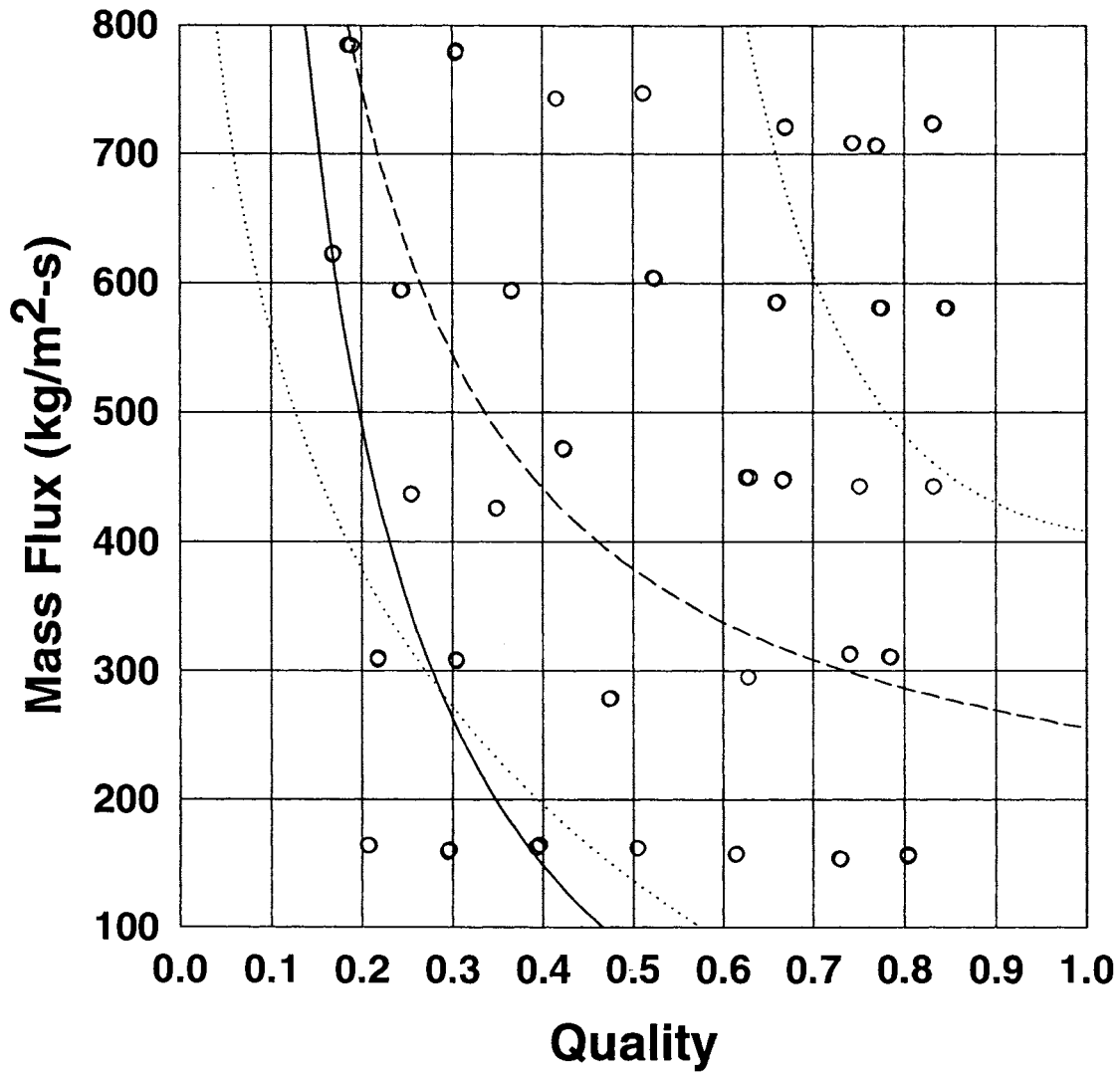


Figure 57. Experimental Data for Test Section C60 with Superimposed Transition Lines

the data were compared with the flow regime-based correlations of Nitheanandan et al. (1990) and Dobson and Chato (1998).

### Intermittent Flow Data

To facilitate the discussion, this section contains a sample calculation for each correlation for a data point collected for test section C30 ( $D_h = 0.761$  mm), which is considered the baseline case for the intermittent flow regime. Relevant parameters required for these calculations are presented in Table 5. For an average test section quality of 0.272 and a mass flux of  $455.5 \text{ kg/m}^2\text{-s}$ , the experimental condensation heat transfer coefficient is  $3,179 \text{ W/m}^2\text{-K}$ . This data point is in both the intermittent and annular regimes (see Figure 56). The wall temperature shown in Table 5 is required for some correlations, and was calculated using the experimentally measured heat transfer coefficient and the applicable resistance network.

**Table 5. Test Section C30 Data Point Summary for Baseline Comparison of Intermittent Data**

Variable	Value	Units
G	455.5	$\text{kg/m}^2\text{-s}$
x	0.272	
h	3,179	$\text{W/m}^2\text{-K}$
$P_{\text{sat}}$	1,378	kPa
$T_{\text{sat}}$	51.77	$^{\circ}\text{C}$
$P_{\text{crit}}$	4,059	kPa
$\sigma$	0.004678	N/m
$h_{\text{lv}}$	149.7	$\text{kJ/kg}$
$T_{\text{wall}}$	48.79	$^{\circ}\text{C}$
<i>Liquid Properties</i>		
$\rho_l$	1,094	$\text{kg/m}^3$
$k_l$	0.06941	$\text{W/m-K}$
$C_{p_l}$	1.58	$\text{kJ/kg-K}$
$\mu_l$	$1.418 \times 10^{-4}$	$\text{kg/m-s}$
$Pr_l$	3.228	
<i>Vapor Properties</i>		
$\rho_v$	69.54	$\text{kg/m}^3$
$k_v$	0.0174	$\text{W/m-K}$
$\mu_v$	$1.366 \times 10^{-4}$	$\text{kg/m-s}$

### Chato (1962)

Chato (1962) presented a Nusselt number correlation for laminar-film, gravity-driven condensation inside a horizontal tube. The results were compared to experiments conducted with R-113 condensing inside a 14.53 mm inside diameter tube at various inclinations. The Nusselt number correlation, as modified by Carey (1992), is as follows:

$$\text{Nu} = \frac{hD_h}{k_1} = 0.553 \left[ \frac{\rho_1(\rho_1 - \rho_v)g \cdot h'_{lv} \cdot D_h^3}{k_1 \cdot \mu_1(T_{\text{sat}} - T_{\text{wall}})} \right]^{1/4} \quad (122)$$

where:

$$h'_{lv} = h_{lv} \left( 1 + 0.68 \frac{Cp_1(T_{\text{sat}} - T_{\text{wall}})}{h_{lv}} \right) \quad (123)$$

Using the values in Table 5, equations 122 and 123 yield a Nusselt number of 39.2. The condensation heat transfer coefficient for this data point is, therefore, 3,576 W/m<sup>2</sup>-K.

The condensation heat transfer coefficient as a function of average test section quality for the gravity-driven heat transfer correlations and the intermittent data from the present study on test section C30 are shown in Figures 58 through 60 for the nominal mass fluxes of 300, 450, and 600 kg/m<sup>2</sup>-s, respectively. The nominal mass fluxes of 150 and 750 kg/m<sup>2</sup>-s have only one data point in the intermittent flow regime for test section C30, and are, therefore, not included. These figures show that the Chato (1962) correlation does not represent the experimental data very well. For these mass fluxes, the slope of the experimental heat transfer coefficients as a function of quality is steeper than that predicted by the Chato's (1962) correlation. In addition, Chato's (1962) correlation over-predicts all of the intermittent data. The primary reason for this lack of agreement may be that the Chato (1962) correlation was derived for stratified flow condensation, which does not exist for the experimental data on test section C30.

### **Jaster and Kosky (1976)**

Jaster and Kosky (1976) presented a Nusselt number correlation for the annular, stratified, and transition flow regimes. However, Carey (1992) and Dobson and Chato (1998) have considered the stratified flow correlation of Jaster and Kosky (1976) to be the most significant contribution because the variation of void fraction along the condensation process is included. The results compared favorably to their experimental data taken on steam/water condensation inside a horizontal tube ( $D_h = 12.5$  mm) for  $12.6 \text{ kg/m}^2\text{-s} < G < 145 \text{ kg/m}^2\text{-s}$ . The stratified correlation with the modified enthalpy of vaporization suggested by Rohsenow (1956) is as follows:

$$\text{Nu} = \frac{hD}{k_1} = 0.725 \cdot \alpha^{3/4} \left[ \frac{\rho_1(\rho_1 - \rho_v)g \cdot h'_{lv} \cdot D^3}{k_1 \cdot \mu_1(T_{\text{sat}} - T_{\text{wall}})} \right]^{1/4} \quad (124)$$

The void fraction required for this correlation is determined from the following correlation presented by Zivi (1964):

$$\alpha = \left[ 1 + \frac{1-x}{x} \left( \frac{\rho_v}{\rho_l} \right)^{2/3} \right]^{-1} \quad (125)$$

The void fraction for the intermittent flow data point under consideration is 0.701. Hence, the Nusselt number is 39.4, which yields a condensation heat transfer coefficient of 3,592 W/m<sup>2</sup>-K. This stratified flow correlation is compared with the experimental data for test section C30 in Figures 58-60. For nominal mass fluxes of 300 and 450 kg/m<sup>2</sup>-s, the correlation over-predicts the data, but has a qualitatively similar slope. For the nominal mass flux of 750 kg/m<sup>2</sup>-s, the intermittent data is predicted well by the correlation.

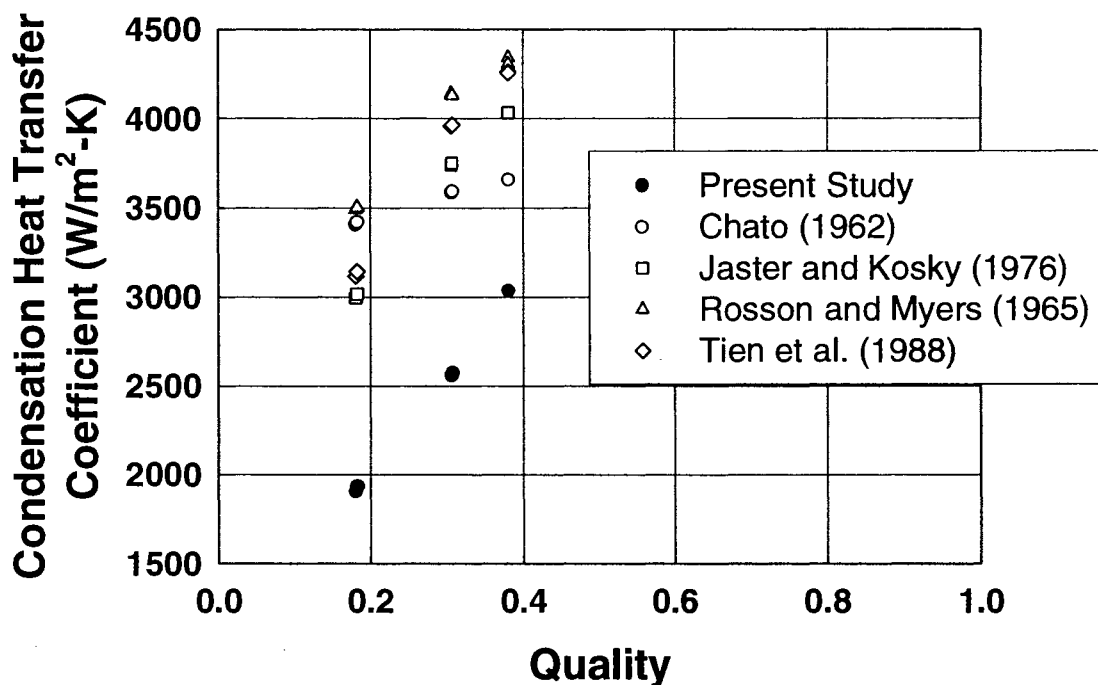


Figure 58. Comparison of Intermittent Flow Data with Literature (Test Section C30,  $G = 300 \text{ kg/m}^2\text{-s}$ )

#### Rosson and Myers (1965)

Rosson and Myers (1965) presented a condensation heat transfer correlation for stratified flow inside horizontal circular tubes. They accounted for film condensation on the top portion of the tube and forced-convective liquid pool heat transfer along the bottom. The result was compared with calculated values for condensation heat transfer coefficients for

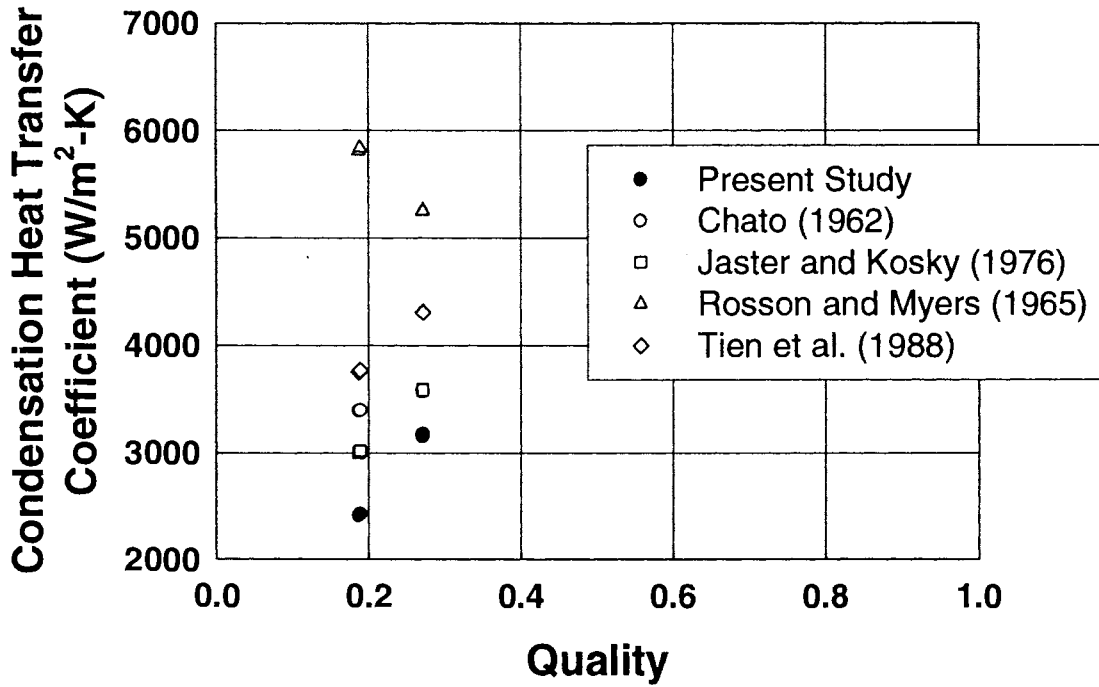


Figure 59. Comparison of Intermittent Flow Data with Literature (Test Section C30,  $G = 450 \text{ kg/m}^2\text{-s}$ )

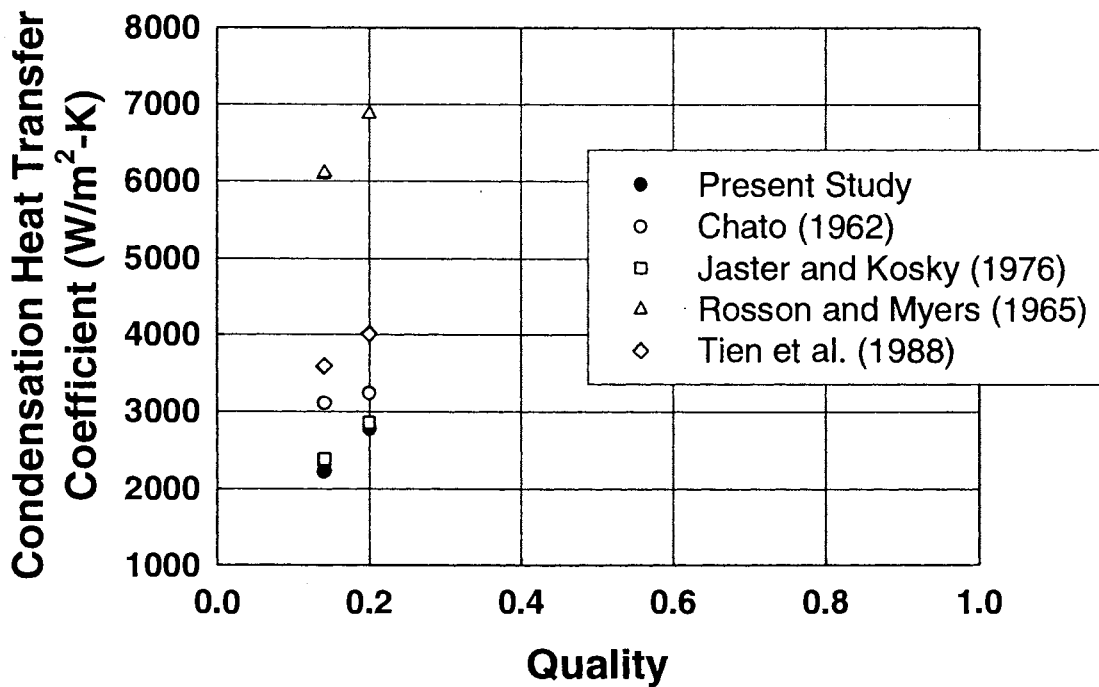


Figure 60. Comparison of Intermittent Flow Data with Literature (Test Section C30,  $G = 600 \text{ kg/m}^2\text{-s}$ )

methanol and acetone condensing inside a 9.53 mm nominal stainless steel pipe. Accounting for the effect of vapor shear on the liquid film, Rosson and Myers (1965) calculated the top Nusselt number as follows:

$$\text{Nu}_{\text{top}} = 0.31 \left( \frac{G \cdot x \cdot D_h}{\mu_v} \right)^{0.12} \left[ \frac{\rho_l (\rho_l - \rho_v) g \cdot h'_{lv} \cdot D_h^3}{k_l \cdot \mu_l (T_{\text{sat}} - T_{\text{wall}})} \right]^{1/4} \quad (126)$$

For the baseline case, the top Nusselt number is 63.5, which yields a heat transfer coefficient of 5,790 W/m<sup>2</sup>-K.

For the bottom Nusselt number, a series of calculations needs to be made. The Reynolds numbers for the liquid and vapor phases flowing alone in the tube are calculated as follows:

$$\text{Re}_l = \frac{G(1-x)D_h}{\mu_l} \quad (127)$$

$$\text{Re}_v = \frac{G \cdot x \cdot D_h}{\mu_v} \quad (128)$$

In the baseline case, the liquid and vapor Reynolds numbers are 1,780 and 6,902, respectively. The corresponding liquid and vapor friction factors are calculated as follows:

$$f = B \cdot \text{Re}^{-n} \quad (129)$$

For laminar flow (i.e.  $\text{Re} < 2000$ ), the constants  $B$  and  $n$  are 16 and 1, respectively, while  $B = 0.079$  and  $n = 0.25$  for turbulent flow (i.e.  $\text{Re} \geq 2000$ ). Rosson and Myers (1965) state that the Lockhart and Martinelli (1949) correlation used for calculating pressure drop does not consider the effect of waves, which may imply that laminar liquid flow is assumed. Also, Rosson and Myers (1965) do not show any alternative calculation to a laminar liquid film assumption. In addition, Carey's (1992) interpretation of Rosson and Myers (1965) states that the liquid film is always laminar for this correlation, and, hence, it is used here. Carey (1992) also assumed that the vapor is always turbulent. Hence, turbulent vapor and laminar liquid are assumed here. Therefore, the baseline case yields liquid and vapor friction factors of  $8.99 \times 10^{-3}$  and  $8.667 \times 10^{-3}$ , respectively.

The frictional pressure gradient for the liquid and vapor phase flowing alone in the pipe are calculated as follows:

$$\left( \frac{dP}{dz} \right)_l = \frac{2 \cdot f_l \cdot G^2 (1-x)^2}{\rho_l D_h} \quad (130)$$

$$\left(\frac{dP}{dz}\right)_v = \frac{2 \cdot f_v \cdot G^2 \cdot x^2}{\rho_v D_h} \quad (131)$$

For the baseline case, the frictional pressure gradients for the liquid and vapor phases are 2.375 kPa and 5.028 kPa, respectively. These frictional pressure gradients are used to define the Martinelli parameter as follows:

$$X = \left[ \frac{\left(\frac{dP}{dz}\right)_l}{\left(\frac{dP}{dz}\right)_v} \right]^{1/2} \quad (132)$$

The Martinelli parameter in this case is 0.687. The Martinelli parameter is used to calculate the liquid two-phase friction multiplier (Lockhart and Martinelli 1949) for laminar liquid and turbulent vapor as follows:

$$\phi_{l,vt} = \left[ 1 + \frac{12}{X} + \frac{1}{X^2} \right]^{1/2} \quad (133)$$

The two-phase multiplier in the baseline case is 4.536.

The liquid pool Nusselt number is calculated as follows:

$$Nu_{bot} = \frac{\phi_{l,vt} \sqrt{8 Re_l}}{5 + 5 Pr_l^{-1} \ln(1 + 5 Pr_l)} \quad (134)$$

For the baseline case, the Nusselt number is 57.58, which yields a condensation heat transfer coefficient of 5,252 W/m<sup>2</sup>-K.

The actual heat transfer coefficient is the average of the top and bottom Nusselt numbers based up the height of the liquid pool. The Galileo number is defined as follows:

$$Ga = \frac{D_h^3 \cdot \rho_l (\rho_l - \rho_v) g}{\mu_l^2} \quad (135)$$

The baseline case has a Galileo number of 2.410 x 10<sup>5</sup>. The parameter  $\beta$  is the ratio of the angle between the top of the tube and the liquid pool height to 180° and is defined as follows:

$$\beta = \begin{cases} 0.27 \cdot Re_v^{0.1} & \text{if } \frac{Re_v^{0.6} \cdot Re_l^{0.5}}{Ga} < 6.4 \times 10^{-5} \\ \frac{1.74 \times 10^{-5} \cdot Ga}{\sqrt{Re_v \cdot Re_l}} & \text{if } \frac{Re_v^{0.6} \cdot Re_l^{0.5}}{Ga} \geq 6.4 \times 10^{-5} \end{cases} \quad (136)$$

For the baseline case,  $\beta$  is 0.001196, indicating that the liquid pool for this case is extremely

small, once again showing that the stratified flow assumption would be inapplicable. With this calculated value of  $\beta$ , the heat transfer coefficient is calculated as follows:

$$h = \beta \cdot h_{\text{top}} + (1 - \beta)h_{\text{bot}} \quad (137)$$

The condensation heat transfer coefficient for the baseline case is  $5,252 \text{ W/m}^2\text{-K}$ .

Figures 58-60 show the condensation heat transfer coefficients as predicted by Rosson and Myers (1965) compared with the experimental values for intermittent flow from the present study. For all of the intermittent data, the correlation of Rosson and Myers (1965) severely over-predicts all of the intermittent data for test section C30.

#### **Tien et al. (1988)**

Tien et al. (1988) presented a condensation heat transfer correlation for non-annular (slug) flow inside horizontal tubes. The model assumes that the two-phase mixture flows in unit cells consisting of a stratified region and a slug region with a total vapor quality ( $x$ ) and volume fraction ( $\alpha$ ). The stratified region is two-phase stratified flow (i.e. a liquid pool with vapor flow above) with a local quality ( $x_b$ ) and void fraction ( $\alpha_b$ ), while the slug region is liquid flowing at the saturation temperature. The system equations describing the slug hydrodynamics behavior are as follows:

$$\alpha = \beta \cdot \alpha_b \quad (138)$$

$$x = \frac{K \frac{x_b}{\alpha_b} - 1}{K - 1} \quad (139)$$

$$K = \frac{U_b}{U_{L,\text{avg}}} = \left( \frac{1 - \alpha}{\alpha} \right) \left( \frac{\rho_l}{\rho_v} \right) \left( \frac{1 - x}{x} \right) \quad (140)$$

Neglecting the liquid film surrounding the vapor on the top portion of the tube, the void fraction of the stratified region is found from geometric considerations. The angle subtended from the top of the tube to the liquid pool level varies from 0 radians to  $\pi$  radians. If the liquid pool level is above the centerline (i.e.  $\theta < \pi/2$  radians), the void fraction of the stratified region can be found as follows:

$$\alpha_b = \frac{\arcsin(\sin(\theta)) - \left| \frac{\sin(2\theta)}{2} \right|}{\pi} \quad (141)$$

The inverse sine of the sine of the subtended angle is to ensure that the value is less than  $\pi/2$  radians, while the absolute value of the sine of the double angle is to ensure a positive value. If the subtended angle is below the centerline (i.e.  $\theta > \pi/2$  radians), the stratified region void

fraction is as follows:

$$\alpha_b = \frac{\pi - \arcsin(\sin(\theta)) + \left| \frac{\sin(2\theta)}{2} \right|}{\pi} \quad (142)$$

Another assumption made by Tien et al. (1988) is that both phases in the slug unit have equal velocity head (i.e. equal kinetic energy per unit volume). This was presented in Smith (1969-70) and results in the following:

$$K = \sqrt{\frac{\rho_l}{\rho_v}} \quad (143)$$

For a given quality and liquid and vapor properties, this equation defines the slip ratio. In the baseline case, the slip ratio is 3.966. Hence, there are four equations (138, 139, 140, and 141 or 142) with five unknowns:  $\alpha$ ,  $\alpha_b$ ,  $\beta$ ,  $\theta$ , and  $x_b$ .

Tien et al. (1988) apply momentum balances to the liquid and vapor phases in the stratified region, where the pressure drop in each phase is assumed to be equal. They also assume that the vapor phase travels at a much higher velocity than the liquid phase. They show the result of this analysis in the following non-dimensional form:

$$\left( \frac{\tilde{D}_L}{\tilde{D}_v} \right)^{0.2} \left( \frac{1 - \alpha_b}{\alpha_b} \right)^{1.8} \frac{\tilde{S}_v(1 - \alpha_b) + \tilde{S}_i}{\alpha_b \cdot \tilde{S}_L} = \left( \frac{\mu_l}{\mu_v} \right)^{0.2} \left( \frac{\rho_v}{\rho_l} \right) \left( \frac{1 - x_b}{x_b} \right)^{1.8} \quad (144)$$

where:

$$\tilde{S}_L = \pi - \theta \quad (145)$$

$$\tilde{S}_v = \theta \quad (146)$$

$$\tilde{S}_i = |\sin(\theta)| \quad (147)$$

For  $\theta < \pi/2$  radians, the dimensionless liquid and vapor hydraulic diameters are as follows:

$$\tilde{D}_L = \frac{\pi - \theta + \frac{\sin(2 \cdot \theta)}{2}}{\pi - \theta + \sin(\theta)} \quad (148)$$

$$\tilde{D}_v = \frac{\theta - \frac{\sin(2 \cdot \theta)}{2}}{\theta + \sin(\theta)} \quad (149)$$

For  $\theta > \pi/2$  radians, the dimensionless liquid and vapor hydraulic diameters are as follows:

$$\tilde{D}_v = \frac{\arcsin(\sin(\theta)) - \left| \frac{\sin(2 \cdot \theta)}{2} \right|}{\pi - \theta + \sin(\theta)} \quad (150)$$

$$\tilde{D}_v = \frac{\pi - \arcsin(\sin(\theta)) + \left| \frac{\sin(2 \cdot \theta)}{2} \right|}{\theta + \sin(\theta)} \quad (151)$$

The fifth required equation is realized by substituting equations 145 through 147 and either 148 and 149 or 150 and 151 into equation 144. After solving the five equations simultaneously, the five unknowns are found. For the intermittent flow baseline case, the void fractions of the unit cell and stratified region are 0.5971 and 0.6743, respectively, which yields a two-phase stratified region length to unit cell length ratio ( $\beta$ ) of 0.8855. The local stratified region vapor quality is 0.3072, while the angle subtended from the top of the tube to the liquid pool level is 1.852 radians.

The film condensation and liquid pool Nusselt numbers for the stratified region are as follows:

$$\text{Nu}_{\text{film}} = F \left( \frac{\text{Pr}_1 \cdot \text{Ga}}{\text{Ja}_1} \right)^{0.25} \quad (152)$$

$$\text{Nu}_{\text{pool}} = \frac{0.15166 \text{Re}_{\text{lo}}^{0.9} \left( \frac{1 - x_b}{1 - \alpha_b} \right)^{0.9}}{\tilde{D}_L^{0.1} \left( 5 + \frac{5}{\text{Pr}_1} \ln(5 \cdot \text{Pr}_1 + 1) \right)} \quad (153)$$

The liquid-only Reynolds number is defined as follows:

$$\text{Re}_{\text{lo}} = \frac{G \cdot D_h}{\mu_1} \quad (154)$$

The heat transfer factor  $F$  is calculated from a curve fit developed by the present author of the graph presented in Tien et al. (1988), which results in the following:

$$F = -2.02067 \cdot 10^{-2} \cdot \theta^2 + 1.94892 \cdot 10^{-3} \theta + 9.16109 \text{E} \cdot 10^{-1} \quad (155)$$

The liquid Jakob number is defined as follows:

$$\text{Ja}_1 = \frac{C_{\text{pl}} (T_{\text{sat}} - T_{\text{wall}})}{h_{\text{lv}}} \quad (156)$$

The Jakob number is 0.03145 for the baseline case. For the subtended angle of 1.852, the heat transfer factor  $F$  is 0.8504, which yields a film condensation Nusselt number of 59.98.

For a dimensionless liquid hydraulic diameter of 0.455 and a liquid-only Reynolds number of 2,445, the liquid pool Nusselt number is 38.57 in the baseline case.

The single-phase liquid slug Nusselt number is calculated as follows:

$$\text{Nu}_L = \begin{cases} 3.658 & \text{if } \text{Re}_{lo} < 2400 \\ 0.023 \cdot \text{Re}_{lo}^{0.8} \cdot \text{Pr}_l^{0.3} & \text{if } \text{Re}_{lo} > 2400 \end{cases} \quad (157)$$

The liquid slug Nusselt number is 16.79 in the baseline case.

The overall Nusselt number was a flow regime average between two-phase stratified and single phase liquid slug flow as follows:

$$\text{Nu} = \left[ \text{Nu}_{\text{film}} \frac{\theta}{\pi} + \text{Nu}_{\text{pool}} \left( 1 - \frac{\theta}{\pi} \right) \right] \beta + \text{Nu}_L (1 - \beta) \quad (158)$$

For the baseline case, the overall Nusselt number is 47.25, which yields a condensation heat transfer coefficient of 4,310 W/m<sup>2</sup>-K.

Figures 58 through 60 show the experimental data for intermittent flow for test section C30 compared with the correlation of Tien et al. (1988). All of the intermittent data are over-predicted by the correlation. As stated above, while condensing in microchannels, the flow changes from mist to annular to intermittent. In the model by Tien et al. (1988), the condensation path was assumed to travel from annular to stratified to intermittent. Therefore, the differences in modeling the vapor region (with the stratified liquid pool) might account for the differences between the data and this model.

## Annular Flow Data

Annular flow data from the present study are compared here with the relevant correlations from the literature. A sample calculation for each correlation at a mass flux of 472.05 kg/m<sup>2</sup>-s and a quality of 0.432 is also included. Relevant parameters required for these calculations are presented in Table 6. For this test condition for tube C60 ( $D_h = 1.524$  mm), the experimental heat transfer coefficient is 3,908.7 W/m<sup>2</sup>-K. This data point is in the annular flow regime (see Figure 57). The wall temperature shown in Table 6 is required for some correlations, and was calculated using the experimentally measured heat transfer coefficient and the applicable resistance network.

## Shear-Driven Correlations

*Soliman et al. (1968)*

Soliman et al. (1968) presented an analytical model for annular flow condensation inside horizontal tubes. Their results were compared with experimental data obtained on

**Table 6. Test Section C60 Data Point Summary for Baseline Comparison of Annular Data**

Variable	Value	Units
G	472.05	kg/m <sup>2</sup> -s
X	0.423	
H	3,908.7	W/m <sup>2</sup> -K
P <sub>sat</sub>	1,434.45	kPa
T <sub>sat</sub>	53.39	°C
P <sub>crit</sub>	4,059	kPa
Σ	4.485 x 10 <sup>-3</sup>	N/m
h <sub>lv</sub>	147.73	kJ/kg
T <sub>wall</sub>	49.20	°C
<i>Liquid Properties</i>		
ρ <sub>l</sub>	1,086	kg/m <sup>3</sup>
k <sub>l</sub>	0.06851	W/m-K
C <sub>p</sub> <sub>l</sub>	1.594	kJ/kg-K
μ <sub>l</sub>	1.386 x 10 <sup>-4</sup>	kg/m-s
Pr <sub>l</sub>	3.225	
<i>Vapor Properties</i>		
ρ <sub>v</sub>	72.7	kg/m <sup>3</sup>
k <sub>v</sub>	0.01758	W/m-K
μ <sub>v</sub>	1.377 x 10 <sup>-5</sup>	kg/m-s

steam, R-113, ethanol, methanol, toluene, trichloroethylene, and R-22 for condensation inside vertical and horizontal tubes of diameters ranging from 7.44 mm to 11.66 mm. To calculate the local condensation heat transfer coefficient while in annular flow, the wall shear stress in the laminar sublayer (the main resistance to heat transfer) needs to be calculated. Soliman et al. (1968) proposed (as did Carpenter and Colburn, 1951) that the wall shear stress was the sum of the gravity, momentum (due to condensation), and friction contributions. For horizontal flow, the gravity contribution is negligible. From a careful analysis of the conservation equations, Soliman et al. (1968) derived the momentum contribution. The ratio of interface velocity to mean film velocity ( $\lambda$ ) is either 1.25 for turbulent film flow, or 2 for laminar film flow. The liquid film Reynolds number is 2,995; hence,  $\lambda$  is 1.25 in this case. The shear stress due to momentum is calculated as follows:

$$\tau_m = \frac{D_h}{4} \left( \frac{G^2}{\rho_v} \right) \frac{dx}{dz} \sum_{n=1}^5 a_n \left( \frac{\rho_v}{\rho_l} \right)^{n/3} \quad (159)$$

where:

$$a_1 = 2 \cdot x - 1 - \lambda \cdot x \quad (160)$$

$$a_2 = 2(1 - x) \quad (161)$$

$$a_3 = 2(1 - x - \lambda + \lambda \cdot x) \quad (162)$$

$$a_4 = \frac{1}{x} - 3 + 2 \cdot x \quad (163)$$

$$a_5 = \lambda \left( 2 - \frac{1}{x} - x \right) \quad (164)$$

The rate of condensation is assumed to be approximately constant; therefore, the following is used to approximate the derivative in equation 159:

$$\frac{dx}{dz} \approx \frac{\Delta x}{\Delta z} \quad (165)$$

The test section quality change for the data point under consideration for a heat exchanger length of 0.3048 m is 0.214. Hence, the derivative is approximately 0.702 m<sup>-1</sup>. The constants a<sub>1</sub> through a<sub>5</sub> are -0.683, 1.154, -0.289, 0.210, and -0.984, respectively. Hence the momentum contribution to wall shear stress is 0.0914 Pa.

Soliman et al. (1968) calculated the frictional contribution to the shear stress as follows:

$$\tau_f = 0.0225 \frac{G^2}{\rho_v} \text{Re}_{vo}^{-0.2} \left[ \begin{aligned} &x^{1.8} + 5.7 \left( \frac{\mu_l}{\mu_v} \right)^{0.0523} (1-x)^{0.47} x^{1.33} \left( \frac{\rho_v}{\rho_l} \right)^{0.261} \\ &+ 8.11 \left( \frac{\mu_l}{\mu_v} \right)^{0.105} (1-x)^{0.94} x^{0.86} \left( \frac{\rho_v}{\rho_l} \right)^{0.522} \end{aligned} \right] \quad (166)$$

The vapor-only Reynolds number is calculated as follows:

$$\text{Re}_{vo} = \frac{G \cdot D_h}{\mu_v} \quad (167)$$

For the annular flow baseline case, the vapor-only Reynolds number is 52,244. Therefore, the frictional shear stress is 13.43 Pa.

The condensation heat transfer coefficient is calculated as follows:

$$h = 0.036 \frac{k_l \rho_l^{1/2}}{\mu_l} \text{Pr}_l^{0.65} \cdot \tau_t^{1/2} \quad (168)$$

The total shear stress is the sum of the friction and momentum (and gravity for inclined tubes) contributions, which is 13.52 Pa in the baseline case. Therefore, the condensation heat transfer coefficient for this point is 4,616 W/m<sup>2</sup>-K.

Figures 61 through 65 show the correlation by Soliman et al. (1968) compared with the experimental data for test section C60 from the present study for the nominal mass fluxes of 150, 300, 450, 600, and 750 kg/m<sup>2</sup>-s, respectively. For the nominal mass flux of 150

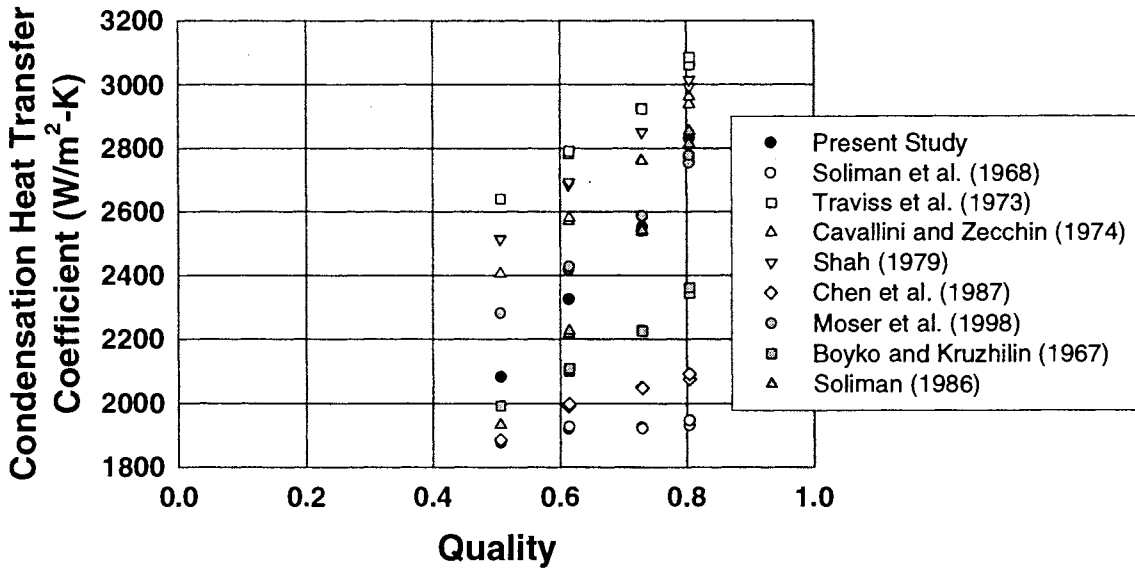


Figure 61. Comparison of Annular Flow Regime Data with the Literature (Test Section C60,  $G = 150 \text{ kg/m}^2\text{-s}$ )

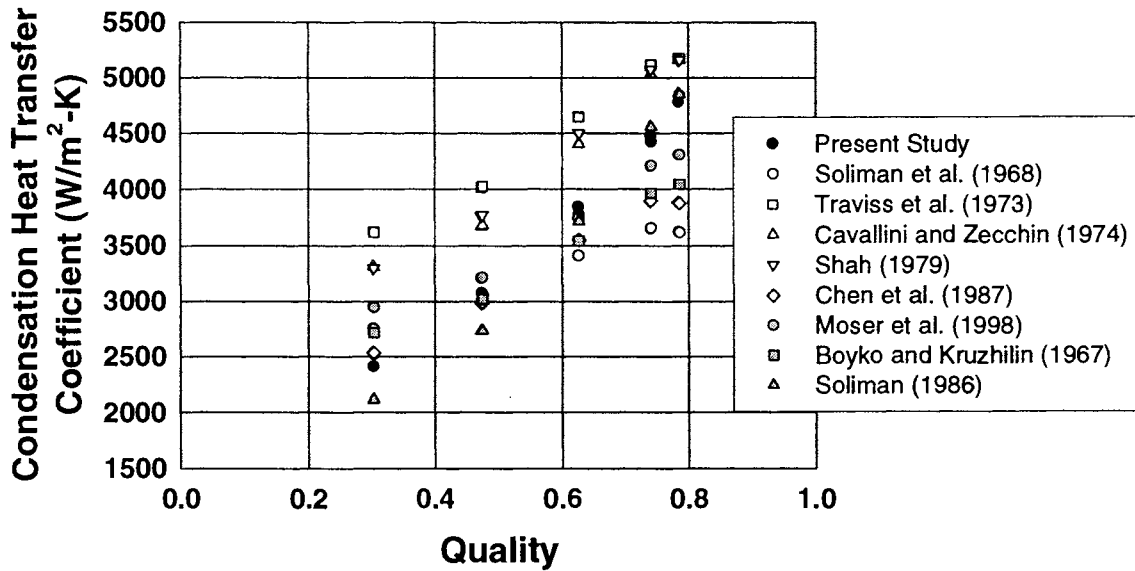


Figure 62. Comparison of Annular Flow Regime Data with the Literature (Test Section C60,  $G = 300 \text{ kg/m}^2\text{-s}$ )

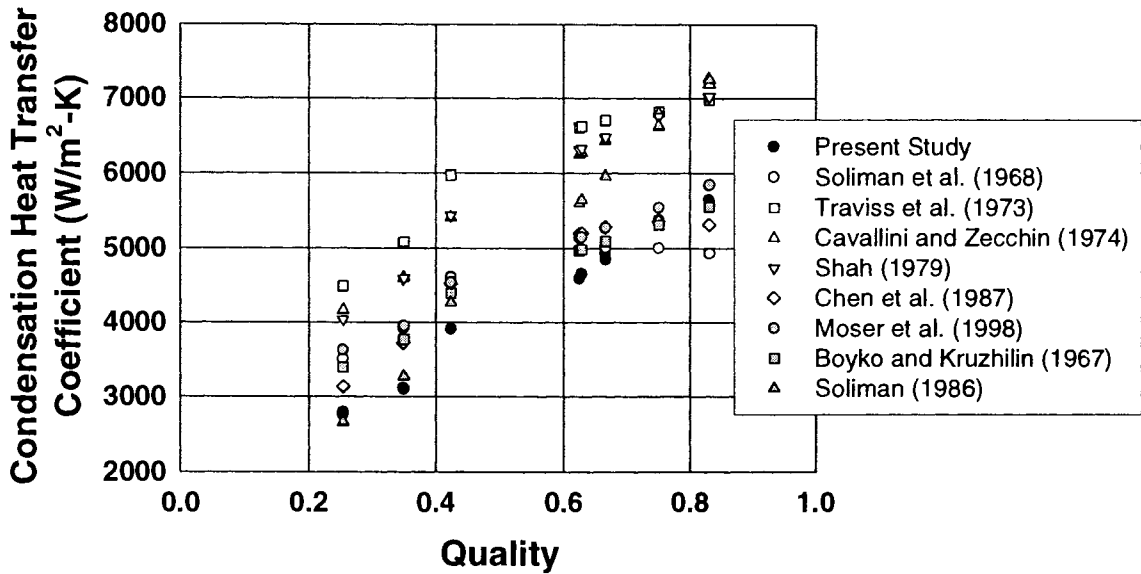


Figure 63. Comparison of Annular Flow Regime Data with the Literature (Test Section C60,  $G = 450 \text{ kg/m}^2\text{-s}$ )

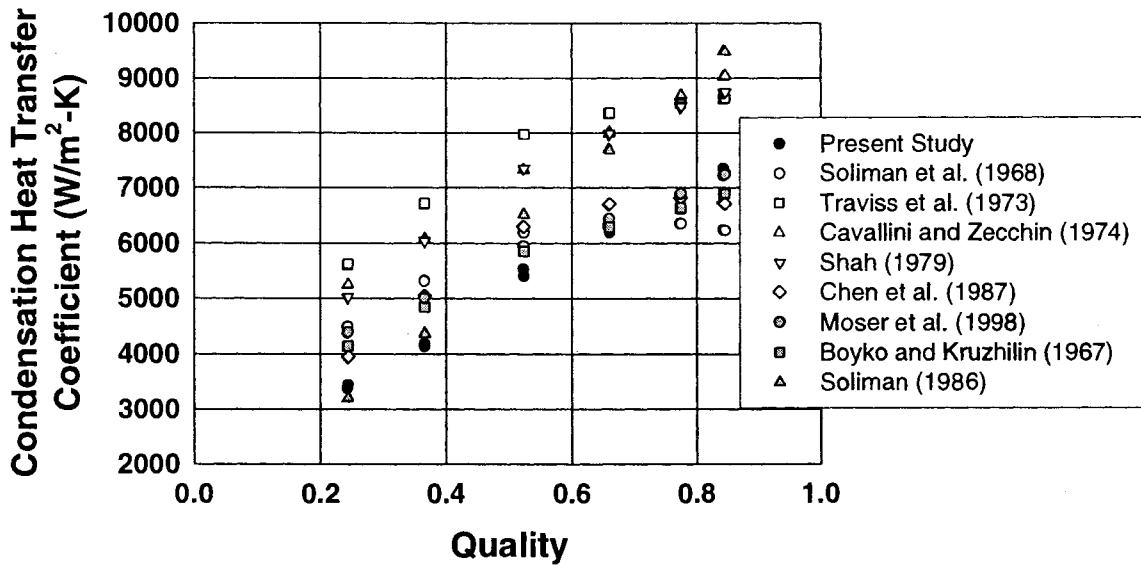


Figure 64. Comparison of Annular Flow Regime Data with the Literature (Test Section C60,  $G = 600 \text{ kg/m}^2\text{-s}$ )

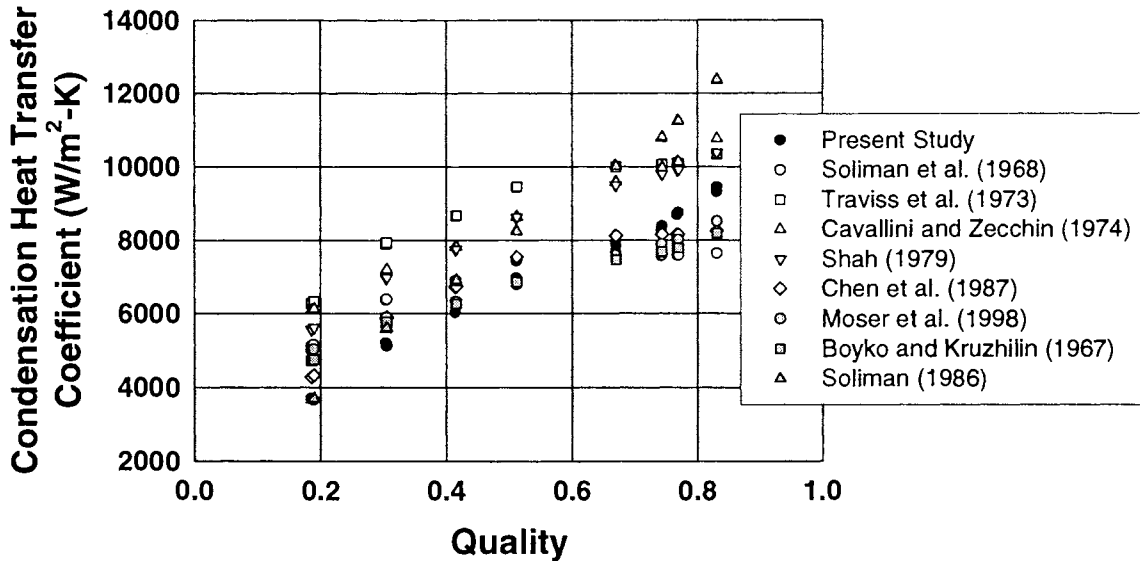


Figure 65. Comparison of Annular Flow Regime Data with the Literature (Test Section C60,  $G = 750 \text{ kg/m}^2\text{-s}$ )

$\text{kg/m}^2\text{-s}$ , the data are under-predicted by the correlation of Soliman et al. (1968). For all other mass fluxes, the data are over-predicted by Soliman et al. (1968) for qualities up to 0.5 to 0.7. At qualities above this, Soliman et al. (1968) under-predicts the data. The correlation does predict the data fairly well, however. For all mass fluxes except  $G = 150 \text{ kg/m}^2\text{-s}$ , the predictions by Soliman et al. (1968) are within  $\pm 30\%$  of the data from the present study. However, because the slope of the experimental data is steeper (causing over- and under-prediction), qualitative agreement is not achieved. Also, at high qualities, liquid entrainment in the vapor core may be high, a phenomenon neglected in the model by Soliman et al. (1968).

*Traviss et al. (1973)*

Traviss et al. (1973) presented a forced-convective Nusselt number model for annular flow condensation using a boundary layer approach. The results were compared with experiments conducted on R-12 and R-22 condensing in an 8 mm tube. The analogy between heat transfer and momentum was applied using the von Karman universal velocity distribution in the liquid film. The resulting Nusselt number correlation is as follows:

$$\text{Nu} = \frac{0.15 \cdot \text{Pr}_l \cdot \text{Re}_l^{0.9}}{F} \left[ \frac{1}{X_{tt}} + \frac{2.85}{X_{tt}^{0.476}} \right] \quad (169)$$

where:

$$F = \begin{cases} 5 \cdot Pr_1 + 5 \ln(1 + 5 \cdot Pr_1) + 2.5 \ln(0.00313 \cdot Re_1^{0.812}) & \text{if } Re_1 \geq 1125 \\ 5 \cdot Pr_1 + 5 \ln \left[ 1 + Pr_1 \left( 0.09636 \cdot Re_1^{0.585} - 1 \right) \right] & \text{if } 50 < Re_1 < 1125 \\ 0.707 \cdot Pr_1 \cdot Re_1^{0.5} & \text{if } Re_1 < 50 \end{cases} \quad (170)$$

The function  $F$  represents the resistance to heat transfer in the laminar sublayer, buffer, and turbulent regions in the annular film. Since the liquid Reynolds number is 2,995 for the baseline case for annular flow, the parameter  $F$  is 32.16.

The turbulent vapor/turbulent liquid Martinelli parameter is calculated as follows:

$$X_{tt} = \left( \frac{1-x}{x} \right)^{0.9} \left( \frac{\rho_v}{\rho_l} \right)^{0.5} \left( \frac{\mu_l}{\mu_v} \right)^{0.1} \quad (171)$$

The annular flow baseline case has a turbulent/turbulent Martinelli parameter of 0.431. Therefore, the Nusselt number is 132.98, which yields a condensation heat transfer coefficient of 5,980 W/m<sup>2</sup>-K.

Figures 61 through 65 show the correlation of Traviss et al. (1973) compared with the experimental data for each of the mass fluxes. For all mass fluxes and qualities, the correlation of Traviss et al. (1973) over-predicts the experimental data. Qualitatively, the slope of the correlation curve is higher at lower qualities and lower at higher qualities than the experimental data. In fact, Traviss et al. (1973) stated that their correlation did not fit their data well at higher qualities, possibly due to the effect of liquid entrainment.

*Cavallini and Zecchin (1974)*

Cavallini and Zecchin (1974) presented an empirical dimensionless correlation for forced-convective condensation inside smooth horizontal tubes. The results of their analysis were compared with data gathered for the condensation of R-11, R-22, and R-114 inside horizontal tubes. The simple dimensionless correlation is as follows:

$$Nu = 0.0344 \cdot Re_{lo}^{0.83} \left( 1 + x \left[ \left( \frac{\rho_l}{\rho_v} \right)^{0.5} - 1 \right] \right)^{0.82} Pr_1^{0.35} \quad (172)$$

where:

$$Re_{lo} = \frac{G \cdot D_h}{\mu_l} \quad (173)$$

The liquid-only Reynolds number for the baseline case is 5,191. Therefore, the Nusselt number for the annular flow baseline case is 120.47, which yields a condensation heat transfer coefficient of 5,416 W/m<sup>2</sup>-K.

Figures 61 through 65 show the correlation by Cavallini and Zecchin (1974) compared with the experimental data from the present study. This empirical correlation over-predicts the experimental data for all mass fluxes and qualities. However, this correlation does not over-predict the data as much as the correlation by Traviss et al. (1973). For the lowest mass flux, all of the data are predicted by the correlation to within  $\pm 17\%$ , but all of the data are over-predicted. For a nominal mass flux of 300 kg/m<sup>2</sup>-s, the data above an average test section quality of 0.6 are over-predicted by up to 20%. However, the data are over-predicted below this quality by as much as 50%. Also, similar trends are seen for the other mass fluxes. For all mass fluxes, the error between the correlation and the data decreases with increasing quality.

*Shah (1979)*

The empirical correlation developed by Shah (1979) was adapted from his previous work on convective boiling. By neglecting the term for nucleate boiling, the following correlation was proposed:

$$h = h_{DB} \left[ (1-x)^{0.8} + \frac{3.8 \cdot x^{0.76} (1-x)^{0.04}}{(P/P_{crit})^{0.38}} \right] \quad (174)$$

where the single-phase Dittus-Boelter equation is as follows:

$$h_{DB} = 0.023 \cdot Re_1^{0.8} \cdot Pr_1^{0.4} \cdot k_1 / D_h \quad (175)$$

The single-phase heat transfer coefficient is 1,549 W/m<sup>2</sup>-K for the annular flow baseline case. Hence, the condensation heat transfer coefficient is 5,444 W/m<sup>2</sup>-K.

Figures 61 through 65 show the correlation by Shah (1979) compared with the experimental data from the present study. The correlation over-predicts the data for all mass fluxes and qualities. Also, the values predicted by Shah (1979) are nearly identical to the values predicted by Cavallini and Zecchin (1974), with the difference between the correlations being less than  $\pm 5\%$  of the values predicted by Shah (1979). Also, the trends stated above for the Cavallini and Zecchin (1974) correlation are the same for the Shah (1979) correlation. It is important to note, however, that Shah (1979) recommends this correlation for the tube diameter range of 7 mm to 40 mm and for the limited mass flux range  $11 \leq G \leq 211$  kg/m<sup>2</sup>-s. Therefore, this correlation may not accurately represent condensation inside the smaller diameter tubes considered in this study.

*Chen et al. (1987)*

Chen et al. (1987) presented annular flow condensation models for vertical and horizontal tubes. The horizontal flow correlation, which neglects the gravity terms, is as follows:

$$\text{Nu} = 0.036 \cdot \text{Pr}_l^{0.65} \cdot (\text{Re}_{l0} - \text{Re}_l)^{0.7} \cdot \text{Re}_l^{0.2} \sqrt{\left( \frac{0.252 \cdot \mu_l^{1.177} \cdot \mu_v^{0.156}}{D_h^2 \cdot g^{2/3} \cdot \rho_l^{0.553} \cdot \rho_v^{0.78}} \right)} \quad (176)$$

The Nusselt number is defined as follows:

$$\text{Nu} = \frac{h}{k_l} \left( \frac{\mu_l^2}{\rho_l^2 \cdot g} \right)^{1/3} \quad (177)$$

For the annular flow baseline case, the Nusselt number is 0.782, which yields a condensation heat transfer coefficient of 4,525 W/m<sup>2</sup>-K.

Figures 61 through 65 show the correlation of Chen et al. (1987) compared with the experimental data for the present study. This correlation does an excellent job of predicting the data: all of the test section C60 annular data are within  $\pm 27\%$  of the experimental value. At the lowest mass flux, however, the data are under-predicted by Chen et al. (1987). Also, at the highest qualities, the correlation under-predicts the experimental data. This correlation is an adaptation of the work done by Soliman et al. (1968). The shear stress at the wall was replaced by Dukler's (1960) relation for dimensionless shear stress in adiabatic two-phase vertical annular flow, which may account for the quantitative difference. However, these differences are not great, mostly within the uncertainties of the experimental heat transfer coefficients.

*Moser et al. (1998)*

Moser et al. (1998) presented a new equivalent Reynolds number model for condensation heat transfer coefficient prediction. The new equivalent Reynolds number represents an equivalent all-liquid annular flow, where a liquid core is surrounded by a liquid film moving at a different, slower velocity. The shear between these two liquids drives the heat transfer. They compared the results with local and average condensation data from various authors for tube diameters ranging from 3.14 to 20 mm.

The two-phase Froude number and homogeneous density required for the model are calculated as follows:

$$\text{Fr}_{\text{tp}} = \frac{G^2}{g \cdot D \cdot \rho_{\text{tp}}^2} \quad (178)$$

$$\rho_{tp} = \left( \frac{x}{\rho_v} + \frac{1-x}{\rho_l} \right)^{-1} \quad (179)$$

For a homogeneous density of  $157.49 \text{ kg/m}^3$ , the two-phase Froude number is 600.94 for the annular flow baseline case. The Weber number is defined as follows:

$$\text{We}_{tp} = \frac{G^2 \cdot D}{\sigma \cdot \rho_{tp}} \quad (180)$$

The Weber number in the baseline case is 480.79.

The friction factors for the liquid-only and vapor-only flow are defined by equation 129. Since the liquid-only and vapor-only Reynolds numbers are 5,191 and 52,244, respectively, and are turbulent, the corresponding friction factors, according to the Blasius equation (equation 129), are 0.0093 and 0.0052, respectively.

The equivalent Reynolds number model is a modification of the work by Akers et al. (1959) and is as follows:

$$\text{Re}_{eq} = \phi_{lo}^{8/7} \cdot \text{Re}_{lo} \quad (181)$$

where the liquid-only two-phase multiplier is defined by (Friedel, 1979) as follows:

$$\phi_{lo}^2 = E + \frac{3.24 \cdot H}{\text{Fr}_{tp}^{0.045} \cdot \text{We}_{tp}^{0.035}} \quad (182)$$

and:

$$E = (1-x)^2 + x^2 \left( \frac{\rho_l}{\rho_v} \right) \left( \frac{f_{vo}}{f_{lo}} \right) \quad (183)$$

$$H = x^{0.78} (1-x)^{0.24} \left( \frac{\rho_l}{\rho_v} \right)^{0.91} \left( \frac{\mu_v}{\mu_l} \right)^{0.19} \left( 1 - \frac{\mu_v}{\mu_l} \right)^{0.70} \quad (184)$$

For the baseline case, the liquid-only two-phase multiplier is 2.826, which yields an equivalent Reynolds number of 17,016.

The Nusselt number correlation used by Moser et al. (1998) was based on the single-phase correlation by Petukhov (1970), which resulted in the following:

$$\text{Nu} = \frac{0.0994 \cdot \text{Pr}_l^{0.126} \cdot \text{Pr}_l^{-0.448} \cdot \text{Re}_l^{-0.113} \cdot \text{Pr}_l^{-0.563} \cdot \text{Re}_{eq}^{1+0.11025 \cdot \text{Pr}_l^{-0.448}} \cdot \text{Pr}_l^{0.815}}{(1.58 \cdot \ln \text{Re}_{eq} - 3.28) (2.58 \cdot \ln \text{Re}_{eq} + 13.7 \cdot \text{Pr}_l^{2/3} - 19.1)} \quad (185)$$

For the annular flow baseline case, the Nusselt number is 101.07, which yields the condensation heat transfer coefficient of  $4,544 \text{ W/m}^2\text{-K}$ .

Figures 61 through 65 show the correlation developed by Moser et al. (1998) compared with the experimental data from the present study. The correlation by Moser et al. (1998) predicts the data well. About 87.5% of the test section C60 data are predicted within  $\pm 25\%$  of the experimental values. This correlation was based on data for tubes with  $3.14 \text{ mm} < D_h < 20 \text{ mm}$ . This diameter range is the closest to the tubes studied here from all the shear-driven correlations in the literature.

### Homogenous Correlations

#### *Boyko and Kruzhilin (1967)*

Boyko and Kruzhilin (1967) presented a modification to the work of Ananiev et al. (1961), which stated that the condensation heat transfer coefficient was equal to Mikheev's (1956) formula for single phase heat transfer, which is as follows:

$$\text{Nu}_{\text{mik}} = 0.024 \cdot \text{Re}_{\text{lo}}^{0.8} \text{Pr}_l^{0.43} \left( \frac{\text{Pr}_l}{\text{Pr}_{l,w}} \right)^{0.25} \quad (186)$$

The Prandtl number evaluated at the wall temperature of  $49.20^\circ\text{C}$  is 3.235. Therefore, the Nusselt number in the annular flow baseline case is 32.22, which yields a heat transfer coefficient of  $1,673 \text{ W/m}^2\text{-K}$ . The two-phase heat transfer coefficient is found as follows:

$$h = h_{\text{mik}} \sqrt{\frac{\rho_l}{\rho_{\text{tp}}}} \quad (187)$$

For the baseline case, the two-phase heat transfer coefficient is  $4,393 \text{ W/m}^2\text{-K}$ .

Figures 61 through 65 show the correlation of Boyko and Kruzhilin (1967) compared with the experimental data from the present study. This correlation predicts the data quite well: 96.8% of the test section C60 annular flow data are within  $\pm 25\%$  of the experimental value. However, the constant used here (0.024) was for stainless steel tube data, not aluminum (the metal used for the construction of the microchannel test sections). Boyko and Kruzhilin (1967) also suggested that a constant of 0.032 be used for copper tubes. As noted by Carey (1992), the fact that different constants were required for different tube-fluid combinations may reduce the usefulness of the correlation.

#### *Soliman (1986)*

Soliman (1986) presented a condensation heat transfer coefficient model for mist flow. The modified Weber number used by Soliman (1983) is defined as follows:

$$We_{so} = \begin{cases} 2.45 \cdot Re_v^{0.64} \left( \frac{\mu_v^2}{\rho_v \cdot \sigma \cdot D_h} \right)^{0.3} / \phi_v^{0.4} & \text{if } Re_1 \leq 1,250 \\ 0.85 \cdot Re_v^{0.79} \left( \frac{\mu_v^2}{\rho_v \cdot \sigma \cdot D_h} \right)^{0.3} \left[ \left( \frac{\mu_v}{\mu_l} \right)^2 \left( \frac{\rho_l}{\rho_v} \right) \right]^{-0.084} \left( \frac{X_{tt}}{\phi_v^{2.55}} \right)^{0.157} & \text{if } Re_1 > 1,250 \end{cases} \quad (188)$$

The vapor two-phase multiplier is defined by Lockhart and Martinelli (1949) as follows:

$$\phi_v = 1 + 1.09 \cdot X_{tt}^{0.039} \quad (189)$$

This two-phase multiplier is 2.055 for the annular flow baseline case, which yields a Weber number of 15.26.

For the mist flow region, the following correlation for the Nusselt number was proposed:

$$Nu = 0.00345 \cdot Re_m^{0.9} \left[ \frac{\mu_v \cdot h_{lv}}{k_v (T_{sat} - T_{wall})} \right]^{1/3} \quad (190)$$

where:

$$Re_m = \frac{GD}{\mu_m} \quad (191)$$

$$\mu_m = \left( \frac{x}{\mu_v} + \frac{1-x}{\mu_l} \right)^{-1} \quad (192)$$

The mixture viscosity is 2.867 kg/m-s for the baseline case, which yields a Reynolds number of 25,094. Therefore, the baseline case has a Nusselt number of 95.02, which yields a condensation heat transfer coefficient of 4,272 W/m<sup>2</sup>-K. As specified by the author, the modified Weber number must be above 30 to use this correlation. For the baseline case, the modified Weber number is 15.26, which does not meet this criterion. In fact, none of the condensation heat transfer data for test section C60 can meet this criterion. To obtain this Weber number criterion, Soliman (1986) compared the correlation of Akers et al. (1959) with data from a variety of horizontal and vertical tube data sets, which included steam, R-113, and R-12 condensing inside tubes ranging in diameter from 7.4 to 12.7 mm. Therefore, this Weber number model may not be valid for either R-134a and/or small tube diameters.

The correlation is compared with the experimental data from the present study in Figures 61 through 65. For the nominal mass fluxes of 150 and 300 kg/m<sup>2</sup>-s, the data are

predicted within  $\pm 16\%$ , with better agreement as the quality increases. For the remaining mass fluxes, the data are predicted well for qualities  $< 0.5$ . Above this quality, the data are over-predicted by the correlation between 20% and 35%. Since mist flow usually happens at high qualities and mass fluxes, this may mean that the correlation is not appropriate for small diameter tubes.

### Flow Regime-Based Correlations

In this section, both the intermittent and annular data are compared with existing flow regime-based heat transfer correlations. To facilitate the discussion, this section contains a sample calculation for each correlation for the annular flow data point presented in Table 6 for test section C60.

#### Nitheanandan et al. (1990)

Nitheanandan et al. (1990) developed an approach for the design of condensers using flow regime criteria. They used an existing heat transfer database, which included R-12, R-113, and steam condensing inside tubes with diameters ranging from 7.4 to 15.9 mm, to develop this approach. The type of flow was divided into three regimes: wavy, annular, and mist flow. For annular flow, the correlation presented by Shah (1979) is used. For mist flow, the correlation by Soliman (1986) is used. For the baseline case, the correlations by Shah (1979) and Soliman (1986) yield condensation heat transfer coefficients of 5,444  $\text{W/m}^2\text{-K}$  and 4,272  $\text{W/m}^2\text{-K}$ , respectively.

For wavy flow, the correlation presented by Akers and Rosson (1960) is used, which is as follows:

$$\text{Nu} = \begin{cases} \frac{13.8 \cdot \text{Pr}_1^{1/3} \left[ \text{Re}_v \left( \frac{\mu_v}{\mu_l} \right) \left( \frac{\rho_l}{\rho_v} \right)^{0.5} \right]^{0.2}}{\left[ \frac{\text{Cp}_1 (T_{\text{sat}} - T_{\text{wall}})}{h_{lv}} \right]^{1/6}} & \text{if } \text{Re}_v \left( \frac{\mu_v}{\mu_l} \right) \left( \frac{\rho_l}{\rho_v} \right)^{0.5} < 20,000 \\ \frac{0.1 \cdot \text{Pr}_1^{1/3} \left[ \text{Re}_v \left( \frac{\mu_v}{\mu_l} \right) \left( \frac{\rho_l}{\rho_v} \right)^{0.5} \right]^{2/3}}{\left[ \frac{\text{Cp}_1 (T_{\text{sat}} - T_{\text{wall}})}{h_{lv}} \right]^{1/6}} & \text{if } \text{Re}_v \left( \frac{\mu_v}{\mu_l} \right) \left( \frac{\rho_l}{\rho_v} \right)^{0.5} \geq 20,000 \end{cases} \quad (193)$$

For the baseline case, this Nusselt number is 208.6, which yields a condensation heat transfer coefficient of 9,376  $\text{W/m}^2\text{-K}$ .

To distinguish between wavy and mist/annular flow, Nitheanandan et al. (1990) used the modified Froude number proposed by Soliman (1982), which is as follows:

$$Fr_{so} = \begin{cases} 0.025 \cdot Re_1^{1.59} \left( \frac{1 + 1.09 \cdot X_{tt}^{0.039}}{X_{tt}} \right)^{1.5} \frac{1}{Ga^{0.5}} & \text{if } Re_1 \leq 1,250 \\ 1.26 \cdot Re_1^{1.04} \left( \frac{1 + 1.09 \cdot X_{tt}^{0.039}}{X_{tt}} \right)^{1.5} \frac{1}{Ga^{0.5}} & \text{if } Re_1 > 1,250 \end{cases} \quad (194)$$

For modified Froude numbers  $< 7$ , the flow is wavy, while a modified Froude number  $\geq 7$  means the flow is either mist or annular. In the baseline case, the modified Froude number is 38.36, which means the flow is either mist or annular.

To distinguish between mist and annular flows, the modified Weber number presented by Soliman (1983) is used, which is 15.26 in this case. For modified Weber numbers  $< 40$ , the flow is annular, while Weber numbers  $\geq 40$  result in mist flow. Therefore, the flow is annular for the baseline case, and the condensation heat transfer coefficient, as determined by Shah (1979), is 5,444 W/m<sup>2</sup>-K. In fact, none of the heat transfer data on the circular microchannels were in the mist flow region based on this criterion, which is not the case in the present study.

Figures 66 through 70 show the correlation of Nitheanandan et al. (1990) compared with the experimental data. Based on the modified Froude number criteria, only the lowest quality at the lowest mass flux lies in the wavy flow regime. At this point, the correlation of Akers and Rosson (1960) substantially over-predicts the experimental heat transfer coefficient (6,580 W/m<sup>2</sup>-K vs. 1,670 W/m<sup>2</sup>-K for the experimental data). This point was not included on Figure 66 to allow for closer examination of the other data points. Moreover, the rest of the experimental data are predicted to be in annular flow for all mass fluxes. Hence, the correlation by Shah (1979) is used for the rest of the condensation heat transfer coefficients. With the exception of the lowest quality at the lowest flow rate, the comparison between the experimental data and Nitheanandan et al. (1990) is the same as the comparison between the data and Shah (1979), which over-predicts all of the heat transfer data. This may also mean that the flow regime criteria described above are not accurate for small diameter tubes.

### **Dobson and Chato (1998)**

Dobson and Chato (1998) developed a flow regime-based correlation for

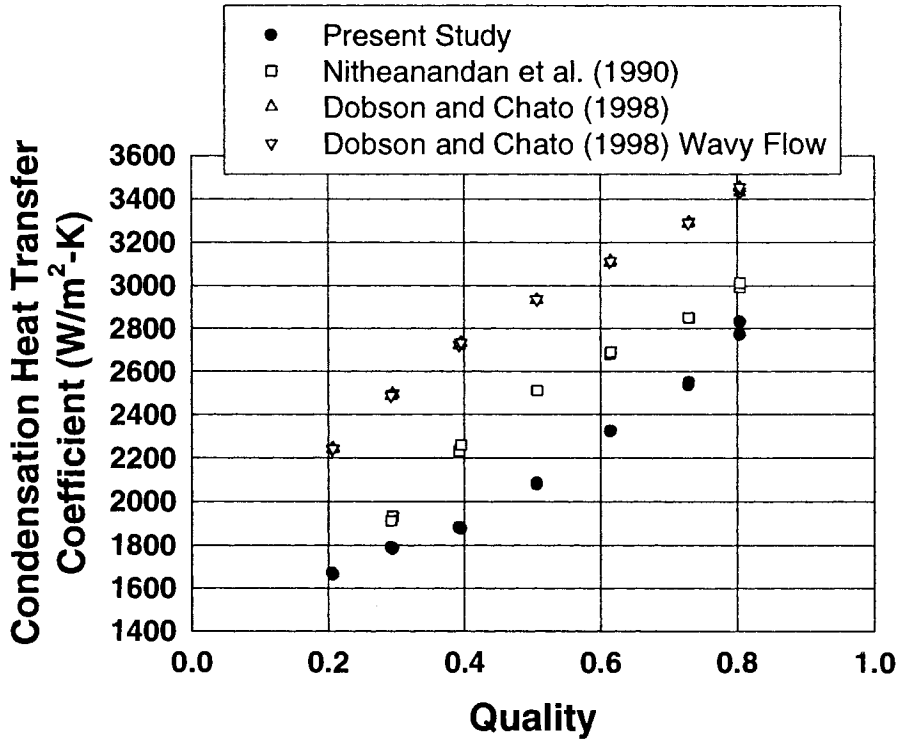


Figure 66. Flow Regime-Based Correlations and Experimental Heat Transfer Coefficients for Test Section C60 at  $G = 150 \text{ kg/m}^2\text{-s}$

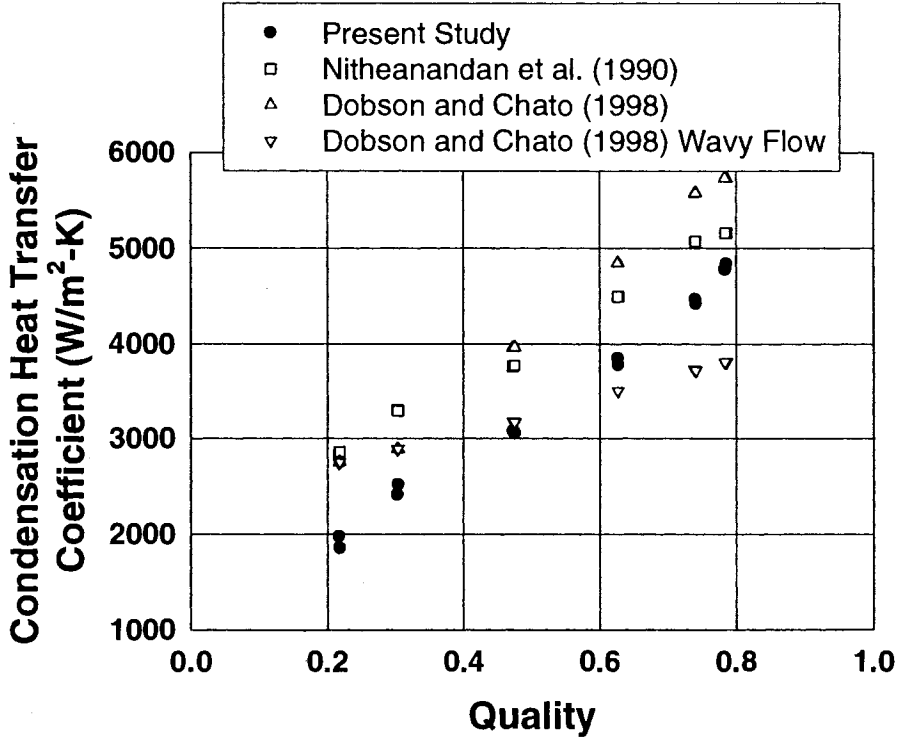


Figure 67. Flow Regime-Based Correlations and Experimental Heat Transfer Coefficients for Test Section C60 at  $G = 300 \text{ kg/m}^2\text{-s}$

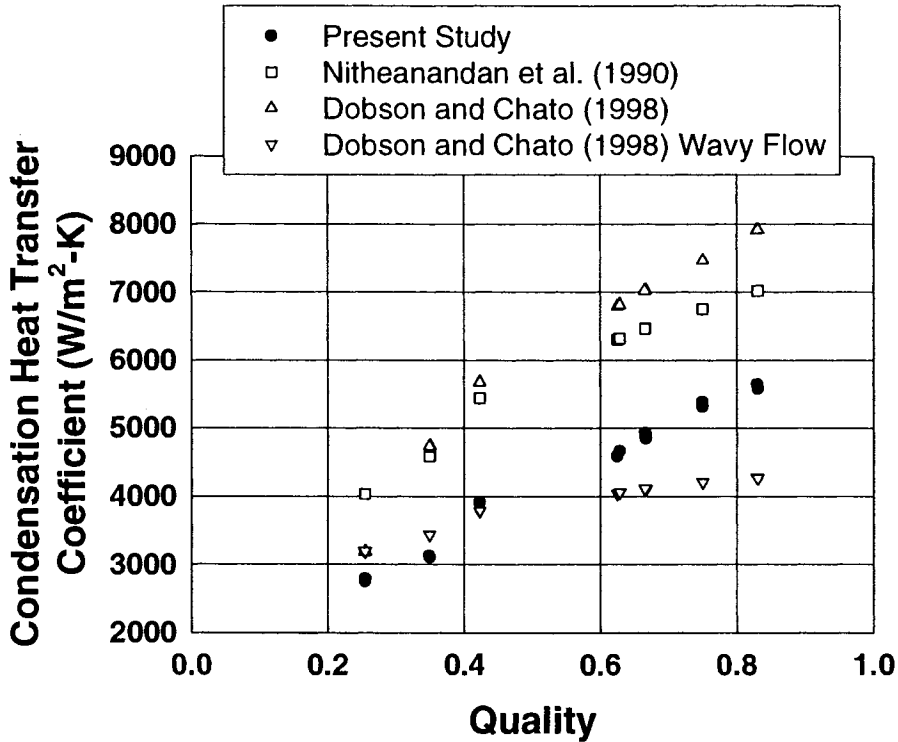


Figure 68. Flow Regime-Based Correlations and Experimental Heat Transfer Coefficients for Test Section C60 at  $G = 450 \text{ kg/m}^2\text{-s}$

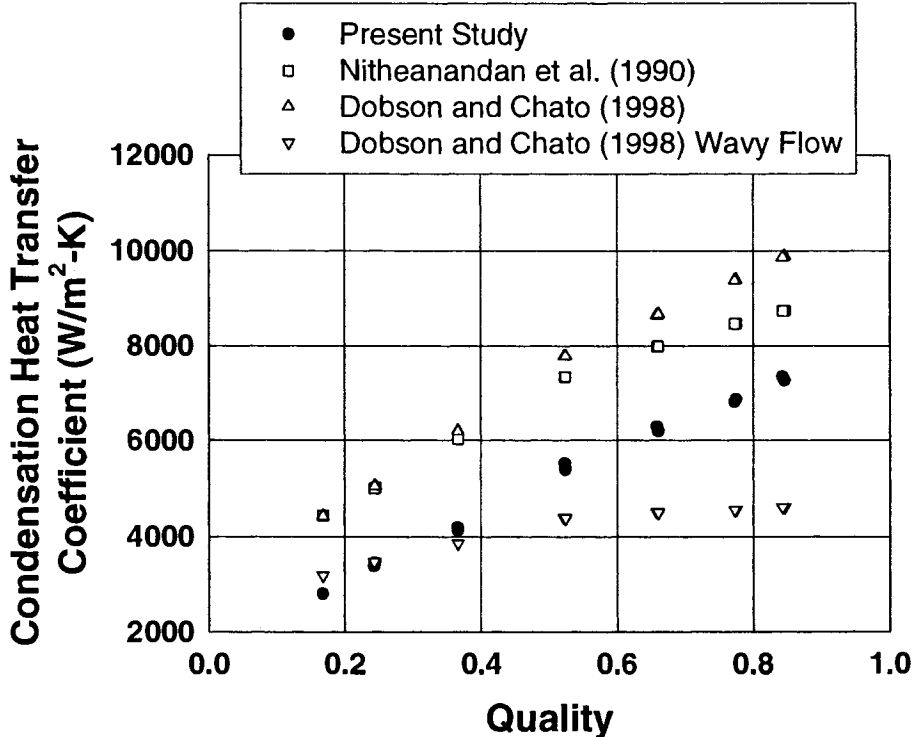


Figure 69. Flow Regime-Based Correlations and Experimental Heat Transfer Coefficients for Test Section C60 at  $G = 600 \text{ kg/m}^2\text{-s}$

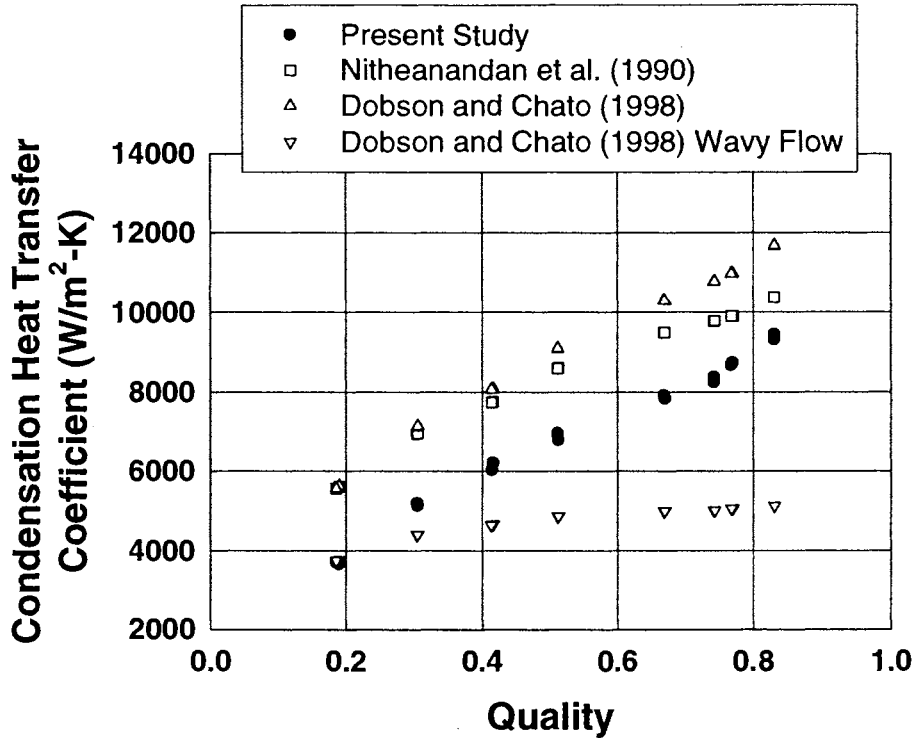


Figure 70. Flow Regime-Based Correlations and Experimental Heat Transfer Coefficients for Test Section C60 at  $G = 750 \text{ kg/m}^2\text{-s}$

condensation heat transfer inside horizontal tubes with diameters ranging from 3.14 mm to 7.04 mm. The two major modes of heat transfer selected by Dobson and Chato (1998) were gravity-driven and shear-driven. Gravity-driven heat transfer exists in wavy flow (i.e. stratified, stratified-wavy, and intermittent), while shear-driven heat transfer occurs in annular flow. To differentiate between the two modes of heat transfer, Dobson and Chato (1998) used the modified Froude number proposed by Soliman (1982), which is 38.36 for the annular flow baseline case.

Similar to Rosson and Myers (1965), Dobson and Chato (1998) hypothesized that heat transfer in wavy flow is dependent on both laminar film condensation and liquid pool forced-convection. The forced convective heat transfer coefficient is as follows:

$$\text{Nu}_{\text{forced}} = 0.0195 \cdot \text{Re}_1^{0.8} \cdot \text{Pr}_1^{0.4} \phi_1 \quad (195)$$

where:

$$\phi_1 = \sqrt{1.376 + \frac{c_1}{X_{tt}^{c_2}}} \quad (196)$$

For  $\text{Fr}_1 \leq 0.7$ , the constants are as follows:

$$\begin{aligned} c_1 &= 4.172 + 5.48 \cdot Fr_1 - 1.564 \cdot Fr_1^2 \\ c_2 &= 1.773 - 0.169 \cdot Fr_1 \end{aligned} \quad (197)$$

For  $Fr_1 > 0.7$ , the constants  $c_1$  and  $c_2$  are 7.242 and 1.655, respectively. The liquid-phase Froude number is defined as follows:

$$Fr_1 = \frac{G^2}{g \cdot D \cdot \rho_l^2} \quad (198)$$

Since the liquid Froude number is 12.65, the constants  $c_1$  and  $c_2$  are 7.242 and 1.655, respectively. This results in a two-phase multiplier of 5.526, which yields a forced-convective Nusselt number of 103.98.

The Nusselt correlation presented by Dobson and Chato (1998) for wavy flow is as follows:

$$Nu = \frac{0.23 \cdot Re_{vo}^{0.12}}{1 + 1.11 \cdot X_{tt}^{0.58}} \left( \frac{Ga \cdot Pr_1}{Ja_1} \right)^{0.25} + \left[ \frac{\arccos(2 \cdot \alpha - 1)}{\pi} \right] Nu_{forced} \quad (199)$$

Using Zivi's (1964) correlation for void fraction (which is 0.8164 for the annular flow baseline case), the two-phase Nusselt number is 84.33, which yields a condensation heat transfer coefficient of 3,791 W/m<sup>2</sup>-K.

The annular flow Nusselt number correlation developed by Dobson and Chato (1998) is as follows:

$$Nu = 0.023 \cdot Re_1^{0.8} \cdot Pr_1^{0.4} \left( 1 + \frac{2.22}{X_{tt}^{0.89}} \right) \quad (200)$$

This Nusselt number is 126.4 for the baseline case, which yields a condensation heat transfer coefficient of 5,682 W/m<sup>2</sup>-K.

Dobson and Chato (1998) also provide criteria for the applicability of their correlations. For mass fluxes above 500 kg/m<sup>2</sup>-s, the annular flow correlation should be used. For mass fluxes below 500 kg/m<sup>2</sup>-s, the annular flow correlation should be used for modified Froude numbers (as defined by Soliman, 1982) greater than 20, while the wavy flow correlation should be used when the modified Froude number is less than 20. Since the modified Froude number is 38.26, the heat transfer coefficient is determined from the annular flow correlation, which is 5,682 W/m<sup>2</sup>-K.

Figures 66-70 show the correlation of Dobson and Chato (1998) compared with the experimental data from the present study. Also included in Figures 66-70 is the wavy flow correlation presented by Dobson and Chato (1998). Their correlation over-predicts all of the

data. At the lowest mass flux, the wavy flow correlation by Dobson and Chato (1998) is selected based on the mass flux and Froude number criteria. The data, however, are still over-predicted by the wavy flow correlation. For the nominal mass flux of  $300 \text{ kg/m}^2\text{-s}$ , only the lowest two quality points use the wavy flow correlation, while the rest of the data are predicted by the annular flow correlation. For this mass flux, the data are still significantly over-predicted by the correlation. However, the wavy flow correlation under-predicts the data at higher qualities. The lowest quality point for the nominal mass flux of  $450 \text{ kg/m}^2\text{-s}$  utilizes the wavy flow correlation, while the rest of the data are predicted by the annular flow correlation. Again, the data are over-predicted by the correlation in all cases, while the wavy flow correlation under-predicts the high quality data. For the nominal mass fluxes of  $600$  and  $750 \text{ kg/m}^2\text{-s}$ , the correlation utilizes the annular flow model, which over-predicts all of the data. However, the wavy flow correlation from Dobson and Chato (1998) under-predicts all of the data for these mass fluxes.

## Summary

Although the comparisons with the literature for intermittent flow and annular flow presented here are for test sections C30 and C60, respectively, the results for the other circular microchannels test sections yielded similar results. The remaining comparisons are given in the Appendix D.

The correlations presented above were selected to represent a wide range of approaches to predict condensation heat transfer coefficients. The gravity-driven correlations did not predict the intermittent data well, suggesting that they may not be applicable to the intermittent data on the microchannel test sections, essentially due to the absence of such stratified regimes for these tubes. The shear driven correlations of Chen et al. (1987) and Moser et al. (1998) predict the annular data very well, but the slight over-prediction at low qualities and under-prediction at high qualities needs to be addressed. The homogeneous correlation of Boyko and Kruzhilin (1967) does predict the data well, but requiring different constants for different fluid/tube combinations is a concern. Although mist flow existed for a wide range of qualities and flow rates, the homogeneous correlation of Soliman (1986) over-predicts the data, especially for high quality/mass flux situations, which are in the mist flow pattern. The correlations of Nitheanandan et al. (1990), and Dobson and Chato (1998) are flow regime-based, but they assume an abrupt change in the flow, as opposed to gradual, and generally over-predict the data.

## Heat Transfer Models

In this section, condensation heat transfer models for annular, mist, and intermittent

flow are developed and compared with the experimental data. As described above, the degree of overlap in the flow regime increases with decreasing diameter. Thus, at first, models are developed for each flow pattern, followed by a quality-based averaging to account for the presence of multiple regimes for a data point.

## Circular Microchannels

### Annular Film Flow

The annular film flow model presented here is based on the boundary layer analyses of Traviss et al. (1973) and Moser et al. (1998). In these models, entrainment is assumed to be negligible. Assuming incompressible, steady-state flow, an axial momentum balance on the liquid film for cylindrical coordinates results in the following:

$$\frac{1}{r} \frac{\partial}{\partial r} (r \cdot \tau) = \frac{dP}{dz} \quad (201)$$

The shear stress is defined by:

$$\tau = \mu \frac{du}{dr} \quad (202)$$

By definition, the shear stress is zero at  $r = 0$ . Therefore, after introducing the variable  $y = R - r$  ( $R$  is the fixed radius of the tube), the shear stress distribution can be expressed as:

$$\frac{\tau}{\tau_w} = 1 - \frac{y}{R} \quad (203)$$

From the von Karman analogy between heat transfer and momentum, the shear stress can also be written as follows:

$$\tau = (\mu + \rho \cdot \epsilon_m) \frac{du}{dy} \quad (204)$$

In addition, the following turbulent boundary layer parameters are defined:

$$u^+ = \frac{u}{u^*} \quad (205)$$

$$y^+ = \frac{y \cdot \rho_1 \cdot u^*}{\mu_1} \quad (206)$$

$$R^+ = \frac{R \cdot \rho_1 \cdot u^*}{\mu_1} \quad (207)$$

where the friction velocity is as follows:

$$u^* = \sqrt{\frac{\tau_w}{\rho_1}} \quad (208)$$

Substituting these parameters into equation 4 and re-arranging results in the following:

$$\frac{\rho_1 \cdot \epsilon_m}{\mu_1} = \frac{1 - y^+/R^+}{du^+/dy^+} - 1 \quad (209)$$

In annular flow, the film thickness is thin compared to the tube radius. Hence, the von Karman universal velocity profile for flat plate flow is assumed to be valid for the liquid film and is as follows:

$$u^+ = \begin{cases} y^+ & \text{if } \delta^+ \leq 5 \\ -3.05 + 5 \cdot \ln y^+ & \text{if } 5 < \delta^+ \leq 30 \\ 5.5 + 2.5 \cdot \ln y^+ & \text{if } \delta^+ \geq 30 \end{cases} \quad (210)$$

The dimensionless turbulent film thickness is defined as follows:

$$\delta^+ = \frac{\delta \cdot \rho_1 \cdot u^*}{\mu_1} \quad (211)$$

Differentiating equation 210 with respect to  $y^+$  results in the following:

$$\frac{du^+}{dy^+} = \begin{cases} 1 & \text{if } \delta^+ \leq 5 \\ 5/y^+ & \text{if } 5 < \delta^+ \leq 30 \\ 2.5/y^+ & \text{if } \delta^+ \geq 30 \end{cases} \quad (212)$$

Substituting this into equation 209 results in the following (Moser et al., 1998):

$$\frac{\rho_1 \cdot \epsilon_m}{\mu_1} = \begin{cases} 0 & \text{if } \delta^+ \leq 5 \\ \frac{y^+}{5} - 1 & \text{if } 5 < \delta^+ \leq 30 \\ \frac{y^+}{2.5} (1 - y^+/R^+) - 1 & \text{if } \delta^+ \geq 30 \end{cases} \quad (213)$$

The expressions for the laminar and buffer shear layers in equation 213 are simplified because the turbulent film thickness is small compared to the dimensional radius.

Returning to the von Karman analogy between heat transfer and momentum, the heat flux is expressed as follows:

$$q'' = -(k + \epsilon_h \cdot \rho \cdot C_p) \frac{dT}{dy} \quad (214)$$

The turbulent dimensionless temperature is defined as follows:

$$T^+ = \frac{\rho_l \cdot C_{p_l} \cdot u^*}{q''} (T_i - T_w) \quad (215)$$

Therefore, for a constant wall temperature over the circumference, equation 214 can be represented as follows:

$$\frac{dT^+}{dy^+} = \left( \frac{1}{Pr_1} + \frac{\rho_l \cdot \epsilon_h}{\mu_l} \right)^{-1} \quad (216)$$

Integrating equation 216 requires the knowledge of the turbulent film thickness. Traviss et al. (1973) obtained the following expression for the film thickness from continuity and a curve-fit while employing the von Karman velocity profile:

$$\delta^+ = \begin{cases} 0.7071 \cdot Re_1^{0.5} & \text{if } Re_1 \leq 50 \\ 0.4018 \cdot Re_1^{0.585} & \text{if } 50 < Re_1 \leq 1125 \\ 0.095 \cdot Re_1^{0.812} & \text{if } Re_1 > 1125 \end{cases} \quad (217)$$

Hence, the turbulent temperature as a function of the turbulent film thickness is as follows:

$$T^+ = \begin{cases} \delta^+ \cdot Pr_1 & \text{if } \delta^+ \leq 5 \\ 5 \cdot Pr_1 + 5 \cdot \ln \left[ Pr_1 \left( \frac{\delta^+}{5} - 1 \right) + 1 \right] & \text{if } 5 < \delta^+ \leq 30 \\ 5 \cdot Pr_1 + 5 \cdot \ln(5 \cdot Pr_1 + 1) + \int_{30}^{\delta^+} \frac{dy^+}{\left( \frac{1}{Pr_1} - 1 \right) + \frac{y^+}{5} \left( 1 - \frac{y^+}{R^+} \right)} & \text{if } \delta^+ \geq 30 \end{cases} \quad (218)$$

Traviss et al. (1973) approximated this as follows:

$$T^+ = \begin{cases} 0.707 \cdot Pr_1 \cdot Re_1^{0.5} & \text{if } Re_1 \leq 50 \\ 5 \cdot Pr_1 + 5 \cdot \ln \left[ Pr_1 (0.09636 \cdot Re_1^{0.585} - 1) + 1 \right] & \text{if } 50 < Re_1 \leq 1125 \\ 5 \cdot Pr_1 + 5 \cdot \ln(5 \cdot Pr_1 + 1) + 2.5 \ln(0.00313 \cdot Re_1^{0.812}) & \text{if } Re_1 \geq 1125 \end{cases} \quad (219)$$

Assuming that the all of the heat is transferred in the liquid film, the condensation heat transfer coefficient is expressed as follows:

$$h = \frac{q''}{(T_{sat} - T_w)} = \frac{\rho_l \cdot C_{p_l} \cdot u^*}{T^+} = \frac{C_{p_l} \sqrt{\rho_l \cdot \tau_w}}{T^+} \quad (220)$$

Hence, the wall shear stress is required to calculate the condensation heat transfer coefficient. Traviss et al. (1973) used the Lockhart and Martinelli (1949) correlation to calculate the frictional pressure drop, which was used to find the wall shear stress. Coleman (2000) showed that his microchannel pressure drop data were severely over-predicted by the correlation of Lockhart and Martinelli (1949). In addition, it was previously shown that the heat transfer data in this study were over-predicted by the heat transfer correlation of Traviss et al. (1973), which is presumably due to the inaccuracy of the pressure drop correlation of Lockhart and Martinelli (1949). To remedy this, the pressure drop correlation presented by Coleman (2000) is used to calculate the wall shear stress.

Coleman (2000) defines the interfacial shear stress as follows:

$$\tau_i = \frac{1}{2} f_i \frac{G^2 \cdot x^2}{\rho_v \cdot \alpha^2} \quad (221)$$

The void fraction is determined from the Baroczy (1965) correlation as follows:

$$\alpha = \left[ 1 + \left( \frac{1-x}{x} \right)^{0.74} \left( \frac{\rho_v}{\rho_l} \right)^{0.65} \left( \frac{\mu_l}{\mu_v} \right)^{0.13} \right]^{-1} \quad (222)$$

The interfacial friction factor is found from the following:

$$f_i = f_l \cdot C_1 \cdot (X_{tt})^{C_2} \quad (223)$$

The circular microchannel tube constants are as follows:

$$C_1 = 0.45 \left[ \frac{g(\rho_l - \rho_v) D^2}{\sigma} \right]^{0.073}$$

$$C_2 = 0.30$$

In Coleman (2000), the liquid friction factor is found from the Churchill (1977b) equation (see equation 41) using the actual liquid Reynolds number, i.e., the liquid phase flow area, rather than the entire tube cross-section, is used. Thus, this Reynolds number was calculated as follows:

$$Re_{l,act} = \frac{G(1-x)D_h}{\mu_l(1-\alpha)} \quad (224)$$

Figure 71 shows that the liquid Reynolds numbers used in Coleman (2000) to develop the interfacial friction factor model are all above 3000. In the present study, however, at the low mass flux cases, low (laminar) liquid phase Reynolds numbers caused a sudden, and perhaps

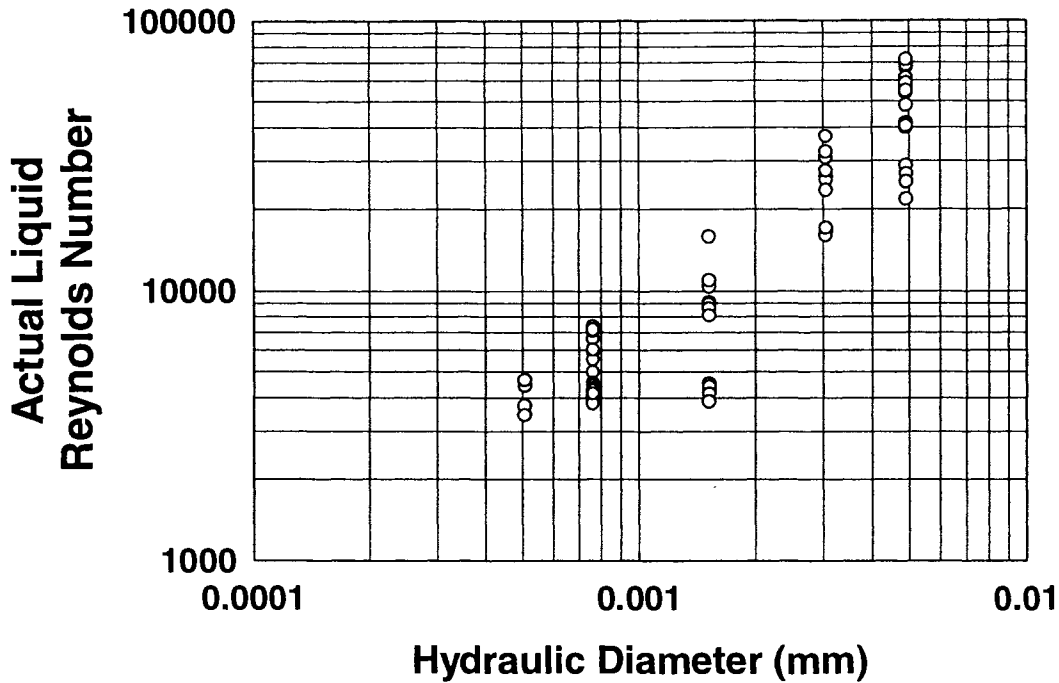


**Figure 71. Actual Liquid Reynolds Numbers as a Function of Hydraulic Diameter in Coleman (2000)**

unrealistic switch in the friction factor and heat transfer coefficient, reflecting a potential change in liquid phase flow regimes. However, this causes a spurious increase in heat transfer coefficient with diameter near the transition between these two regimes. To avoid this problem, the present work utilizes the turbulent friction factor correlation of Colebrook (1939) to ensure that only turbulent friction factors are obtained within the range of data considered in this region, which is as follows:

$$\frac{1}{\sqrt{f}} = -2.0 \cdot \log_{10} \left( \frac{\epsilon/D}{3.7} + \frac{2.51}{\text{Re} \sqrt{f}} \right) \quad (225)$$

For the annular film flow data points in Coleman (2000), the Churchill (1977b) and Colebrook (1939) are compared in Figure 72, which shows that the difference in friction factors is less than  $\pm 2\%$  of the Churchill (1977b) equation. For the present study, the relative roughnesses for test sections C20, C30, and C60 are all 0 for computing the liquid friction factor (Coleman, 2000).

The interfacial friction factor and shear stress are now used to determine the wall shear stress as follows:

$$\tau_w = \frac{\tau_i}{1 - \frac{\delta^+}{R^+}} \quad (226)$$

Since  $R^+$  is a function of the wall shear stress,  $\tau_w$  must be computed iteratively.

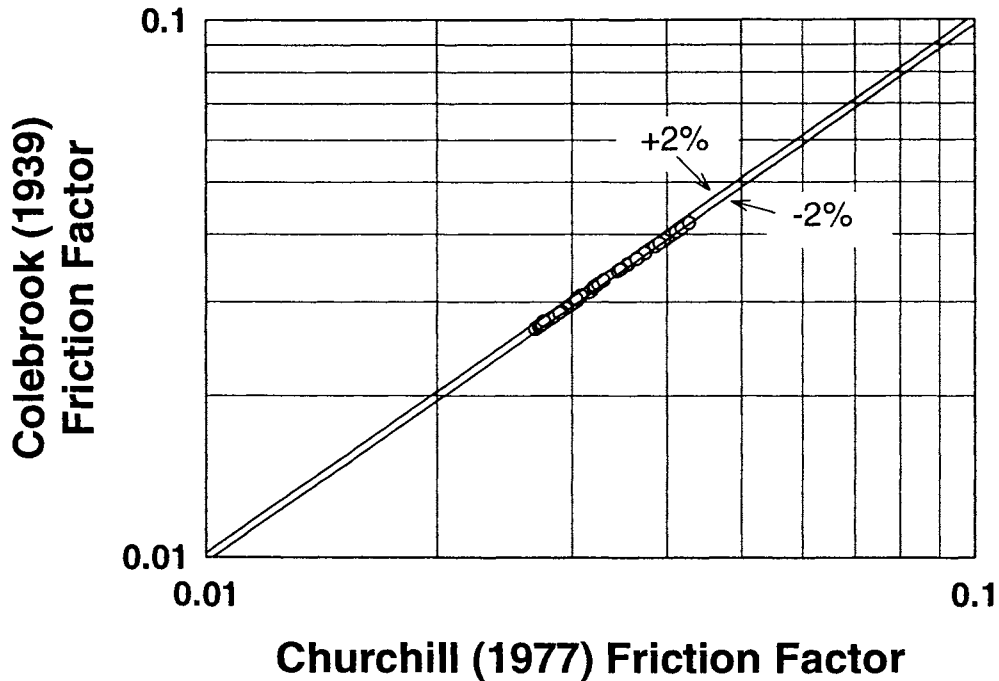


**Figure 72. Churchill (1977b) and Colebrook (1939) Friction Factors for Actual Liquid Reynolds Numbers in Coleman (2000)**

### Mist Flow

Mist flow, as described by Coleman (2000), consists of a uniform vapor mist with entrained liquid droplets. As discussed previously, Soliman (1986) developed a correlation for mist flow, but this correlation appears not to be valid for tubes with small hydraulic diameters. The proposed method for determining the condensation heat transfer coefficient for mist flow is based partly on Soliman's (1986) correlation.

The flow is assumed to be a homogeneous mixture of vapor and liquid, with both phases flowing at the same velocity. As in Soliman's (1986) correlation, the mixture Reynolds number is defined as follows:

$$Re_m = \frac{GD}{\mu_m} \quad (227)$$

The mixture viscosity is as follows:

$$\mu_m = \left( \frac{x}{\mu_v} + \frac{1-x}{\mu_l} \right)^{-1} \quad (228)$$

As in Soliman's (1986) correlation, this mixture Reynolds number and the vapor Prandtl number are used as the basis for the condensation heat transfer coefficient correlation. The final form of the condensation heat transfer coefficient is as follows:

$$h_{tp} = \frac{k_v \cdot Nu_{tp}}{D} = C \cdot \frac{k_v \cdot Nu_{m,Churchill}}{D} \quad (229)$$

The vapor thermal conductivity was selected for this equation because the mixture properties are closer to those of a vapor than a liquid due to the high qualities required for mist flow and the absence of a clearly discernible liquid film. The constant was found by comparing the mixture heat transfer coefficient ( $h_m$ ) with the experimental heat transfer coefficients in the present study for mist flow and near mist flow. (The near mist flow data included all points in the annular flow regime that are less than  $\Delta x = 0.15$  from the upper annular film flow transition. This was done because only ten data points existed in the solely mist flow pattern.) Contrary to the annular flow model, the relative roughnesses determined experimentally in Coleman (2000) for test sections C20, C30, and C60 (0.0003, 0.0005, and 0.0001, respectively) are used for the liquid Nusselt number and friction factor. The resulting constant was 4.987.

### Intermittent Flow

Relatively few data points were collected in the purely intermittent regime in this study (3 out of a total of 82) for the three circular tubes under consideration. Therefore, a linear interpolation between the liquid-only heat transfer coefficient at the end of the condensation process and the heat transfer coefficient at the beginning of the pure intermittent flow regime was used. For the tubes in this study, the two-phase flow regime changes from annular flow to intermittent flow to single-phase liquid flow with overlaps between these respective regimes during condensation. Hence, the lower limit of annular flow is the used as the upper limit of the pure intermittent flow regime. This interpolation scheme is as follows:

$$h_{int} = h_{lo} + \frac{x}{x_{ann,low}} (h_{ann,low} - h_{lo}) \quad (230)$$

The liquid only friction factor and Nusselt number (and, therefore,  $h_{lo}$ ) are calculated using the liquid only Reynolds number defined in equation 154 and the Churchill (1977b-a)

equations (41 and 72, respectively) with the relative roughness from Coleman (2000). The heat transfer coefficient at the lower limit of annular flow, required for this equation, is explained in the following section.

### Overall Model

The annular, mist, and intermittent models presented above assume that only one flow regime is exhibited at a given combination of mass flux and quality. However, as stated previously, large regions of overlap between multiple flow regimes existed for the circular microchannel test sections. Consequently, interpolation schemes were used to calculate the condensation heat transfer coefficient for transitioning flow between multiple flow regimes.

Figure 73 shows the possible two-phase flow zones during the condensation process for test section C30 ( $D_h = 0.761$  mm). These zones are the same for test sections C20 and C60, with one notable exception. In Figure 57, we can see that for low mass fluxes, specifically the  $G = 150$  kg/m<sup>2</sup>-s case, the flow pattern changes from annular to an undefined region to intermittent flow. In Coleman (2000), wavy flow existed for the 2 x 2 mm tube but not for the 1 x 1 mm tube. Since the hydraulic diameter for test section C60 (1.524 mm) is in between the diameters of these two tubes, this very small region could be wavy flow. However, the flow in this zone is assumed to be purely annular film for the present study.

In Figure 73, the horizontal line at  $G \sim 470$  kg/m<sup>2</sup>-s represents the distinction between two condensation paths and occurs when  $x_{mist,low} = x_{int,up}$ . Below this line, the flow changes from mist to mist/annular (where applicable) to annular to annular/intermittent to intermittent to single-phase liquid during condensation. Above this line, the flow path is different. No pure annular film flow exists, whereas intermittent/annular/mist flow is present. Therefore, the interpolation schemes depend on whether the  $x_{mist,low} < x_{int,up}$  or  $x_{mist,low} > x_{int,up}$  for the mass flux and hydraulic diameter under consideration. A brief description of each of the condensation zones is given in Table 7.

In Zone 1, the flow is purely intermittent and equation 230 is used to find the condensation heat transfer coefficient. The heat transfer coefficient at the lower annular film flow limit is calculated as follows:

$$h_{ann,low} = h_{lo} + \frac{x_{ann,low}}{x_{int,up}} (h_{int,up} - h_{lo}) \quad (231)$$

The heat transfer coefficient at the upper limit of intermittent flow is calculated using the annular film flow model at that quality. This equation also works for test section C60 because the lower limit of annular film flow is equal to the upper limit of intermittent flow, i.e., there is no overlap between these two regimes for that test section.

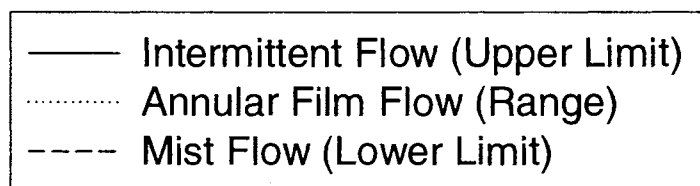
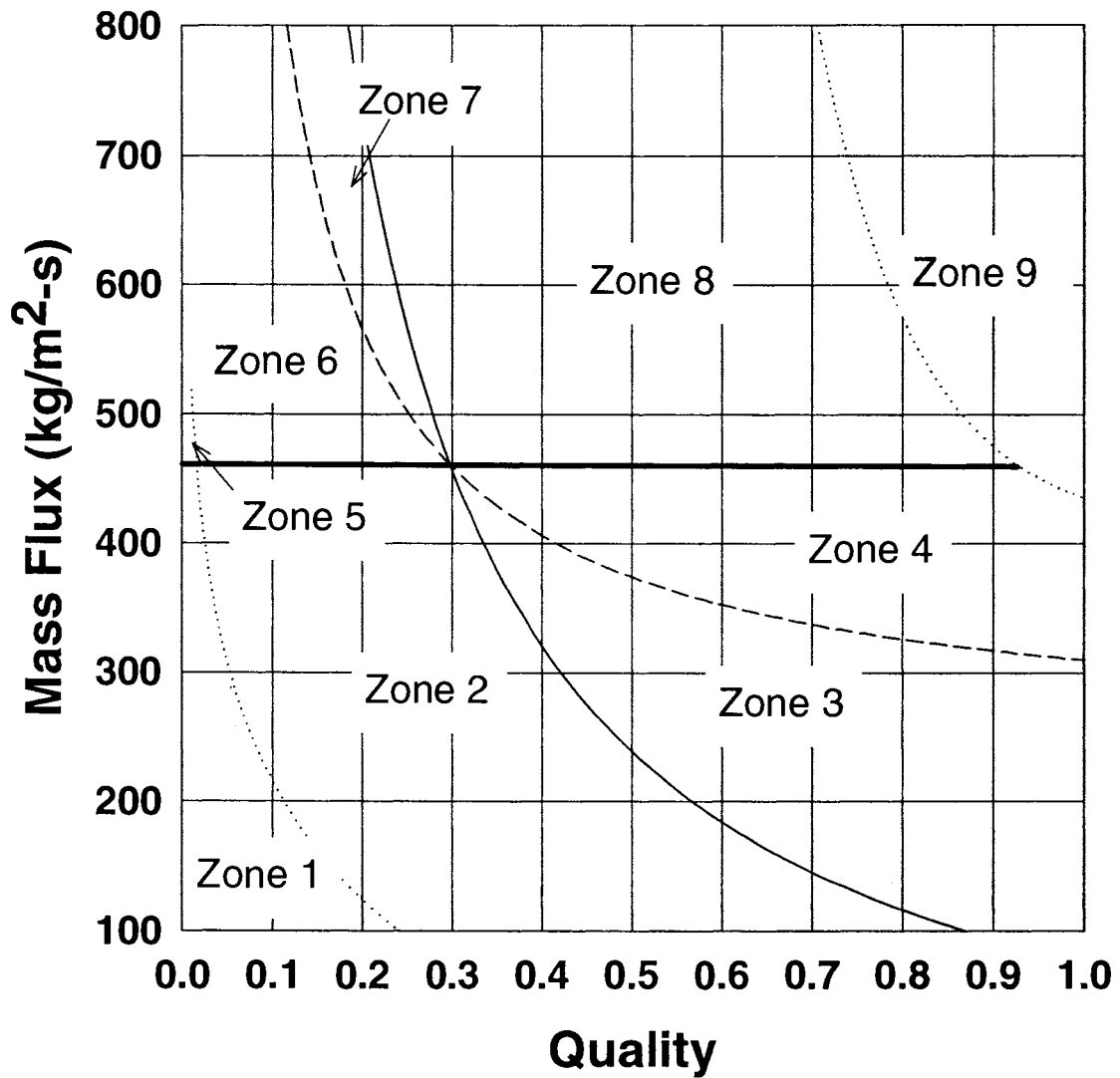


Figure 73. Condensation Heat Transfer Zones for Test Section C30

**Table 7. Description of Condensation Heat Transfer Zones in the Present Study**

<b>Zone</b>	<b>Description</b>
1	Intermittent
2	Intermittent/Annular Film
3	Annular Film
4	Annular Film/Mist
5	Intermittent
6	Intermittent/Annular Film
7	Intermittent/Annular Film/Mist
8	Annular Film/Mist
9	Mist

following interpolation equation is used for this region:

$$h_{int/ann} = h_{ann,low} + \frac{x - x_{ann,low}}{x_{int,up} - x_{ann,low}} (h_{int,up} - h_{ann,low}) \quad (232)$$

The heat transfer coefficients for the lower limit of annular film flow and the upper limit of intermittent flow for Zone 2 are the same as those described above for Zone 1.

Zones 3 and 9 are both pure annular film and mist flows, respectively, and the corresponding models presented previously are used to find their heat transfer coefficients. Zone 4 represents the transition region between annular film and mist flows, and the interpolated heat transfer coefficient is calculated as follows:

$$h_{ann/mist} = h_{mist,low} + \frac{x - x_{mist,low}}{x_{ann,up} - x_{mist,low}} (h_{ann,up} - h_{mist,low}) \quad (233)$$

The heat transfer coefficients at the lower and upper quality limits for mist and upper annular film flow, respectively, are calculated using the annular film and mist flow models. This ensures that the correct heat transfer coefficient is obtained at both extremes.

Zone 5 is pure intermittent flow, but, unlike Zone 1, the flow does not directly change from intermittent to annular film. The heat transfer coefficient for Zone 5 is calculated using equation 230, but  $h_{ann,low}$  is calculated differently as follows:

$$h_{ann,low} = h_{lo} + \frac{x_{ann,low}}{x_{mist,low}} (h_{mist,low} - h_{lo}) \quad (234)$$

The heat transfer coefficient at the lower limit of mist flow is calculated as follows:

$$h_{mist,low} = h_{lo} + \frac{x_{mist,low}}{x_{int,up}} (h_{int,up,total} - h_{lo}) \quad (235)$$

At the intermittent upper quality limit, the flow is both mist and annular film, and the total

heat transfer coefficient is calculated as follows:

$$h_{\text{int,up,total}} = h_{\text{mist,low}} + \frac{X_{\text{int,up}} - X_{\text{mist,low}}}{X_{\text{ann,up}} - X_{\text{mist,low}}} (h_{\text{int,up}} - h_{\text{mist,low}}) \quad (236)$$

The local heat transfer coefficients at the mist lower limit and intermittent upper limit are found using the annular film and mist flow models, respectively.

Zone 6 is both annular film and intermittent, and the corresponding heat transfer coefficient is calculated as follows:

$$h_{\text{int/ann}} = h_{\text{lo}} + \frac{X}{X_{\text{mist,low}}} (h_{\text{mist,low}} - h_{\text{lo}}) \quad (237)$$

The heat transfer coefficient at the lower limit of mist flow is calculated using equations 235 and 236.

Zone 7 is intermittent/annular/mist flow, and the corresponding heat transfer coefficient is calculated as follows:

$$h_{\text{int/ann/mist}} = h_{\text{mist,low}} + \frac{X - X_{\text{mist,low}}}{X_{\text{int,up}} - X_{\text{mist,low}}} (h_{\text{int,up,total}} - h_{\text{mist,low}}) \quad (238)$$

The total and local heat transfer coefficients at the upper limit of intermittent flow and lower limit of mist flow are calculated using equations 235 and 236.

Zone 8 is a combination of annular and mist flows, with the heat transfer coefficient calculated as follows:

$$h_{\text{ann/mist}} = h_{\text{int,up,total}} + \frac{X - X_{\text{int,up}}}{X_{\text{ann,up}} - X_{\text{int,up}}} (h_{\text{ann,up}} - h_{\text{int,up,total}}) \quad (239)$$

The total heat transfer coefficient at the intermittent flow upper limit is calculated using equation 236, while the heat transfer coefficient at the annular film flow upper limit is calculated using the pure mist flow model.

The models discussed above for annular, mist, and intermittent flow are compared with the condensation heat transfer data from the circular microchannels in Figure 74, with 91% of data predicted by the overall model within  $\pm 25\%$  of the experimental value.

Figures 75-79 show the present model compared with the experimental heat transfer coefficients (with their associated uncertainties) for test section C60 with nominal mass fluxes of 150, 300, 450, 600, and 750 kg/m<sup>2</sup>-s. In general, these figures show good agreement between the experimental and predicted values.

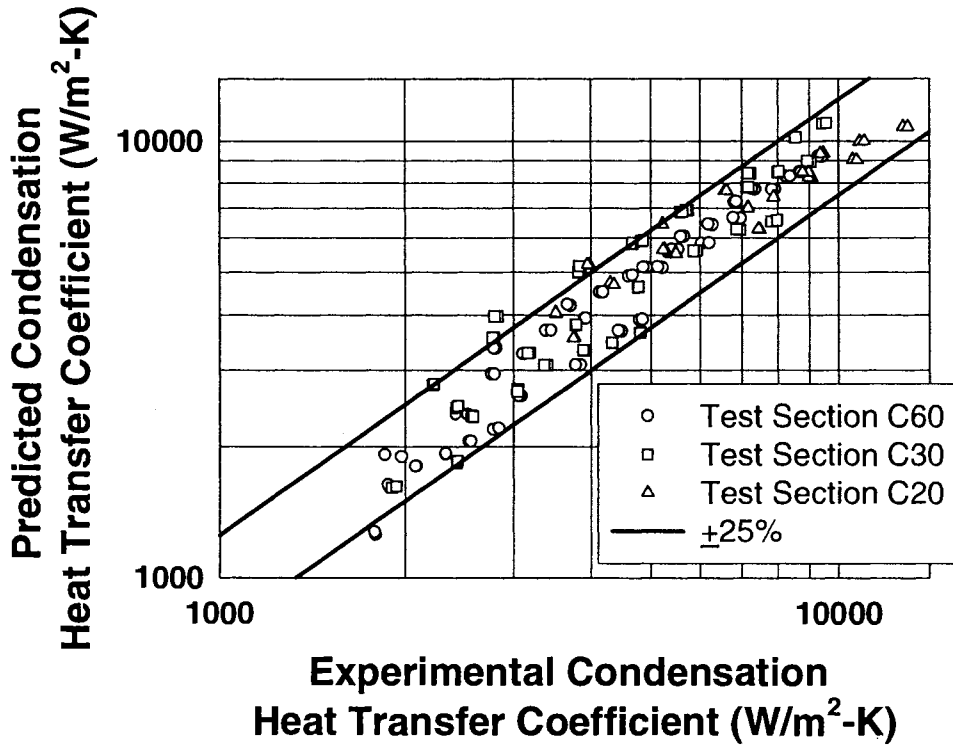


Figure 74. Predicted versus Experimental Condensation Heat Transfer Coefficients for Test Sections C20, C30, and C60

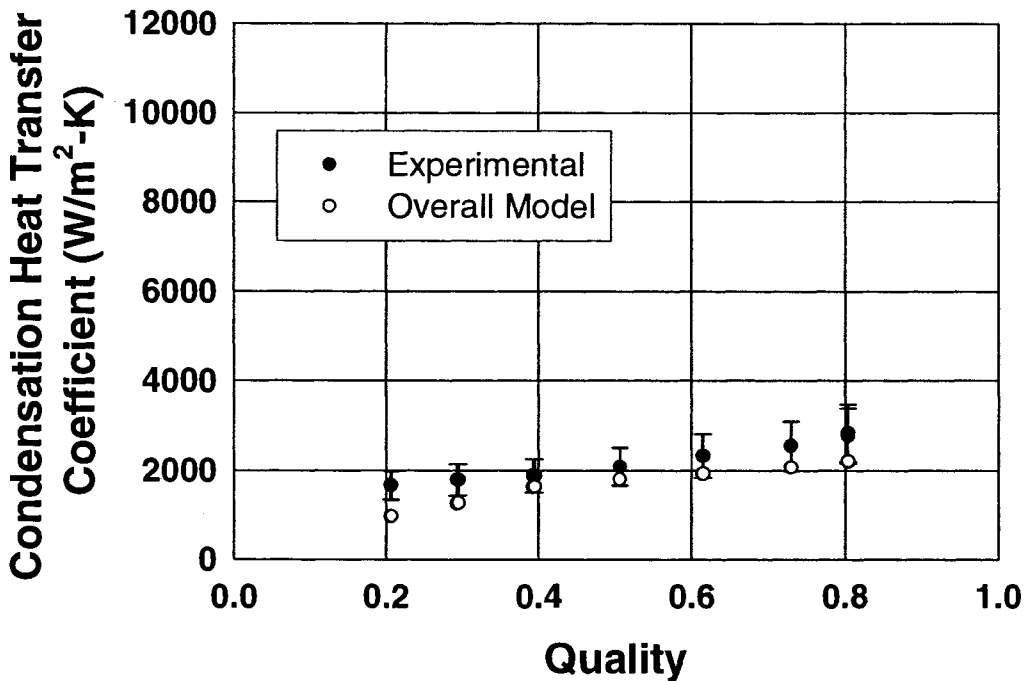


Figure 75. Predicted and Experimental Condensation Heat Transfer Coefficients for Test Section C60 and  $G = 150 \text{ kg/m}^2\text{-s}$

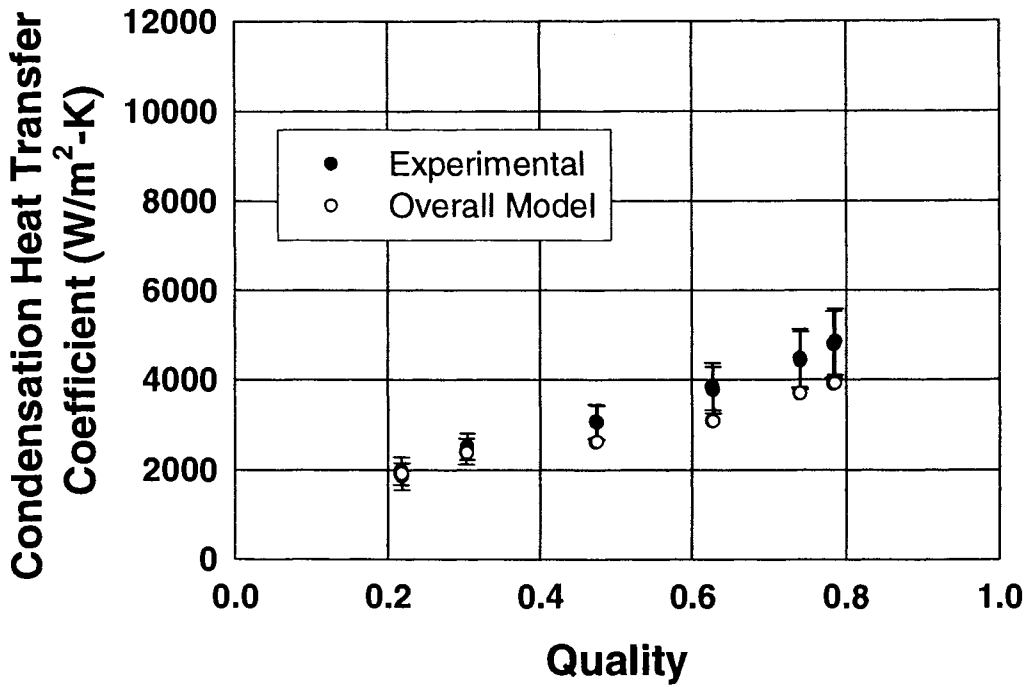


Figure 76. Predicted and Experimental Condensation Heat Transfer Coefficients for Test Section C60 and  $G = 300 \text{ kg/m}^2\text{-s}$

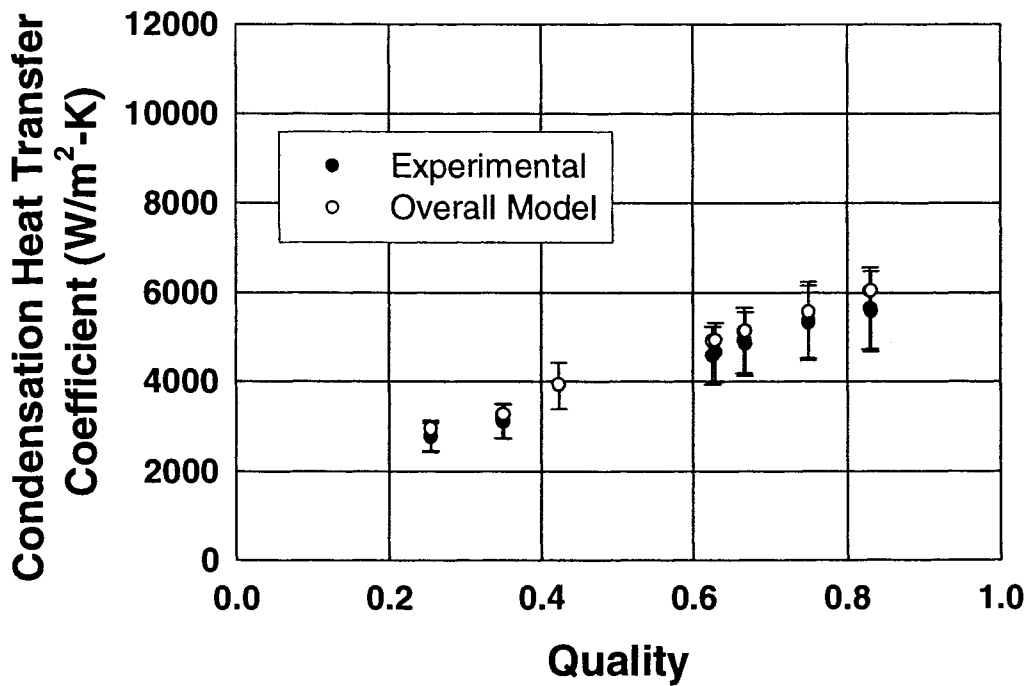


Figure 77. Predicted and Experimental Condensation Heat Transfer Coefficients for Test Section C60 and  $G = 450 \text{ kg/m}^2\text{-s}$

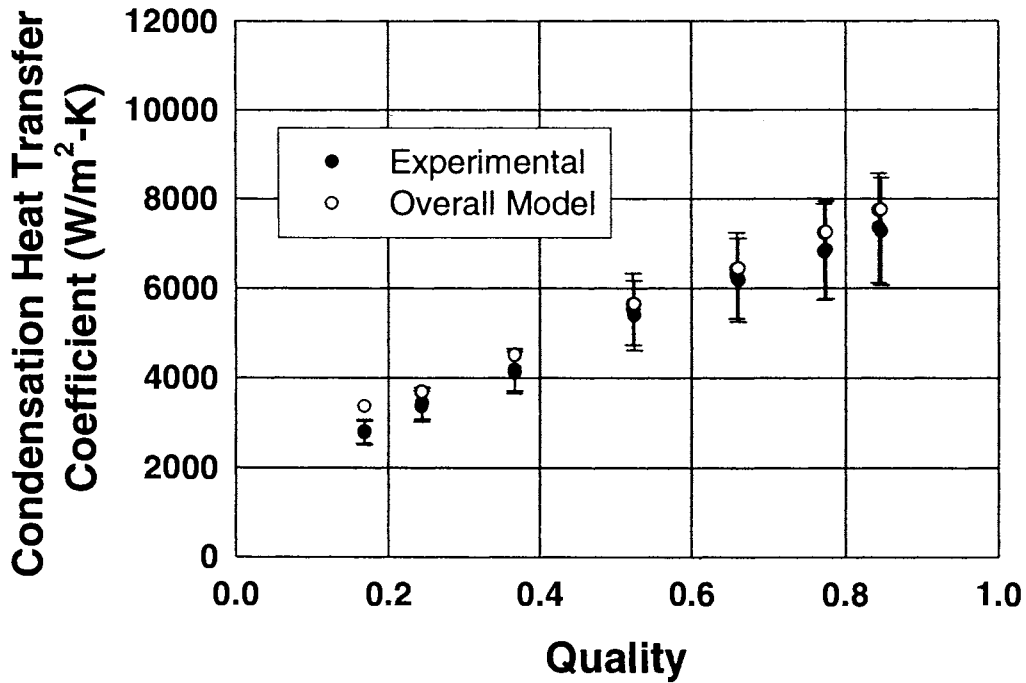


Figure 78. Predicted and Experimental Condensation Heat Transfer Coefficients for Test Section C60 and  $G = 600 \text{ kg/m}^2\text{-s}$

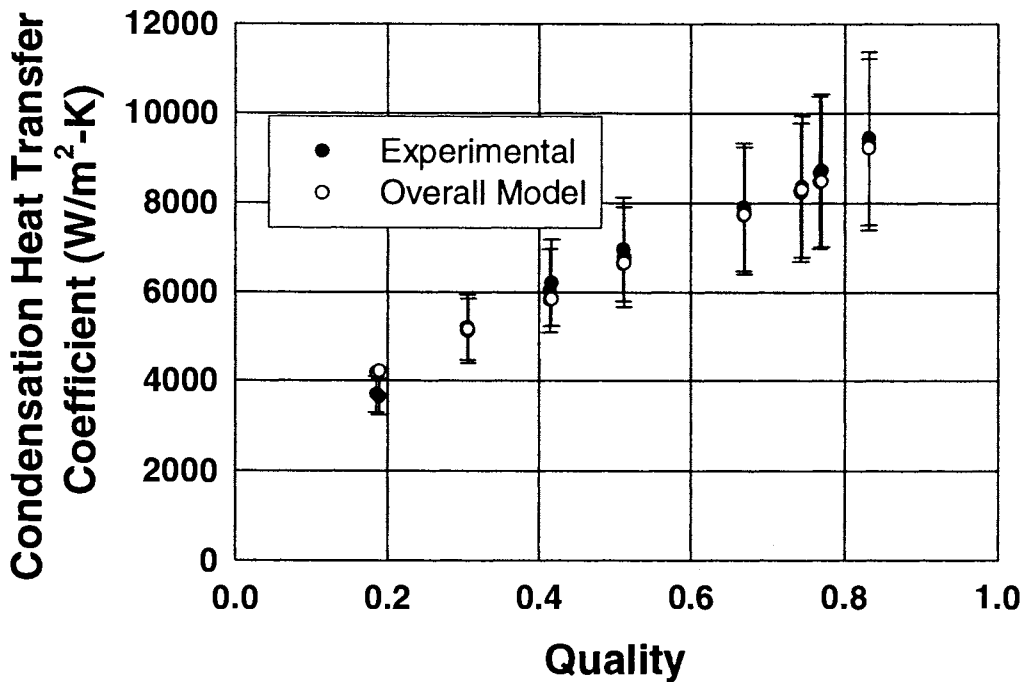


Figure 79. Predicted and Experimental Condensation Heat Transfer Coefficients for Test Section C60 and  $G = 750 \text{ kg/m}^2\text{-s}$

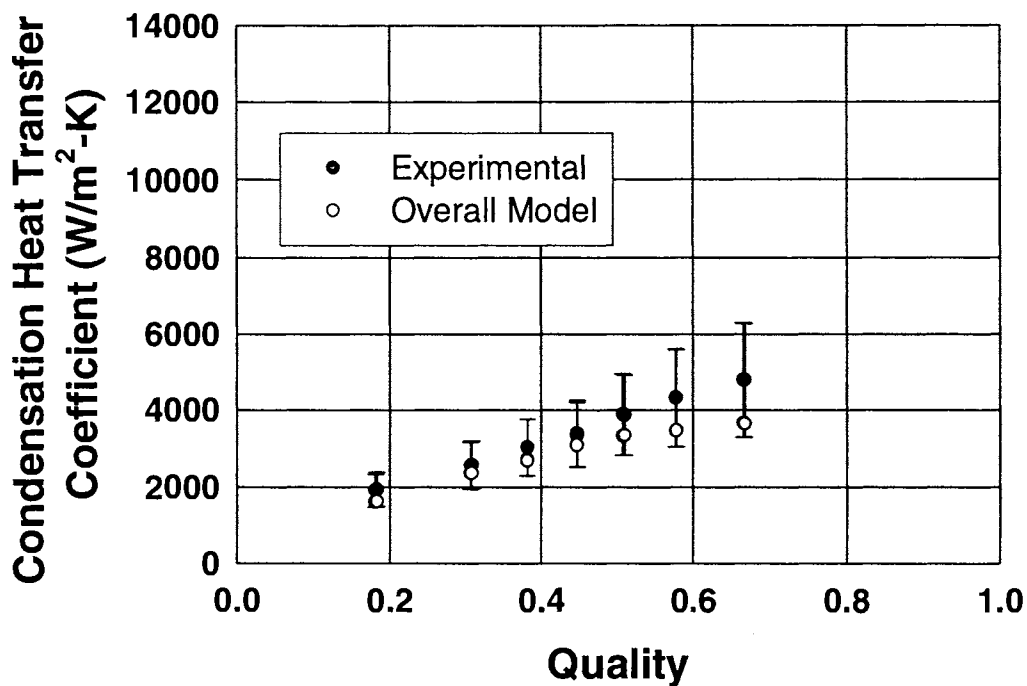


Figure 80. Predicted and Experimental Condensation Heat Transfer Coefficients for Test Section C30 and  $G = 300 \text{ kg/m}^2\text{-s}$

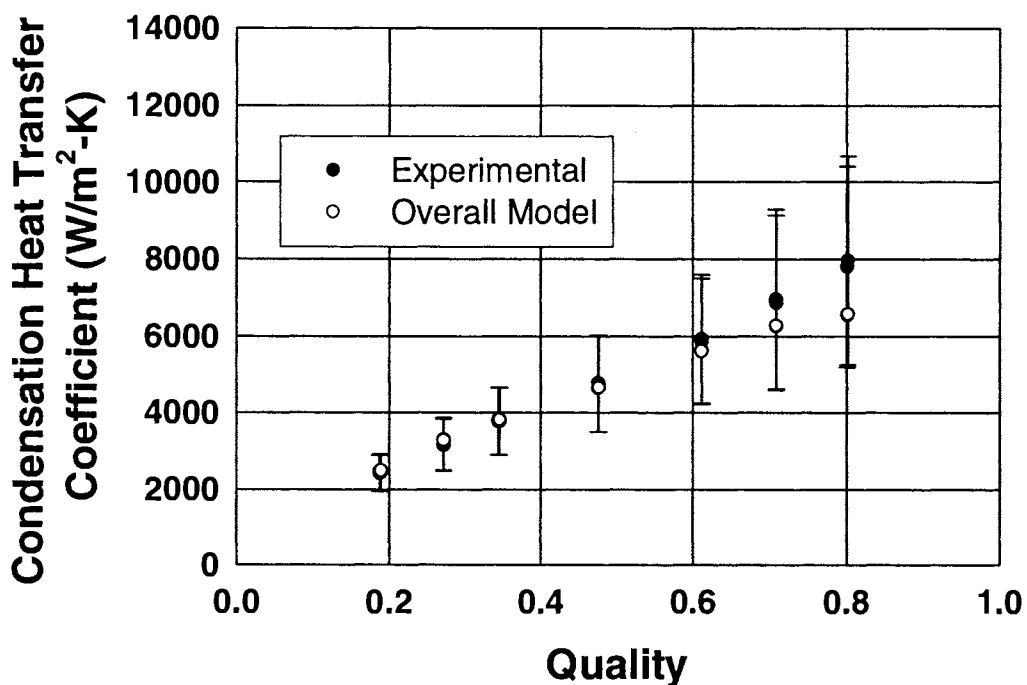


Figure 81. Predicted and Experimental Condensation Heat Transfer Coefficients for Test Section C30 and  $G = 450 \text{ kg/m}^2\text{-s}$

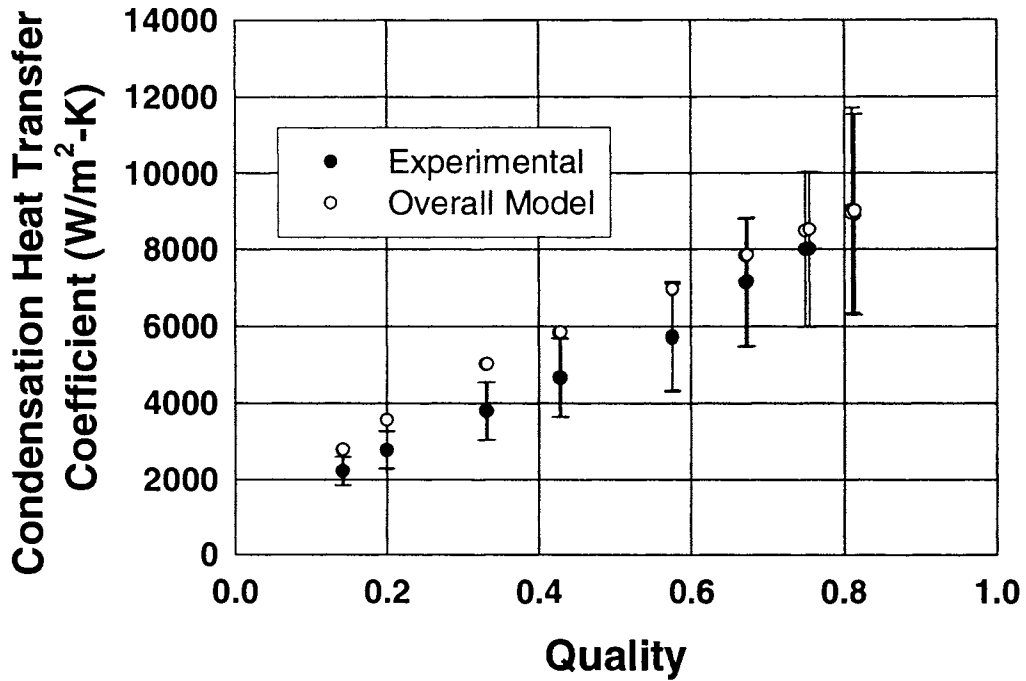


Figure 82. Predicted and Experimental Condensation Heat Transfer Coefficients for Test Section C30 and  $G = 600 \text{ kg/m}^2\text{-s}$

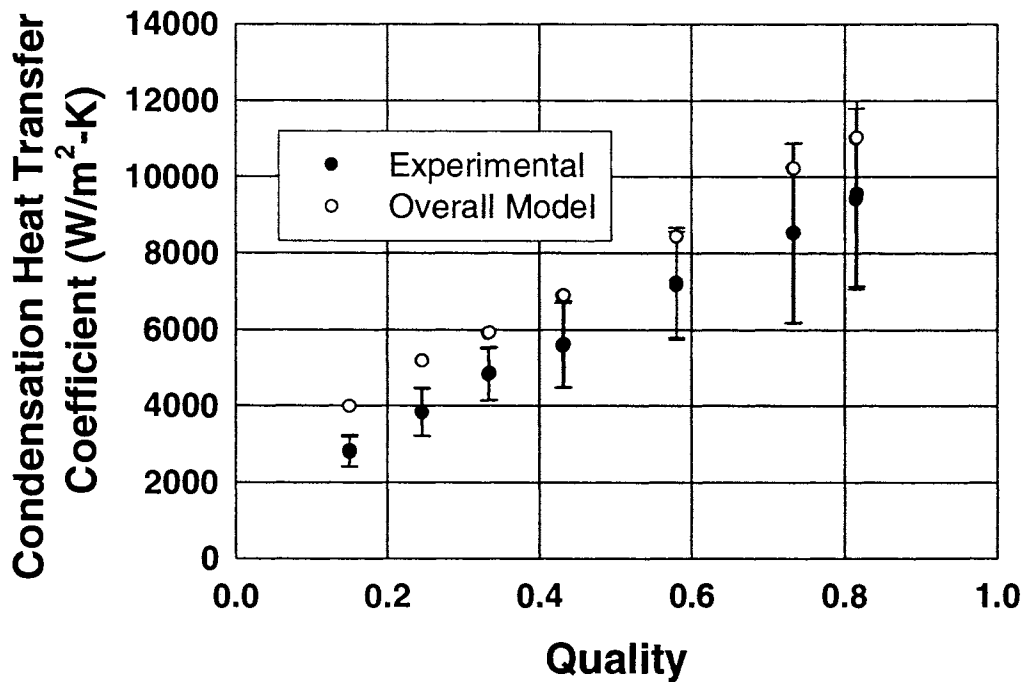


Figure 83. Predicted and Experimental Condensation Heat Transfer Coefficients for Test Section C30 and  $G = 750 \text{ kg/m}^2\text{-s}$

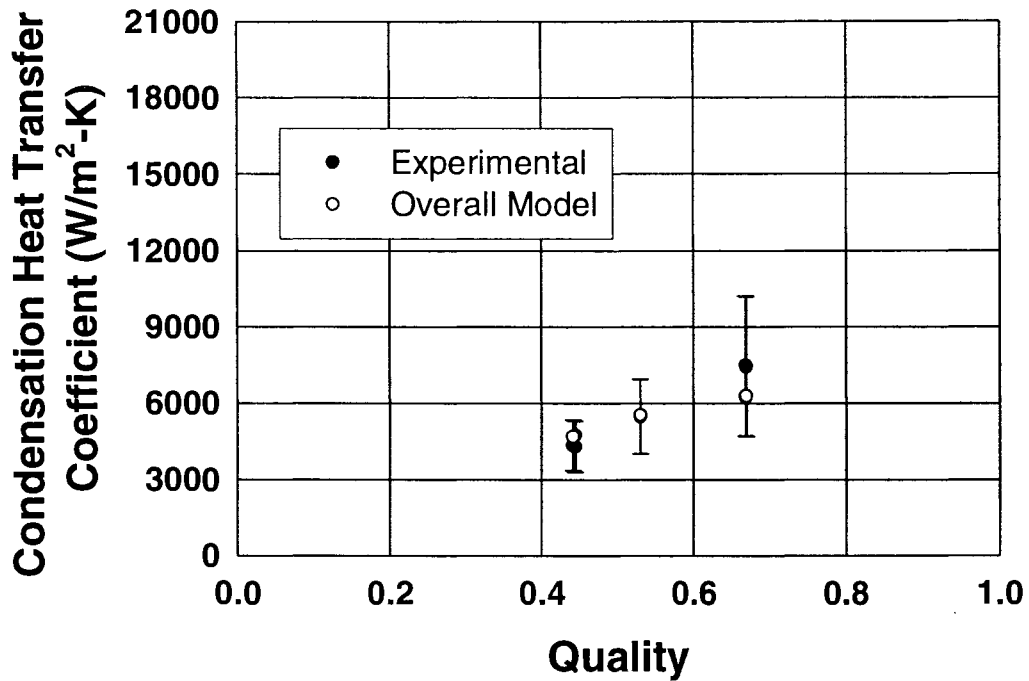


Figure 84. Predicted and Experimental Condensation Heat Transfer Coefficients for Test Section C20 and  $G = 450 \text{ kg/m}^2\text{-s}$

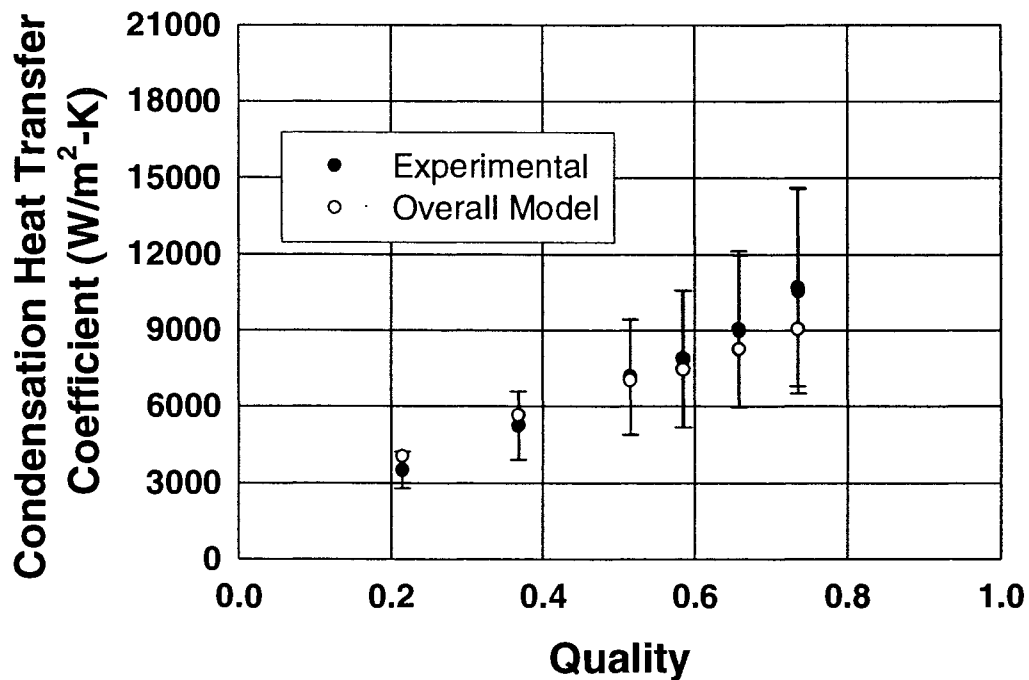
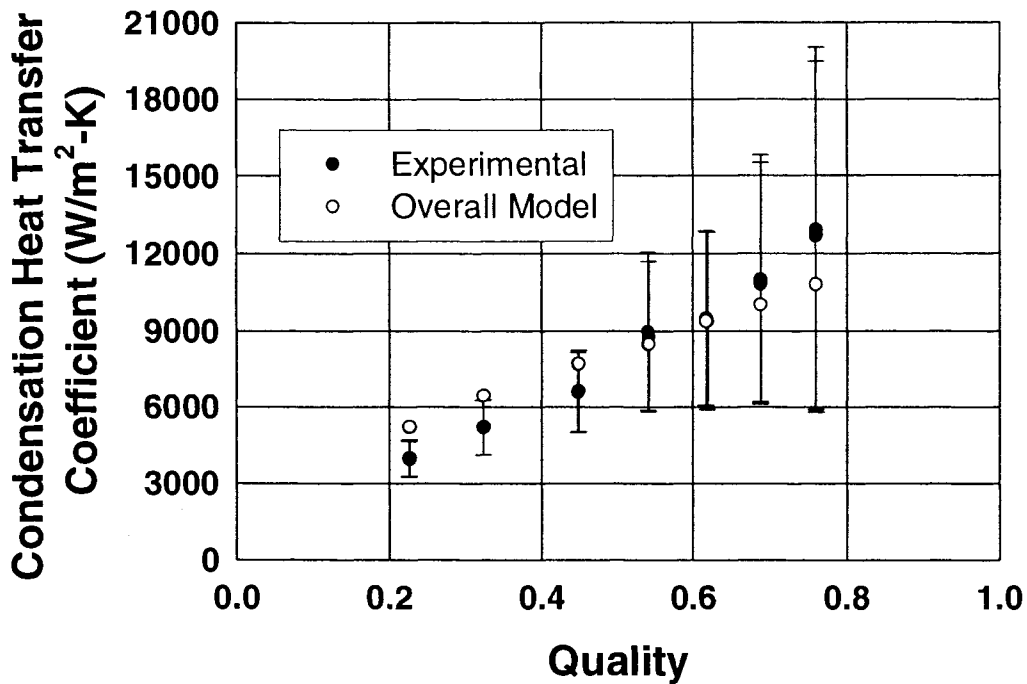


Figure 85. Predicted and Experimental Condensation Heat Transfer Coefficients for Test Section C20 and  $G = 600 \text{ kg/m}^2\text{-s}$



**Figure 86.** Predicted and Experimental Condensation Heat Transfer Coefficients for Test Section C20 and  $G = 750 \text{ kg/m}^2\text{-s}$

Figures 80-83 show the present model compared with the experimental heat transfer coefficients (with their associated uncertainties) for test section C30 with nominal mass fluxes of 300, 450, 600, and  $750 \text{ kg/m}^2\text{-s}$ . In general, these figures show good agreement between the data and the model, although, as the mass flux increases, low quality points (intermittent/annular flow) are over-predicted.

Figures 84-86 show the present model compared with the experimental heat transfer coefficients (with their associated uncertainties) for test section C20 for nominal mass fluxes of 450, 600, and  $750 \text{ kg/m}^2\text{-s}$ . In general, these figures show good agreement between the model and the data.

Figures 87-91 show the effect of hydraulic diameter for the mass fluxes of 150, 300, 450, 600, and  $750 \text{ kg/m}^2\text{-s}$  using the model developed in this study for an average test section pressure of 1,450 kPa. The three lines represented in these graphs correspond to test sections C20, C30, and C60. It should be noted that no data were taken for test section C20 for the nominal mass flux of  $150 \text{ kg/m}^2\text{-s}$ , and that only one point was taken for both test section C20 for a mass flux of  $300 \text{ kg/m}^2\text{-s}$  and test section C30 for a mass flux of  $150 \text{ kg/m}^2\text{-s}$ . Thus, the predictions for these two tubes at low mass fluxes are not expected to be very

reliable.

For annular and mist flows (moderate to high qualities), the heat transfer coefficient increases with decreasing diameter. For lower qualities, the condensation heat transfer coefficients are relatively independent of diameter. However, as the mass flux is increased to 450 kg/m<sup>2</sup>-s and beyond, the heat transfer coefficients for test section C60 are higher (in the low quality region) than for both test sections C20 and C30. Also, at the mass flux of 750 kg/m<sup>2</sup>-s, the heat transfer coefficients for test section C30 are higher than those for test section C20. This is the opposite of the expected trend, but it can be explained by examining the corresponding limiting liquid-only heat transfer coefficients.

The ratio of the liquid heat transfer coefficients for test section C60 and test section C30 is as follows:

$$\frac{h_{C60}}{h_{C30}} = \frac{D_{C30}}{D_{C60}} \cdot \frac{Nu_{C60}}{Nu_{C30}} = 0.5 \cdot \frac{Nu_{C60}}{Nu_{C30}} \quad (240)$$

For laminar flow, the heat transfer coefficient ratio is 0.5 because the Nusselt number is 4.364 for both test sections. However, as the mass flux is increased, the liquid only Reynolds number changes from laminar to turbulent. The ratio of liquid-only Reynolds numbers between test sections C60 and C30 is approximately 2 due to the doubling of the hydraulic diameter. In other words, the single-phase Reynolds number for test section C60 could be turbulent while the flow is laminar for test section C30. For example, for a liquid-phase viscosity of  $1.38 \times 10^{-4}$  kg/m-s and  $G = 300$  kg/m<sup>2</sup>-s, the liquid-only Reynolds numbers (equation 154) for test sections C30 and C60 are 1,657 and 3,319, respectively. Also, the Churchill (1977b) friction factors (equation 41) for test sections C30 and C60 are 0.039 and 0.043, respectively, while their Churchill (1977a) Nusselt numbers are 4.364 and 16.35, respectively. Using equation 40, the ratio of the liquid heat transfer coefficients for test section C60 and test section C30 is 1.87. Therefore, the limiting single-phase heat transfer coefficient can be higher for test section C60 than for test section C30 for the same mass flux, which explains this unexpected trend in the two-phase heat transfer coefficient.

The model described above predicts 90% of the circular tube data in the present study to within  $\pm 25\%$ . The range of validity for this model is as follows: 0.506 mm < D < 1.524 mm, 150 kg/m<sup>2</sup>-s < G < 750 kg/m<sup>2</sup>-s, and 1,240 kPa < P < 1,725 kPa. Pressures outside this range may cause deviations between the model and data, especially as the critical pressure (4,059 kPa for R-134a) is approached, and application of the model beyond this range of diameters and mass fluxes could result in inexplicable trends.

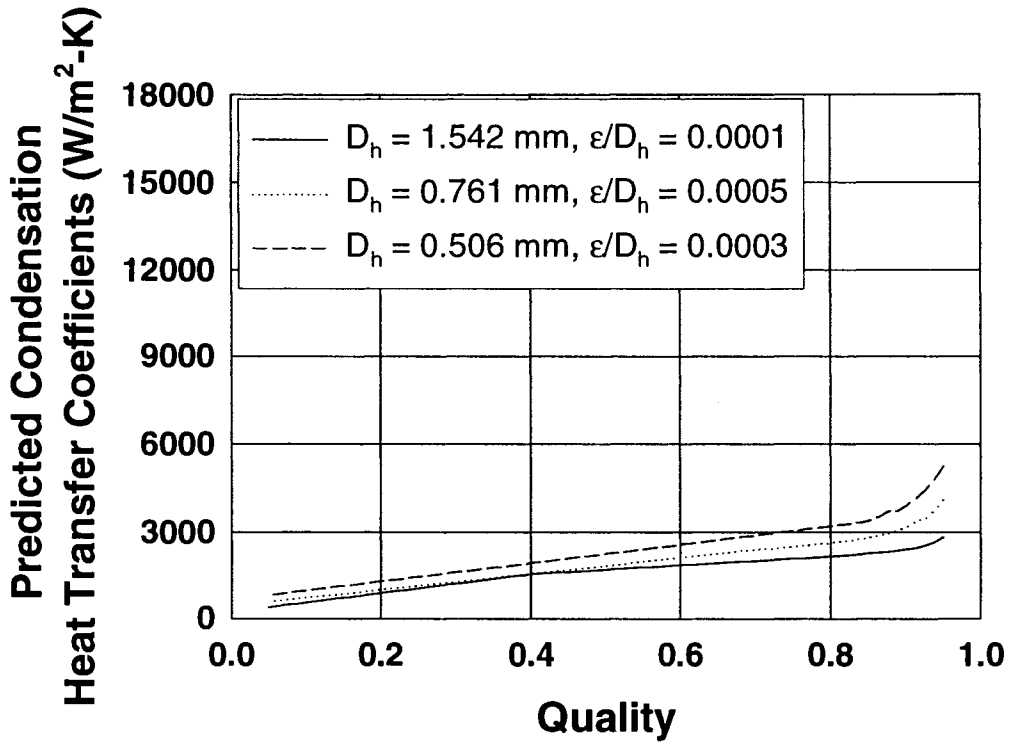


Figure 87. Present Model Condensation Heat Transfer Coefficients as a Function of Quality for Test Section C20, C30, and C60 and  $G = 150 \text{ kg/m}^2\text{-s}$

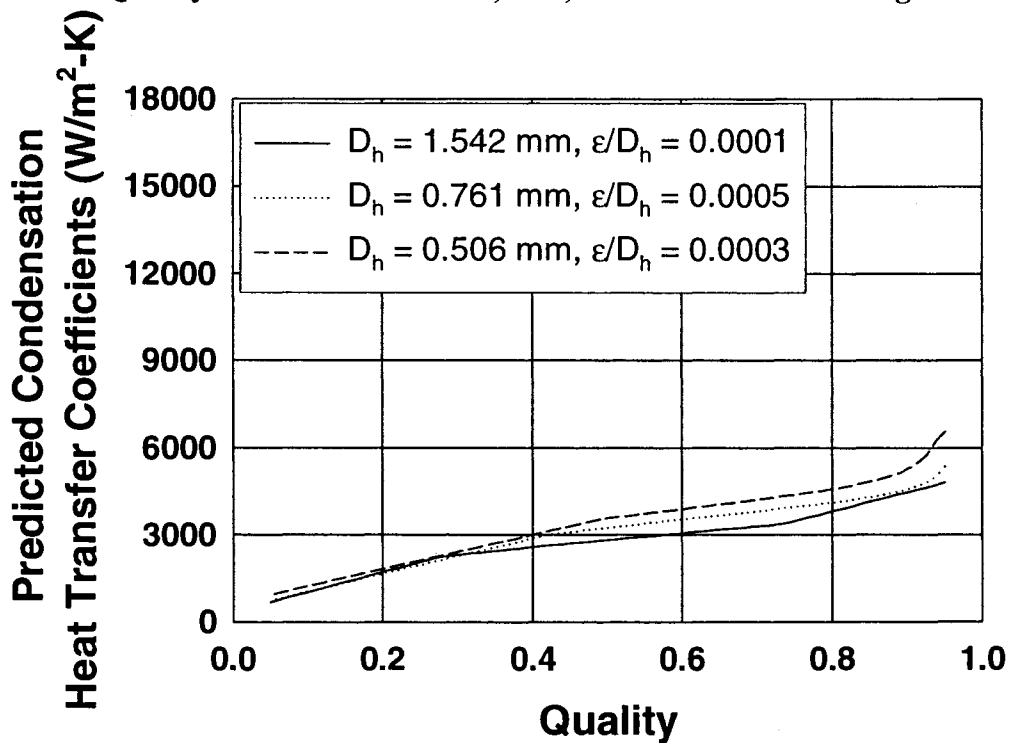


Figure 88. Present Model Condensation Heat Transfer Coefficients as a Function of Quality for Test Section C20, C30, and C60 and  $G = 300 \text{ kg/m}^2\text{-s}$

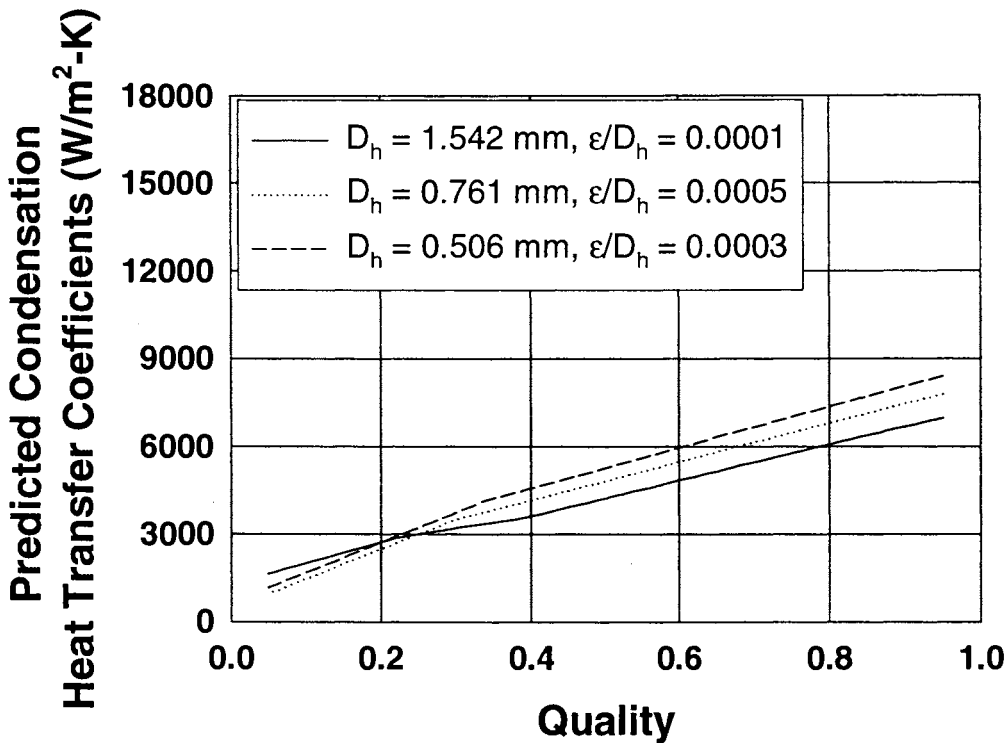


Figure 89. Present Model Condensation Heat Transfer Coefficients as a Function of Quality for Test Section C20, C30, and C60 and  $G = 450 \text{ kg/m}^2\text{-s}$

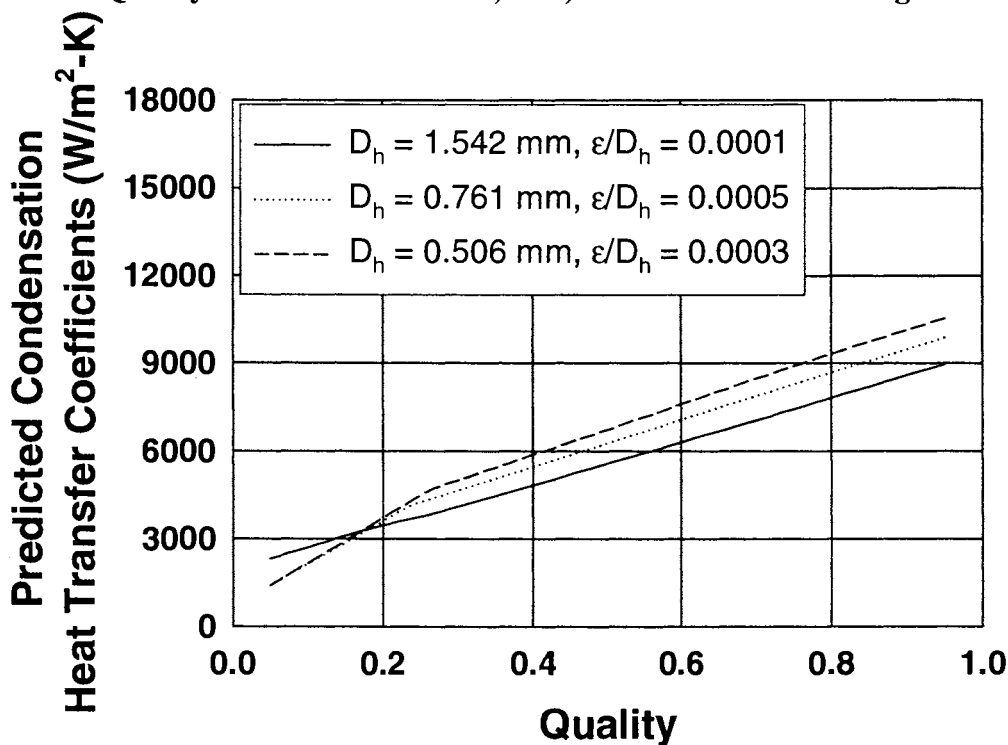


Figure 90. Present Model Condensation Heat Transfer Coefficients as a Function of Quality for Test Section C20, C30, and C60 and  $G = 600 \text{ kg/m}^2\text{-s}$

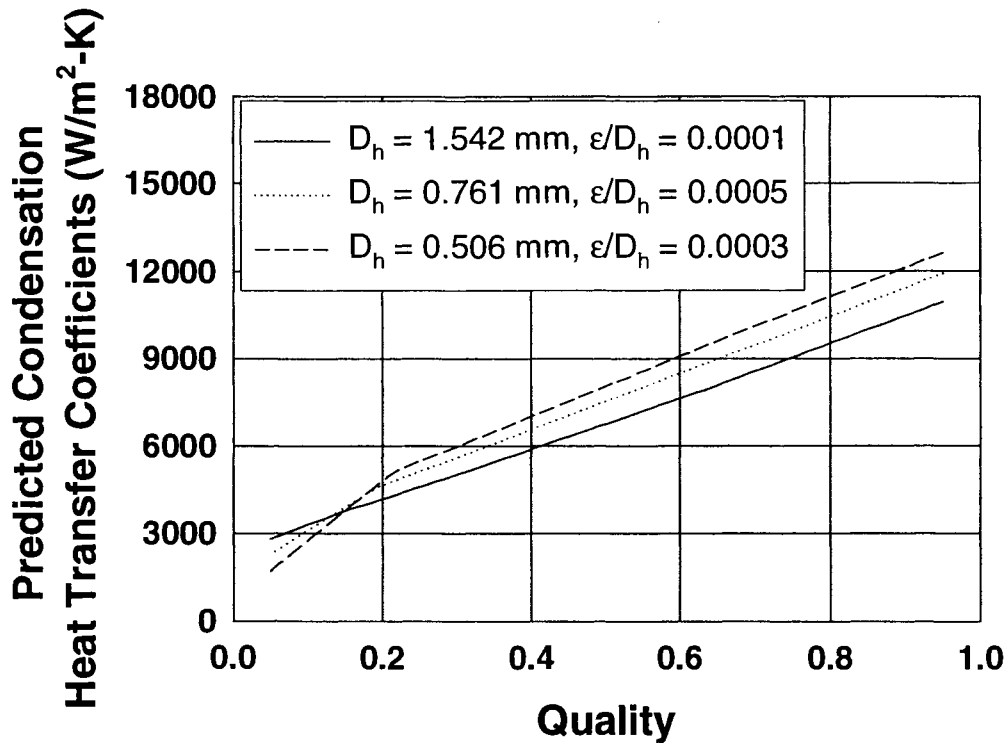


Figure 91. Present Model Condensation Heat Transfer Coefficients as a Function of Quality for Test Section C20, C30, and C60 and  $G = 750 \text{ kg/m}^2\text{-s}$

## Non-Circular Microchannels

### Annular Film Flow

The annular flow models for the non-circular tubes are the same as the model for the circular tubes, with different constants and, for the triangular test sections T33 and W29, different equivalent diameters. The constants  $C_1$  and  $C_2$  in equation 223 were given in Coleman (2000), and are shown here for both laminar and turbulent flow ( $Re_{crit} \sim 2300$ ) for test sections N21, S30, RK15, T33, and W29 in Table 8. For laminar flow, the friction factor is as follows:

$$f_{lam} = \frac{A}{Re} \quad (241)$$

The different values for the laminar friction factor constant for each tube are also given in Table 8. As shown later, the data for test section W29 are predicted well using the test section T33 constants; both of these tubes have the same triangular geometry, with W29 using a corrugated insert, while T33 consists of extruded triangular ports.

The diameters used in the model for the non-circular tubes were simply the hydraulic

**Table 8. Non-Circular Test Section Annular Film Flow Constants for Laminar and Turbulent Liquid Flow (Coleman 2000)**

Tube	$C_1$ (laminar)	$C_2$ (laminar)	$C_1$ (turbulent)	$C_2$ (turbulent)	f Re (laminar)
N21	1.060	0.356	0.664	0.239	57
S30	0.821	0.378	0.525	0.340	57
RK15	1.749	0.461	1.210	0.352	69.4
T33	2.663	0.300	0.816	0.314	53
W29*	2.663	0.300	0.816	0.314	53

\*assumed that constants for test section T33 are valid for this test section also

diameters for test sections N21, S30, and RK15. The diameters for the two triangular test sections (W29 and T33) are the diameters of the largest inscribed circles within one microchannel. Figure 92 shows the cross section of one microchannel for T33 (or an approximation for test section W29) with the equivalent circle inside. The equivalent diameters for test sections T33 and W29 are 0.6614 mm and 0.5724 mm, respectively, whereas the corresponding hydraulic diameters were 0.839 mm and 0.732 mm, respectively. Table 9 shows the hydraulic and equivalent diameters for the 6 non-circular tube geometries.

**Table 9. Hydraulic and Equivalent Diameters for the Non-circular Tubes**

Tube	$D_h$ , mm	$D_e$ , Mm
S30	0.762	0.762
RK15	0.424	0.424
T33	0.839	0.661
W29	0.732	0.572
B32	0.799	0.799
N21	0.536	0.536

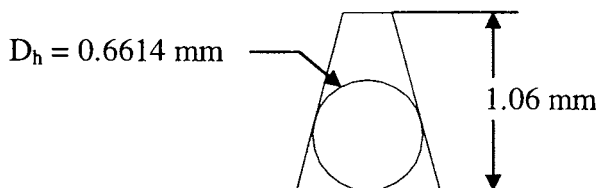


**Figure 92. Cross-Section of One Channel for Test Section T33 with Largest Inscribed Circle**

### Mist Flow

The mist flow models for the non-circular tubes are the same as the circular tube models with different multiplication constants (see equation 229) for each tube. The constants for test sections N21, S30, RK15, T33, and W29 are shown in Table 10. Again the equivalent diameters were used for the models, but the actual relative roughness, also given in Table 10, were used for the friction factor and Nusselt number calculations.

**Table 10. Mist Flow Constants and Relative Roughness (Coleman 2000) for the Non-Circular Test Sections**

Tube	C	$\epsilon/D$
N21	6.512	0.0030
S30	4.437	0.0009
RK15	4.908	0.0390
T33	6.251	0.0065
W29	3.560	0.0950

### Intermittent Flow

No data in the purely intermittent regime were collected for the non-circular tubes under consideration. Hence, the interpolation technique that was used for intermittent flow in the circular tubes (equation 230) is also used for each non-circular tube.

### Overall Model

Since large overlaps in the flow regime exist for the tubes in the present study, the quality-based averaging techniques used for the circular tubes are also used for the microchannel tubes. Using the equivalent diameters for each tube, the circular tube interpolation schemes (equations 231-239) are coupled with the non-circular annular film, mist, and intermittent heat transfer models to arrive at the overall models.

Figure 93 shows the predicted heat transfer coefficients versus the experimental heat transfer coefficients. Although 84% of the experimental values are predicted within  $\pm 30\%$ , the deviations can, in part, be explained by examining the uncertainty in the experimental values.

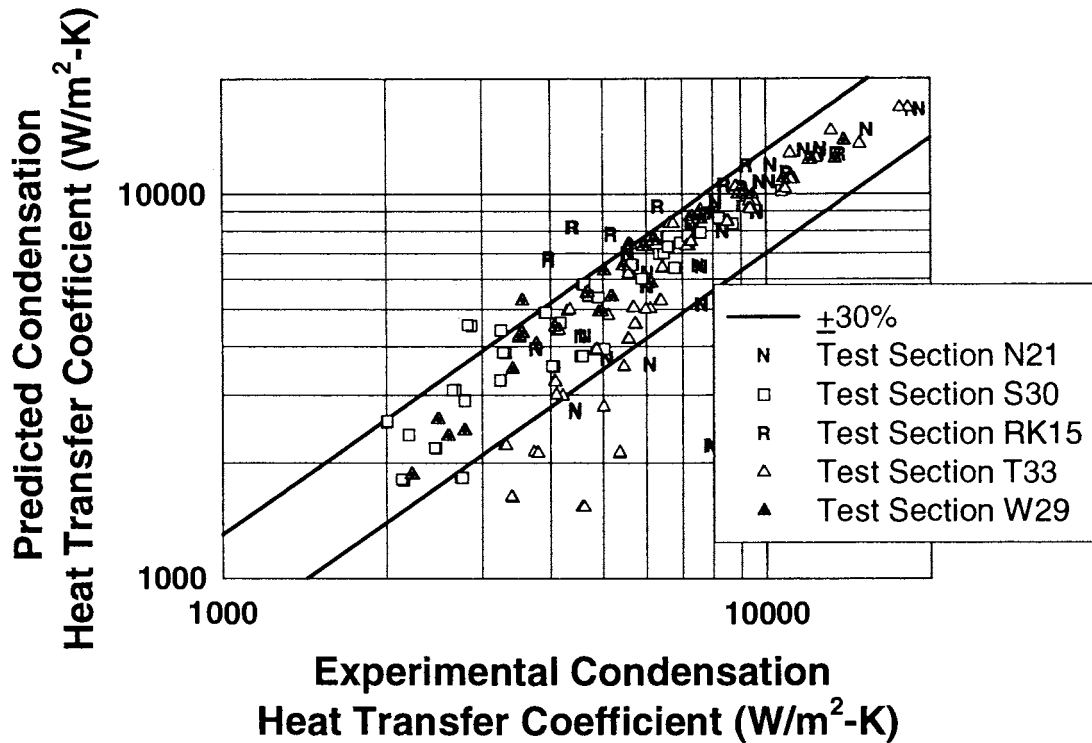


**Figure 93. Predicted versus Experimental Condensation Heat Transfer Coefficients for Test Sections N21, S30, RK15, T33, and W29**

Figures 94-97 show the present model compared with the experimental heat transfer coefficients (with their associated uncertainties) for test section N21 for nominal mass fluxes of 300, 450, 600, and 750 kg/m<sup>2</sup>-s. At  $G = 300$  kg/m<sup>2</sup>-s, these two points were under-predicted by the model significantly, but only slightly outside the range of experimental uncertainties in the data. The rest of the data are predicted well by the model.

Data for test section S30 are compared with the non-circular tube model in Figures 98-101 for nominal mass fluxes of 300, 450, 600, and 750 kg/m<sup>2</sup>-s. In general, the data are predicted well by the model. However, there is over-prediction of the data at the two highest mass fluxes and lowest qualities.

Test section RK15 data are compared with the model in Figures 102 and 103 for nominal mass fluxes of 600 and 750 kg/m<sup>2</sup>-s. The data are over-predicted (outside the experimental uncertainty) for low qualities, and predicted well for high qualities, for both mass fluxes. However, very little data were taken for this tube (10 data points) due to the comparatively low mass flow rate required.

Figures 104-108 show the experimental data for test section T33 compared with the model for the nominal mass fluxes of 150, 300, 450, 600, and 750 kg/m<sup>2</sup>-s. For  $G = 150$  and

300 kg/m<sup>2</sup>-s, the data are under-predicted by the model. However, most of the model predictions are within the experimental uncertainty, which is quite high for the lowest mass flux. The remaining data are, in general, predicted well by the model.

Test section W29 data are compared with the non-circular tube model in Figures 109-113 for the nominal mass fluxes of 150, 300, 450, 600, and 750 kg/m<sup>2</sup>-s. In general, the data are predicted well by the model.

As stated above, the data for test section B32 seemed to have errors. Therefore, it is tentatively recommended that the circular tube model be used for predicting the test section B32 heat transfer coefficients. Although this recommendation is put forth with caution, the geometry of test section B32 (elliptical cross-section) is not too different than that of a circular microchannel.

Figures 114-118 show the effect of tube shape for test sections N21, S30, RK15, T33, and W29 for the nominal mass fluxes of 150 (except for test section RK15), 450, and 750 kg/m<sup>2</sup>-s and an average test section pressure of 1,450 kPa. The non-circular model was compared to the circular model in each of these graphs for the same effective diameter and relative roughness.

As seen in Figure 114, the N-shape cross-section increases the heat transfer coefficient from the corresponding circular channel. This effect increases as the mass flux increases. Figure 115 shows that the square tube heat transfer coefficients are nearly the same as for a circular tube with the same diameter. This is consistent with the comparison between the data for test section S30 ( $D_h = 0.762$ ) and C30 ( $D_h = 0.761$  mm) given earlier (see Figures 43-47). In Figure 116, the rectangular tube has much larger heat transfer coefficients than a circular tube with the same diameter and roughness. Compared with a circular tube with the same *equivalent* diameter, test section T33 (Figure 117) has higher heat transfer coefficients. If this tube model was compared with a circular tube with a similar *hydraulic* diameter (such as test section C30) the increase would be even greater. Similarly, a W-shaped tube (Figure 118) yields higher heat transfer coefficients than a circular tube of the same effective diameter (0.5724 mm) at low qualities and mass fluxes. However, as the mass flux is increased, the W-shaped tube results in lower heat transfer coefficients than the circular tube at qualities greater than about 0.3. This roughly coincides with the beginning of the mist flow regime. The difference in mist flow constants for test section W29 (3.56) and the circular tube model (4.987) accounts for this decrease at high mass fluxes and qualities.

Figure 119-121 show a comparison of the heat transfer coefficients in the different non-circular tubes N21, RK15, S30, T33, and W29 for the mass fluxes of  $G = 150, 450,$  and  $750$  kg/m<sup>2</sup>-s, respectively. Consistent with the experimental data, the effects of geometry

predicted by the models are small at low local vapor qualities. As the quality increases, test sections T33 and W29 have higher heat transfer coefficients, with test section T33 having slightly higher values than test section W29. For test sections N21 and RK15, the model predicts similar values to those of test section T33 and W29, with test section RK15 slightly higher for higher qualities.

The non-circular models have the same range of applicability as the circular model. The mass flux range is  $150 \text{ kg/m}^2\text{-s} < G < 750 \text{ kg/m}^2\text{-s}$ , and the test section pressure range is  $1,240 \text{ kPa} < P < 1,725 \text{ kPa}$ . However, since no data were collected for  $G = 150$  and  $300 \text{ kg/m}^2\text{-s}$  for test section RK15, the model is not expected to provide accurate results for low mass fluxes for this tube.

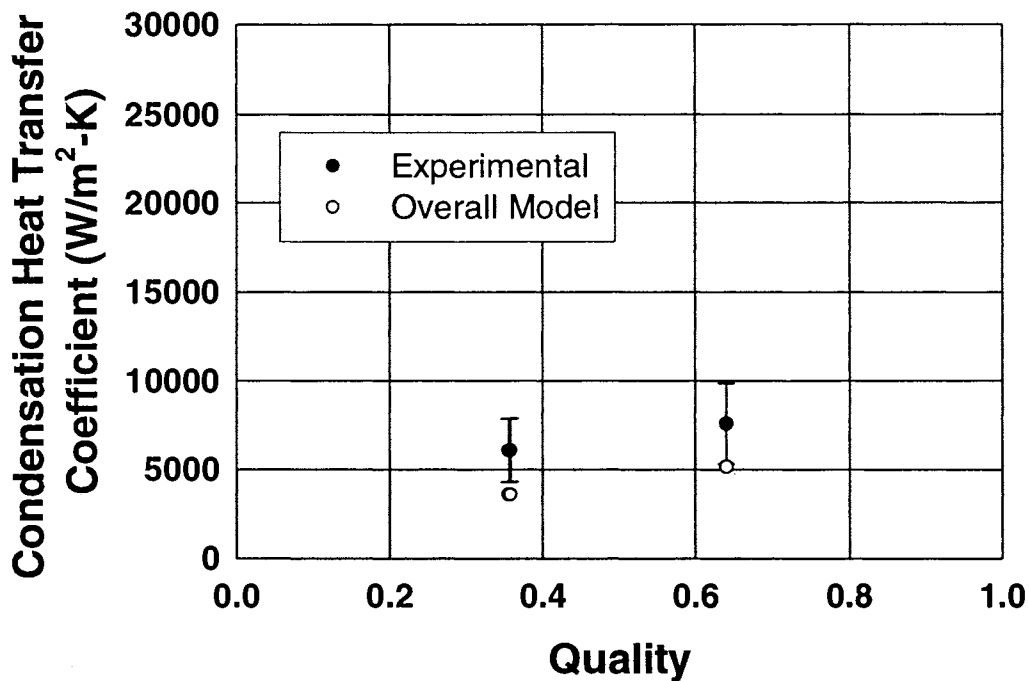


Figure 94. Predicted and Experimental Condensation Heat Transfer Coefficients for Test Section N21 and  $G = 300 \text{ kg/m}^2\text{-s}$

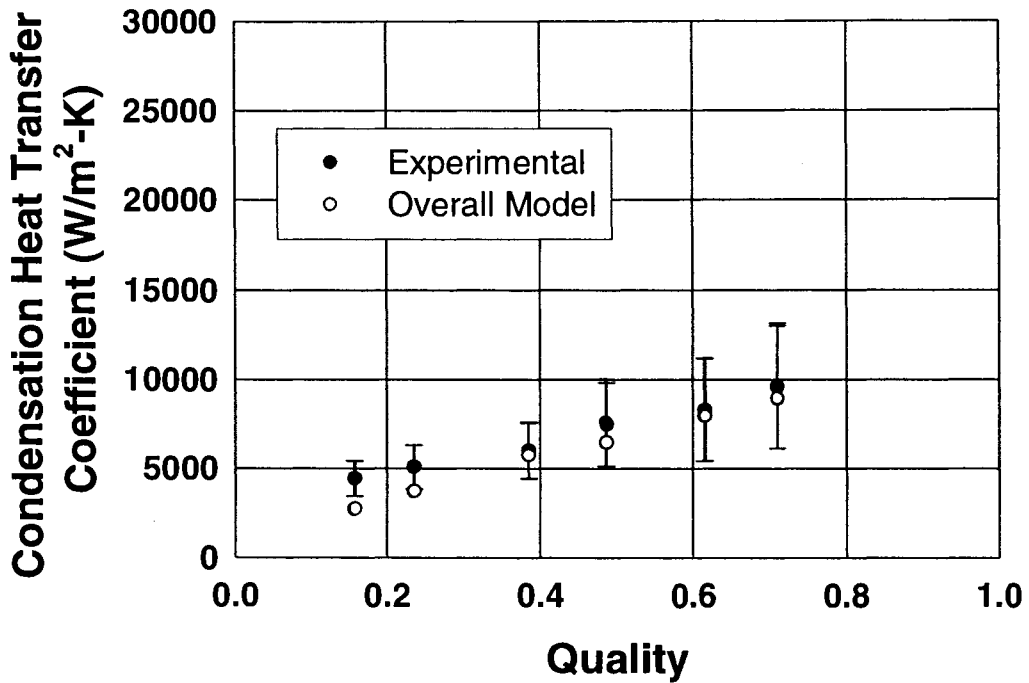


Figure 95. Predicted and Experimental Condensation Heat Transfer Coefficients for Test Section N21 and  $G = 450 \text{ kg/m}^2\text{-s}$

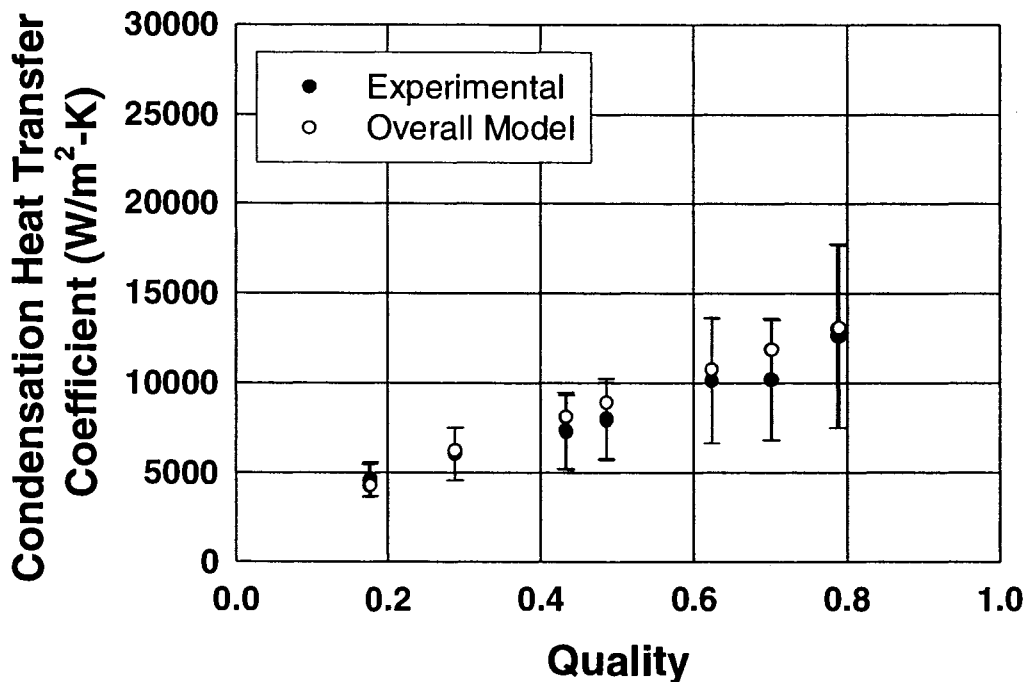


Figure 96. Predicted and Experimental Condensation Heat Transfer Coefficients for Test Section N21 and  $G = 600 \text{ kg/m}^2\text{-s}$

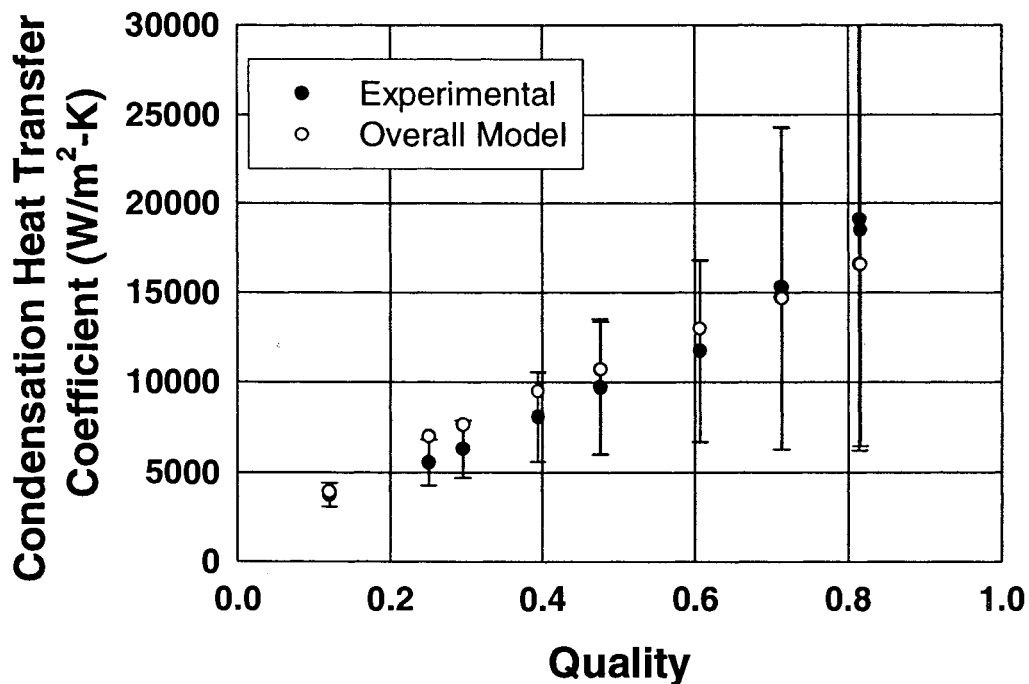


Figure 97. Predicted and Experimental Condensation Heat Transfer Coefficients for Test Section N21 and  $G = 750 \text{ kg/m}^2\text{-s}$

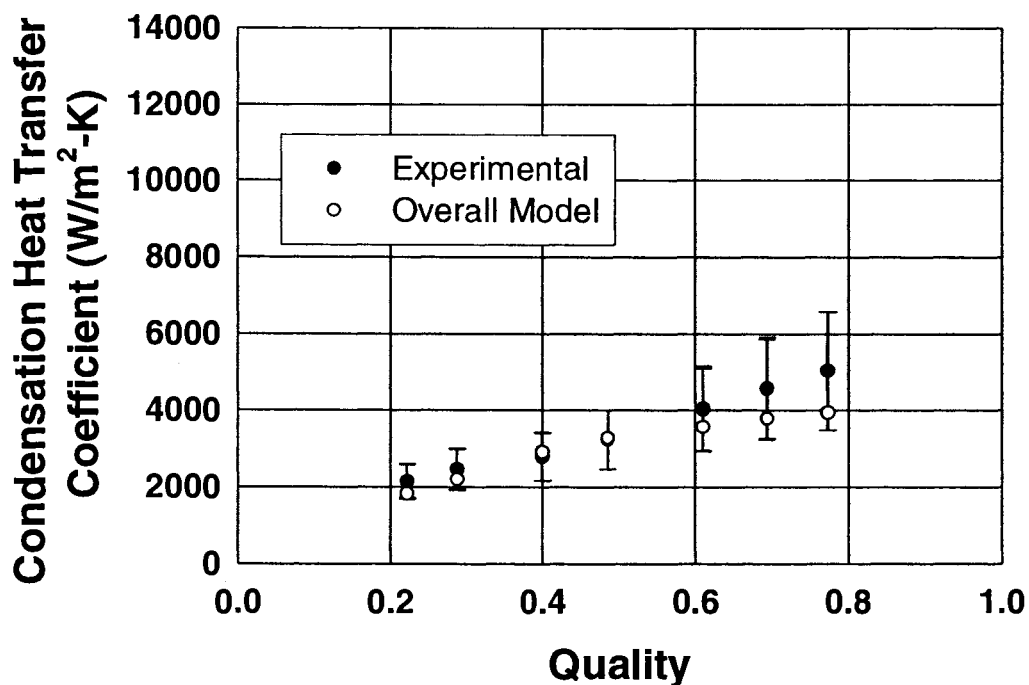


Figure 98. Predicted and Experimental Condensation Heat Transfer Coefficients for Test Section S30 and  $G = 300 \text{ kg/m}^2\text{-s}$

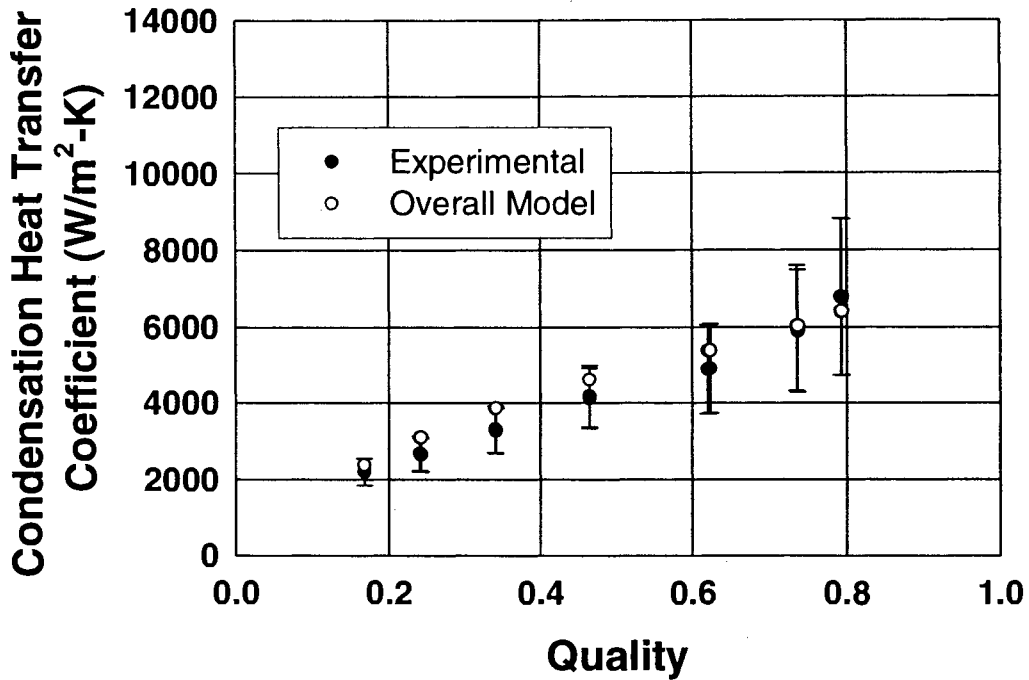


Figure 99. Predicted and Experimental Condensation Heat Transfer Coefficients for Test Section S30 and  $G = 450 \text{ kg/m}^2\text{-s}$

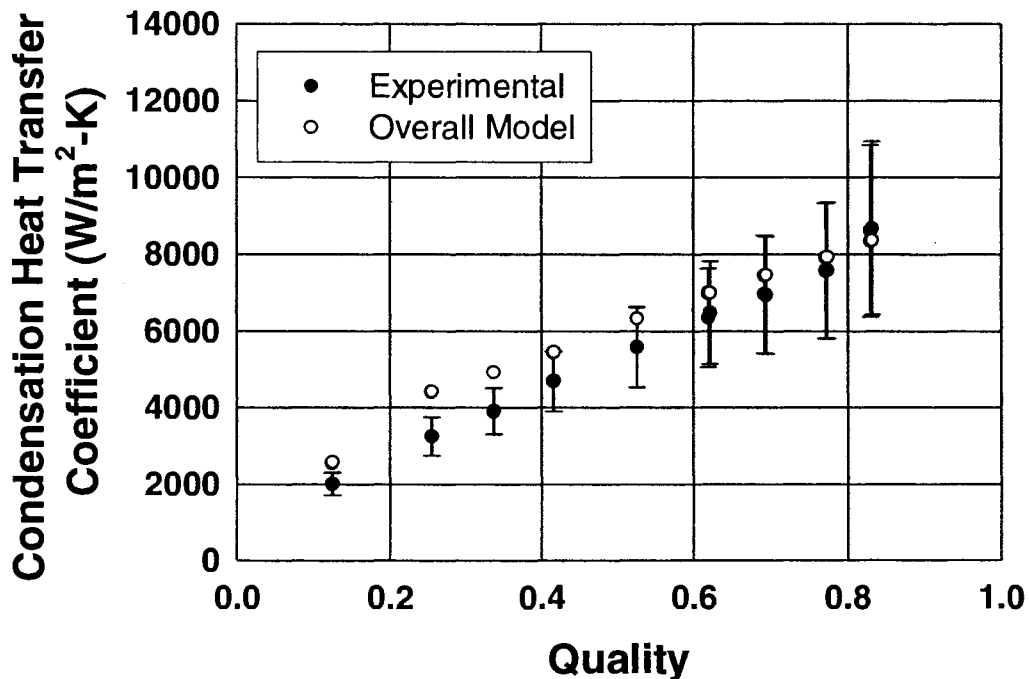


Figure 100. Predicted and Experimental Condensation Heat Transfer Coefficients for Test Section S30 and  $G = 600 \text{ kg/m}^2\text{-s}$

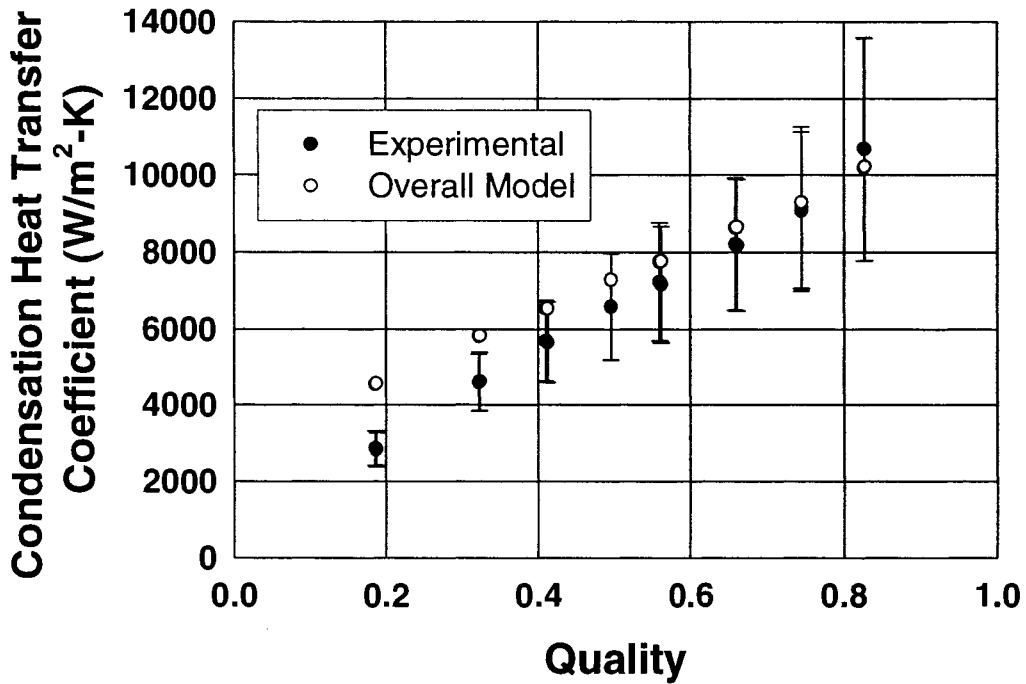


Figure 101. Predicted and Experimental Condensation Heat Transfer Coefficients for Test Section S30 and  $G = 750 \text{ kg/m}^2\text{-s}$

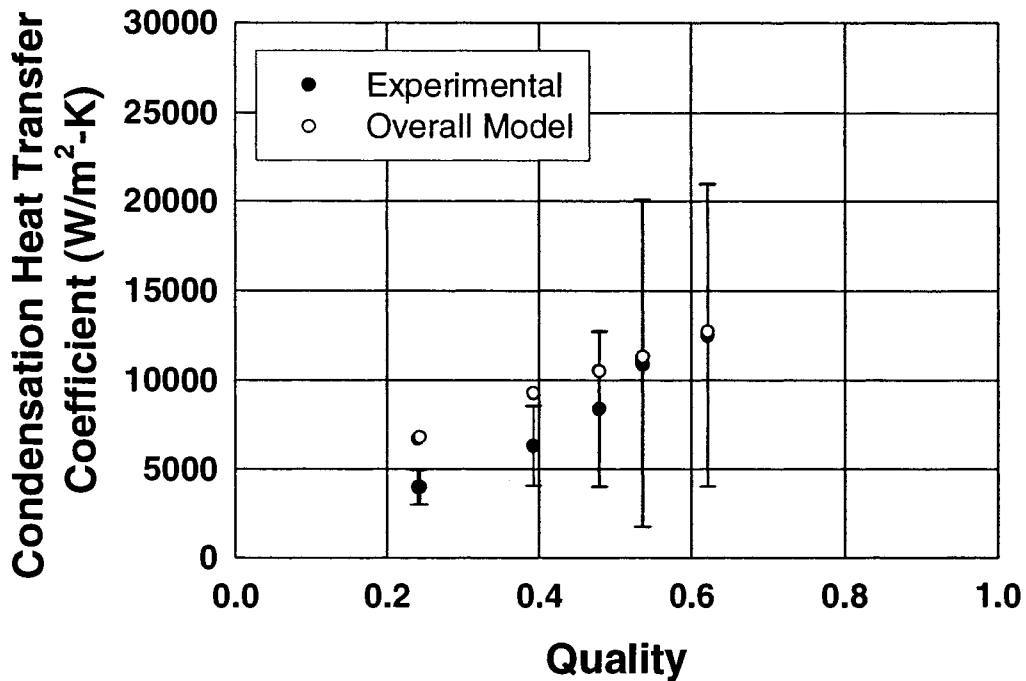


Figure 102. Predicted and Experimental Condensation Heat Transfer Coefficients for Test Section RK15 and  $G = 600 \text{ kg/m}^2\text{-s}$

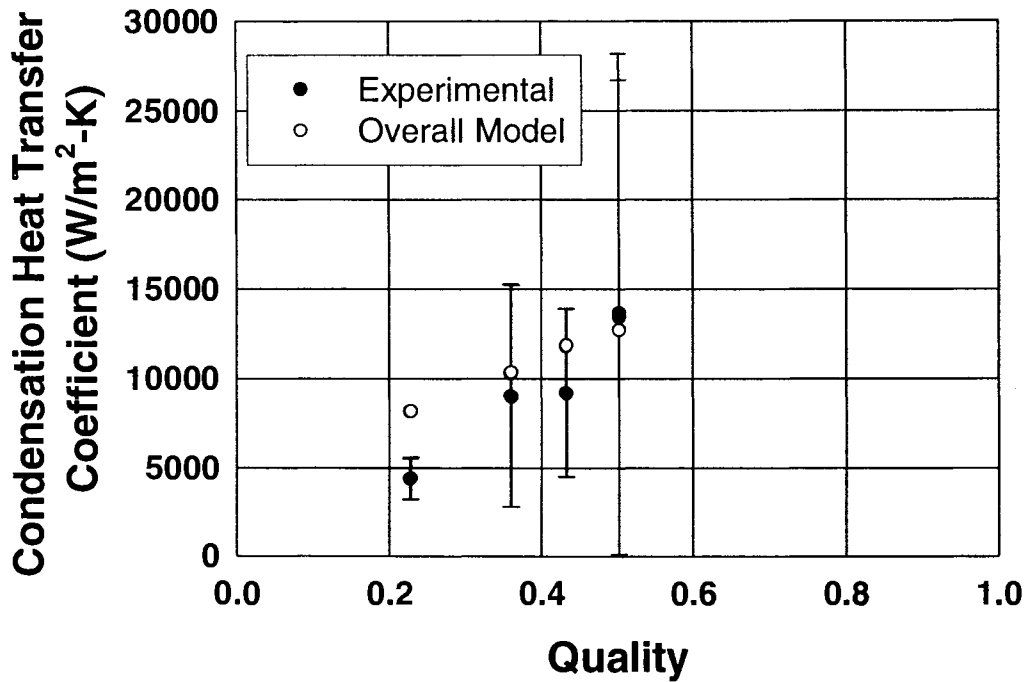


Figure 103. Predicted and Experimental Condensation Heat Transfer Coefficients for Test Section RK15 and  $G = 750 \text{ kg/m}^2\text{-s}$

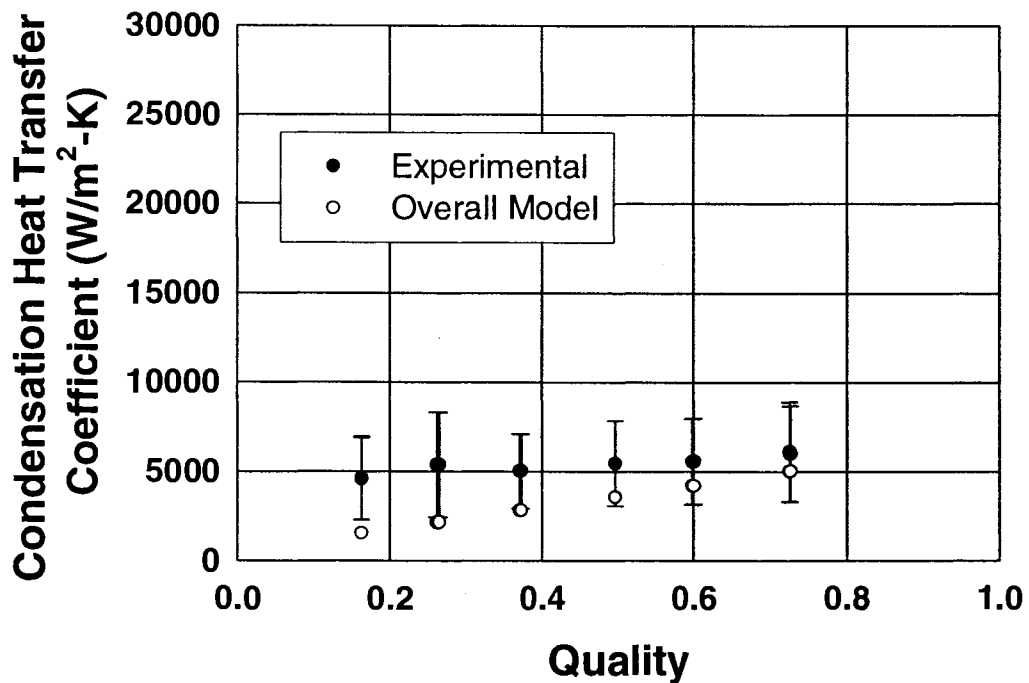


Figure 104. Predicted and Experimental Condensation Heat Transfer Coefficients for Test Section T33 and  $G = 150 \text{ kg/m}^2\text{-s}$

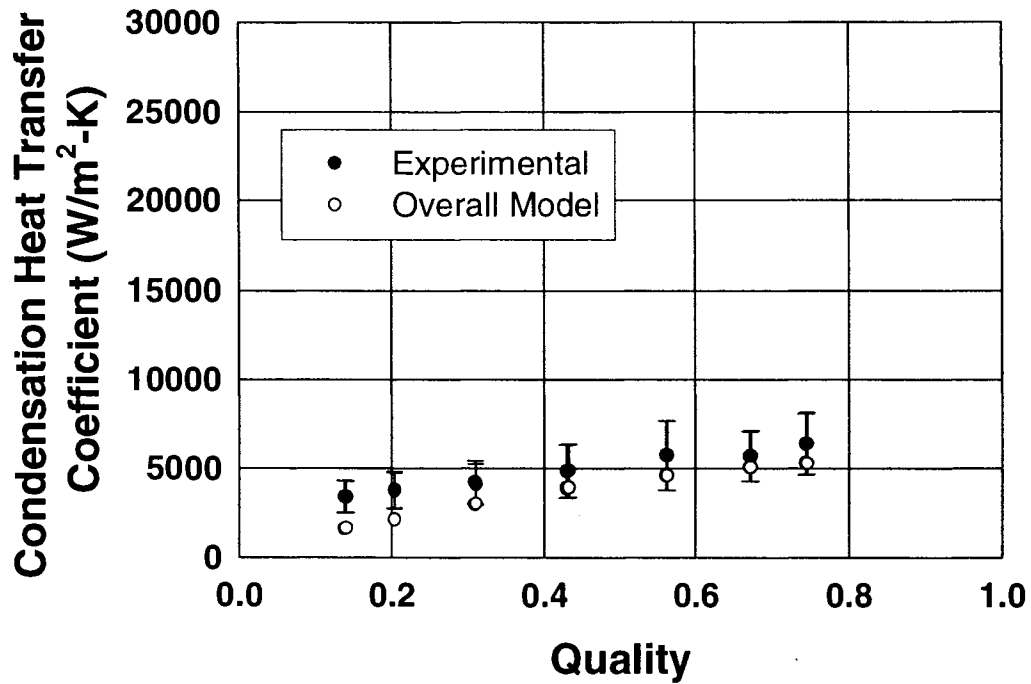


Figure 105. Predicted and Experimental Condensation Heat Transfer Coefficients for Test Section T33 and  $G = 300 \text{ kg/m}^2\text{-s}$

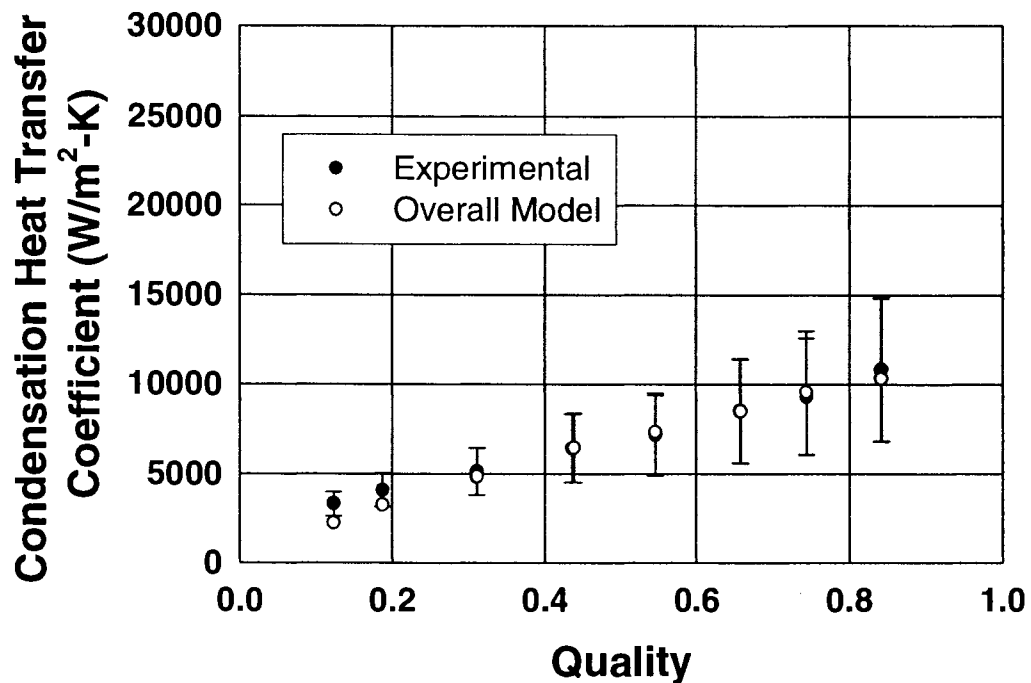


Figure 106. Predicted and Experimental Condensation Heat Transfer Coefficients for Test Section T33 and  $G = 450 \text{ kg/m}^2\text{-s}$

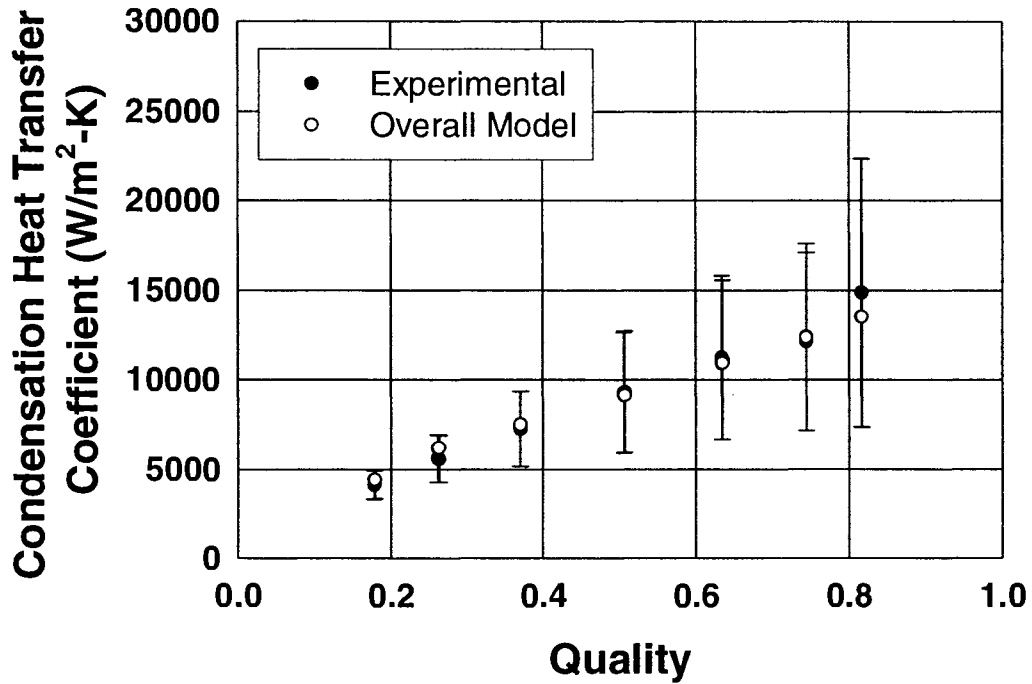


Figure 107. Predicted and Experimental Condensation Heat Transfer Coefficients for Test Section T33 and  $G = 600 \text{ kg/m}^2\text{-s}$

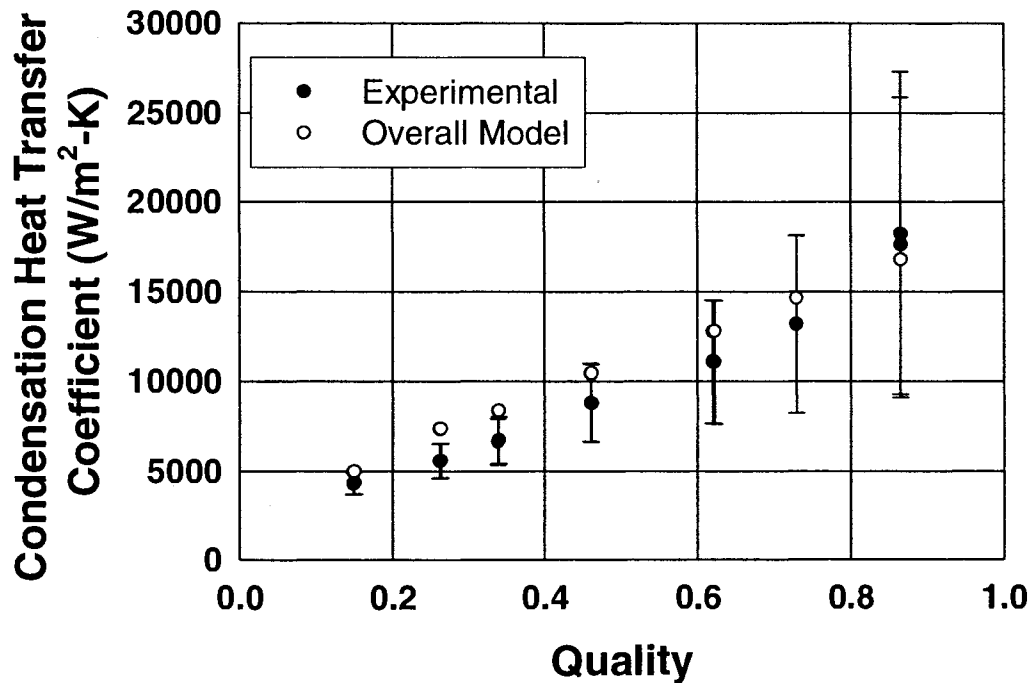


Figure 108. Predicted and Experimental Condensation Heat Transfer Coefficients for Test Section T33 and  $G = 750 \text{ kg/m}^2\text{-s}$

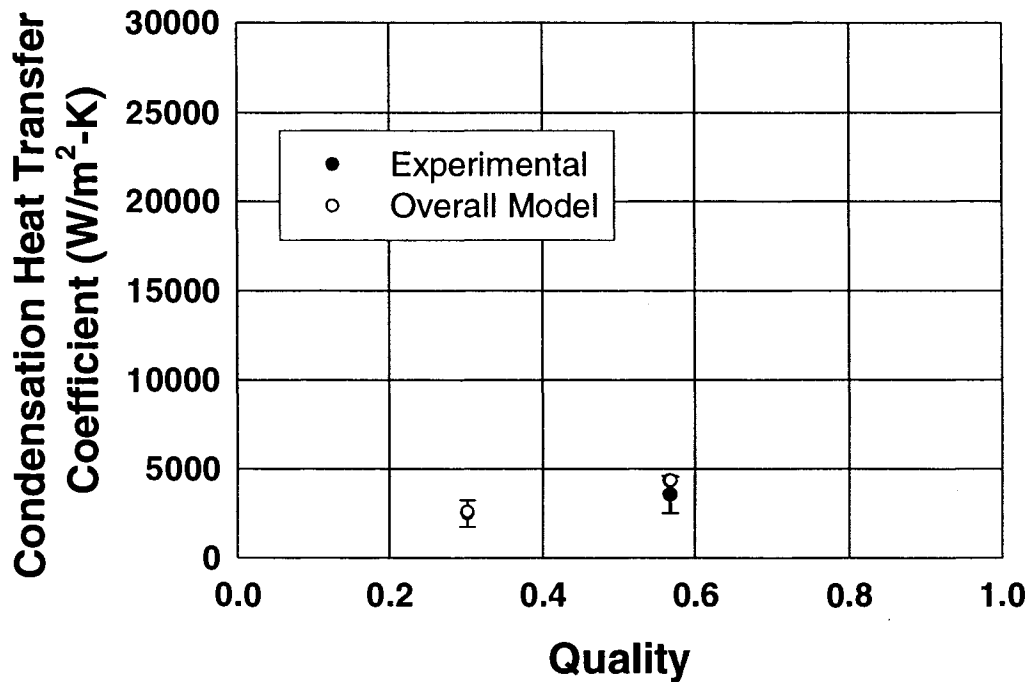


Figure 109. Predicted and Experimental Condensation Heat Transfer Coefficients for Test Section W29 and  $G = 150 \text{ kg/m}^2\text{-s}$

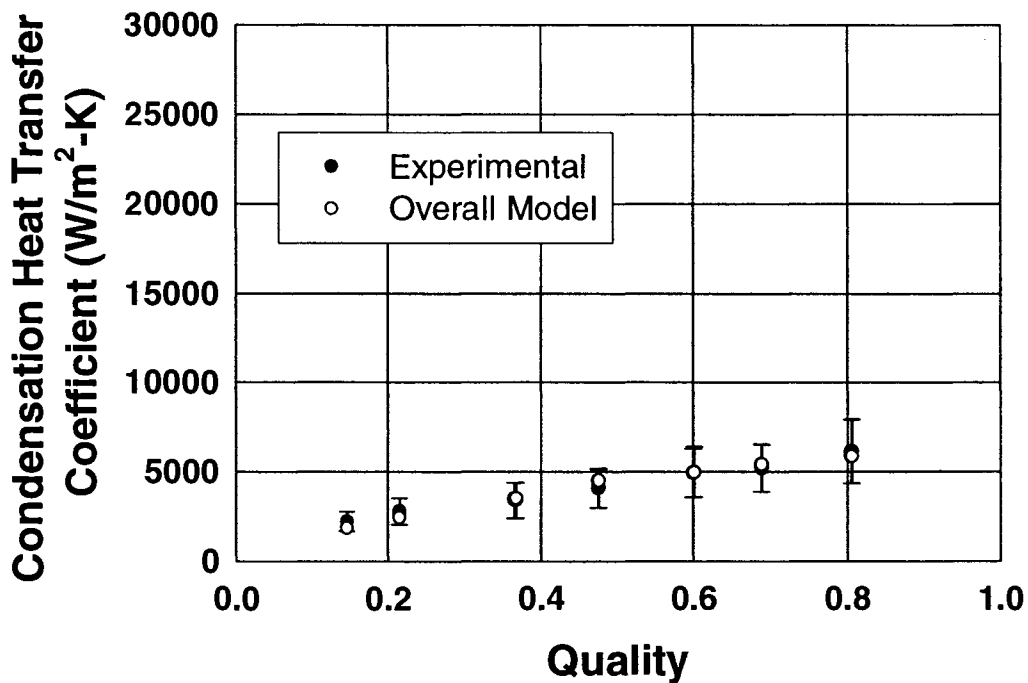


Figure 110. Predicted and Experimental Condensation Heat Transfer Coefficients for Test Section W29 and  $G = 300 \text{ kg/m}^2\text{-s}$

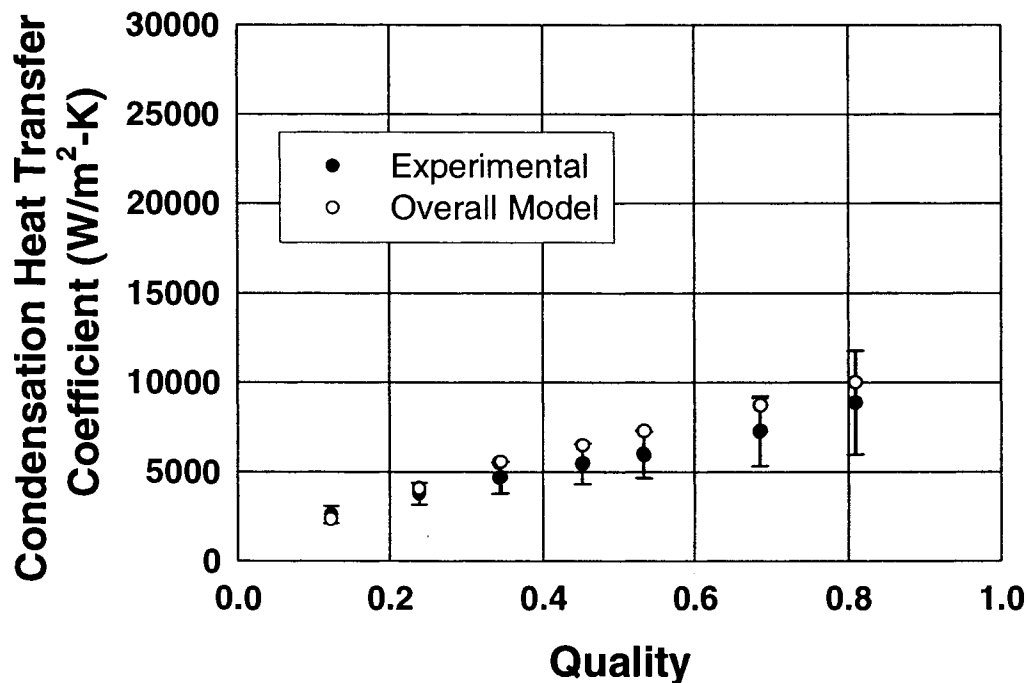


Figure 111. Predicted and Experimental Condensation Heat Transfer Coefficients for Test Section W29 and  $G = 450 \text{ kg/m}^2\text{-s}$

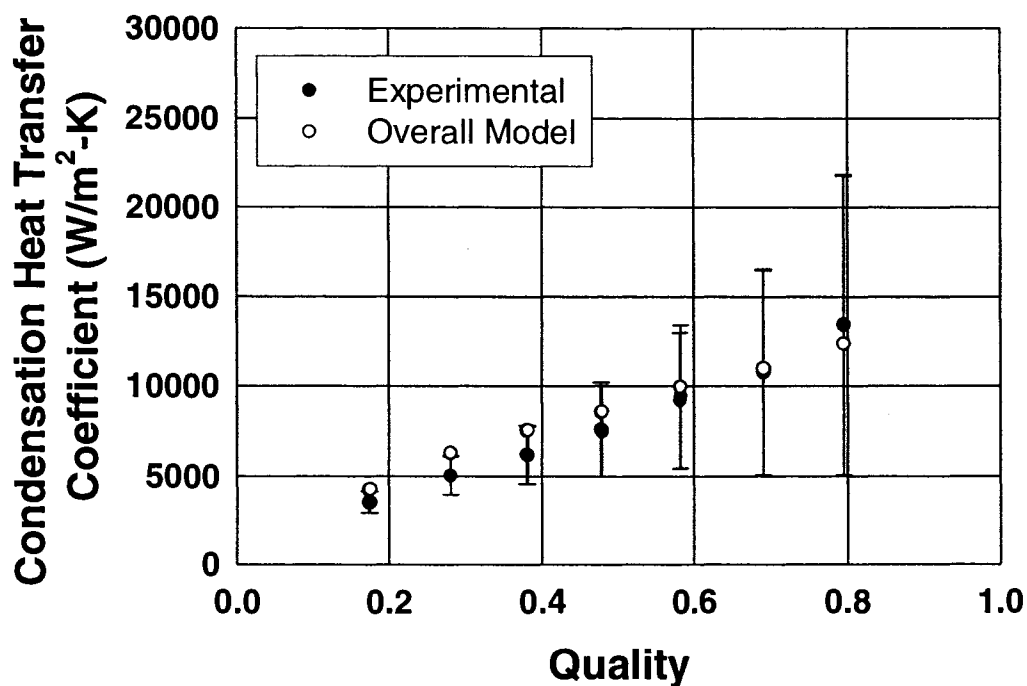


Figure 112. Predicted and Experimental Condensation Heat Transfer Coefficients for Test Section W29 and  $G = 600 \text{ kg/m}^2\text{-s}$

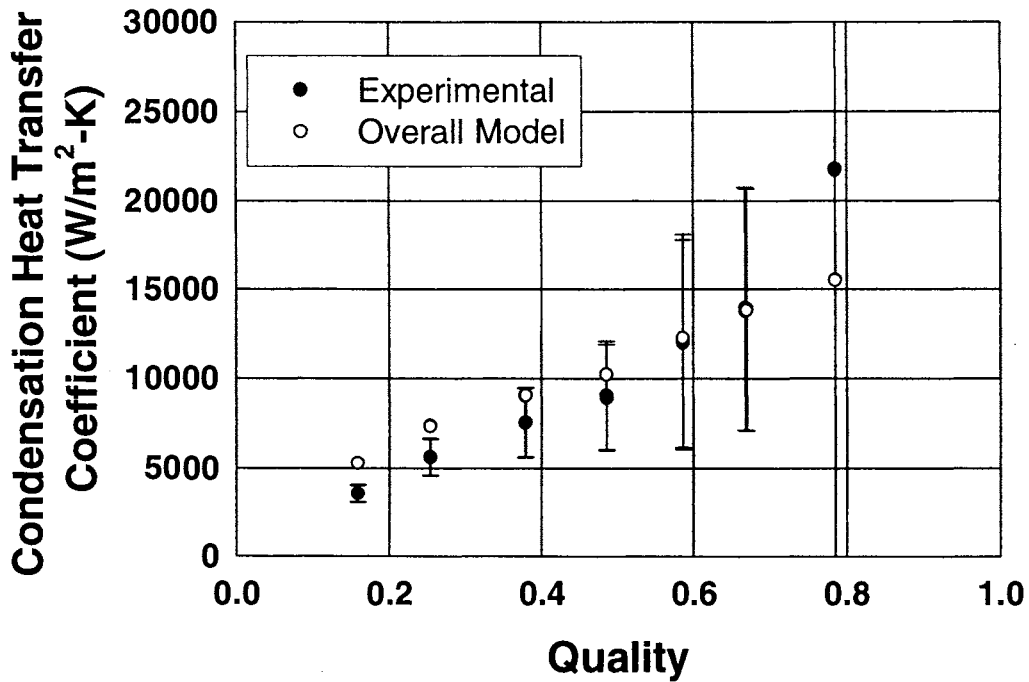


Figure 113. Predicted and Experimental Condensation Heat Transfer Coefficients for Test Section W29 and  $G = 750 \text{ kg/m}^2\text{-s}$

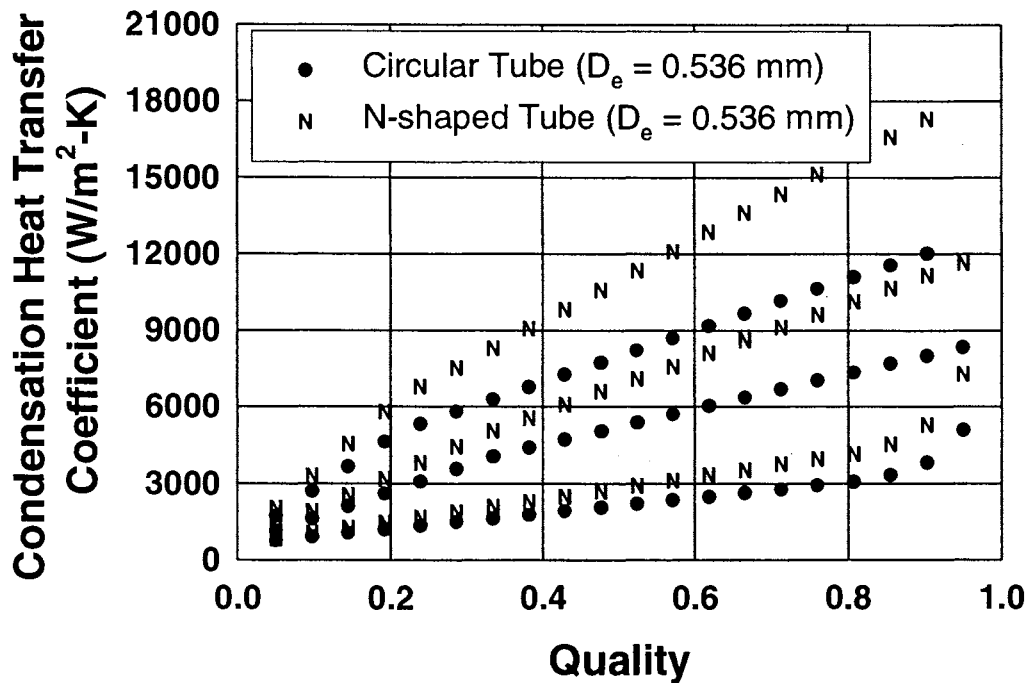


Figure 114. Comparison of Heat Transfer Coefficients in N-shaped and Circular Tubes for  $G = 150, 450, \text{ and } 750 \text{ kg/m}^2\text{-s}$

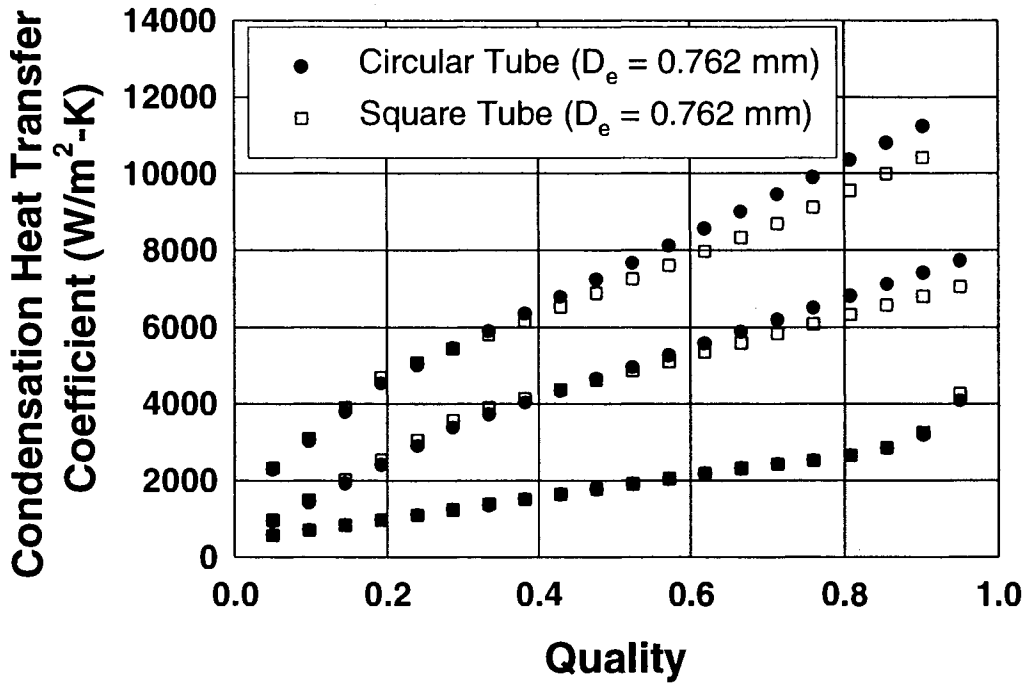


Figure 115. Comparison of Heat Transfer Coefficients in Square and Circular Tubes for  $G = 150, 450, \text{ and } 750 \text{ kg/m}^2\text{-s}$

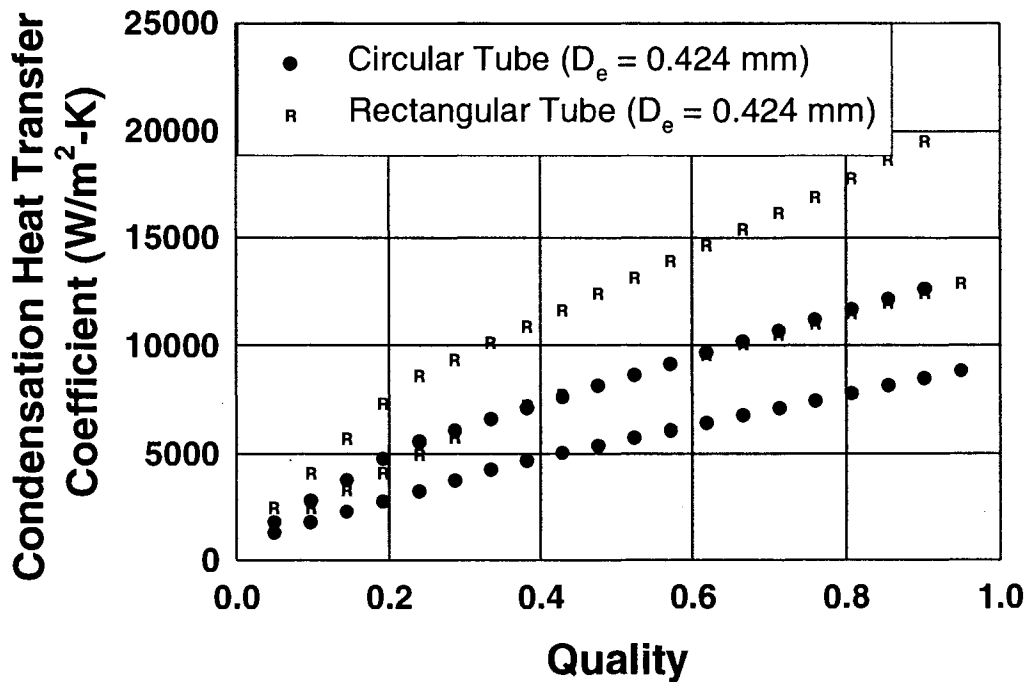


Figure 116. Comparison of Heat Transfer Coefficients in Rectangular and Circular Tubes for  $G = 450 \text{ and } 750 \text{ kg/m}^2\text{-s}$

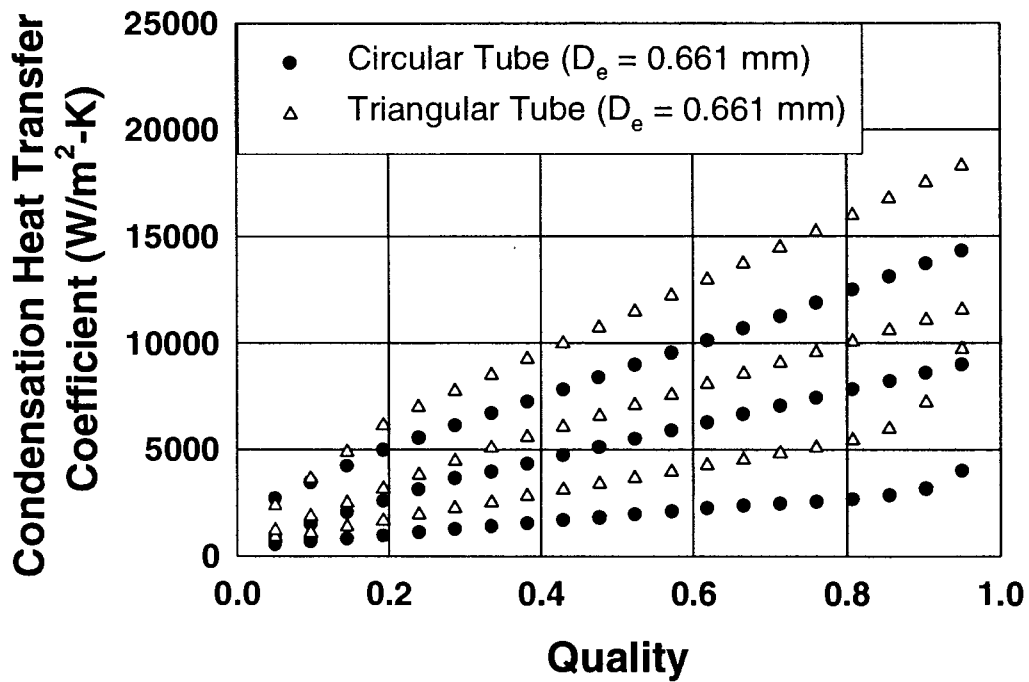


Figure 117. Comparison of Heat Transfer Coefficients in Triangular and Circular Tubes for  $G = 150, 450, \text{ and } 750 \text{ kg/m}^2\text{-s}$

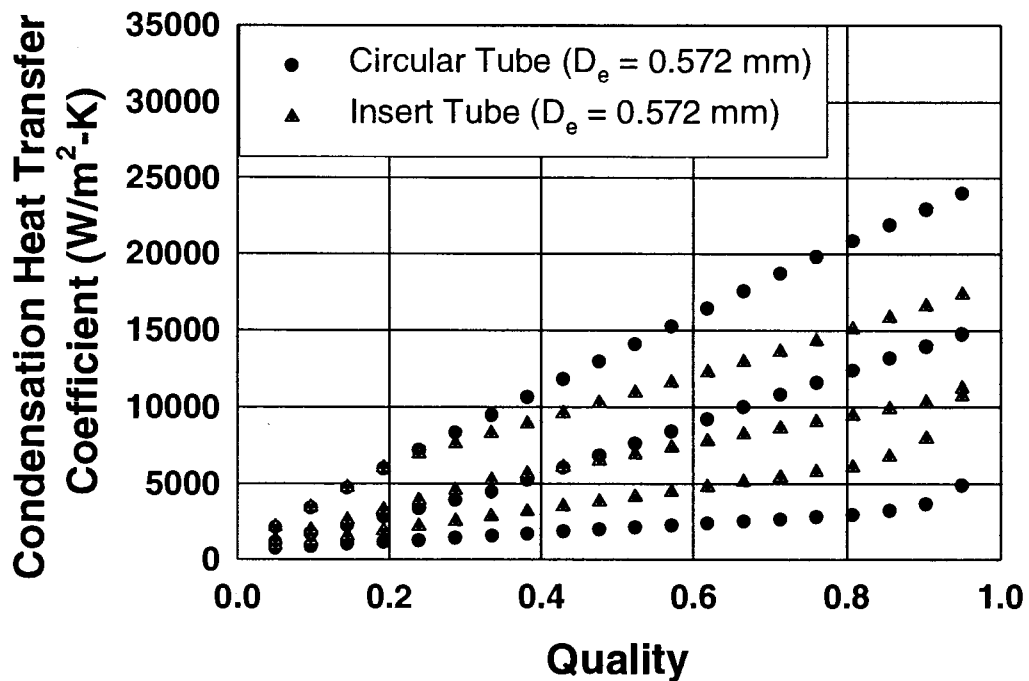


Figure 118. Comparison of Heat Transfer Coefficients in W-shaped and Circular Tubes for  $G = 150, 450, \text{ and } 750 \text{ kg/m}^2\text{-s}$

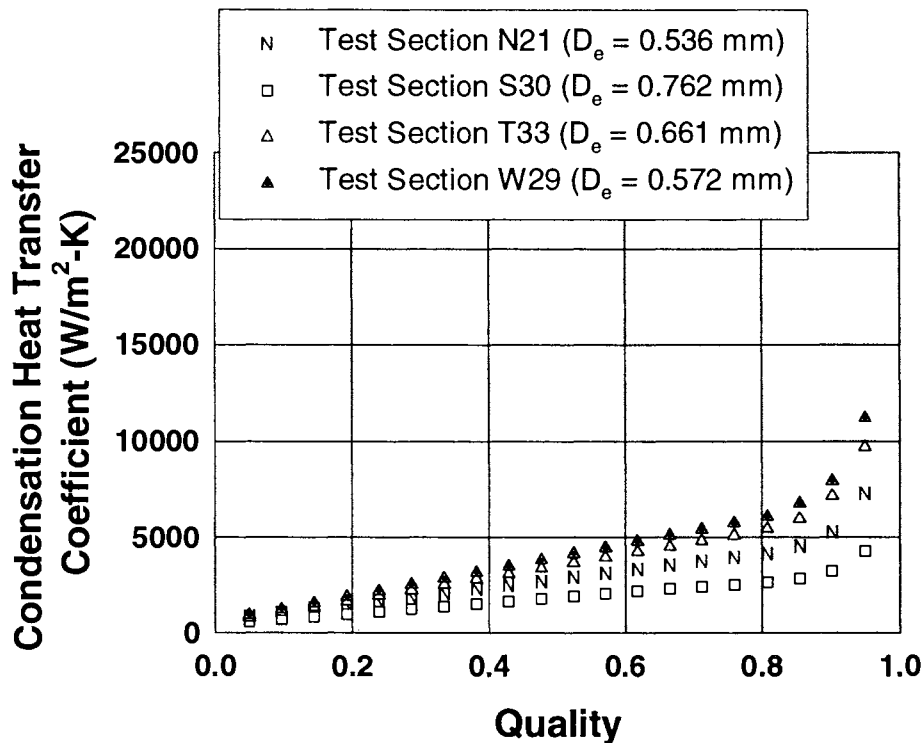


Figure 119. Effect of Tube Shape on Heat Transfer Coefficient,  $G = 150$  kg/m<sup>2</sup>-s

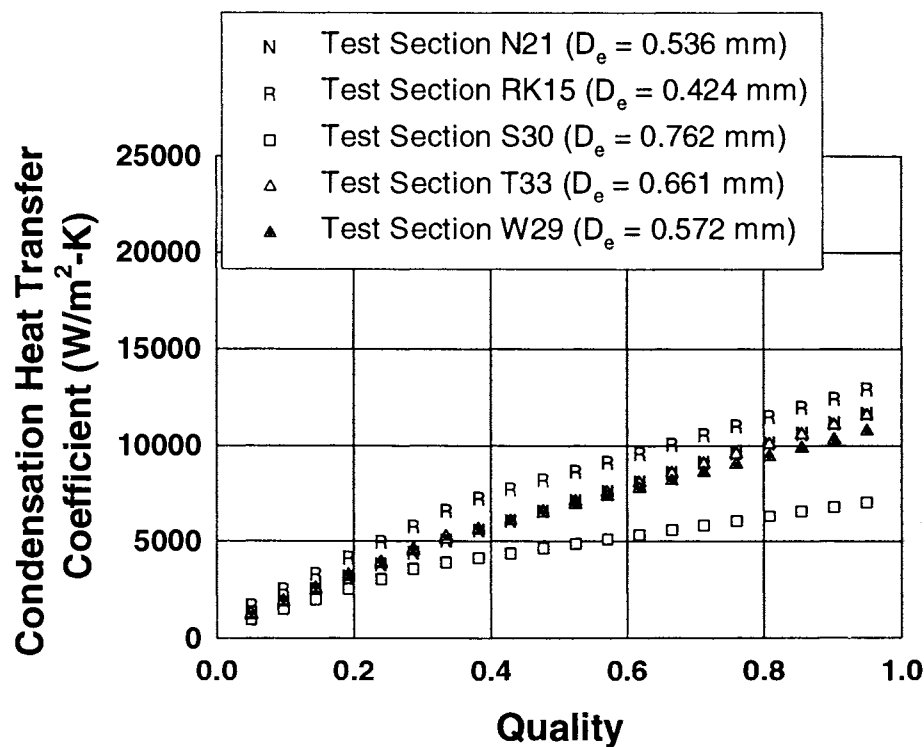


Figure 120. Effect of Tube Shape on Heat Transfer Coefficient,  $G = 450$  kg/m<sup>2</sup>-s

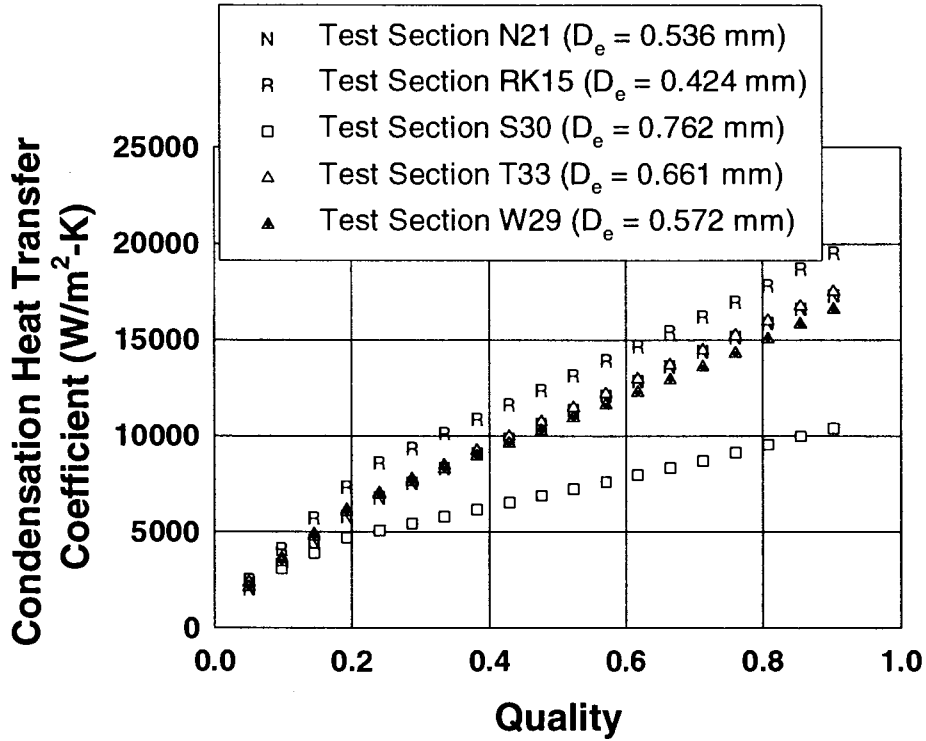


Figure 121. Effect of Tube Shape on Heat Transfer Coefficient,  $G = 750$  kg/m<sup>2</sup>-s

## CHAPTER SIX: CONCLUSIONS

In the present study, innovative heat duty and heat transfer coefficient measurement techniques were used to determine local heat transfer coefficients for R-134a condensing inside small hydraulic diameter tubes. The geometries included 3 circular tubes and 6 non-circular tubes (barrel, N-shaped, rectangular, square, and triangular extruded tubes, and a triangular corrugated insert tube) with hydraulic diameters ranging from 0.424 mm to 1.524 mm. The heat transfer coefficients were determined for local vapor qualities ranging from 0.05 to 0.95 and a mass flux range of  $150 < G < 750 \text{ kg/m}^2\text{-s}$ . An uncertainty analysis showed that most of the heat transfer coefficients were known to within  $\pm 30\%$ . For all but the barrel-shaped tube, the heat transfer coefficients increased with quality and mass flux. The data for the barrel-shaped tube are presumed to be in error: either the low mass flux data are incorrect or the high mass flux data are incorrect.

The effect of hydraulic diameter on local condensation heat transfer coefficients was documented for the three circular tubes ( $D_h = 0.506 \text{ mm}$ ,  $0.761 \text{ mm}$ , and  $1.524 \text{ mm}$ ). Little effect of hydraulic diameter was seen for qualities below about 0.45. Above this value, the heat transfer coefficient increased about 10% to 40% as the diameter decreased from 1.524 mm to 0.761 mm to 0.506 mm. This phenomenon can be mainly attributed to the expansion of the annular flow regime at smaller diameters, especially the mist flow pattern. As observed by Coleman (2000), no discernible liquid film exists for the mist flow pattern. As the liquid film surrounding the vapor core thins (from more entrainment or increased vapor inertia), the resistance to heat transfer decreases, thereby increasing the heat transfer coefficient (Soliman, 1986).

To document the effect of geometry on condensation heat transfer coefficients, the barrel ( $D_h = 0.799 \text{ mm}$ ), square ( $D_h = 0.762 \text{ mm}$ ), and triangular ( $D_h = 0.839 \text{ mm}$ ) extruded tubes and the triangular corrugated insert tube ( $D_h = 0.732 \text{ mm}$ ) data were compared with data for a circular tube of a similar hydraulic diameter ( $D_h = 0.761 \text{ mm}$ ). Overall, the triangular extruded and corrugated insert tubes seem to have the highest heat transfer coefficients, with the effect of tube shape not being very significant for the other test sections. However, the large pressure drops in these two test sections (as high as 210 kPa for test section for the corrugated insert) led to steep drops in the refrigerant saturation temperatures across the test section. This invariably lowered the LMTD for the tests, and in turn decreased the accuracy of the calculated UA values.

The work of Coleman (2000) was used (and extrapolated to develop curve fits for

transition lines) and thus designate the prevailing flow regime for a given combination of mass flux, quality, and diameter. Three flow regimes were possible: wavy flow, intermittent flow, and annular flow, which can be further sub-divided into the annular film and mist flow patterns. Wavy flow comprised an insignificant portion of the test matrix for present study, and was therefore neglected. For the range of diameters in the present study, large flow regime overlaps occurred throughout the condensation path. For example, only a small portion of the data exhibit only one kind of flow pattern (3.65% of the total data sets in intermittent, 19.5% in annular, and 12.2% in mist). Similarly, a small portion of the data are in transition regions adjacent to intermittent flow (11% in intermittent/annular and 3.65% in intermittent/annular/mist). However, 50% of the data are in annular/mist transition flow.

For comparison with the literature, the circular tube data were divided into two sets: intermittent and annular. The gravity-driven correlations of Chato (1962), Jaster and Kosky (1976), and Rosson and Myers (1965), as well as the horizontal intermittent model of Tien et al. (1988), did not successfully predict the intermittent data set, essentially due to the absence of such stratified regimes for the circular tubes considered here. The annular flow data were compared with various shear-driven and homogenous correlations. The shear-based correlations of Traviss et al. (1973), Cavallini and Zecchin (1974), and Shah (1979) over-predicted all of the circular tube data. The shear driven correlations of Soliman et al. (1968), Chen et al. (1987), and Moser et al. (1998) predict the annular data very well, but there is slight over-prediction at low qualities and under-prediction at high qualities. The homogenous correlation of Boyko and Kruzhilin (1967) does predict the data well, but requiring different constants for different fluid/tube combinations is a concern. Although mist flow existed for a wide range of at qualities and flow rates, the homogeneous correlation of Soliman (1986) over-predicts the data, especially for high quality/mass flux situations, which are in the mist flow pattern. All of the circular data were compared with the flow regime-based correlations of Nitheanandan et al. (1990), and Dobson and Chato (1998), but they assume an abrupt change in the flow, as opposed to gradual, and generally over-predict the data.

Condensation heat transfer models for annular, mist, and intermittent flow were developed for both the circular and non-circular tubes. Quality-based averaging accounted for the presence of multiple regimes for a given condition. The annular film flow model was an adaptation to the boundary layer approach of Traviss et al. (1973), where the present study proposes the microchannel pressure drop correlation of Coleman (2000) be used to estimated the friction velocity. Similar to the approach of Soliman (1986), the mist flow heat transfer coefficient is predicted using a constant multiplier (different depending on geometry) to the

mixture Churchill (1977a) Nusselt number. The intermittent flow heat transfer coefficient was calculated using a linear interpolation between the liquid only heat transfer coefficient corresponding to the end of the condensation process, and the annular flow-based heat transfer coefficient at the upper boundary of the intermittent regime. Using the quality-based averaging techniques, the models predicted 90% of the circular data to within  $\pm 25\%$  and 84% of the non-circular data to within  $\pm 30\%$ . The range of validity for these model is as follows:  $0.424 \text{ mm} < D < 1.524 \text{ mm}$ ,  $150 \text{ kg/m}^2\text{-s} < G < 750 \text{ kg/m}^2\text{-s}$ , and  $1,240 \text{ kPa} < P < 1,725 \text{ kPa}$ . Pressures outside this range may cause deviations between the model and data, especially as the critical pressure (4,059 kPa for R-134a) is approached. Application of the model beyond this range of diameters and mass fluxes could result in inexplicable trends.

The flow regime-based correlations developed in the present study lead to better prediction of R-134a condensation heat transfer coefficients inside microchannel tubes, which should lead to more accurate design of condensers. It is expected that this will enable the development of smaller, more efficient condensers that use less material and refrigerant charge.

## REFERENCES CITED

- Abis, L. V. (1969). Forced Convection Condensation Inside Horizontal Tubes. Ph.D. Dissertation. Department of Mechanical Engineering. Manhattan, KS, Kansas State University.
- Akers, W. W., H. A. Deans and O. K. Crosser (1959). "Condensation Heat Transfer within Horizontal Tubes." Chemical Engineering Progress Symposium Series **55**(29): 171-176.
- Akers, W. W. and H. F. Rosson (1960). "Condensation Inside a Horizontal Tube." Chemical Engineering Progress Symposium Series **59**: 145-149.
- Ananiev, E. P., L. D. Boyko and G. N. Kruzhilin (1961). "Heat Transfer in the Presence of Steam Condensation in a Horizontal Tube." International Heat Transfer Conference: Part II: 290.
- Asali, J. C., T. J. Hanratty and P. Andreussi (1985). "Interfacial Drag and Film Height for Vertical Flow." AIChE Journal **36**1: 895-902.
- Baroczy, C. J. (1965). "Correlation of Liquid Fraction in Two-Phase Flow with Applications to Liquid Metals." Chemical Engineering Progress Symposium Series **61**(57): 179-191.
- Blangetti, F. and E. O. Schlunder (1978). "Local Heat Transfer Coefficients of Condensation in a Vertical Tube." Proceedings of the 6th International Heat Transfer Conference **2**: 437-442.
- Boyko, L. D. and G. N. Kruzhilin (1967). "Heat Transfer and Hydraulic Resistance During Condensation of Steam in a Horizontal Tube and in a Bundle of Tubes." International Journal of Heat and Mass Transfer **10**: 361-373.
- Breber, G., J. W. Palen and J. Taborek (1980). "Prediction of Horizontal Tubeside Condensation of Pure Components Using Flow Regime Criteria." Journal of Heat Transfer **102**(3): 471-476.
- Carey, V. P. (1992). Liquid-Vapor Phase-Change Phenomena: An Introduction to the Thermophysics of Vaporization and Condensation Processes in Heat Transfer Equipment, Hemisphere Publishing.
- Carpenter, F. G. and A. P. Colburn (1951). "The Effect of Vapor Velocity on Condensation Inside Tubes." ASME Proceedings of the General Discussion of Heat Transfer: 20-26.
- Cavallini, A. and R. Zecchin (1974). "A Dimensionless Correlation for Heat Transfer in

- Forced-Convective Condensation." Proceedings of the Fifth International Heat Transfer Conference, JSME **3**: 309-313.
- Chato, J. C. (1962). "Laminar Condensation Inside Horizontal and Inclined Tubes." ASHRAE Journal **4**: 52-60.
- Chen, I. Y. and G. Kocamustafaogullari (1987). "Condensation Heat Transfer Studies for Stratified, Cocurrent Two-Phase Flow in Horizontal Tubes." International Journal of Heat and Mass Transfer **30**(6): 1133-1148.
- Chen, S. L., F. M. Gerner and C. L. Tien (1987). "General Film Condensation Correlations." Experimental Heat Transfer **1**: 93-107.
- Chitti, M. S. and N. K. Anand (1995). "An Analytical Model for Local Heat Transfer Coefficients for Forced Convective Condensation Inside Smooth Horizontal Tubes." International Journal of Heat and Mass Transfer **38**(4): 615-627.
- Chitti, M. S. and N. K. Anand (1996a). "Condensation Heat Transfer Inside Smooth Horizontal Tubes for R-22 and R-32/125 Mixture." ASHRAE HVAC&R Research **2**(1): 79-100.
- Chitti, M. S. and N. K. Anand (1996b). "Heat Transfer Correlation for Condensation Inside Horizontal Smooth Tubes Using the Population Balance Approach." International Journal of Heat and Mass Transfer **39**(14): 2947-2956.
- Chun, K. R. and R. A. Seban (1971). "Heat Transfer to Evaporating Liquid Films." Journal of Heat Transfer **93**: 391-396.
- Churchill, S. W. (1977a). "Comprehensive Correlating Equations for Heat, Mass and Momentum Transfer in Fully Developed Flow in Smooth Tubes." Ind. Eng. Chem. Fundamentals **16**(1): 109-116.
- Churchill, S. W. (1977b). "Friction Factor Equations Spans All Fluid Flow Regimes." Chemical Engineering **84**(24): 91-92.
- Churchill, S. W. and H. H. S. Chu (1975). "Correlating Equations for Laminar and Turbulent Free Convection from a Vertical Plate." International Journal of Heat and Mass Transfer **18**: 1323.
- Colebrook, C. F. (1939). "Turbulent Flow in Pipes with Particular Reference to the Transition Between the Smooth and Rough Pipe Laws." Journal of the Institute of Civil Engineers **11**: 133-156.
- Coleman, J. W. (2000). Flow Visualization and Pressure Drop in Small Hydraulic Diameter Geometries During Phase Change of Refrigerants. Ph.D. Dissertation. Department of Mechanical Engineering. Ames, Iowa State University.
- Dobson, M. K. (1994). Heat Transfer and Flow Regimes During Condensation in Horizontal

- Tubes. Ph.D. Dissertation. Department of Mechanical and Industrial Engineering. Urbana-Champaign, University of Illinois at Urbana-Champaign.
- Dobson, M. K. and J. C. Chato (1998). "Condensation Inside Smooth Horizontal Tubes." Journal of Heat Transfer **120**: 193-213.
- Dobson, M. K., J. C. Chato, D. K. Hinde and S. P. Wang (1994). "Experimental Evaluation of Internal Condensation of Refrigerants R-12 and R-134a." ASHRAE Transactions Symposia **94-5-3**: 744-754.
- Dukler, A. E. (1960). "Fluid Mechanics and Heat Transfer in Vertical Falling Film Systems." Chemical Engineering Progress Symposium Series **56(30)**: 1-10.
- Dukler, A. E., M. Wicks and R. G. Cleveland (1962). "Frictional Pressure Drop in Two-Phase Flow. An Approach Through Similarity Analysis." Presented at the 55th Annual AIChE Meeting, Chicago, IL.
- Friedel, L. (1979). "Improved Friction Pressure Drop Correlations for Horizontal and Vertical Two Phase Pipe Flow." European Two Phase Flow Group Meeting Paper E2.
- Garimella, S. and R. N. Christensen (1995). "Heat Transfer and Pressure drop Characteristics of Spirally Fluted Annuli: Part II-Heat Transfer." Journal of Heat Transfer **117**: 61-68.
- Gnielinski, V. (1979). "New Equations for Heat and Mass Transfer in Turbulent Pipe and Channel Flow." International Chemical Engineering **16**: 359-368.
- Guo, Z. (1998). Condensation of R-410a in Horizontal Rectangular Channel. Ph.D. Dissertation Department of Mechanical Engineering. College Station, TX, Texas A&M University.
- Guo, Z. and N. K. Anand (2000). "An Analytical Model to Predict Condensation in a Horizontal Rectangular Channel." Journal of Heat Transfer **122**: 613-620.
- Hassan, K. E. and M. Jakob (1958). "Laminar Film Condensation of Pure Saturated Vapors on Inclined Circular Cylinders." Transactions of the ASME **80**: 887-894.
- Hurlburt, E. T. and T. A. Newell (1999). "Characteristics of Refrigerant Film Thickness, Pressure Drop, and Condensation Heat Transfer in Annular Flow." ASHRAE HVAC&R Research **5(3)**: 229-248.
- Ibrahim, O. M. (1994). "Prediction of Local Heat Transfer Coefficients During Annular Flow Condensation." Proceedings of the 1994 ASME Fluids Engineering Division Summer Meeting **180**: 77-81.
- Incropera, F. P. and D. P. DeWitt (1996). Fundamentals of Heat and Mass Transfer. New York, John Wiley & Sons, Inc.
- Jaster, H. and P. G. Kosky (1976). "Condensation in a Mixed Flow Regime." International

Journal of Heat and Mass Transfer **19**: 95-99.

- Kakac, S., R. K. Shah and W. Aung (1987). Handbook of Single-Phase Convective Heat Transfer. New York, Wiley.
- Kays, W. M. and E. Y. Leung (1963). "Heat Transfer in Annular Passages: Hydrodynamically Developed Flow with Arbitrarily Prescribed Heat Flux." International Journal of Heat and Mass Transfer **6**: 537-557.
- Klein, S. A. and F. L. Alvarado (2000). Engineering Equation Solver. f-chart Software, Madison, WI.
- Kosky, P. G. and F. W. Staub (1971). "Local Condensing Heat Transfer Coefficients in the Annular Flow Regime." AIChE Journal **17**: 1037.
- Lin, S. T. (1979). Augmentation of Two-Phase Heat Transfer with In-Line Static Mixers. Ph.D. Dissertation. Department of Mechanical Engineering. Manhattan, KS, Kansas State University.
- Lockhart, R. W. and R. C. Martinelli (1949). "Proposed Correlation of Data for Isothermal Two-Phase Two-Component Flow in Pipes." Chemical Engineering Progress **45**: 39.
- Mikheev, M. A. (1956). Heat Transfer Fundamentals. Moscow, Gosenergoizdat.
- Miropolsky, Z. L. (1962). "Heat Transfer During Condensation of High Pressure Steam Inside a Tube." Teploenergetika **3**: 79-83.
- Moser, K., R. L. Webb and B. Na (1998). "A New Equivalent Reynolds Number Model for Condensation in Smooth Tubes." Journal of Heat Transfer **120**: 419-417.
- Munson, B. R., D. F. Young and T. H. Okiishi (1998). Fundamentals of Fluid Mechanics. New York, John Wiley & Sons, Inc.
- Myers, J. A. and H. F. Rosson (1961). "Condensing Coefficient Inside a Horizontal Tube Near Atmospheric Pressure." Chemical Engineering Progress Symposium Series **57**: 150-156.
- Nitthanandan, T., H. M. Soliman and R. E. Chant (1990). "A Proposed Approach for Correlating Heat Transfer During Condensation Inside Tubes." ASHRAE Transactions **96**(1): 3328-3333.
- Nusselt, W. (1916). "Die Oberflächenkondensation des Wasserdampfes." Zeitschrift Vereines Deutsch Ingenieure **60**: 541, 569.
- Petukhov, B. S. (1970). "Heat Transfer and Friction in Turbulent Pipe Flow with Variable Physical Properties." Advances in Heat Transfer **6**. Academic Press, New York, NY.
- Rohsenow, W. M. (1956). "Heat Transfer and Temperature Distribution in Laminar Film Condensation." Transactions of the ASME **78**: 1645-1648.
- Rohsenow, W. M., J. H. Webber and A. T. Ling (1956). "Effect of Vapor Velocity on

- Laminar and Turbulent-Film Condensation." Transactions of the ASME **78**: 1637-1643.
- Rosson, H. F. and J. A. Myers (1965). "Point Values of Condensing Film Coefficients Inside a Horizontal Tube." Chemical Engineering Progress Symposium Series **61**(59): 190-199.
- Rufer, C. E. (1965). Two-Phase, One-Component Stratified Flow with Condensation. Ph.D. Dissertation. Illinois Institute of Technology.
- Rufer, C. E. and S. P. Kezios (1966). "Analysis of Two-Phase, One-Component Stratified Flow with Condensation." Journal of Heat Transfer **88**: 265-275.
- Sacks, P. S. (1975). "Measured Characteristics of Adiabatic and Condensing Single-Component Two-Phase Flow of Refrigerant in a 0.377 Inch Diameter Horizontal Tube." ASME Paper 75-WA/HT-24.
- Shah, M. M. (1976). "A New Correlation for Heat Transfer During Flow Boiling Through Pipes." ASHRAE Transactions **82**(2): 66-86.
- Shah, M. M. (1979). "A General Correlation for Heat Transfer During Film Condensation Inside Pipes." International Journal of Heat and Mass Transfer **22**: 547-556.
- Shah, M. M. (1981). "Heat Transfer During Film Condensation in Tubes and Annuli: A Review of the Literature." ASHRAE Transactions **87**(1): 1086-1105.
- Singh, A., M. M. Ohadi and S. V. Dessiatoun (1996). "Empirical Modeling of Stratified-Wavy Flow Condensation Heat Transfer in Smooth Horizontal Tubes." ASHRAE Transactions **102**(2): 596-603.
- Smith, S. L. (1969-70). "Void Fractions in Two-Phase Flow: a Correlation Based upon an Equal Velocity Head Model." Institute of Mechanical Engineering **184**(647-657).
- Soliman, H. M. (1982). "On the Annular-to-Wavy Pattern Transition During Condensation Inside Horizontal Tubes." Canadian Journal of Chemical Engineering **60**: 475-481.
- Soliman, H. M. (1983). "Correlation of Mist-to-Annular Transition During Condensation." Canadian Journal of Chemical Engineering **61**: 178-182.
- Soliman, H. M. (1986). "The Mist-Annular Transition During Condensation and its Influence on the Heat Transfer Mechanism." International Journal of Multiphase Flow **12**(2): 277-288.
- Soliman, H. M., J. R. Schuster and P. J. Berenson (1968). "A General Heat Transfer Correlation for Annular Flow Condensation." Journal of Heat Transfer **90**: 267-276.
- Swagelok (1995). "Swagelok Product Catalog."
- Taylor, B. N. and C. E. Kuyatt (1994). "Guidelines for Evaluating and Expressing the Uncertainty of NIST Measurement Results." National Institute of Standards and

Technology Technical Note 1297.

- Tien, C. L., S. L. Chen and P. F. Patterson (1988). Condensation Inside Tubes: EPRI Project 1160-3 Final Report. Palo Alto, CA, EPRI.
- Traviss, D. P., W. M. Rohsenow and A. B. Baron (1973). "Forced-Convective Condensation in Tubes: A Heat Transfer Correlation for Condenser Design." ASHRAE Transactions **79**(1): 157-165.
- Walker, J. E., G. A. Whan and R. R. Rothfus (1957). "Fluid Friction in Noncircular Ducts." American Institute of Chemical Engineering Journal **3**(4): 484-489.
- Yang, C. Y. and R. L. Webb (1996). "Condensation of R-12 in Small Hydraulic Diameter Extruded Aluminum Tubes with and without Micro-Fins." International Journal of Heat and Mass Transfer **39**(4): 791-800.
- Zivi, S. M. (1964). "Estimation of Steady-State Steam Void-Fraction by Means of the Principle of Minimum Entropy Production." Journal of Heat Transfer **86**: 247-252.

**APPENDIX A: TEST SECTION DATA POINT RANGES**

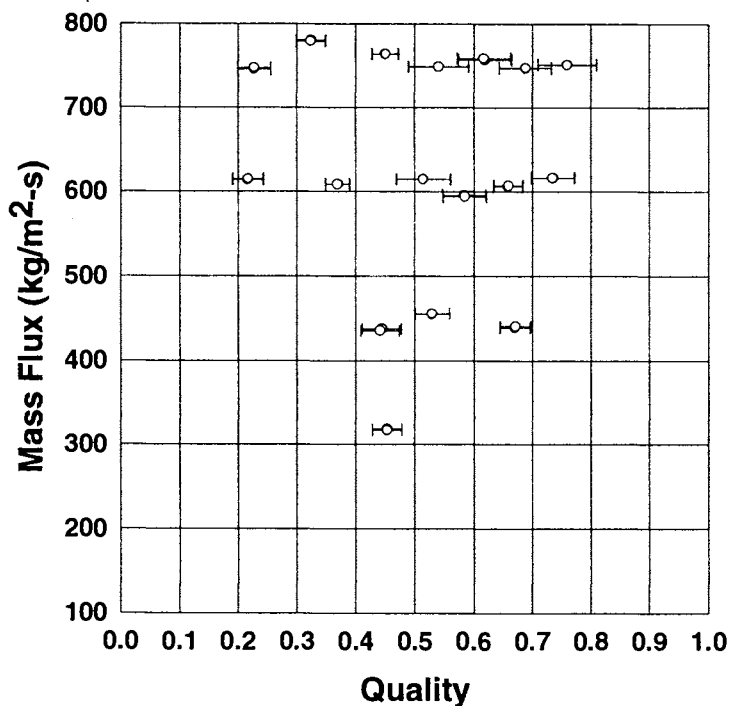


Figure A1. Range of Data Points for Test Section C20

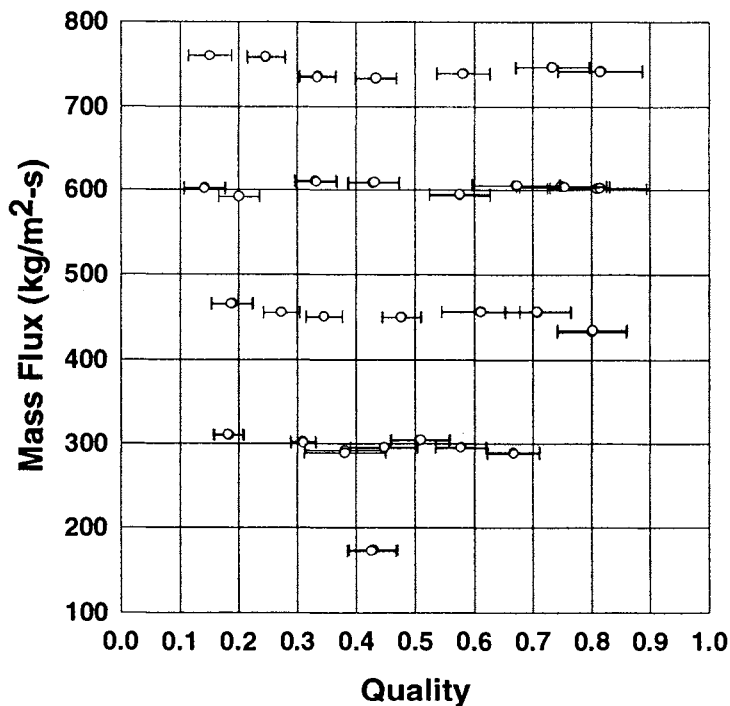


Figure A2. Range of Data Points for Test Section C30

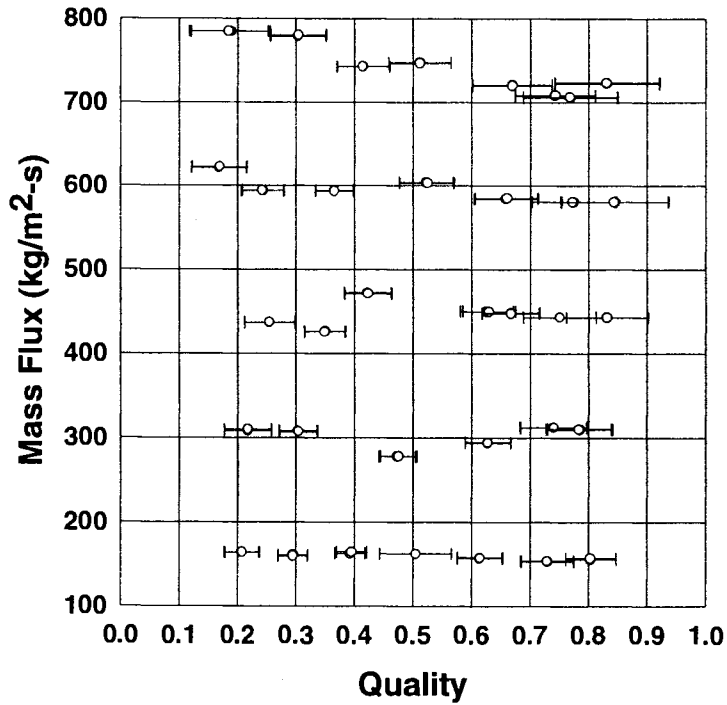


Figure A3. Range of Data Points for Test Section C60

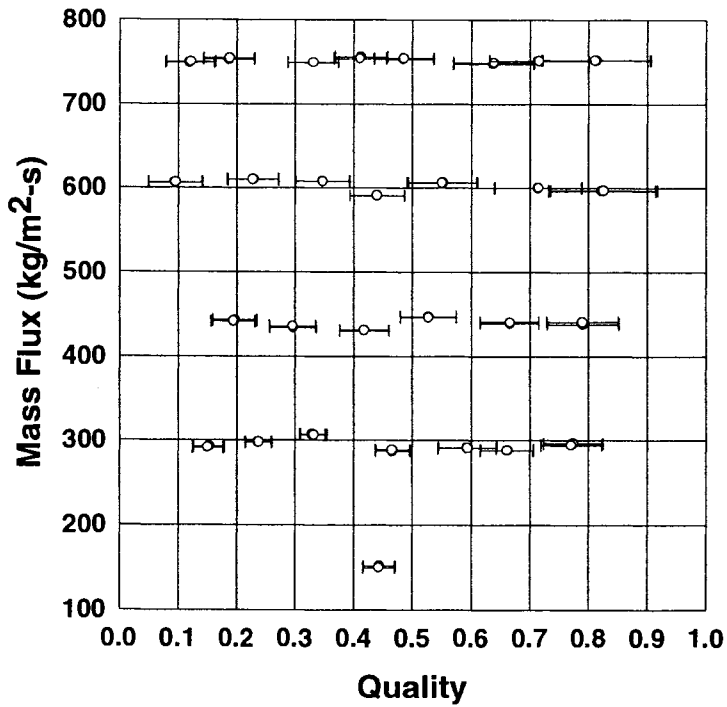


Figure A4. Range of Data Points for Test Section B32

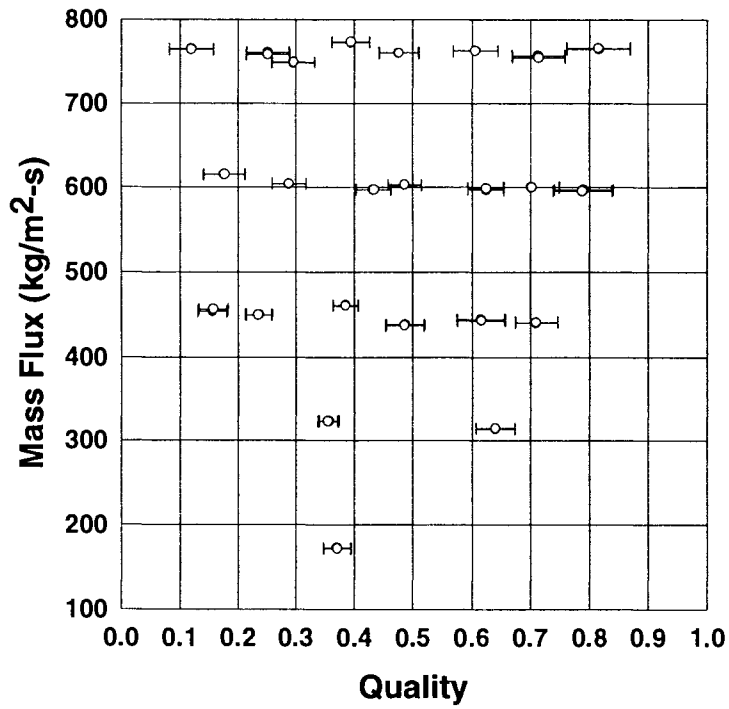


Figure A5. Range of Data Points for Test Section N21

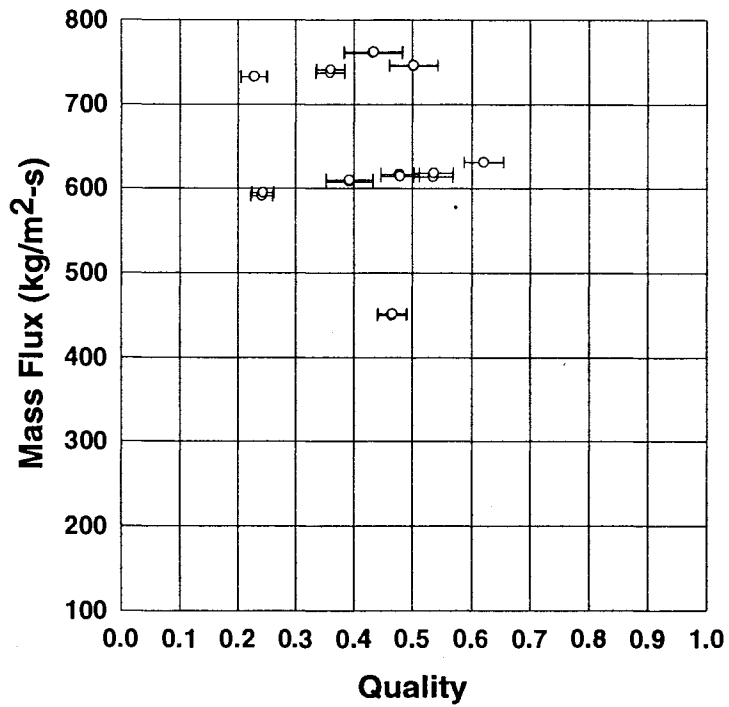


Figure A6. Range of Data Points for Test Section RK15

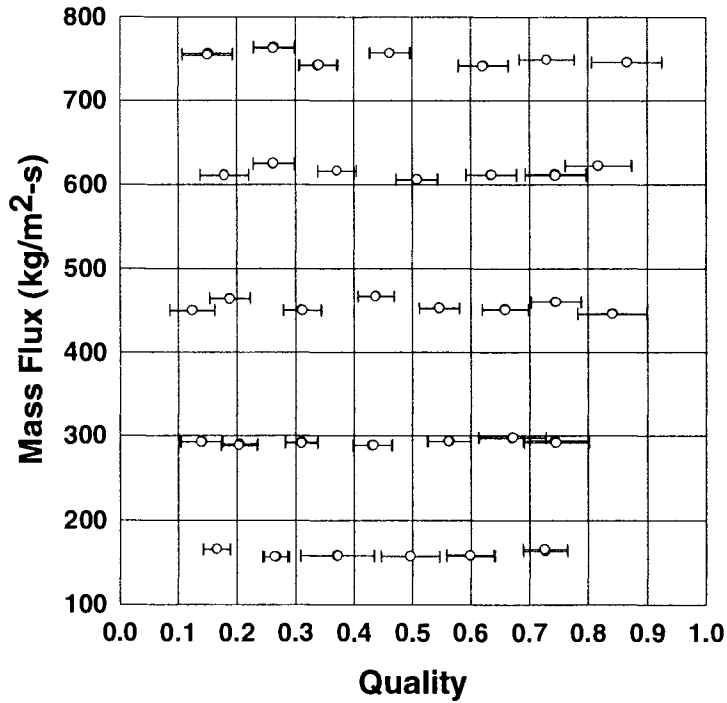


Figure A7. Range of Data Points for Test Section T33

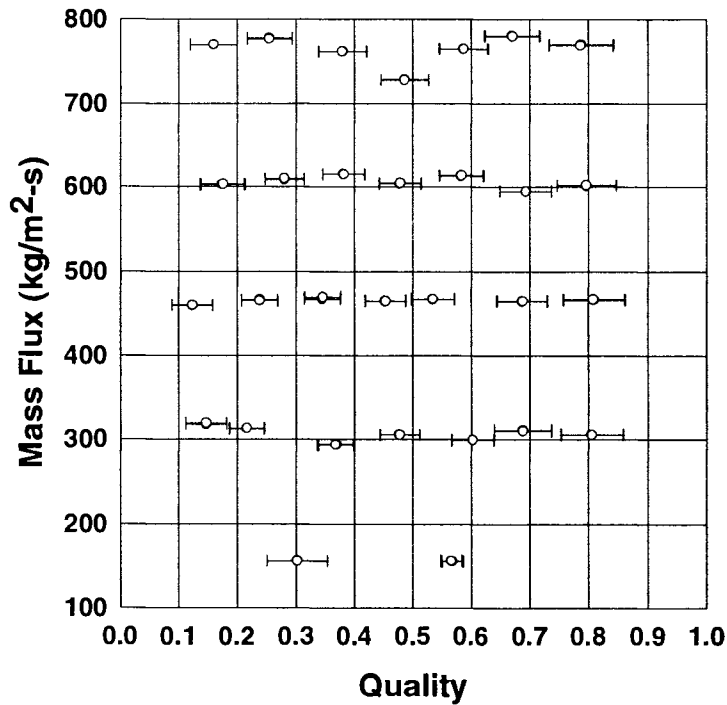


Figure A8. Range of Data Points for Test Section W29

**APPENDIX B: FLOW TRANSITION EQUATIONS**

**Annular Film Flow Lower Limit**

$$G \geq a + b \cdot \ln(x)$$

**where:**

$$a = -89.59 - 23.76 \cdot D_h + 34.56 \cdot D_h^2$$

$$b = 12.57 - 197.6 \cdot D_h + 10.77 \cdot D_h^2$$

**Annular Film Flow Upper Limit**

$$G \leq a + b \cdot e^{-c \cdot x}$$

**where:**

$$a = 422.08 - e^{D_h + 1.8884}$$

$$b = 614504 \cdot e^{-1.2431 \cdot D_h}$$

$$c = 9.4531 - e^{D_h - 1.7484}$$

**Mist Flow Lower Limit**

$$G \geq a + \frac{b}{x}$$

**where**

$$a = -1075 + 1446 \cdot e^{-0.119 \cdot D_h}$$

$$b = -671.59 + 680.3 \cdot e^{0.10275 \cdot D_h}$$

**APPENDIX C: NON-CIRCULAR TUBE FLOW REGIME  
MAPS**

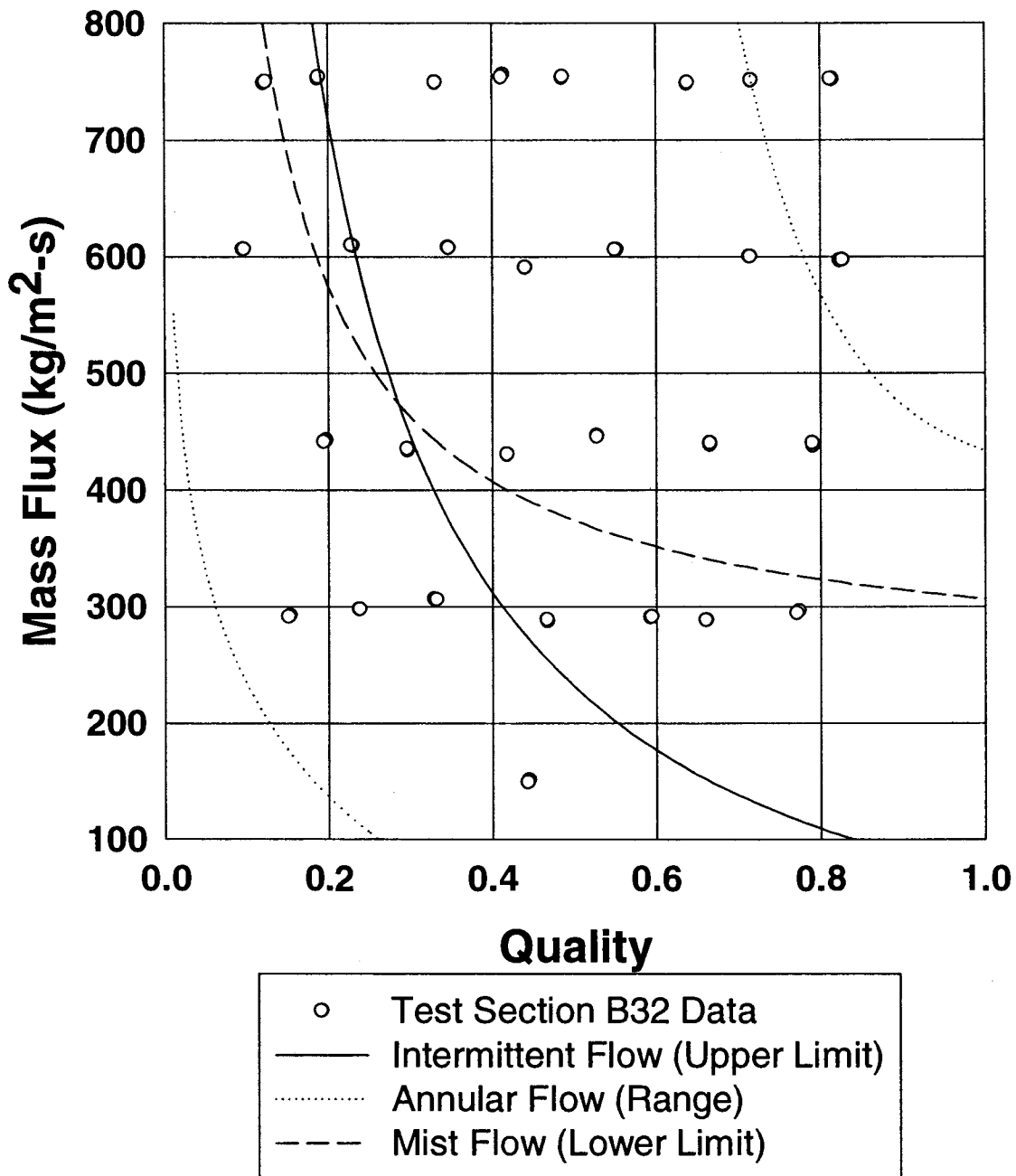


Figure C1. Experimental Data for Test Section B32 with Superimposed Transition Lines

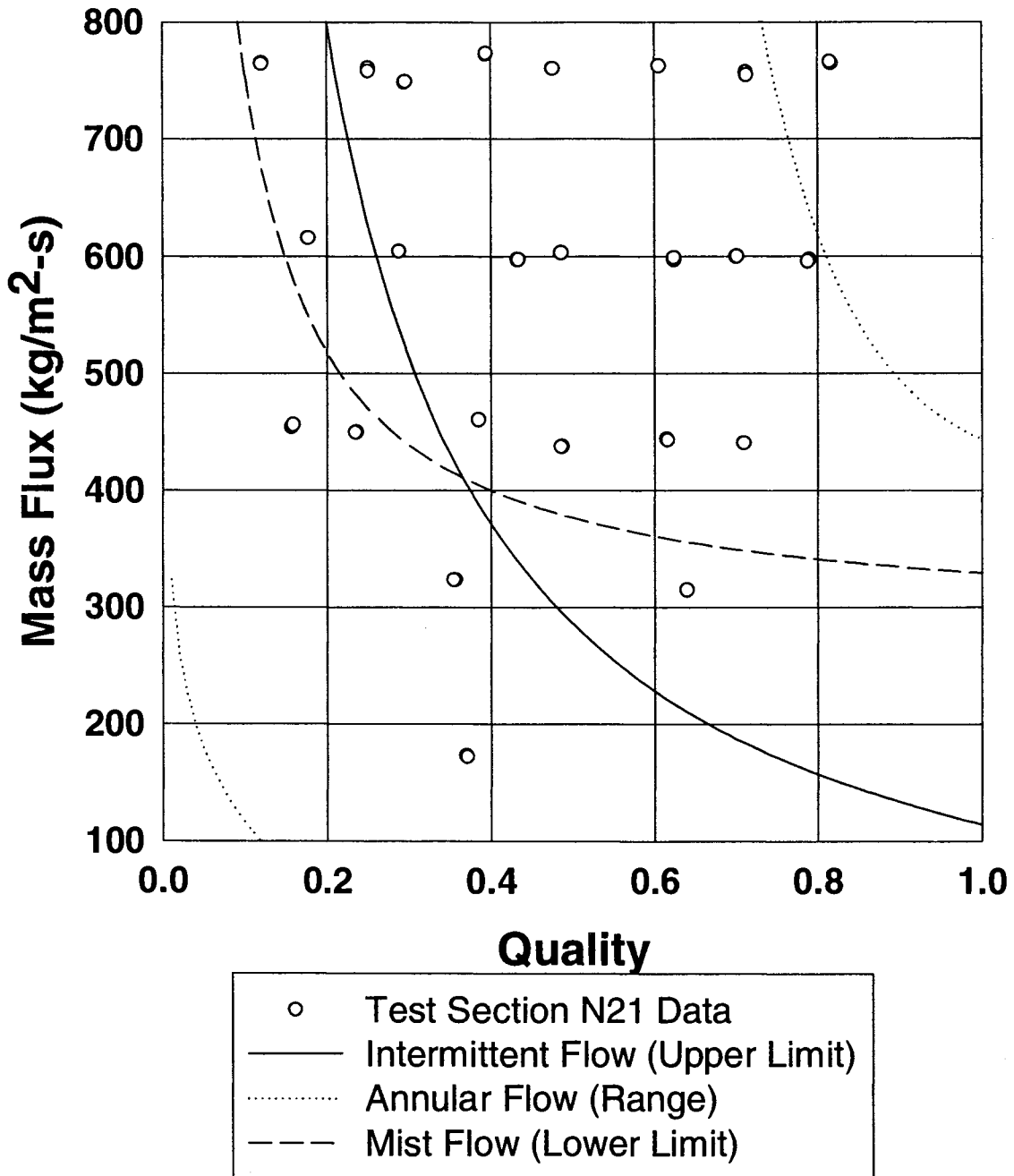


Figure C2. Experimental Data for Test Section N21 with Superimposed Transition Lines

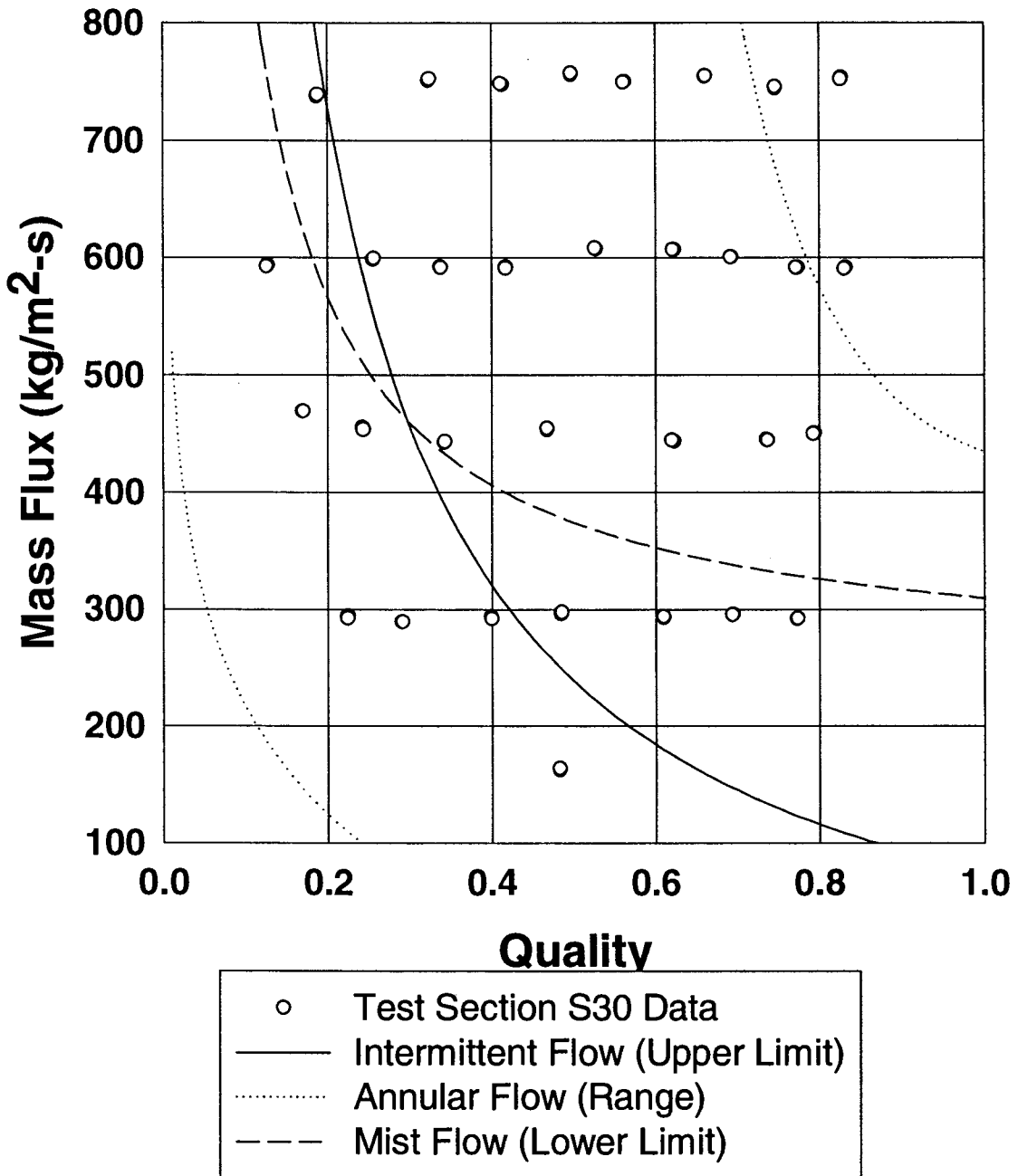


Figure C3. Experimental Data for Test Section S30 with Superimposed Transition Lines

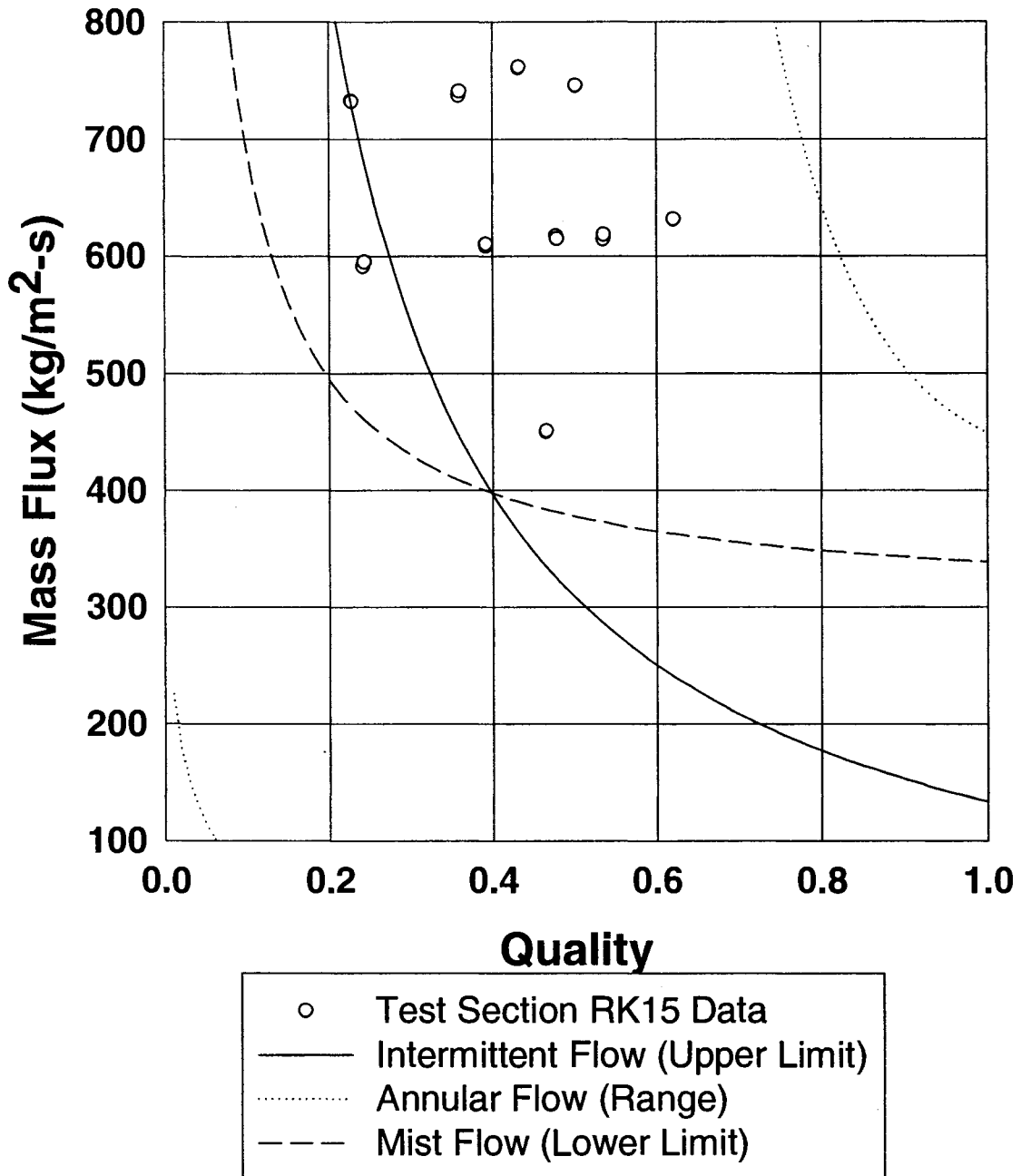


Figure C4. Experimental Data for Test Section RK15 with Superimposed Transition Lines

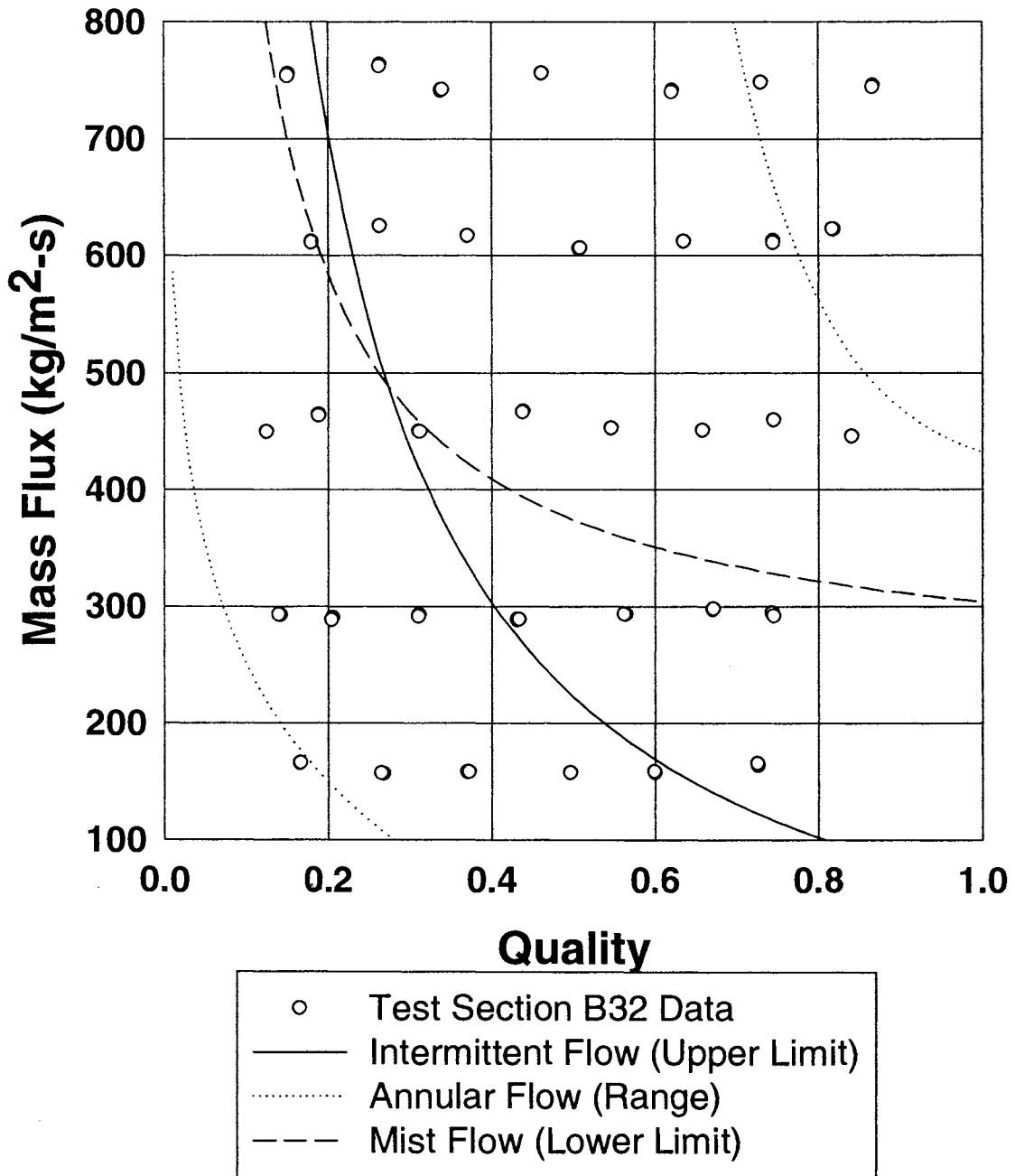


Figure C5. Experimental Data for Test Section T33 with Superimposed Transition Lines

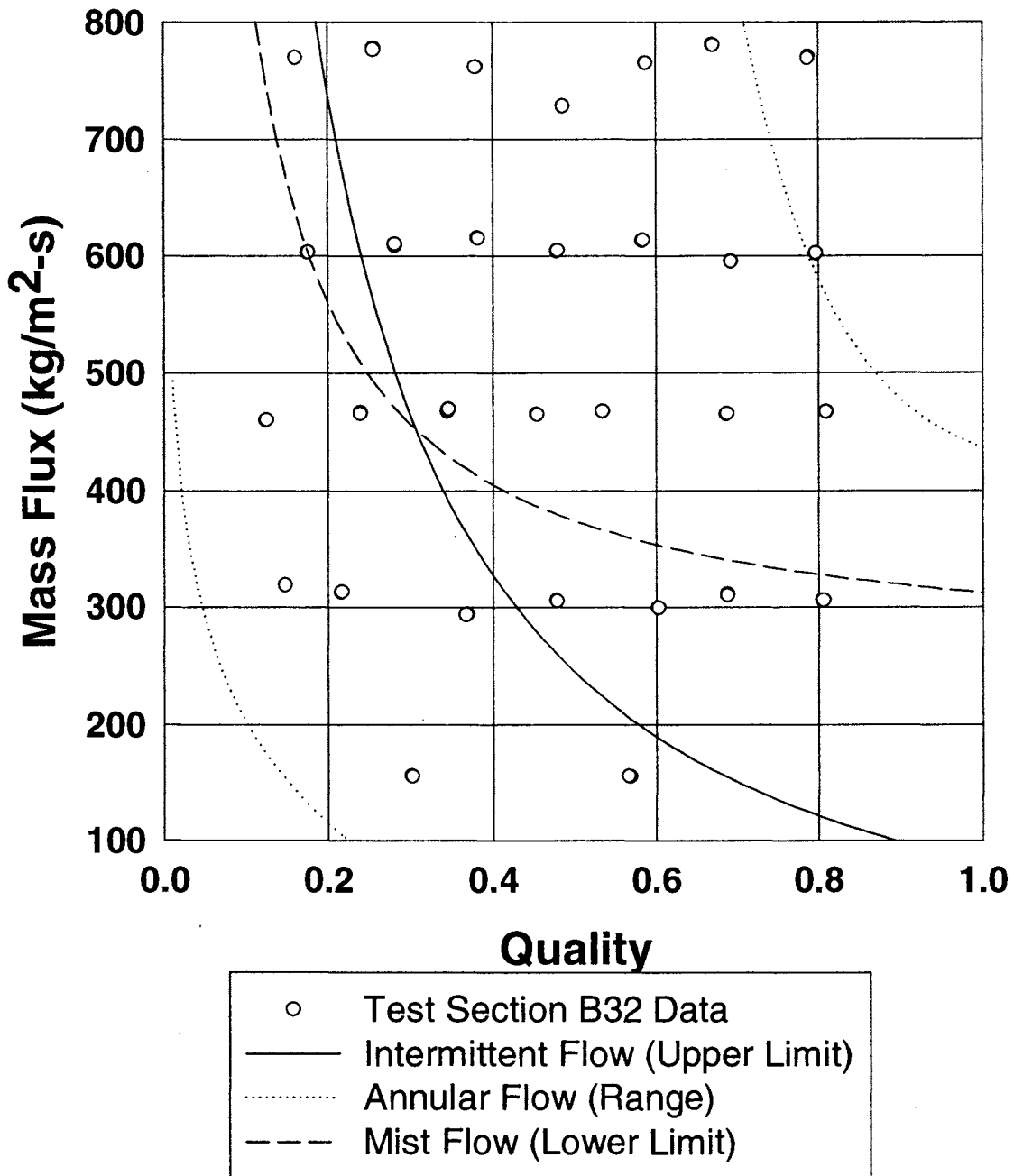
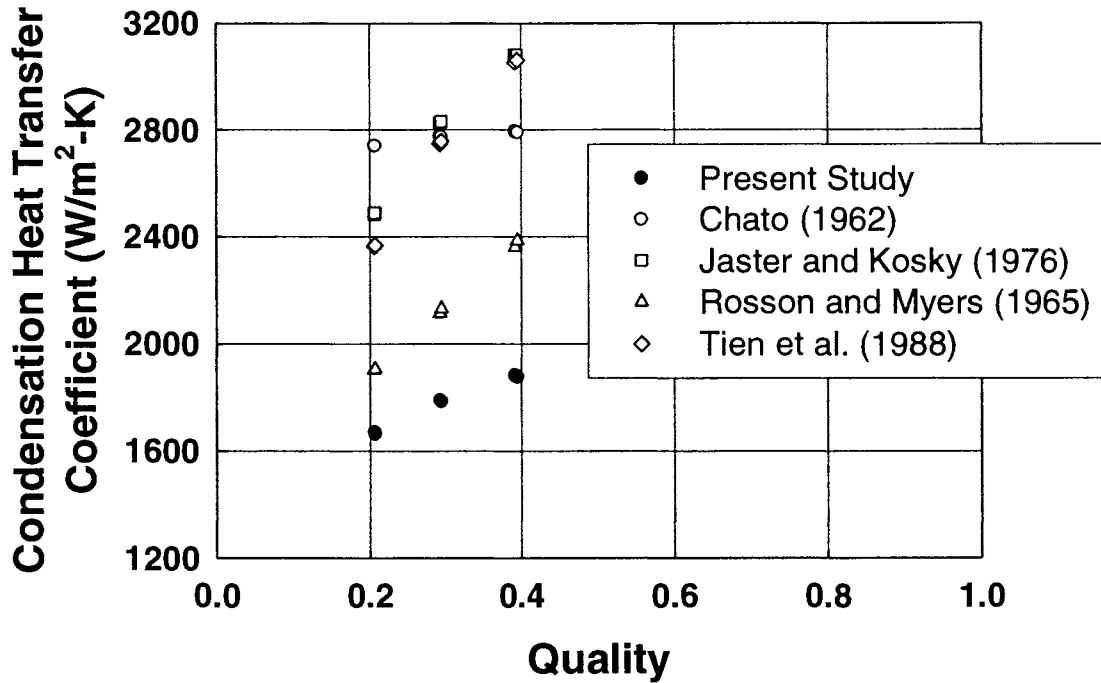


Figure C6. Experimental Data for Test Section W29 with Superimposed Transition Lines

**APPENDIX D: CIRCULAR TUBE COMPARISON WITH  
LITERATURE**

**Intermittent Flow Regime**



**Figure D1. Comparison of Intermittent Flow Data with Literature (Test Section C60,  $G = 150 \text{ kg/m}^2\text{-s}$ )**

**Annular Flow Regime**

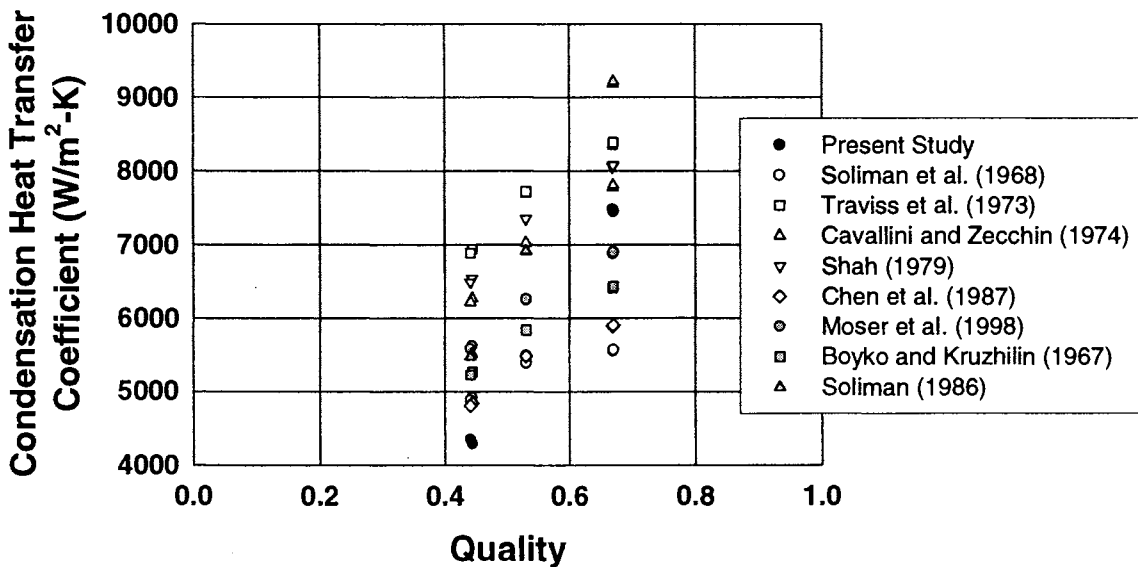


**Figure D2. Comparison of Annular Flow Regime Data with the Literature (Test Section C20,  $G = 450 \text{ kg/m}^2\text{-s}$ )**

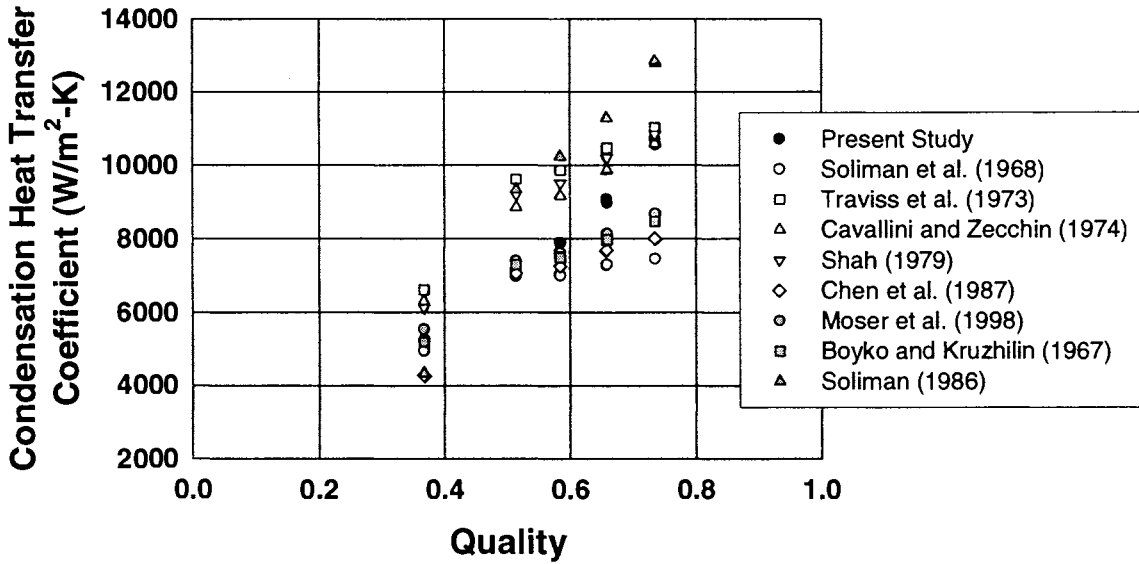


Figure D3. Comparison of Annular Flow Regime Data with the Literature (Test Section C20, G = 600 kg/m<sup>2</sup>-s)

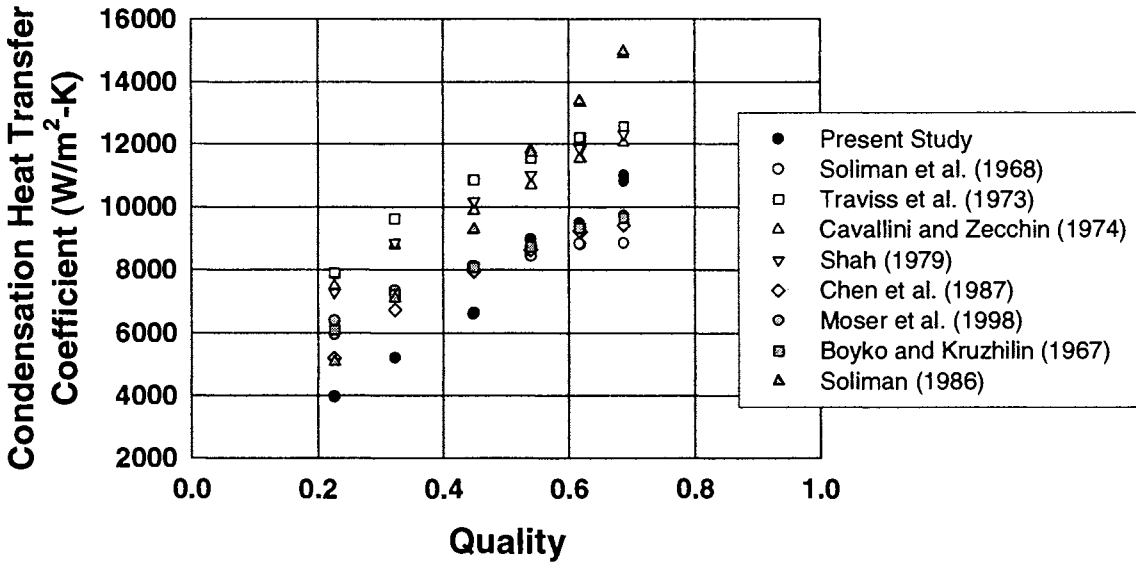


Figure D4. Comparison of Annular Flow Regime Data with the Literature (Test Section C20, G = 750 kg/m<sup>2</sup>-s)

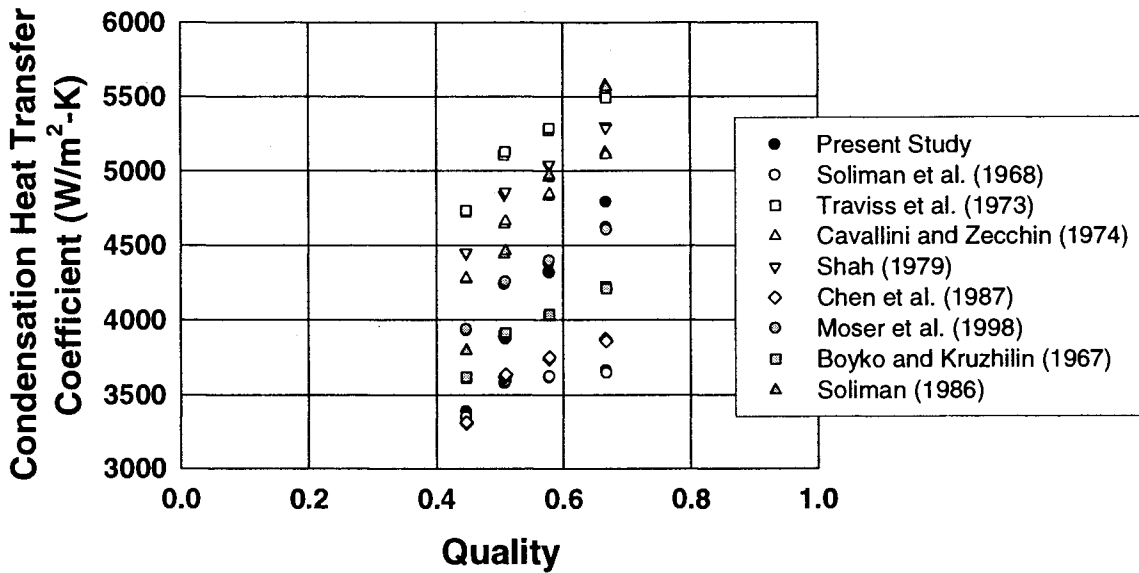


Figure D5. Comparison of Annular Flow Regime Data with the Literature (Test Section C30,  $G = 300 \text{ kg/m}^2\text{-s}$ )

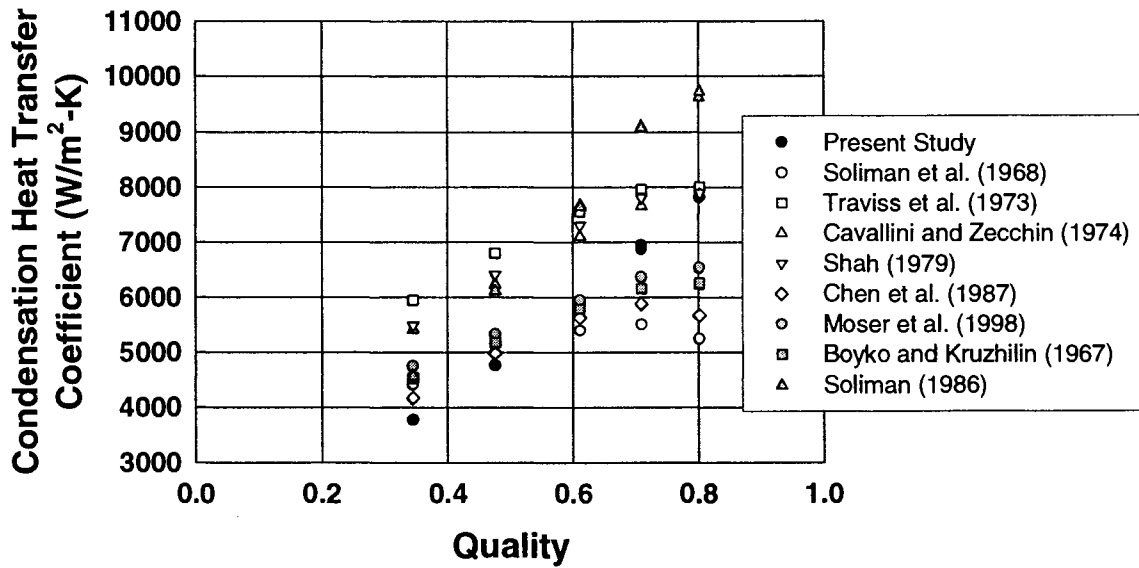


Figure D6. Comparison of Annular Flow Regime Data with the Literature (Test Section C30,  $G = 450 \text{ kg/m}^2\text{-s}$ )

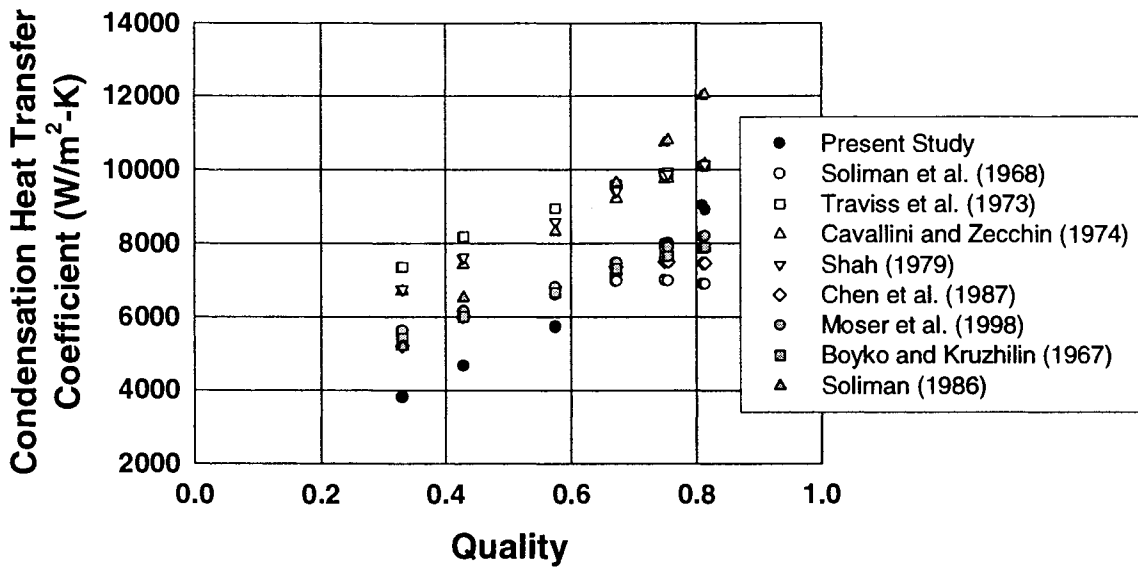


Figure D7. Comparison of Annular Flow Regime Data with the Literature (Test Section C30,  $G = 600 \text{ kg/m}^2\text{-s}$ )

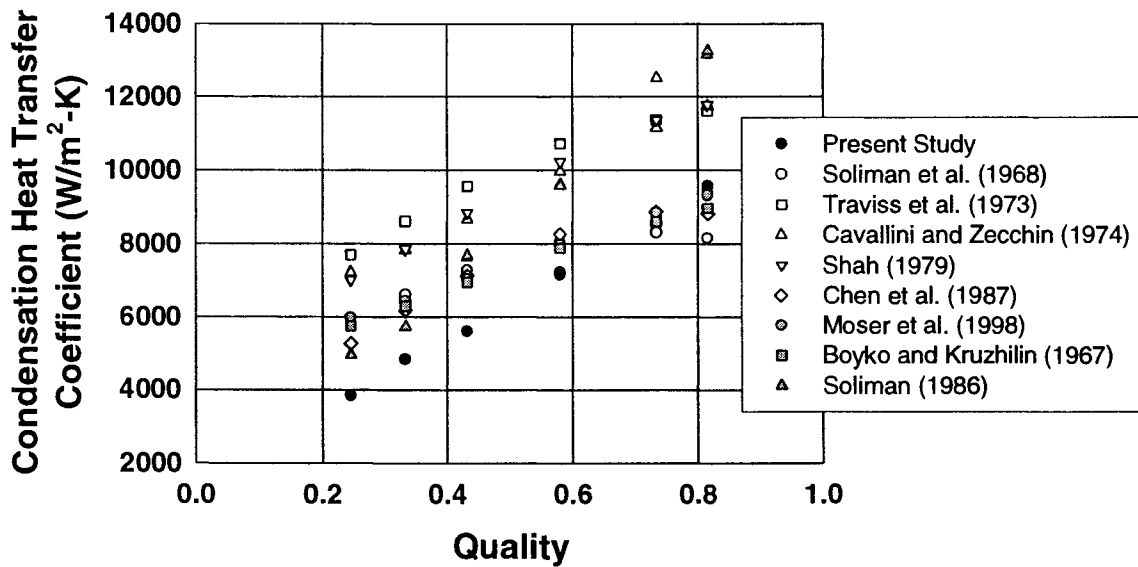


Figure D8. Comparison of Annular Flow Regime Data with the Literature (Test Section C30,  $G = 750 \text{ kg/m}^2\text{-s}$ )

All Regimes

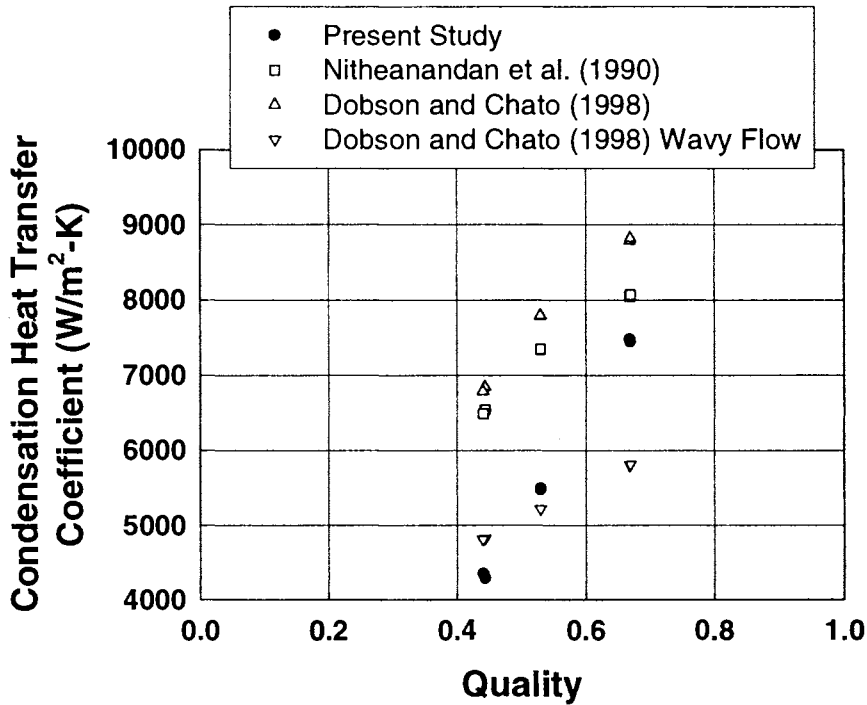


Figure D9. Flow Regime-Based Correlations and Experimental Heat Transfer Coefficients for Test Section C20 at  $G = 450 \text{ kg/m}^2\text{-s}$

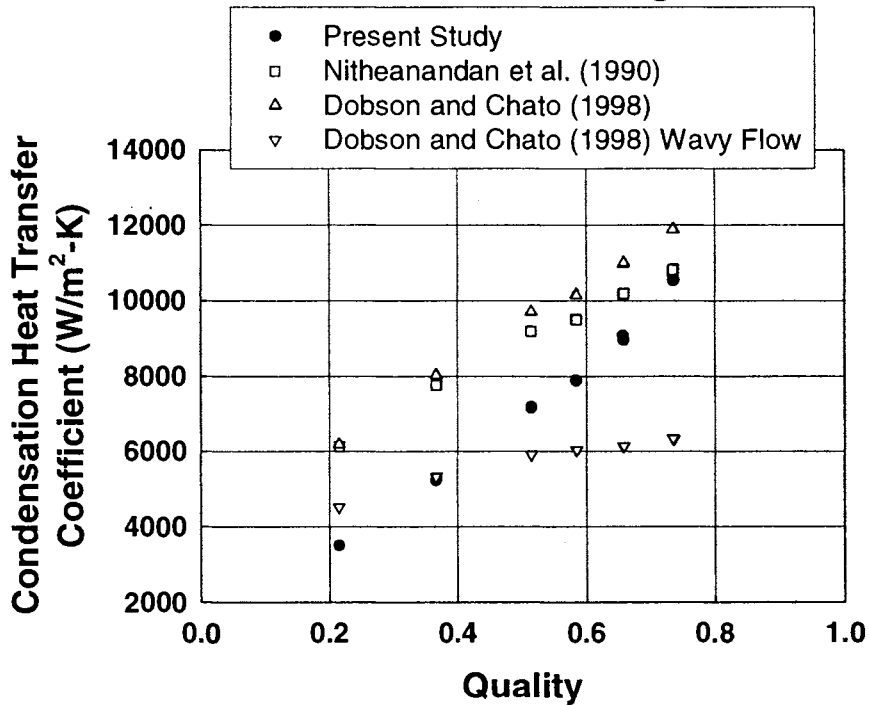


Figure D10. Flow Regime-Based Correlations and Experimental Heat Transfer Coefficients for Test Section C20 at  $G = 600 \text{ kg/m}^2\text{-s}$

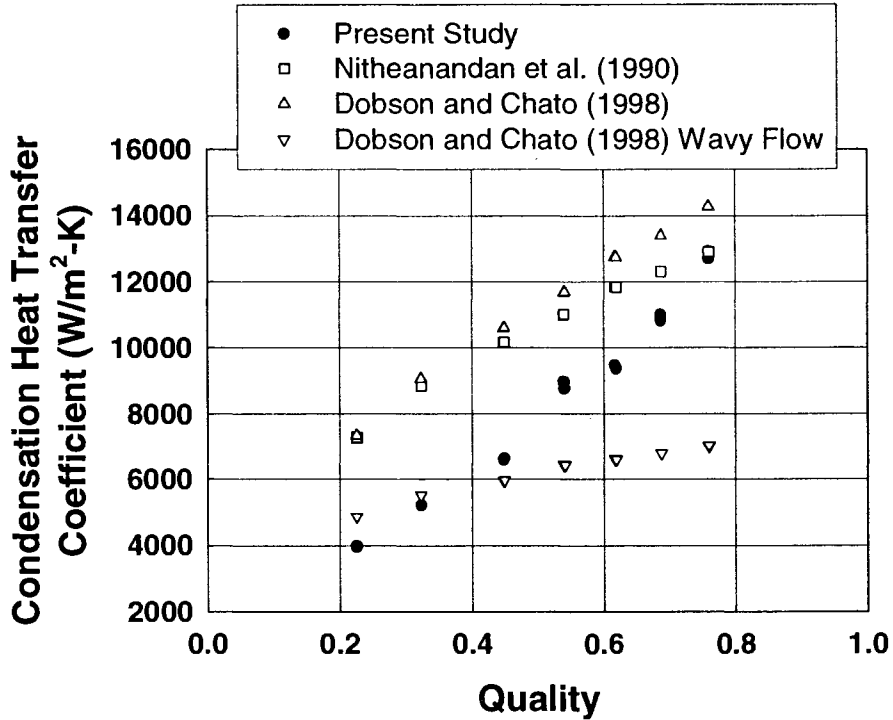


Figure D11. Flow Regime-Based Correlations and Experimental Heat Transfer Coefficients for Test Section C20 at  $G = 750 \text{ kg/m}^2\text{-s}$

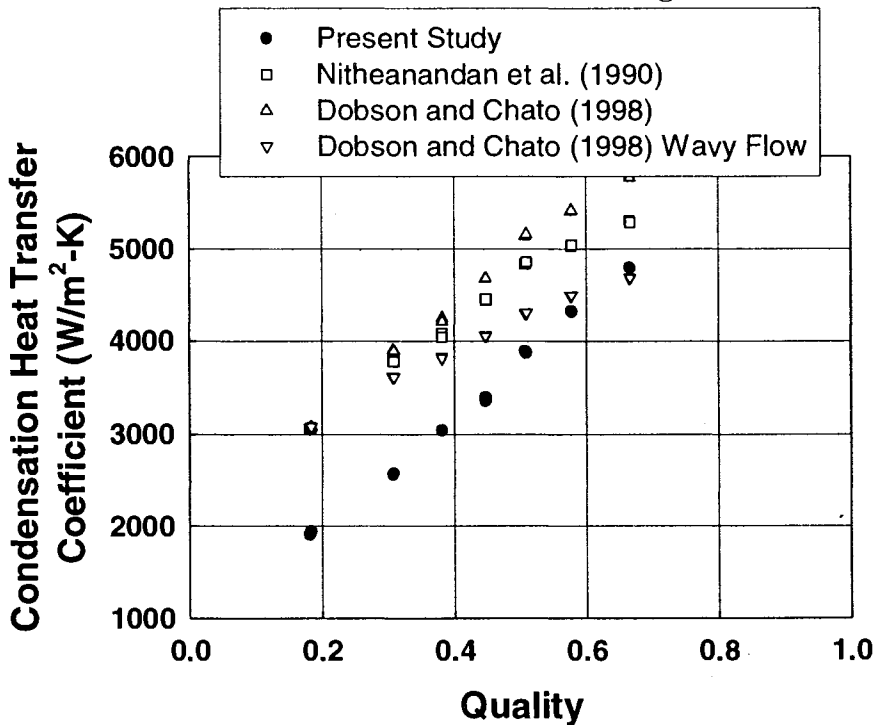


Figure D12. Flow Regime-Based Correlations and Experimental Heat Transfer Coefficients for Test Section C30 at  $G = 300 \text{ kg/m}^2\text{-s}$

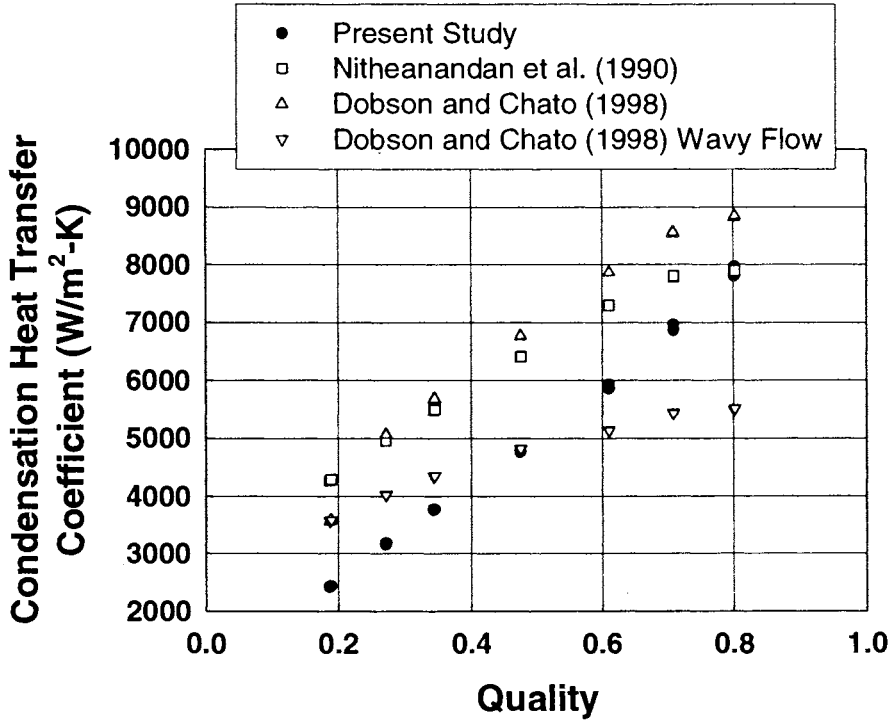


Figure D13. Flow Regime-Based Correlations and Experimental Heat Transfer Coefficients for Test Section C30 at  $G = 450 \text{ kg/m}^2\text{-s}$

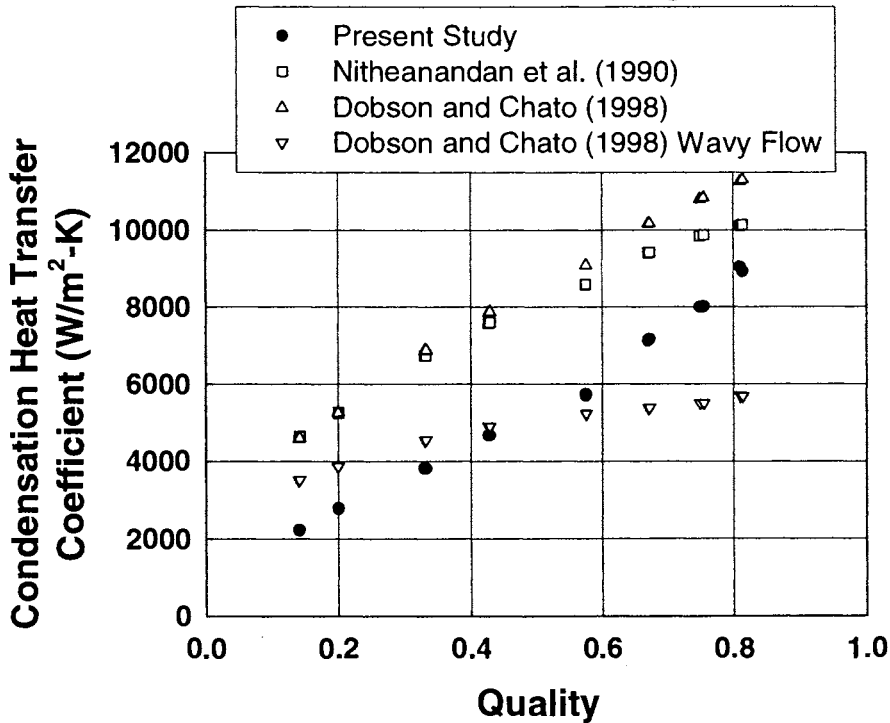


Figure D14. Flow Regime-Based Correlations and Experimental Heat Transfer Coefficients for Test Section C30 at  $G = 600 \text{ kg/m}^2\text{-s}$

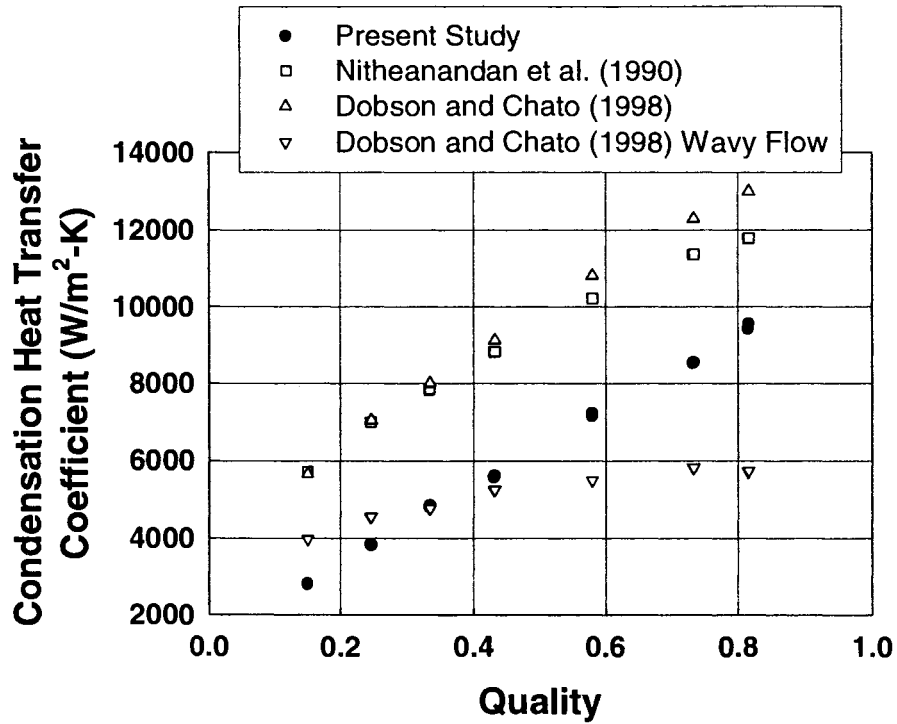


Figure D15. Flow Regime-Based Correlations and Experimental Heat Transfer Coefficients for Test Section C30 at  $G = 750 \text{ kg/m}^2\text{-s}$